Realistic Wind Loads on Unreinforced Masonry Walls

A Thesis Submitted to the College of

Graduate Studies and Research

In Partial Fulfillment of the Requirements

For the Degree of Master of Science

In the Department of Civil and Geological Engineering

University of Saskatchewan

Saskatoon

By

Alexander Udey

Permission to Use

In presenting this thesis in partial fulfillment of the requirements for a Postgraduate degree from the University of Saskatchewan, I agree that the Libraries of this University may make it freely available for inspection. I further agree that permission for copying of this thesis in any manner, in whole or in part, for scholarly purposes may be granted by the professor or professors who supervised my thesis work or, in their absence, by the Head of the Department or the Dean of the College in which my thesis work was done. It is understood that any copying or publications or use of this thesis or parts thereof for financial gain shall not be allowed without my written permission. It is also understood that due recognition shall be given to me and to the University of Saskatchewan in any scholarly use which may be made of any material in my thesis.

Requests for permission to copy or to make other uses of materials in this thesis in whole or part should be addressed to:

Head of the Department of Civil and Geological Engineering
University of Saskatchewan
57 Campus Drive
Saskatoon, Saskatchewan S7N 5A9

Abstract

Twenty full-scale unreinforced masonry walls were constructed and tested to failure in the Structures Laboratory at the University of Saskatchewan. The focus of the testing related to two primary objectives. The first objective was to study the effects that the support conditions of the walls had on their behaviour. The masonry wall specimens tested spanned vertically under the application of out-of-plane loads. Ten of the full scale walls were tested with support conditions that modeled ideal pinned connections at the top and bottom of the wall, while the remaining half of the walls were tested with nominally "pinned" supports that were similar to the supports typically encountered in practice. The second objective was to determine the effects that dynamic loads had on the behaviour of the walls. Half of the masonry specimens for each group of support conditions were loaded laterally with monotonically increasing quasi-static loads representative of the effects of uniform wind pressure, while the remaining specimens were loaded laterally with dynamic time histories that varied randomly in a manner that was representative of real "gusty" winds. The research was therefore done to determine the influence of load and connection type on the behavior of the masonry walls.

When comparing the effects of the support conditions, it was found that the walls constructed with realistic support conditions were able to resist larger out-of-plane loads, with greater ductility than the walls that had ideally-pinned supports. Specifically, the realistically-pinned walls required an average moment (of both the statically and dynamically loaded walls) that was 63% larger to cause mid-height cracking than the average mid-height moment required to cause mid-height cracking in the ideally-pinned walls.

After mid-height cracking occurred, the realistically-pinned walls exhibited reserve capacity, resulting in additional strength, such that the ultimate moment capacity of the realistically-pinned walls was 140% greater than the ultimate strength of the ideally-pinned walls, where the ultimate strength was the capacity of the wall at mid-height cracking. As a result, the ductility of the realistically-pinned walls was also significantly larger than that of the ideally-pinned walls. Specifically, the ductility ratio of the realistically-pinned walls was 70 (where the ductility ratio is defined as the displacement at the ultimate load divided by the displacement at mid-height cracking), while the ductility ratio of the ideally-pinned walls was unity (the ultimate load coincided with formation of the mid-height crack).

The results of the dynamically and quasi-statically loaded walls were harder to evaluate. In comparing the ideally-pinned walls it was found that the specimens that were loaded dynamically had an average moment capacity that was approximately 10% larger than the walls that were loaded quasi-statically, which was found to be statistically significant at the 90% level. However, the results from the realistically-pinned walls were not as conclusive. At mid-height cracking the dynamically loaded walls had an average moment capacity that was 24% lower than the quasi-statically loaded walls, which seems to contradict with the data from the ideally-pinned walls and from the literature suggesting that dynamic strengths should be higher. At the ultimate condition, the dynamically loaded walls had an average strength that was 12% larger than the quasi-statically loaded walls; however, these comparative results were not statistically significant at the 90% confidence level. It was also found that the dynamic loading failed the wall specimens as a result of sustained, large amplitude "gusts" rather than at the largest instantaneous peak load.

The displacement behaviour of the walls was generally independent of the method of loading, but, rather, largely dependent on the support conditions. The collapse of the wall specimens were all initiated when they reached a geometrically unstable displaced shape that was fairly consistent for a given support configuration, regardless of the type of load that was applied.

Lastly, results from a numerical model suggested that the dynamically loaded walls exhibited higher apparent stiffness properties as compared to the quasi-statically loaded walls. The difference in the apparent stiffness between the dynamic and quasi-static specimens decreased with increasing damage levels until the dynamic stiffness converged to the static stiffness near the collapse of the walls.

Acknowledgements

I would like to thank my supervisor Dr. Bruce Sparling for all of his encouragement and support. His guidance throughout the project was excellent, and I am thankful for the opportunity to work with such a knowledgeable and supportive mentor.

I would like to thank my committee members Dr. Lisa Feldman, Dr. Mohamed Boulfiza for their suggestions and support throughout this research.

I would like acknowledge the laboratory technicians Brennan Pokoyoway and Dale Pavier for their help and assistance during the construction and testing phases of the project. Additional acknowledgements go to Roy Nicolas from Gracom for his time and expertise in constructing the test specimens, and for the Engineering Shops for all of their time fabricating all of the parts needed to conduct the tests.

I would also like to thank the Saskatchewan Masonry Institute (SMI), the Canadian Masonry Design Centre (CMDC) and the National Science and Engineering Research Council (NSERC) for all of the finical support needed to complete this project.

Lastly, I would like to thank my family, friends and other graduate students, for the support and encouragement throughout the project. I would like to acknowledge the help of Brian Sibley, Aleksander (Sasha) Kisin, Daniel Cossette, Denise Sanchez, and Roanne Kelln for their help throughout the construction and testing of the masonry, and for making every day enjoyable.

Table of Contents

Table of Figures

Table of Tables

Table of Equations

List of Abbreviations

C.O.V.	Coefficient of Variation
FFT	Fast Fourier Transform
PSD	Power Spectrum Density

List of Symbols

$[C]$, C_{sys}	System damping matrix used in Newmark's β method
f	Frequency in Hz
f_n	Natural frequency
f_L	Lower frequency limit used in the autoregressive simulation
f_U	Upper frequency limit used in the autoregressive simulation
$F(t)$	Force at incremental time
$\{F_A\}$, F_{sys}	Vector of applied external forces for finite element model
$\{\Delta F_A\}$	Incremental force vector
$\{\Delta \hat{F}_A\}$	Incremental Pseudo-force vector used in Newmark's β method
$\{\delta F\}$	Unbalanced force vector for the nonlinear-response in Newmark's β method
k	Increment number (1,2,3,4) used in autoregressive simulation
k	Structure stiffness used in natural frequency
K_d	Factored quasi-static stiffness used in the numerical model
K_s	Quasi-static stiffness used in the numerical model
$[K]$, K_{sys}	System stiffness matrix used in Newmark's β method
$[\hat{K}]$	Pseudo-stiffness matrix used in Newmark's β method
L	Total height of the model wall (3.0 m)
m	Structure mass used in natural frequency
m_w	Weight of wall
$[M]$,M_{sys}	System mass matrix used in Newmark's β method
q	Wind pressure
$R^u(k\Delta\tau)$	Autocorrelation value
$S^u(f)$	Power spectral density function of gusty wind
t	Current time increment used in autoregressive simulation
T_A	Period of wind time history
$u(t)$	Instantaneous fluctuating wind velocity
u_*	Friction velocity of wind
$\bar{U}(z)$	Mean wind speed at an elevation of z above the ground surface
$\bar{U}_{10}$	Mean wind speed at a 10 m elevation
$\{v\}$	System displacement vector used in Newmark's β method
$\{\dot{v}\}$	System velocity vector used in Newmark's β method
$\{\ddot{v}\}$	System acceleration vector used in Newmark's β method

V_s	Wind speed
x	Normalized horizontal displacement
y	Wall height
y_h	Mid-height of the wall crack (1.6 m)
z	Reference height
z_o	Characteristic roughness parameter
β_N, γ_N	Parameters used in Newmark's β method
Δt	Time step increment used in time domain analysis
$\Delta\tau$	Time step increment used to generate simulated wind turbulence
$\{\delta v\}$	Incremental displacement vector for the nonlinear-response in Newmark's β method
$\{\delta \dot{v}\}$	Incremental velocity vector for the nonlinear-response in Newmark's β method
$\{\delta \ddot{v}\}$	Incremental acceleration vector for the nonlinear-response in Newmark's β method
κ_d	Quasi-static stiffness factor
ρ	Density of air
σ^2	Variance of original time history
$\phi_1,\phi_2,\phi_3,\phi_4,\phi_\varpi$	Weighting parameters used in autoregressive simulation of wind turbulence
$\Psi(y)$	Mode shape
$\varpi(t)$	Random Gaussian "shock" used in autoregressive simulation

Chapter 1: Introduction

1.1 Background

Masonry has been used as one of the main structural systems in building construction for thousands of years. Historic masonry structures were massive, and were constructed such that all of the components were primarily in compression. In that case, the mass of the structure typically accounted for the largest forces that the structure needed to resist. However, modern masonry is much lighter and more slender, and masonry assemblages are routinely designed to resist out-of-plane loads though bending, rather than primarily in compression.

Concrete masonry block construction is commonly used for partition walls in buildings or as a non-structural infill between the primary steel or concrete structure. In the case of internal partition walls, the masonry is only subjected to lateral loads arising from internal pressure differentials, which tend to be relatively small and steady. On the other hand, masonry that is used for the building envelope can experience larger, non-steady wind pressures.

Wind is generally considered to have two components: a steady mean component, and a dynamic component that fluctuates randomly (gusts) about the mean value of the wind. Current code methods for the structural design of buildings approximate wind loads using constant static pressure that is intended to represent the peak effective out-of-plane pressure that is applied from the wind. However, the representative static pressure may not accurately reproduce the behaviour of the structure due to the real wind since the dynamic interaction of the loading and the structure is not explicitly considered.

For any structure to fail, it needs to deform as a result of movement. However, because of the large mass inherent in masonry, inertial effects in masonry walls may play a role in helping to resist the applied forces. This physical characteristic of masonry may be important to the behaviour of the wall under wind loading because the out-of-plane forces generated by wind gusts are short-lived and may, therefore, be less effective in activating such a massive system.

An additional feature of structural design using masonry is the support conditions that are assumed during design. For simplicity, pin connections are generally assumed at the supports of unreinforced masonry walls that have no ability to resist rotation. However, when a support is constructed in practice with masonry, the physical properties of the masonry do not allow for free rotation. Specifically, the finite width and rectangular shape of the wall means that the wall has to rotate along one edge of the block

rather than about its centroid; also, there is added resistance from the bond between the block and mortar. The added restraint introduced by the support conditions can add reserve strength that was unaccounted for in the original design of the wall.

1.2 Objective

The primary objective of this research is to investigate the out-of-plane behaviour of unreinforced masonry walls subjected to lateral loads. Specifically, the research is intended to:

- Examine the displacement and ductility characteristics of unreinforced masonry walls that have different support conditions and are subjected to differing loading types;
- Investigate the influence that the support conditions have on the load-resistance characteristics of unreinforced masonry walls;
- Study the load-resistance characteristics of unreinforced masonry that is subjected to different loading types; and
- Identify possible physical mechanisms that may cause the different behavioural characteristics in the unreinforced masonry walls tested as part of this study.

1.3 Scope

One focus of the testing program was to determine the difference in strength and ductility between idealized masonry walls that approximate typical design assumptions and realistic walls that more closely resemble conditions implemented in practice. Two types of pin connections at the base of the walls were tested: idealized pin connection created by placing masonry walls on a knife edge; and the realistic “pin” connection created by bonding the first course of masonry block with mortar onto a concrete foundation, similar to construction methods used in practice.

Additionally, two types of out-of-plane loading were applied to the unreinforced masonry walls. Quasi-static loading was applied under displacement control during which the applied load was monotonically increased to failure. Dynamically loaded walls, on the other hand, were tested under load control whereby the walls were subjected to predefined patterns of fluctuating loads that were increased in intensity until failure was achieved. Each dynamic wall test therefore comprised several simulated wind time histories, each of which lasted approximately 10 minutes.

All of the wall specimens were constructed using a constant nominal block size of 200 mm and mortar made using the same mix design. Each masonry wall specimen was 3 m tall and two and a half blocks

wide. Therefore, each wall specimen was fundamentally the same; the type of support connection and loading type were the only differences between the various test series.

1.4 Methodology

Testing was done to determine the effects on the behaviour of the masonry walls associated with the fixidity of the support connections (ideal or realistic) and the type of loading (quasi-static or dynamic) applied to the wall. To determine the effects of each condition, twenty unreinforced wall specimens were tested in four series:

- Ideally pinned, with monotonically increasing quasi-static load;
- Ideally pinned, with randomly fluctuating loads representative of gusty wind;
- Realistically pinned, with monotonically increasing quasi-static load; and
- Realistically pinned, with randomly fluctuating loads representative of gusty wind.

Ten wall specimens with the same connection types were tested in succession, with the load type alternating between static and dynamic loading. Additionally, vibration tests were conducted on each wall prior to the load tests to determine the natural frequencies of each wall specimen. Companion specimens were tested in conjunction with the wall specimens in order to correlate material and assemblage properties with the strength and behaviour of the wall specimens.

1.5 Thesis Overview

This thesis has five chapters, plus references and appendices. Chapter One presents the background, objectives, scope, and methodology of the thesis.

Chapter Two contains a literature review, presenting past research related to masonry walls under static and dynamic loading. Additionally, Chapter Two presents the theory required for the development of the mathematical models that were used for generating wind time histories used throughout the study, as well as a mathematical model to predict the behaviour of dynamically loaded wall specimens.

Chapter Three describes the design, construction and testing apparatus for the masonry wall specimens and the companion specimens that were tested.

Chapter Four presents the results from each individual physical wall test, a discussion of the results of these physical tests, and the implementation of a mathematical model study that was used to help determine the behavioral differences between the statically and dynamically loaded walls.

Chapter Five presents the conclusions obtained from the study and recommendations for future research work.

Chapter 2: Literature Review

2.1 Research on Masonry and Wind

A review of previous studies regarding the strength of masonry walls subjected to out-of-plane loads reveals that there is little work that has been done with loads representing dynamic gusty wind. This chapter presents past studies that have been completed related to the out-of-plane behaviour of masonry subjected to out-of-plane loads. In addition, studies where wind is applied to civil engineering structures are presented.

2.1.1 Mechanics of Cementitious Materials

One material property that greatly influences the out-of-plane strength of vertically spanning masonry walls is the tensile bond strength between block or brick and the mortar. Laird (2013) describes problems with the empirical design method that is currently included in the Canadian masonry code, CSA S304.1 (CSA 2004). One problem is that the specified values of tensile strength given by CSA S304.1 do not reflect the actual bond strength that is seen in practice. There were multiple reasons cited for the difference in strength, including the fact that current mortars are not the same as the mortars that were in use when the code was established, or that the curing condition of the mortar plays a significant role in the bond strength.

An additional factor that can influence the strength of cementitious materials is the rate at which the material is being loaded. Zielinski and Reinhardt (1982) and Burnett et al. (2007) completed testing on the tensile strength of mortar cylinders and brick-mortar bond using a Split Hopkinson Pressure Bar (SHPB) test. The results of these tests showed that a rate of loading that is faster than quasi-static can increase the tensile strength by a factor of as much as three.

It was suggested by Zielinski and Reinhardt (1982) and Burnett et al. (2007) that the increase in tensile strength of the mortar is based on the failure mechanics of the mortar. In quasi-static loading, cracking originates from areas where micro-cracking was already present. The slow application of load allows time for the stresses to redistribute throughout the mortar, and cracking can occur along the path of least resistance. Under high rates of loading, forces do not have time to redistribute themselves and cracking cannot form along a path of least resistance. This causes an apparent increase in strength of the mortar for a short time.

2.1.2 Out-of-Plane Loading of Masonry

Most of the out-of-plane masonry wall testing performed to date has been done with quasi-static load schemes. Furthermore, within this small set of studies considering out-of-plane testing, the behaviour of

unreinforced masonry was not a focal point, limiting the information relating to the behaviour of unreinforced masonry walls.

The laboratory tests conducted by Baker (1972), Drysdale and Essaway (1988), Hoeppner et al. (2002), and Derakshen and Ingham (2008) were performed on a verity of unreinforced wall specimens made of either brick or concrete block. All of the wall panels in the cited studies were loaded quasi-statically by airbag load systems, applying pressure across the entire face of the wall specimens. Additionally, different configurations of the supports where studied making the walls span horizontally or vertically, generally using simple supports. The simple supports were typically created by using either a roller or a knife edge, where the wall was placed on a thin vertical support. From these studies a small selection of wall specimens was of interest to the current study.

Since the masonry specimens in each of the cited studies had different dimensions, a direct comparison of the failure loads of the specimens cannot be made. Therefore, the modulus of rupture for these specimens was calculated using the cited failure loads and given dimensions of the walls, and assuming the values from Appendix B of Drysdale and Hamid (2005) for the bedded area and section modulus of the specimens. Additionally, for Baker (1972), the dimensions of the bricks that were used were not given; therefore, the modulus of rupture was not calculated for that study.

Baker (1972) conducted tests on 21 brick wall panels. However, only one wall panel test is relevant. The brick masonry specimen in question had a vertical span of 27 inches (0.686 m) and was simply supported at the top and bottom of the wall. The ultimate load reported by Baker (1972) for this specimen was 51 psf (2.44 kPa). However, since the focus of the study was wall panels that were supported on all sides, information pertaining to the mode of failure or displacements of the single simply supported panel was not given.

The purpose of the Drysdale and Essaway (1988) study was to determine the behaviour of unreinforced block masonry with different support configurations. Simple supports where placed along two, three or four edges of the wall panel. Three vertically spanning wall specimens with a span length of 2.8 m are of note. The strength of these walls was governed by a single crack that formed at the mid-height of the wall; the appearance of the crack and the designated failure of the wall coincided with each other. The formation of the crack occurred at a deflection less than 1 mm with an average pressure of 3.10 kPa, corresponding to an approximate modulus of rupture of 0.62 MPa.

In addition to the wall tests, bond wrench testing was completed with companion specimens, using two different concrete blocks; autoclaved and bubble cured. The mean bond strength was reported to be 0.37

MPa for the autoclave block, averaged over ten tests, and 0.47 MPa for the bubble cured blocks, for which 86 mortar joints were tested.

The research conducted by Hoeppner et al. (2002) was focused on strengthening unreinforced brick masonry with CFRP strips. Two different types of brick were used for the two vertically spanning (unreinforced) control specimens. These walls had a vertical span of approximately 1.25 m, and the failure of the walls was governed by the formation of a crack within the middle third of the walls. It was noted that the wall specimens may have been unevenly loaded by the airbag since the required pressure to fail the unreinforced walls was so low that the airbag may have been unevenly filled, resulting in a non-uniform pressure being applied to the walls. The walls failed at pressures of 1.40 kPa and 2.01 kPa, corresponding to a calculated modulus of rupture of 0.31 MPa and 0.27 MPa respectively. Complete collapse of one of the walls occurred at approximately 12 mm of mid-height deflection.

Lastly, Derakshen and Ingham (2008) conducted testing on New Zealand brick. Three walls where tested with different levels of axial compression. For the non-load bearing wall, the maximum lateral pressure achieved was 1.15 kPa, corresponding to a modulus of rupture of 0.18 MPa. At the maximum loading, a horizontal crack formed at approximately 60% of the height of the wall (3.5 m), at a location suggesting that a crack was already present or had formed with low amounts of energy being released.

Like the previously cited studies, Grimm and Tucker (1985) conducted out-of-plane testing on unreinforced brick masonry wall specimens where load was applied by an airbag loading system. However, the supports conditions were less like ideal pinned supports than those used in the previously cited studies. The walls were tested insitu, where the load frame was moved into position behind the wall and reaction beams were placed around the wall to connect it to the loading frame. In total 23 wall specimens with a vertical span of 2.43 m where tested and an average strength of 326 psi (2248 kPa) was found, although this bond strength appears to be very high relative to other values published in the literature, corresponding to an approximate modulus of rupture of 1176 MPa, here, the non-idealized supports are most likely the cause of the very large loads, as compared to the other cited studies. No additional information on the behaviour of the walls was presented.

Seven full scale walls of various sizes where tested by de Veky and West (1980) as a way to compare the results that they obtained from smaller wallet tests. Like all of the previously cited studies, the load applied to the walls was supplied by an airbag system. Four of the walls were constructed of an aerated concrete block while the remaining three walls where constructed from a lightweight aggregate block. The tallest walls (5.5 m) had strengths of 0.83 kPa and 1.5 kPa (modulus of rupture of 2.3 MPa and 4.2 MPa, respectively) for the aerated and lightweight block, respectively; the strength of the walls increased

as the walls became shorter (2.7 m), for which the strength of the walls was 1.4 kPa (modulus of rupture of 0.9 MPa) and 2.3 kPa (modulus of rupture of 1.5 MPa), respectably. It was noted that the support conditions used for these tests were somewhere between a simple support and a fully fixed support, resulting in the large apparent moduli of rupture of these specimens compared to the specimens in the other cited studies that were simply supported.

The smaller wallets where tested in both the vertical and horizontal direction. The wallets where simply supported and, rather than being loaded by airbags, were loaded using a multi-point loading scheme, where the wallets were loaded with a four-point loading method. Loads were applied in a line across the face of the wall at two locations, in addition to the two ideal support reactions. This method of loading created a region of constant moment between the two points of loading. Since the wallets were shorter than full sized walls, the wallets carried higher applied pressures; however moduli of rupture values ranged from 0.09 MPa to 0.67 MPa.

Unlike all of the previously cited studies where airbags where used to load full scale wall specimens, Albert et al. (2001) applied loads to masonry specimens using a four-point loading method. Like Hoeppner et al. (2002) the purpose was to determine the behaviour of unreinforced masonry strengthened by FRP. The unreinforced control specimen of interest was simply supported with knife edges, having a span of 4 m. The reported maximum load of the specimen was equated 1 kN with a mid-span deflection of 0.7 mm. Assuming a correlated pressure over the area of the wall, the maximum pressure resisted by the specimen was 0.21 kPa, corresponding to a modulus of rupture of 0.06 MPa, the lowest bond strength of the full sized walls cited. However, similar to the other cited studies, the strength of the wall was determined when a single crack formed at the 13^{th} of 19 mortar joints (within the constant moment region).

Bean Popehn et al. (2008) used two additional points of loads, resulting in a six-point loading system: four-points of load applied to the face of the walls and two ideal supports. The moment distribution produced by this method closely approximated the moments obtained with uniform loading. The test walls considered by these researchers were axially loaded and, therefore, cannot be directly compared to previously discussed studies. However, the failure mode of these walls was consistent with the others, where a single crack formed at or near mid-height of the walls. Additionally the bond strength between the concrete block and mortar was reported to be 0.105 MPa.

Lastly, ASTM standard C1717 (ASTM 2010) gives procedures for strength testing of masonry wall panels. The methods used by the masonry researchers cited above have been carried out in accordance

with the test methods described within the ASTM standards. The standard recommends the use of four-point loading, but does make allowances for the use of an airbag system.

From the above cited studies, regardless of the method of loading, support conditions, or material of the wall, the behaviour of all the wall specimens shared similar characteristics at failure. As the applied load increased, a single horizontal crack forming at the interface between the block/brick and mortar was observed near, or at, the middle of the wall specimen. The formation of the crack coincided with the maximum strength of the wall specimens. When the deflections of the walls at cracking where noted, the displacement required to crack the walls was typically less than 1 mm, as noted in Drysdale and Essaway (1988) and Albert et al. (2001), where concrete block was used in both studies.

From the above cited studies, only three conducted their research on concrete block specimens. The modulus of rupture of the 2.8 m tall walls found in Drysdale and Essaway (1988) was 0.62 MPa. In de Veky and West (1980), the two 2.7 m spanning walls had moduli of rupture of 0.9 MPa and 1.5MPa from the different block types that were described previously. These results are within the same order of magnitude for walls that where of similar height. The last study conducted by Albert et al. (2001) had walls spanning 4 m and had a calculated bond strength that was an order of magnitude lower at 0.06 MPa. The increased height and differing load system used by Albert et al. (2001) may have caused the decrease in strength of the wall specimen, in addition to other material factors.

Of additional note, the mortar/block bond strength was measured by Drysdale and Essaway (1988) for two different types of blocks, giving strengths of 0.37 MPa and 0.47 MPa, respectively for the blocks mentioned above. Additionally, Bean-Popehn et al. (2008) gives a value for the bond strength at 0.105 MPa. The large difference in dates of these two studies (1988 vs. 2008) may explain the reason for the large difference between the bond strengths. As described by Laird (2013), different types of cement that are used can generate large differences in tensile strength.

2.1.3 Dynamic Loading of Masonry Walls

There is limited research pertaining to out-of-plane load testing of masonry walls subjected to wind loads. Work that has been completed includes support motions that represent earthquake loads, and blast loads.

Griffith et al. (2004) studied static and dynamic testing on brick walls with different degrees of slenderness. Using a shake table apparatus, the walls were subjected to different forms of support motion (impulse support displacement and earthquake excitation). Quasi-static loading was applied at mid-height of some wall specimens so that comparisons could be made. The authors found that the static tests gave a good approximation to the response of a wall dynamically loaded by support motion. When the walls

were loaded by support motion, they did not fail as soon as cracking formed; instead, there was some added capacity due to dynamic rocking of the wall. The authors concluded that the peak displacement of the wall has more influence on the ultimate state at collapse of the wall than the forces that were applied.

In addition to the support motion tests, Beak et al. (1994) compared plain concrete and brick masonry walls under static and blast loads. The wall panels were 2-way spanning, and were confined by a steel frame. Each wall had its natural frequency tested after each blast phase to check for any damage in the wall due to the blast. It was found that static tests were not suitable to predict the behaviour of the wall specimens under blast loading. This was due to the methodology of the static testing where the weight of the walls was a major portion of the failure load, resulting in a failure load that was unable to approximate the dynamic response.

Similarly, blast tests were recently conducted at McMaster University on one-third scale models of reinforced concrete masonry walls. The research of Elsayed et al. (2013) and Simonds et al. (2013) was focused on one-way spanning walls, while the specimens of Simonds et al. (2013) had boundary elements in the horizontal direction. Under sufficiently large blast loads, the wall specimens formed horizontal cracking at the mid-height of the walls. This again shows that the general mode of failure of the wall specimens is the same regardless of the type of loading.

2.1.4 Wind Loads on Structures

There currently is little work done with masonry that is subjected to wind-like loads. However, wind on structural systems is well researched. Since wind is spatially and temporally random, there are infinite possibilities of the load that can be produced by the wind. Therefore, there are multiple methods that can be used to obtain time histories of wind that can be used to load structural systems.

A popular method of obtaining wind data is to conduct wind tunnels studies on small-scale replicates of a structure. The pressure profile that is obtained from the wind tunnel can then be applied onto the test specimens. Barnard (2000), Surry et al. (2007), Morrison and Kopp (2010), and Kopp et al. (2012) have used this method for obtaining wind time histories for full-scale testing. This method of wind profile generation is well suited to the studies done by Surry et al. (2007), Morrison and Kopp (2010), and Kopp et al. (2012) at the “Three Little Pigs” testing facility in which the pressure profiles that were measured in the wind tunnel can be applied to full-scale structures.

The second type of wind load that can be used are in-situ measurements of real wind that are recorded for structures or locations of interest. Juhásová (1997) applied real wind-time histories to models of slender structures, and Henderson and Gineger (2011) applied measured real wind to roof cladding. In both cases,

they were able to use the real wind record effectively within their studies. However, a problem with using real wind, as noted by Gani et al. (2009), is that, in some cases, it is not practical to measure the in-situ wind profile since the structures of interest can be too large. Also, the probability of being able to observe and record a design wind storm is quite remote since the return period for such a storm is so long.

A third method of obtaining wind profiles is to mathematically generate simulated wind-time histories. Deodatis (1996), Sparling and Davenport (1998), and Gani et al. (2009) were able to create wind profiles that agree with the spatial and temporal characteristics of real wind, and used them effectively in numerical response calculations. The benefits of this method include being able to obtain wind profiles at all locations of interest for the use in modeling, where similarly intensive measurements of real wind would not be practical to obtain; in addition, the modeling of a complex structure is often difficult and expensive in wind tunnel tests. Therefore, numerical simulations of turbulent wind were used in this study. Details of the method for the generation of wind are described in Section 2.2.1.

2.1.5 Summary of Literature Related to the Loading of Masonry Walls

Most of the research that was conducted used airbags to load the wall specimens. The benefit of using an airbag is that the loads applied by the airbag give a moment distribution that is similar to that produced by a uniform wind. However, an airbag applies increasing load in a single direction (like quasi-static loads), making it unsuitable to reproduce a highly dynamic fluctuating load (wind). Therefore, a load system that uses a hydraulic actuator applied in four-point loading was deemed to be the most appropriate type of loading for this study.

Secondly, the supports of the wall specimens have typically been designed as ideal pin connections. Of the papers cited, the behaviour of the wall specimens during testing was not presented. This leaves missing information on the effects of supports on the strength of the walls.

Lastly, the behaviour of masonry walls when subjected to wind loads has not been researched, leaving a gap in the existing knowledge base. However, when conducting research using wind-like loading, mathematically generating a wind profile can be effectively used to replace wind profiles that are obtained from recording real wind or wind tunnel studies.

2.2 Theory for Wind and Dynamic Simulations

This section presents the theory required for the use of the autoregressive process that mathematically constructs the wind time histories that were used to load the test specimens dynamically. Additionally, the theory required for a time domain model of the dynamic behaviour of a wall specimen is presented.

2.2.1 Modeling of Wind

The numerical simulated wind time histories for this study were created using the process described below. In general, the method works by extrapolating the next time step in the wind speed series by weighting previous values of the wind speed and applying a weighted random "shock" value. By correlating the future value with past values, the time history will not be completely random; instead, by using appropriate weighting factors, the time history will have a temporal structure that is similar to patterns observed in real wind.

2.2.2 Autoregressive Process

The method used for mathematically generating wind in this study was an "autoregressive" process. The methodology used for this research was the same as the methods used in Sparling (1995); however, the autoregressive process was simplified to a single point. The general form of the equation for determining the instantaneous fluctuating wind speeds for n_p points in a three dimensional space is given as:

$$\{u(t)\}_{n_p\times 1} = \sum_{k=1}^{p} [\phi_k]_{n_p\times n_p} \{u(t-k\Delta\tau)\}_{n_p\times 1} + [\phi_\varpi]_{n_p\times n_p} \{\varpi(t)\}_{n_p\times 1} \qquad \text{Eq. 2.1}$$

where p is the order of the autoregressive process. The matrix of weight factors $[\phi_k]_{n_p\times n_p}$ weighs the k^{th} previous wind speeds, given by $\{u(t-k\Delta\tau)\}_{n_p\times 1}$. The vector of random shocks is denoted by $\{\varpi(t)\}_{n_p\times 1}$ and, like the previous wind speeds, the random shocks are weighted by $[\phi_\varpi]_{n_p\times n_p}$.

A fourth order autoregressive process was used in the current study, where four prior, known, wind speeds are used to extrapolate the next wind speed value. For simplicity, though, a second order process is described here. The fourth order equations are expanded from the second order and are presented in Section 2.2.6, once the entire method is developed. By simplifying Eq. 2.1 to the second order (p = 2), the resulting equation is:

$$\{u(t)\} = [\phi_1]\{u(t-\Delta\tau)\} + [\phi_2]\{u(t-2\Delta\tau)\} + [\phi_\varpi]\{\varpi(t)\} \qquad \text{Eq. 2.2}$$

In this study, the wind being applied to the wall specimens was assumed to be perfectly correlated spatially (non-varying through space), so that n_p was equal to 1, allowing Eq. 2.2 to be simplified to:

$$u(t) = \phi_1 u(t-\Delta\tau) + \phi_2 u(t-2\Delta\tau) + \phi_\varpi \varpi(t) \qquad \text{Eq. 2.3}$$

where $u(t)$ is the instantaneous wind speed at the current time increment, t, and $u(t-k\Delta\tau)$ is the wind speed at the k^{th} previous increment of the time step, $\Delta\tau$. The weighting parameters ϕ_1 and ϕ_2 weight the values of the previous wind speeds, influencing the magnitude of the new wind speed. Similarly, ϕ_ϖ

weights the value of the random shock, $\varpi(t)$. The random shock value is generated such that is has an average value of zero and a variance of one; this random shock value is used to introduce the necessary random variation in the next point in the series.

2.2.3 Weighting Factors

At the start of the simulation process, the weighting factors in Eq. 2.2 are the only unknowns, and need to be determined before the wind speed series can be generated. Therefore, by post-multiplying Eq. 2.3 by $u(t-\Delta\tau)$ and averaging over time, the result is:

$$\overline{u(t)\,u(t-\Delta\tau)} = \phi_1\overline{u(t-\Delta\tau)\,u(t-\Delta\tau)} + \phi_2\overline{u(t-2\Delta\tau)\,u(t-\Delta\tau)} + \phi_\varpi\overline{\varpi(t)u(t-\Delta\tau)} \quad \text{Eq. 2.4}$$

where $\overline{u(t)\,u(t-\Delta\tau)}$ is the time-averaged value of the product of $u(t)$ and $u(t-\Delta\tau)$, defined as the autocorrelation value $R^u(\Delta\tau)$. Similarly, the products of $\overline{u(t-\Delta\tau)\,u(t-\Delta\tau)}$ and $\overline{u(t-2\Delta\tau)\,u(t-\Delta\tau)}$ give the autocorrelation terms $R^u(0)$ and $R^u(\Delta\tau)$, respectively. Since the value of $\varpi(t)$ is random and uncorrelated with past or future values the product time-averaged of $\varpi(t)u(t-\Delta\tau)$ is zero; therefore, Eq. 2.4 simplifies to:

$$R^u(\Delta\tau) = \phi_1 R^u(0) + \phi_2 R^u(\Delta\tau) \quad \text{Eq. 2.5}$$

Similarly, post-multiplying Eq. 2.4 by $u(t-2\Delta\tau)$ and averaging over time results in:

$$R^u(2\Delta\tau) = \phi_1 R^u(\Delta\tau) + \phi_2 R^u(0) \quad \text{Eq. 2.6}$$

Eq. 2.5 and Eq. 2.6 are known as the Yule-Walker equations and can be written in the combined form of:

$$\begin{bmatrix} R^u(\Delta\tau) \\ R^u(2\Delta\tau) \end{bmatrix} = \begin{bmatrix} R^u(0) & R^u(\Delta\tau) \\ R^u(\Delta\tau) & R^u(0) \end{bmatrix} \begin{bmatrix} \phi_1 \\ \phi_2 \end{bmatrix} \quad \text{Eq. 2.7}$$

Rearranging Eq. 2.7 to solve for the weighting parameters yields:

$$\begin{bmatrix} \phi_1 \\ \phi_2 \end{bmatrix} = \begin{bmatrix} R^u(0) & R^u(\Delta\tau) \\ R^u(\Delta\tau) & R^u(0) \end{bmatrix}^{-1} \begin{bmatrix} R^u(\Delta\tau) \\ R^u(2\Delta\tau) \end{bmatrix} \quad \text{Eq. 2.8}$$

From Eq. 2.8, the wind speed weight parameters can be determined. In a manner similar to determining Eq. 2.8, the weight factor for the random shocks can be determined by post-multiplying Eq. 2.3 by $u(t)$ and averaged over time, results in:

$$R^u(0) = \phi_1 R^u(\Delta\tau) + \phi_2 R^u(2\Delta\tau) + \phi_\varpi R^{\varpi u}(0) \quad \text{Eq. 2.9}$$

where:

$$R^{\varpi u}(0) = \overline{\varpi(t)u(t)} \quad \text{Eq. 2.10}$$

If Eq. 2.3 is substituted into Eq. 2.10 for $u(t)$, this results in:

$$R^{\varpi u}(0) = \phi_1\overline{\varpi(t)u(t-\Delta\tau)} + \phi_2\overline{\varpi(t)u(t-2\Delta\tau)} + \phi_{\varpi}\overline{\varpi(t)\varpi(t)} \quad \text{Eq. 2.11}$$

where $\overline{\varpi(t)u(t-k\Delta\tau)}$ is uncorrelated and therefore is zero, reducing Eq. 2.11 to:

$$R^{\varpi u}(0) = \phi_{\varpi}R^{\varpi}(0) \quad \text{Eq. 2.12}$$

where $R^{\varpi}(0)$ is the autocorrelation term for the random shocks, and is mathematically equal to the variance, which is unity. Substituting Eq. 2.12 into Eq. 2.9 and simplifying, the resulting equation is:

$$R^{u}(0) = \phi_1 R^{u}(\Delta\tau) + \phi_2 R^{u}(2\Delta\tau) + {\phi_{\varpi}}^2 \quad \text{Eq. 2.13}$$

which, rewritten to solve for the weighting parameter, gives:

$$\phi_{\varpi}^2 = R^{u}(0) - \phi_1 R^{u}(\Delta\tau) - \phi_2 R^{u}(2\Delta\tau) \quad \text{Eq. 2.14}$$

2.2.4 Autoregressive Parameters

With Eq. 2.8 and Eq. 2.14, the weighting parameters can be determined once the autocorrelation terms are known. The autocorrelation parameter can be described in the frequency domain by applying a Fourier transform to the wind power spectral density function (spectrum), resulting in:

$$R^{u}(k\Delta\tau) = \int_0^{\infty} S^{u}(f)e^{i2\pi fk\Delta\tau}\mathrm{d}f \quad \text{Eq. 2.15}$$

where f is frequency and $S^{u}(f)$ is wind velocity auto-spectrum, a known (or assumed) function that describes how the energy of the wind is distributed with frequency. The exponential portion of Eq. 2.15 can be removed by using Euler's formula and, neglecting the imaginary component, the autocorrelation function can be rewritten as:

$$R^{u}(k\Delta\tau) = \int_0^{\infty} S^{u}(f)\cos(2\pi fk\Delta\tau)\mathrm{d}f \quad \text{Eq. 2.16}$$

However, stable results for $R^{u}(k\Delta\tau)$ can be obtained by numerically integrating Eq. 2.16 in the form of:

$$R^u(k\Delta\tau) = \int_{\ln(f_L)}^{\ln(f_U)} S^u(f)\cos(2\pi f k\Delta\tau)\mathrm{d}(\ln f) \qquad \text{Eq. 2.17}$$

where f_U and f_L are the upper and lower frequency limits of the numerical integration. The wind velocity auto-spectrum, $S^u(f)$, that was used was proposed by Kaimal et al. (1972). Presented in its normalized form, the elevation dependent expression for the wind velocity auto spectrum is expressed as:

$$\frac{fS^u(z,f)}{u_*^2} = \frac{200\left(\frac{f\,z}{\bar{U}(z)}\right)}{\left[1+50\left(\frac{f\,z}{\bar{U}(z)}\right)\right]^{5/3}} \qquad \text{Eq. 2.18}$$

where z is the reference height, $\bar{U}(z)$ is the mean wind speed at the reference height, and u_* is given by the formula:

$$u_* = \frac{0.4\,\bar{U}_{10}}{\ln\left(10/z_o\right)} \qquad \text{Eq. 2.19}$$

where z_o is surface roughness parameter and $\bar{U}_{10}$ is the mean wind speed at an elevation of 10 m. Therefore, the spectrum of the wind can be defined, and the wind speed profiles can be generated. Since the method is dependent on previous values in the time series, errors occur at the beginning of the time history due to the effect of artificial boundary conditions. To mitigate this effect, an initial 5000 "dummy" time series points were generated and removed from the beginning of the time history. Details regarding specifics of the simulations used in this study are provided in Section 3.8.

2.2.5 Interpolation

Lastly, the autoregressive process is only conditionally stable (Box et al. 2008). For reliable results, there needs to be a measureable change between the values $u(t)$ and $u(t-\Delta\tau)$ to produce meaningful values of $R^u(k\Delta\tau)$. Therefore, a larger time step than what was desired for the final time history was necessarily used for generating the wind profile. A *sinc* function, proposed by Wyatt and May (1973), was therefore used to interpolate intermediate points at more closely spaced time steps, since it does not add any undesired frequency content.

The *sinc* function expands $u(t)$ generated at a time interval of $\Delta\tau$ by interpolating additional points at a new interval of Δt between the range of $t = k\Delta\tau$ and $t = (k+1)\Delta\tau$ by using:

$$u(k\Delta\tau + i\Delta t) = \sum_{j=-n}^{n+1} a_j \, u(\{k+j\}\Delta\tau) \frac{\sin\left[\pi\left(\frac{i\Delta t}{\Delta\tau} - j\right)\right]}{\pi\left(\frac{i\Delta t}{\Delta\tau} - j\right)} \qquad \text{Eq. 2.20}$$

where i is the i^{th} increment of Δt and n is the number of points from the unexpanded series used to interpolate the new points, and

$$a_j = \begin{cases} 1 \text{ for } -n+1 < j < n \\ 1/2 \text{ for } j = -n \text{ or } (n+1) \end{cases} \qquad \text{Eq. 2.21}$$

2.2.6 Fourth Order Equations

The instantaneous wind speed given at time, t, by converting Eq. 2.3 to the forth order is:

$$u(t) = \phi_1 u(t-\Delta\tau) + \phi_2 u(t-2\Delta\tau) + \phi_3 u(t-3\Delta\tau) + \phi_4 u(t-4\Delta\tau) + \phi_\varpi \varpi(t) \qquad \text{Eq. 2.22}$$

Similarly, expanding the Yule-Walker equations to find all of the weighting parameters, Eq. 2.8 becomes:

$$\begin{bmatrix} \phi_1 \\ \phi_2 \\ \phi_3 \\ \phi_4 \end{bmatrix} = \begin{bmatrix} R^u(0) & R^u(\Delta\tau) & R^u(2\Delta\tau) & R^u(3\Delta\tau) \\ R^u(\Delta\tau) & R^u(0) & R^u(\Delta\tau) & R^u(2\Delta\tau) \\ R^u(2\Delta\tau) & R^u(\Delta\tau) & R^u(0) & R^u(\Delta\tau) \\ R^u(3\Delta\tau) & R^u(2\Delta\tau) & R^u(\Delta\tau) & R^u(0) \end{bmatrix}^{-1} \begin{bmatrix} R^u(\Delta\tau) \\ R^u(2\Delta\tau) \\ R^u(3\Delta\tau) \\ R^u(4\Delta\tau) \end{bmatrix} \qquad \text{Eq. 2.23}$$

Lastly, the equation to determine the weighting parameter for the random shocks is given by:

$$\phi_\varpi^2 = R^u(0) - \phi_1 R^u(\Delta\tau) - \phi_2 R^u(2\Delta\tau) - \phi_3 R^u(3\Delta\tau) - \phi_4 R^u(4\Delta\tau) \qquad \text{Eq. 2.24}$$

2.3 Modeling of a Dynamic System

A single degree of freedom model was constructed to determine the theoretical response of masonry walls subjected to wind loads. Newmark's β method (Bathe and Wilson 1976) was selected as the method for the step-by-step integration scheme for the time domain analysis, assuming constant-average accelerations. For non-linear systems, an additional Newton-Raphson iteration procedure was included within each time step to ensure the equilibrium of the system. The model therefore consists of two parts, with the linear response of the system first determined with Newmarks's β method, followed by Newton-Raphson iteration to account for the non-linear behaviour of the system. This modeling method is similar to that successfully employed by Sparling and Davenport (1998).

2.3.1 Linear Response

The equation of motion that defines the response of a structural system is defined as:

$$[M]\{\ddot{v}\} + [C]\{\dot{v}\} + [K]\{v\} = \{F_A\} \quad \text{Eq. 2.25}$$

where [*M*], [*C*], and [*K*] are the mass, damping and stiffness matrices, respectively, which are used to define the model structure in Eq. 2.25. The force vector is given by $\{F_A\}$ represents the applied forces on the system, and $\{\ddot{v}\}$, $\{\dot{v}\}$ and $\{v\}$ are the accelerations, velocities, and displacements, respectively, that correspond to the system degrees of freedom.

For non-linear systems, using an incremental form of the equation of motion is preferable over the absolute values of the motion vectors. The incremental form is defined as:

$$[M]\{\Delta\ddot{v}\} + [C]\{\Delta\dot{v}\} + [K]\{\Delta v\} = \{\Delta F_A\} \quad \text{Eq. 2.26}$$

The incremental acceleration, velocity, and displacement vectors for the period of *t* to *t* + *Δt* are defined as:

$$\begin{aligned} \{\Delta v\} &= \{v\}_{t+\Delta t} - \{v\}_t \\ \{\Delta\dot{v}\} &= \{\dot{v}\}_{t+\Delta t} - \{\dot{v}\}_t \\ \{\Delta\ddot{v}\} &= \{\ddot{v}\}_{t+\Delta t} - \{\ddot{v}\}_t \end{aligned} \quad \text{Eq. 2.27}$$

Similarly, the incremental force is given as:

$$\{\Delta F_A\} = \{F_A\}_{t+\Delta t} - \{F_A\}_t \quad \text{Eq. 2.28}$$

It is assumed that the acceleration, velocity, and displacements are known at time *t* and that the applied force vector is known at times *t* and *t* + *Δt*. Additionally, the non-linear stiffness and damping matrices are known at time *t* and are assumed to remain constant over *Δt* during each iteration.

Newmark's β method assumes a relationship of the known acceleration at time *t*, with the unknown accelerations at the end of the time step. The equations that describe the relationship between the motion vectors were defined by Bathe and Wilson (1976) and are:

$$\begin{aligned} \{\ddot{v}\}_{t+\Delta t} &= \frac{1}{\beta_N(\Delta t)^2}(\{v\}_{t+\Delta t} - \{v\}_t) - \frac{1}{\beta_N(\Delta t)}\{\dot{v}\}_t - \left(\frac{1}{2\beta_N} - 1\right)\{\ddot{v}\}_t \\ \{\dot{v}\}_{t+\Delta t} &= \{\dot{v}\}_t + [(1+\gamma_N)\{\ddot{v}\}_t + \gamma_N\{\ddot{v}\}_{t+\Delta t}](\Delta t) \\ \{v\}_{t+\Delta t} &= \{v\}_t + \{\dot{v}\}_t(\Delta t) + \left[\left(\frac{1}{2} - \beta_N\right)\{\ddot{v}\}_t + \beta_N\{\ddot{v}\}_{t+\Delta t}\right](\Delta t)^2 \end{aligned} \quad \text{Eq. 2.29}$$

where β_N controls the variation of the acceleration within the time step; a constant acceleration that equals the average of the acceleration at the beginning and the end of the time step was assumed. To achieve

this, β_N equal to 1/4 was used. Similarly, γ_N defines the numerical (artificial) damping of the model. Since no numerical damping was desired, γ_N was set equal to 1/2.

For the use of these relationships in the incremental form, the incremental motion vectors from Eq. 2.27 where substituted into Eq. 2.29, resulting in incremental motion vectors being defined by:

$$\{\Delta\ddot{v}\} = \frac{1}{\beta_N(\Delta t)^2}\{\Delta v\} - \frac{1}{\beta_N(\Delta t)}\{\dot{v}\}_t - \left(\frac{1}{2\beta_N} - 1\right)\{\ddot{v}\}_t$$
$$\{\Delta\dot{v}\} = \frac{\gamma_N}{\beta_N(\Delta t)}\{\Delta v\} - \frac{\gamma_N}{\beta_N}\{\dot{v}\}_t - \left(\frac{\gamma_N}{2\beta_N} - 1\right)(\Delta t)\{\ddot{v}\}_t \qquad \text{Eq. 2.30}$$

Substituting Eq. 2.30 into the incremental equation of motion (Eq. 2.26), the resulting form is:

$$\left[\hat{K}\right]\{\Delta v\} = \left\{\Delta\hat{F}_A\right\} \qquad \text{Eq. 2.31}$$

where $\left[\hat{K}\right]$ is the pseudo-stiffness matrix and $\left\{\Delta\hat{F}_A\right\}$ is the pseudo-force vector, which are defined as:

$$\left[\hat{K}\right] = [K]_t + \frac{1}{\beta_N(\Delta t)^2}[M] + \frac{\gamma_N}{\beta_N(\Delta t)}[C]_t$$
$$\left\{\Delta\hat{F}_A\right\} = \{\Delta F_A\} + [M]\left(\frac{1}{\beta_N(\Delta t)}\{\dot{v}\}_t + \frac{1}{2\beta_N}\{\ddot{v}\}_t\right) \qquad \text{Eq. 2.32}$$
$$+ [C]_t\left(\frac{\gamma_N}{\beta_N}\{\dot{v}\}_t - \left(\frac{\gamma_N}{2\beta_N} - 1\right)(\Delta t)\{\ddot{v}\}_t\right)$$

where $[K]_t$ and $[C]_t$ are the stiffness and damping matrices that are redefined with each iterative solution step. The incremental approach for modeling non-linear systems using Newmark's Beta Method scheme is similar to the method described by Sparling (1995).

2.3.2 Iterative process for Nonlinear Response

Since the stiffness and damping of the system changes over Δt in nonlinear systems , a state of dynamic equilibrium will generally not be achieved at time $t + \Delta t$ using the linear methods described above. An unbalanced force is created from the linear model:

$$\{\delta F\}^i_{t+\Delta t} = \{F_A\}_{t+\Delta t} - [M]\{\ddot{v}\}^i_{t+\Delta t} - [C]^i_{t+\Delta t}\{\dot{v}\}^i_{t+\Delta t} - \{F_R\}^i_{t+\Delta t} \qquad \text{Eq. 2.33}$$

where i indicates the iteration, and the damping matrix $[C]$ is calculated at time step $t + \Delta t$. The vector $\{F_R\}$ represents the elastic restoring force at the end of the i^{th} iteration. Additionally, the incremental motion vectors found within the iteration are defined as:

$$\{\delta v\}^{i+1} = \{v\}^{i+1}_{t+\Delta t} - \{v\}^i_{t+\Delta t}$$
$$\{\delta\dot{v}\}^{i+1} = \{\dot{v}\}^{i+1}_{t+\Delta t} - \{\dot{v}\}^i_{t+\Delta t} \qquad \text{Eq. 2.34}$$

$$\{\delta\ddot{v}\}^{i+1} = \{\ddot{v}\}_{t+\Delta t}^{i+1} - \{\ddot{v}\}_{t+\Delta t}^{i}$$

When these equations are substituted into Eq. 2.30, the resulting equations that define the incremental changes in acceleration and velocity as a function of the new displacements are:

$$\{\delta\ddot{v}\}^{i+1} = \frac{1}{\beta_N(\Delta t)^2}\{\delta v\}^{i+1}$$
$$\{\delta\dot{v}\}^{i+1} = \frac{\gamma_N}{\beta_N(\Delta t)}\{\delta v\}^{i+1} \qquad \text{Eq. 2.35}$$

These equations are used in the incremental form of the equation of motion to determine when the iterative process is complete, where the incremental equations of motion for the i+1[th] iteration are given by:

$$[M]\{\delta\ddot{v}\}^{i+1} + [C]_{t+\Delta t}^{i}\{\delta\dot{v}\}^{i+1} + [K]_{t+\Delta t}^{i}\{\delta v\}^{i+1} = \{\delta F_A\}^{i}$$

or

$$\left[\hat{K}\right]^{j+1}\{\delta v\}^{j+1} = \{\delta F_A\}^{j} \qquad \text{Eq. 2.36}$$

where the updated pseudo-stiffness matrix is defined by:

$$\left[\hat{K}\right]^{j+1} = [K]_{t+\Delta t}^{j} + \frac{1}{\beta_N(\Delta t)^2}[M] + \frac{\gamma_N}{\beta_N(\Delta t)}[C]_{t+\Delta t}^{j} \qquad \text{Eq. 2.37}$$

2.3.3 Initial Conditions

At time $t = 0$, it is assumed that the wall is at rest, under static mean wind load. The static air pressure will cause initial displacement within the system. The elastic deflection of the system at $t = 0$ is found through iteration, where the initial displacement is found by:

$$[K]^0\{\bar{v}\}^{j=1} = \{\bar{F}\} \qquad \text{Eq. 2.38}$$

where $[K]^0$ is the stiffness of the system at its undeflected position, and $\{\bar{F}\}$ defines the mean wind load. The deflected position of the system results in an unbalanced force found by:

$$\{\delta F\}^{j=1} = \{\bar{F}\} - \{F_R\}^{j=1} \qquad \text{Eq. 2.39}$$

where $\{F_R\}^{j=1}$ is calculated from the deflected position of the system and the stiffness of the system at $[K]^{j=1}$; this allows for the incremental displacement for the iteration to be found by:

$$[K]^{j=1}\{\delta\bar{v}\}^{j=1} = \{\delta\bar{F}\}^{j=1} \qquad \text{Eq. 2.40}$$

from which the displacement of the next iteration of the static equilibrium position is:

$$\{\bar{v}\}^{j=2} = \{\bar{v}\}^{j=1} + \{\delta\bar{v}\}^{j=1} \quad \text{Eq. 2.41}$$

The iteration to find the initial deflection continues as $\{\delta\bar{v}\}$ approaches zero to a specified tolerance level. Once complete, the initial conditions of the wall at $t = 0$ is given as:

$$\{v\}_{t=0} = \{\bar{v}\}; \quad \{\dot{v}\}_{t=0} = \{0\}; \quad \{\ddot{v}\}_{t=0} = \{0\} \quad \text{Eq. 2.42}$$

2.3.4 Procedure for step-by-step integration

The procedure for determining the initial estimates of the equations of motion at $t + \Delta t$ using the linear method of Newmark's β method is as follows:

- The pseudo-static stiffness and pseudo-incremental force are determined using Eq. 2.32 using the stiffness and damping at time "t",
- The incremental displacement is calculated from Eq. 2.31,
- The incremental acceleration and velocity are from Eq. 2.30, and
- The new displacement, velocity and acceleration at $t + \Delta t$ are calculated from Eq. 2.27.

After the initial linear estimation of the motion at $t + \Delta t$, the iterative process that follows brings the system into dynamic equilibrium, to correct for errors that occurred during the time step from the non-linearity of the system. The procedure for the iterative process is:

- Update the pseudo-stiffness matrix using Eq. 2.37,
- The incremental displacement is determined using Eq. 2.36,
- The incremental velocity and accelerations are then updated using Eq. 2.35,
- New displacement, velocity, and acceleration vectors are calculated with Eq. 2.34, and lastly
- The unbalanced force vector is found from Eq. 2.33.

This iterative process continues as the unbalanced force approaches zero to a specified tolerance level, from which point the motion vectors are used as the initial estimate for the next time step at $t + \Delta t$.

Chapter 3: Experimental Design, Specimen Construction, and Test Setup

3.1 Introduction

All masonry wall specimens constructed for testing were of the same geometric design. The wall specimens were loaded with dynamic load time histories (representative of gusty wind) or quasi-static monotonically increasing loads (representing static pressures in design) until failure. Additionally, the effects of the support conditions were studied. This chapter describes the design, construction and methodology used for testing the masonry wall specimens and companion specimens.

3.2 Experimental Design

The test program comprised four sets of wall specimens addressing all possible combinations of the two primary test variables: static versus dynamic loading, and ideal versus realistic pinned support conditions. It was determined that five replicate specimens within each set would allow observed differences in the order of 13% to be statistically differentiated at a 90% confidence level, assuming a 10 % coefficient of variation (C.O.V.). The assumed 10% C.O.V. was determined from typical values of C.O.V. found in other masonry research. Therefore, a total of 20 wall specimens were included in the test program.

3.3 Materials

3.3.1 Concrete Masonry Block

For construction of the masonry specimens, two batches of normal density 200 mm concrete masonry stretcher blocks with nominal strength of 15 MPa were used. The blocks were supplied by Cindercrete Products Ltd. and delivered to the structures lab at the University of Saskatchewan in Saskatoon, Saskatchewan in mixed pallets, with 60 frog-ended blocks and 30 flat ended blocks per pallet. In order to ensure that all blocks within a given specimen were from the same batch, the flat ended blocks were used to make the half-width units required at one end of each course of blocks. Despite the intent to use a single batch of blocks, it became necessary to order an additional batch to complete construction.

As illustrated Figure 3.1, flat ended stretcher blocks were cut in half and oriented within the wall such that the cut faces of the half blocks were positioned on the exterior end of the wall so that they were not used in any head joints in the masonry assemblage. Two batches of frog ended blocks were needed to complete the construction of the masonry specimens. Specimens 1-13 were constructed using the first batch of block, while specimens 14-20 were constructed of the second batch of block. Schematics of the blocks used in the wall construction are shown in Figure 3.1.

For each of the two batches of masonry block, three blocks from each batch were tested in compression to verify the nominal compressive strength of the block, in addition to determining strength differences

between the two block batches. Additionally, absorptive tests were completed on an additional three blocks from each batch.

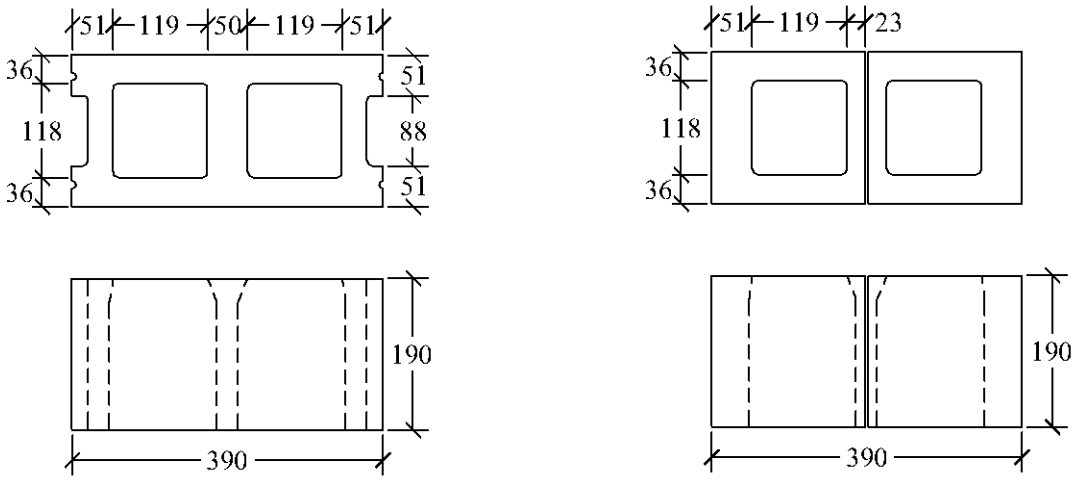

(a) (b)

Figure 3.1: Block dimensions: (a) Frog-end stretcher block; and (b) Cut half blocks

3.3.2 Mortar

The strength of the mortar plays a significant role in the strength of the masonry wall specimens. Specifically, the bond strength between the masonry block and the mortar bed joint will determine when the wall specimen will crack, therefore determining the ultimate strength of the unreinforced specimens. Lafarge type S mortar cement was used for making the mortar. The mortar was batched using a 3:1 sand to cement ratio commonly used in practice by Gracom Masonry Ltd. A water to cement ratio of approximately 0.7 was used. The preparation of the mortar and a description of the preparation of mortar companion specimens is given in Section 3.5.1.

3.4 Specimen Description

3.4.1 Wall Specimens

A schematic of the walls is depicted in Figure 3.2. The left side of Figure 3.2 depicts walls that were constructed on the concrete beams, and the right side depicts walls constructed on steel bases. Each masonry wall constructed was 15 courses tall and 2.5 blocks wide and was constructed in running bond. The nominal dimensions of the walls were 2990 mm X 1000 mm X 190 mm.

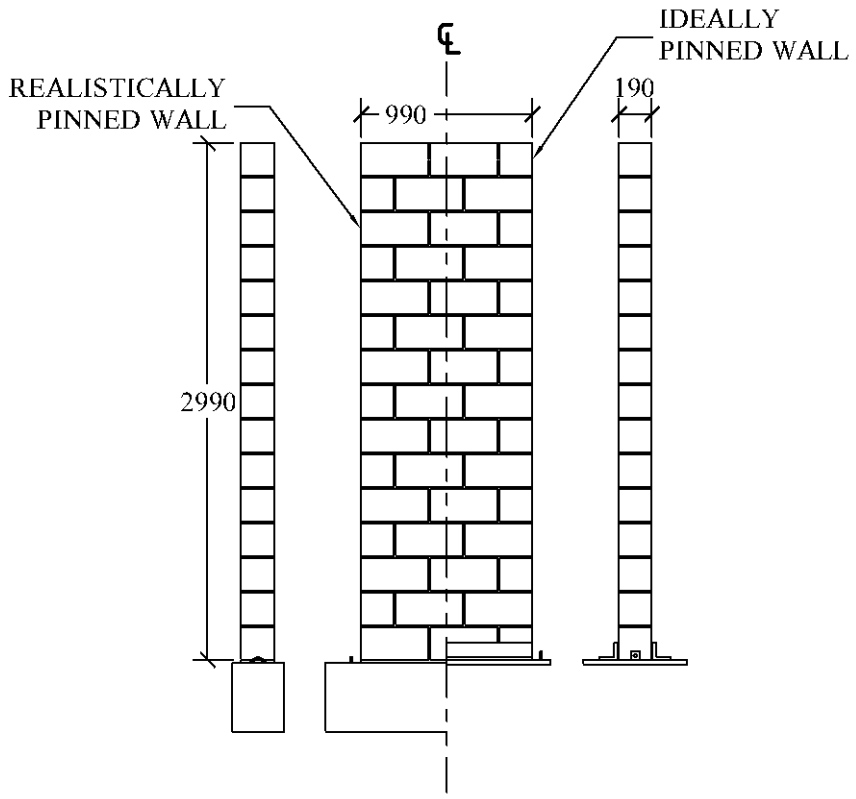

Figure 3.2: Typical masonry wall specimens

3.4.2 Supporting Bases

The ten wall specimens included in the "ideal pinned support" category were constructed on steel bases. The steel bases were 25 mm X 1219 mm X 610 mm (thickness X length X width) as depicted in Figure 3.3. The steel plates featured slotted holes, allowing full width steel angles to be positioned flush with both faces of the first course of the wall specimens to prevent sliding of the wall on the base plates under load.

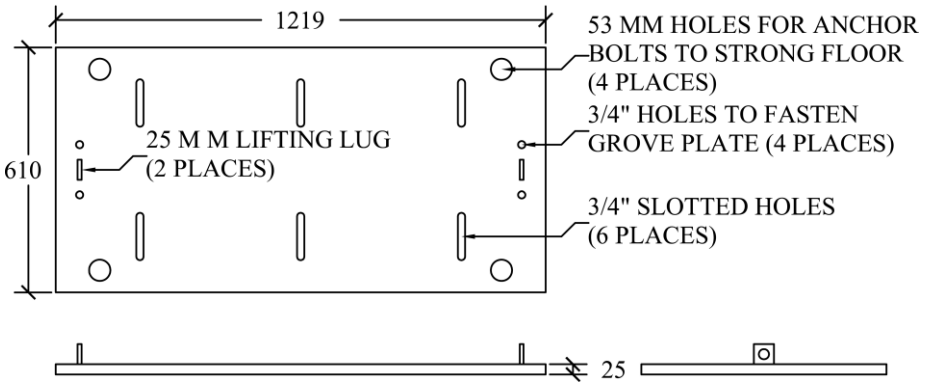

Figure 3.3: Steel base plate for ideal pin supports

The remaining ten wall specimens were constructed on concrete beams. As shown in Figure 3.4, the concrete beams had dimensions of 406 mm X 1700 mm X 305 mm and featured embedded lift hooks on both ends. A 10 mm mortar bed joint was laid between the bottom course of block and the concrete beam to simulate typical field practice.

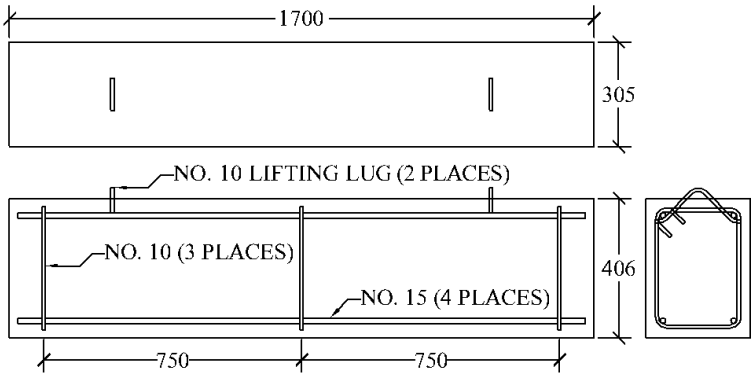

Figure 3.4: Concrete beam for realistic pin supports

The walls with the steel bases were used to create the walls with the ideal pin connections, while the realistically pin supported walls were created using the walls constructed on the concrete bases. In addition to the formation of the support conditions, the bases had lifting lugs, allowing for lifting of the walls and moving them into the test frame. Additional details regarding the end support conditions are provided in Section 3.7.2.

3.4.3 Masonry Prisms

Three companion prism specimens were constructed for each wall specimen. These prisms were constructed after the ninth course of the wall was laid using the same batch of block and mortar as was used in the wall. One three-course prism was constructed for compression testing. In addition, two two-course prisms were constructed for bond wrench testing.

Both types of prisms where constructed in a stacked bond pattern, where the length and width of the prisms was 390 mm by 190 mm. The height of the three-course prism with a 10 mm nominal bed joint was 590 mm, whereas the two-course bond wrench prism was 390 mm in height, as depicted in Figure 3.5.

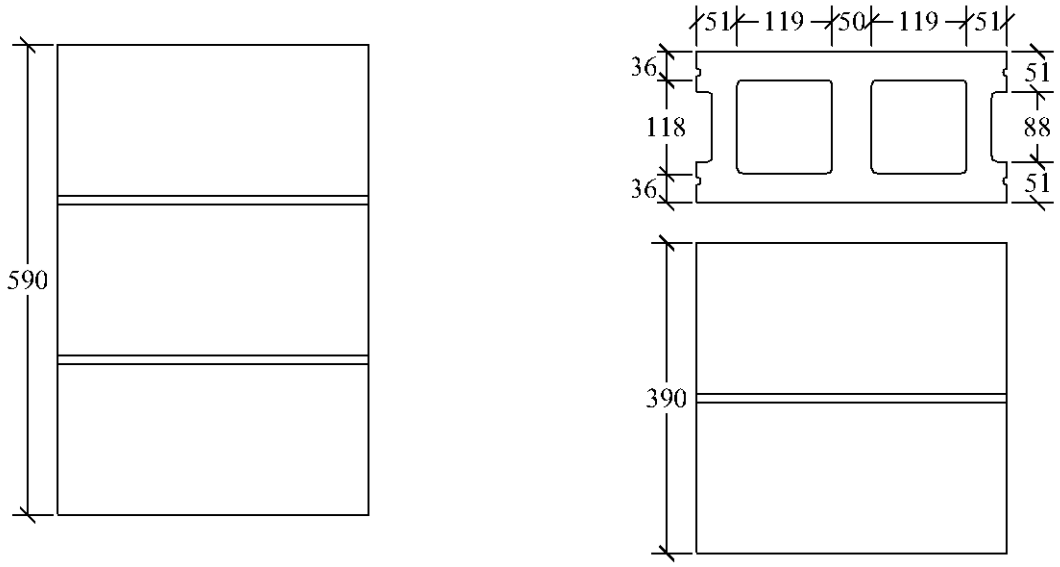

Figure 3.5: Companion specimens: (a) Compression prism; and (b) Bond-wrench prism

Once the construction of the prisms was completed, they were left to cure in the open air of the Structures Laboratory with their companion wall specimen. The test procedure for the three-course prisms that were tested in compression is detailed in Section 3.6.1.2. Similarly, the procedure used to test the two-course bond wrench prism is described in Section 3.6.1.3.

3.5 Construction

3.5.1 Mortar Preparation

Each batch of mortar was mixed by a mortar mixer in the structures lab under the supervision of a qualified mason (Figure 3.6). Mortar preparation started with two ten-gallon buckets of mortar sand and approximately 25 liters of water. Next, a 34 kg bag of type S mortar cement was added. An additional bucket of sand was slowly added to the mortar. Water was added to give a workability that was requested by the mason.

Figure 3.6: Mortar mixer

Six 50 mm mortar cubes were cast for every batch of mortar in accordance with CSA A179 (CSA 2004a). The exception for this was batch 17, which corresponded to the 16th and 17th walls in construction, for which only 3 cubes were made due to a lack of molds available at the time. Tempering of the mortar was allowed during construction; if the mortar was tempered, then an additional three mortar cubes were cast with the tempered mortar. The cubes were de-molded after 24 hours and left to cure in ambient conditions in the Structures Laboratory. The test procedure for the mortar cubes is presented in Section 3.6.1.1.

3.5.2 Wall specimen

Construction of the walls started on September 28 and finished October 6, 2011, in the University of Saskatchewan's Engineering Structures Laboratory. An experienced mason from Gracom Masonry Ltd. constructed all of the masonry wall and companion specimens.

Construction started with the walls on the steel bases. The steel plates were placed on masonry blocks, raising the steel plates off of the ground and allowing access to the heads of bolts on the underside of the steel.

After the mason laid the first course of block (placed directly on the steel plate without an initial mortar bed joint) the base course of block was secured to the steel base with full-width steel angles positioned snugly against both faces of the wall (Figure 3.7). A thin layer of drywall plaster was placed between the block and steel angles to achieve uniform contact between the angles and blocks. The walls were then built to the ninth course, at which point the mason constructed the companion masonry prisms. After the prisms were completed the mason finished the remainder of the wall.

Figure 3.7: Wall specimen constructed on steel base (ideal pin support)

Once the construction of the walls on the steel bases was complete, construction then moved onto the walls built on the concrete beams. Construction of these walls started with a bed joint between the first layer of block and the concrete beam (Figure 3.8). Otherwise, the overall construction procedure was the same as for the specimens with steel bases, with companion specimens being constructed after the ninth course.

Figure 3.8: Concrete base with initial mortar bed joint

All of the wall and companion specimens were left to air-cure in the Structures Laboratory. In total, twenty walls, twenty three-course prisms, and forty two-course prisms were constructed. Additionally, 131 mortar cubes were cast.

3.6 Companion Specimen Instrumentation and Tests

3.6.1.1 Mortar Cubes Tests

The mortar cube specimens were tested in parallel with the wall tests, using an Instron DX600 Universal Testing Machine (600 kN capacity) located in the Materials Laboratory section of the University of Saskatchewan's Structures Laboratory (Figure 3.9). The Instron load frame is computer controlled using

"Partner" software (Instron 2007). The mortar cubes were tested at a rate of 10 kN/min until failure, in accordance with CSA A179 (CSA 2004a).

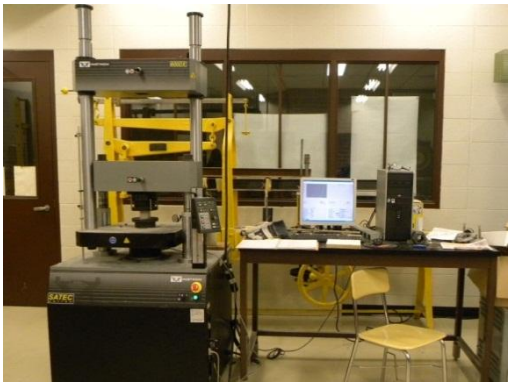

Figure 3.9: Instron UTM testing a mortar cube

3.6.1.2 Masonry Prism Tests

Like the mortar cubes, the masonry prisms were tested in parallel with the wall tests. The prisms were lifted onto the Amsler beam bender (1500 kN capacity) located in the Structures Laboratory. Figure 3.10 shows a schematic of the prism test apparatus.

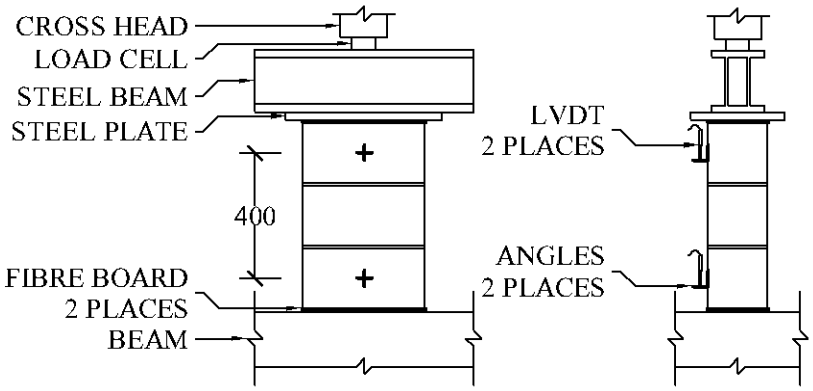

Figure 3.10: Prism test schematic

The prisms were placed on fiber board with another piece of fiber board placed on the top of the prism for testing. A steel plate and steel beam were used to spread the load over the total area of the prism. Steel angles were glued onto the prism at a 400 mm gauge length. Linear variable differential transducers (LVDTs) supported independently from the prisms were placed against the attached angles. The displacement measurements were used to estimate the strain in the prism throughout the test. A picture of a sample being tested is shown in Figure 3.11.

Figure 3.11: Prism test setup

Load and displacement readings were recorded by a computer using LabView (version 8.6) software at a sampling rate of 2 Hz. The prisms were loaded to failure manually by an experienced operator, at an approximate rate of 1 kN/sec. This test was performed to determine the compressive strength and elastic modulus of the masonry assemblage.

3.6.1.3 Bond Wrench Tests

The bond wrench test was used to characterize the tensile bond strength between mortar located in the bed joint and the adjacent masonry blocks. Bond wrench testing was performed in accordance with Annex E of S304.1-04 (CSA 2004b). The test apparatus used was a modified version of the test apparatus given in ASTM C1072 (ASTM 2010), for which the apparatus was increased in size to handle the larger concrete blocks.

The apparatus consists of: the top block clamp, the bottom block clamp and frame, a hydraulic piston, a 2 kN load cell, and a 50 mm LVDT (Figure 3.12).

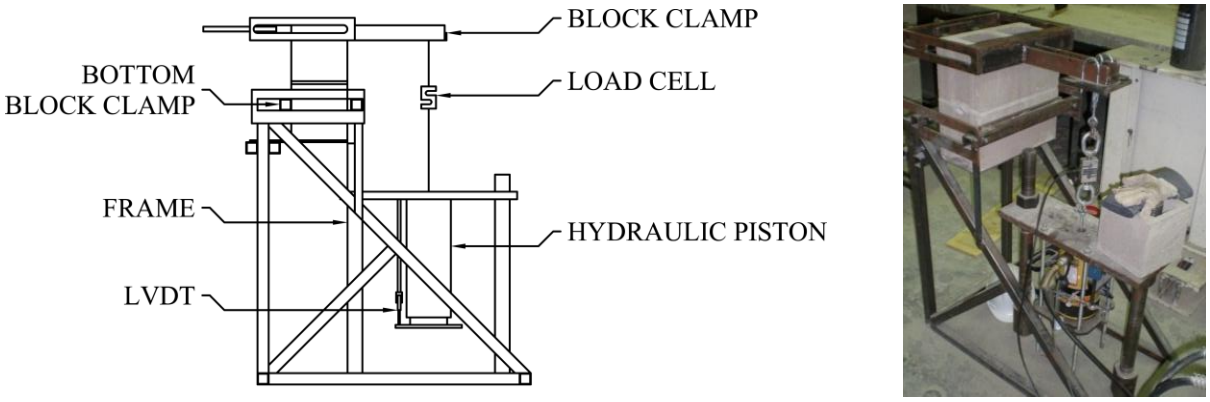

(a) (b)

Figure 3.12: Bond wrench apparatus: (a) Schematic; and (b) Photograph

The test set-up started with marking the centre line of the 2-course masonry prism, and carefully placing the prism into the test frame. The bottom block was then clamped to the test frame 25 mm below the mortar joint. The top block clamp and arm was placed onto the top block, leveled and secured. The load cell was connected to the arm and given approximately 50 N of preload. Lastly, the LVDT was set in place.

The load was applied by the hydraulic piston, at a rate of approximately 1mm/min. The loading rate and data collection was controlled by a computer using LabView© (version 8.6) software. Load was recorded by the computer at a sampling rate of 400 Hz.

3.7 Wall Tests

3.7.1 Transportation of test specimens

With the walls being constructed in the open lab space, the wall specimens had to be moved into the test frame. Prior to moving, each wall was enclosed in a temporary wooden frame that covered the face of both sides of the wall. The wood frames were intended to protect the wall during transportation, taking any loads that were applied. Figure 3.13 depicts an ideally pinned wall being transported into the test frame. All walls were lifted and moved using the 10-ton crane located in Structures Laboratory operated by the Laboratory technician.

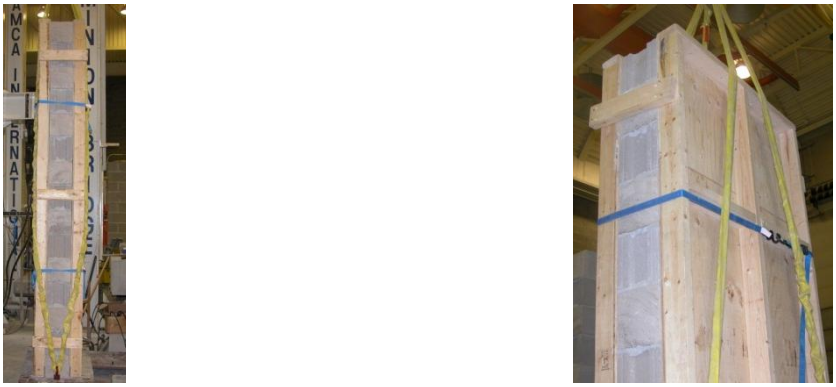

(a) (b)

Figure 3.13: Transportation of the wall test specimens

3.7.2 Set-Up for Pinned-Supported Conditions

Except for specific procedures to create the two different pinned support conditions, the remainder of the set-up and loading process was the same for all specimen types. A schematic of the test apparatus for the realistically pinned walls is shown on the left side of Figure 3.14, while the ideally pinned walls are shown on the right side.

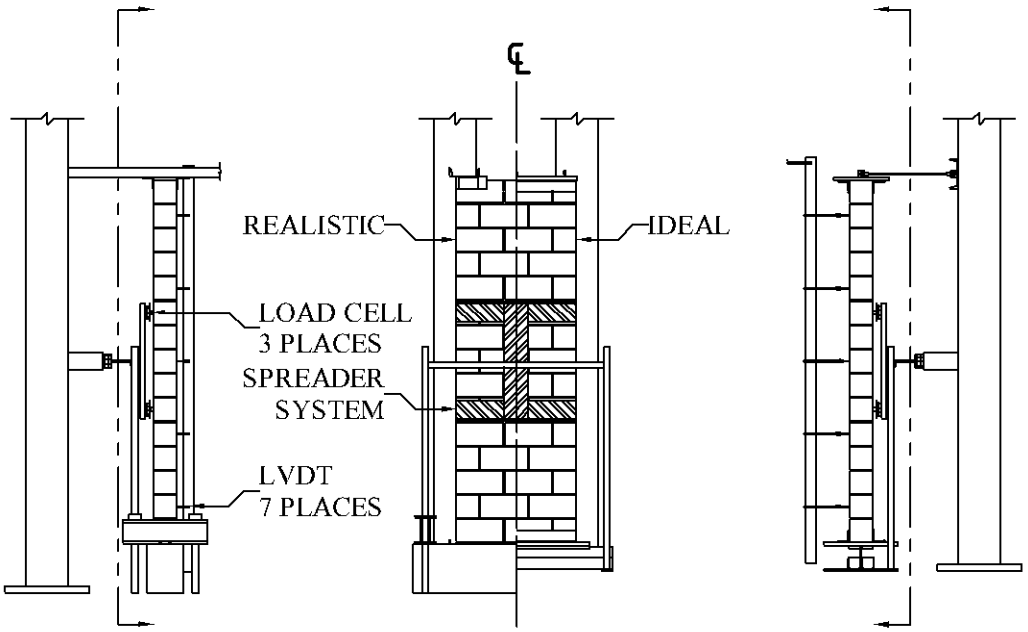

Figure 3.14: Schematic of wall test set-up

After the walls were moved into the test frame, the support set-up was the first thing to be completed. The realistically pinned walls had their supporting concrete beams bolted to the strong floor at both ends with a steel beam, as shown in Figure 3.15. With the beam bolted in place, an approximation of a pin joint would be created when a crack formed in a bed joint near the concrete beam. Rotation that would then occur at the location of the crack would replicate a pin-like connection that is common in field conditions.

Figure 3.15: Realistic pin support specimen showing the bottom connection

For the ideally pinned walls, a steel plate with a full-width groove inscribed along the centre line on its bottom face was bolted to the underside of the steel base upon which the walls were constructed. The walls were placed onto the edge of a vertically oriented ¼ inch steel plate (Figure 3.16); this knife-edge connection was used to create the ideal pin connection at the bottom of the wall.

Figure 3.16: Ideal pin showing the bottom knife-edge connection.

After the bottom support connection was completed, the top connection was put into place. The "realistic" top support reproduced a typical method used in masonry construction with steel angle segments providing lateral support to the top of the walls; the angle segments were connected to a steel channel spanning across the top of the wall. In practice, these angles are typically six inches (150 mm) long, have four inch (100 mm) legs and are spaced at approximately six feet (2 m) on center. However, with the masonry specimens being 1 m wide, the supports were placed near both ends of the wall to prevent rotation of the wall during the test. The top supports were positioned so that the top three inches (75 mm) of the wall was in contact with the steel support angles, with a one inch (25 mm) gap above the wall, and fastened with two 5/8 inch bolts. Concern that the half block at one end of the top course would be wrenched off the top of the wall prematurely resulted in the insertion of an additional ten inch (250 mm) long steel plate being added between the angles and the masonry block (Figure 3.17); this extended the contact of the support laterally to engage the adjacent full-width block.

Figure 3.17: Realistic pin showing the top connection

The top support for the ideally pinned walls was created by placing a steel plate (Figure 3.18(a)) on the top of the wall that featured full-width angles attached to the bottom side of the plate on both sides of the wall. The angles were then snugged up and clamped to the top course of block with a thin layer of plaster

placed between the block and steel to achieve uniform contact. The steel plate was then connected to the test frame though three horizontal threaded rods that were pin-connected to the top plate on one end and to the test frame on the other, thereby providing lateral support but no rotational restraint (Figure 3.18(b)). In addition, the plate was connected to steel cables which were attached to the frame above in order to catch the plate when the wall collapsed and prevent the steel plate from falling and damaging the test apparatus below.

(a) **(b)**

Figure 3.18: Top ideal pin support: (a) Top plate; and (b) Pinned lateral support rod and restraining cable

3.7.3 Vibration Testing

Tests to determine the natural frequency of each wall were performed before the out-of-plane load tests were carried out. Seven Kinemetrics EpiSensor Model ES-U accelerometers were used, calibrated to a maximum range of ±0.25g, where g = 9.81 m/s^2. The accelerometers were attached to the wall by gluing steel angles to the wall, then attaching the accelerometers to the angles. The accelerometers were placed at mid-height of the wall and along its vertical center line, as illustrated in Figure 3.19 .

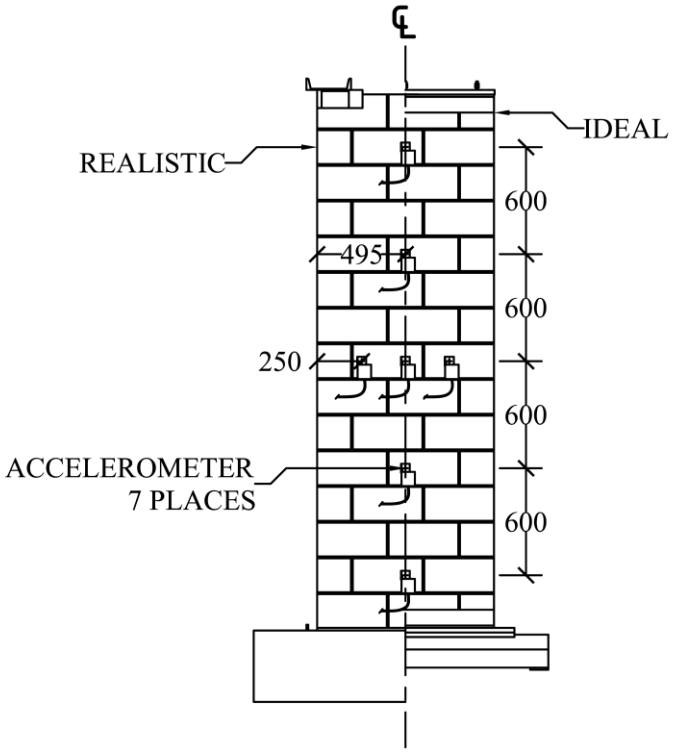

Figure 3.19: Accelerometer positions for vibration tests

Impact and ambient tests were conducted. For the impact tests, the walls were hit with a small hammer at their center, along the right side, and at the top of the wall. Two impact tests were conducted: the walls where struck once in the first test and ten times in the second. The duration of the recorded response ranged from 10 s to 45 s. For the ambient excitation tests, 600 s records of accelerometer data were obtained of the wall vibration without any overt external forces applied to the walls. Data was collected from the accelerometers by a computer using LabView© (2011 version) software at a sampling rate of 500 Hz. Accelerometers and steel angles were removed from the wall at the completion of the vibration test.

3.7.4 Lateral Loading Tests

Loading was applied to the walls using the horizontally oriented hydraulic actuator shown in Figure 3.20(a). The load cell attached to the actuator was used to measure the total applied load as well as control the loading for dynamic tests. Using a computer running Labview© (2011 version) software, the dynamically loaded walls were tested under load control based on the force time histories described in Section 3.8. The LVDT attached to the hydraulic actuator (Figure 3.20(b)) was used to measure the piston displacement throughout the test and to control the loading for the static tests that were conducted under displacement control using the same computer control system as used for the dynamic tests. The static walls were loaded in a quasi-static, monotonically increasing, manner at a rate of 3 mm/min.

The load was applied to the wall specimens using a four-point loading arrangement. The load configuration was generated by using a spreader system to split the load vertically between two levels separated by a distance of 800 mm; these applied loads were then spread across the width of the wall as shown in Figure 3.20(b). Two load cells were located at the top and bottom of the vertical spreader to measure how the loads were being distributed to the wall specimens.

(a) (b)

Figure 3.20: Loading setup for lateral loading tests: (a) Hydraulic actuator; and (b) LVDT and spreader system

In addition to recording loads, displacement measurements were taken. Seven independently supported LVDTs were placed on the unloaded face of each wall. Two 10 mm stroke LVDTs were used at the top and bottom of the wall along with five 50 mm stroke LVDTs that were distributed evenly across the wall at mid-height. The positioning of the LVDTs is shown in Figure 3.21. The LVDTs were removed from the wall prior to the collapse of the walls to avoid damage to the LVDTs; after that, wall displacement measurements were limited to the central LVDT attached to the hydraulic actuator.

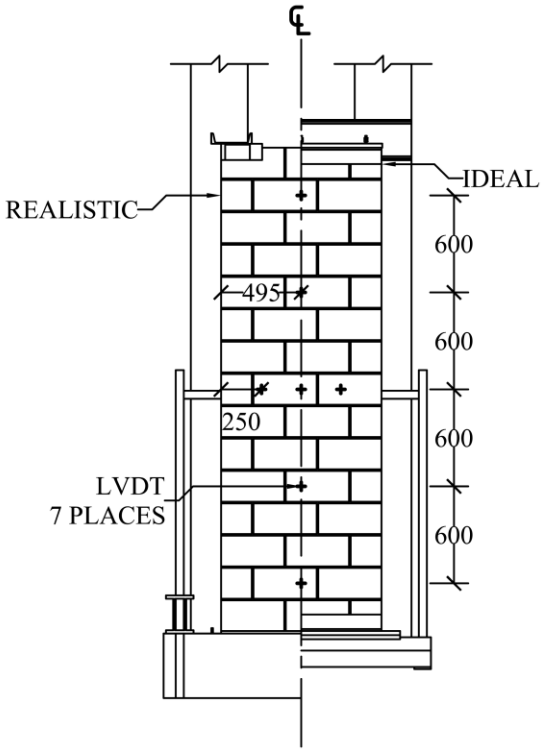

Figure 3.21: LVDT positions on wall specimens.

All of the instrumentation was controlled using LabView© (2011 version) software. The data from the three Interface 110AF-10k load cells were collected by a NI 9237 data acquisition card in a NI cDAC-9178 chassis from National Instruments™, whereas, the data from the Penny & Giles SLS190/300 LVDT's were obtained through a NI 9215 card within the same chassis. The data from the additional five Micro-Measurements (MM) HS50 and two MM HS10 LVDTs were captured by a NI-SCXI-1321 acquisition card in a NI-SCXI-1000 chassis by National Instruments™. The data was sampled at rates ranging from 16 to 20 Hz and stored electronically for subsequent processing. There was a variation in the sampling rate because of the limited processing power of the controlling computer which caused a varying degree of delay between subsequent readings.

The cracking behaviour of the walls was recorded by a webcam and manually observed throughout each wall test. When an observable crack appeared, the location, the wind speed (for dynamic tests), and the approximate time within the test were noted. By correlating the observed cracking behaviour to the measured load and displacement data, the cracking load level could be determined.

The realistically-pinned static and dynamic series were the first tests series to be conducted. Walls for each series were tested in alternating order so that there would be paired specimens within both series that

had approximately the same age. Following the completion of the two realistically-pinned test series, the two ideally-pinned wall test series were conducted in a similar manner to the realistically-pinned walls.

In the realistically-pinned dynamically loaded test series each wall specimen within the series had its own set of wind storm time histories generated for it. As described in Section 3.8, each set began with a mean reference wind speed of 14 m/s. The intensity of the wind storms was increased by 2 m/s with each subsequent trials until the walls collapsed. Since the ideally-pinned dynamically loaded wall tests were performed after the realistically-pinned dynamic tests, the wind time history sets that were created for the realistically-pinned cases were reused in the same order on the ideal walls. Therefore, one wall from the ideally-pinned series was paired with a wall from the realistically-pinned series, using the same set of wind time histories.

3.8 Wind Load Generation

An integral part of the wall tests was to load masonry walls dynamically with load time histories that resemble real wind. As described in Section 2.2, the wind time histories were mathematically generated using a 4^{th} order autoregressive function to produce a generated dynamic time history representing gusty wind. The wind generation program required multiple input variables, including: the desired mean wind speed, length of time step, reference height, surface roughness, and low and high frequency integration limits for calculating autoregression parameters (see equations 2.17 to 2.19).

To choose the mean wind speeds required for the dynamic test series, preliminary static analysis was used to determine that the wall specimens should theoretically fail at an equivalent mean wind speed of approximately 20 m/s. This calculation was based on the assumption that the wall was 3 m tall, ideally-pinned on both ends, and subjected to four-point loading with the load points separated by 800 mm; in addition, the tensile strength of the masonry assemblage was taken in accordance with the values provide in CSA-S304.1-04 (CSA. 2004), and a gust factor of 2.0 was assumed for the wind loading.

However, since the wind time histories were generated using a preselected mean wind speed, and it was uncertain which storm would cause damage to the masonry walls specimens, a set of generated wind time histories were required. The first time wind time history set was selected such that it was known that no damage would be caused to the wall specimens. As the test progressed, the intensity of the wind storms was increased such that the responses of the walls throughout all phases of its life were captured.

Therefore the mean wind speed for the first time history in the set was set at 14 m/s. The intensity of the wind storms within the set was increased by 2 m/s with each subsequent wind time history until collapse

of the wall specimen was reached. Therefore, approximately eight to eleven wind storms were required in each set of time histories; these sets were used in both the ideal and realistic support dynamic test series.

In order to capture the desired high frequency content in the wind (up to approximately 20 Hz), the initial target time step chosen for wind generation was 0.050 s. However, since the computer controlling the loading was unable to perform the looping at the specified rate, a resulting time step of approximately 0.057 s per cycle was found to be the smallest step that could be reliably maintained. Therefore, all wind time histories were generated with a time interval of 0.057 s. As explained in Section 2.2.5, however, for the autoregressive process to work properly, a sufficiently large time step was needed to ensure numerical stability. The time step used for the autoregression process was chosen to be 0.228 s (i.e. four times the desired time step of 0.057 s). As described in Section 2.2.5, a secondary program then interpolated additional points into the time history, resulting in a wind loading time history with a time step of 0.057 s.

The majority of the energy in wind is known to be bounded between finite low and high frequency limits; these frequency limits had to be defined explicitly in the definition of the autoregression parameters used in the calculation of $R^u(k\Delta t)$ (see equation 2.27). Vibration analysis of the natural frequency of two wall specimen types indicated that the natural frequency of the walls was approximately 7 Hz; therefore, an upper frequency limit of 10 Hz was chosen to contain the natural frequency of the walls in the time history. On the other hand, the low frequency limit is generally determined as a function of the duration of the wind time history, T_A, being considered. Generally, the low frequency limit is determined by:

$$f_L = \frac{2}{T_A} \qquad \text{Eq. 3.1}$$

which was recommended by the Iannuzzi (1986). However, the lower frequency limit chosen was 2.441 mHz which corresponds to a wind record with a duration of 820 s.

Lastly, a reference height of 10 m above ground level and surface roughness, z_o, of 0.300 m were chosen as standard values for the generation of the wind time histories. This surface roughness value is representative of a typical suburban terrain (Simiu and Scanlan. 1986). A sample wind time history for a mean wind speed of 18 m/s is shown in Figure 3.22.

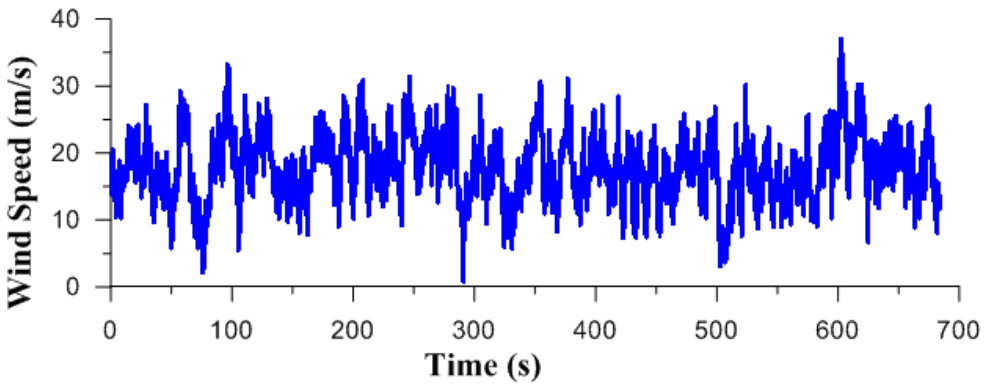

Figure 3.22: Sample wind time history ($\bar{U}_{10}$ = 18 m/s).

The wind simulation program output generated a time history in terms of wind speed (m/s). However, the loading was done under load control, so that the wind speeds had to be converted to force (kN). The National Building Code of Canada (NBCC) [NRC 2010] gives the following equation to convert the wind speed to a pressure:

$$q = \frac{1}{2} \cdot \rho \cdot V_s^{\,2} \qquad \text{Eq. 3.2}$$

where the density of air (ρ) used was 1.2929 kg/m^3, as defined in the NBCC. The pressure was then multiplied by the area of the wall specimens (3m^2) to convert it to a force (Figure 3.23), assuming that the wind pressure was perfectly correlated over the entire tributary area. To ensure that the wall was not damaged at the beginning of the test due to a sudden large gust, an initialization stage of approximately two minutes was implemented at the beginning of the test. A load of 0.4 kN was first applied and held for 30 seconds; then, the applied load was slowly increased to the mean value of the time history in a quasi-static manner. Finally, there was an additional 25 seconds during which the turbulent component of the wind was gradually increased from zero to its full value. All of the time histories that were generated for use in this study are shown in Appendix A.

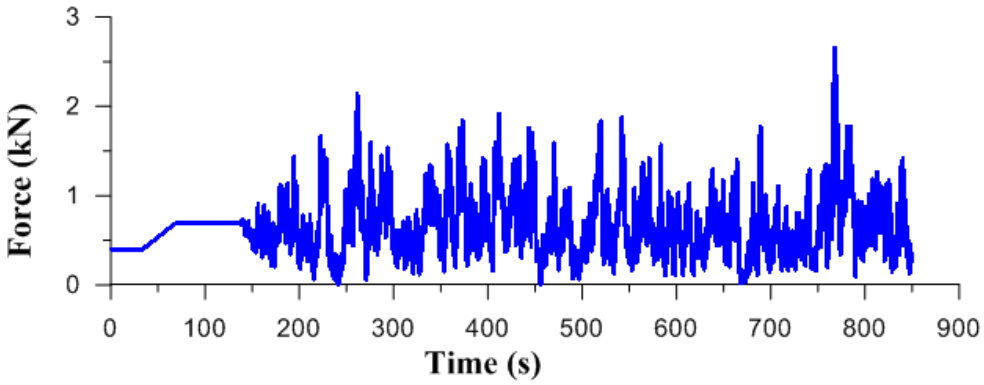

Figure 3.23: Sample force time history including the initial phase-in period

3.9 Numerical Model

3.9.1 Overview

Section 2.3 describes the theory required for the use of a numerical model that predicts the dynamic response of a single degree of freedom model. In the following sections, the modeling of the physical parameters of the test specimens is described. The mode shape, mass and the application of forces are described. The definition of the representative wall stiffness, as well as the calibration, and application of the model is described in Section 4.14.

3.9.2 Mode shape

The mode shape that was used to model the deflection behaviour of the walls was assumed to have a bilinear form. The movement of the wall was assumed to correspond to a rotation at the top and bottom of the wall, with an additional internal hinge forming near mid-height of the wall. The internal hinge was assumed to form in the 8th mortar joint corresponding to a height of 1.6 m, measured from the base of the wall. Therefore, the equation that defined the assumed mode shape is:

$$\Psi(y) = \begin{cases} x = \dfrac{y}{y_h} \; for \; y < y_h \\ x = 1 - \dfrac{y - y_h}{L - y_h} \; for \; y \geq y_h \end{cases} \qquad \text{Eq. 3.3}$$

where y_h is the mid-height of the wall (1.6 m), L is the total height of the wall (3.0 m), y is the vertical distance measured upwards from the bottom of the wall, and x is the horizontal displacement of the wall at the height of y; as a result, x varies from 0 to 1, where x is 0 at the base and top of the wall and 1 at the mid-height (y_h) of the wall.

3.9.3 System Mass

The generalized mass of the wall corresponding to the chosen mode shape was described by:

$$\mathrm{M}_{sys} = \int_0^L [m_w \cdot \Psi(y) \cdot \Psi(y)] \, dy \qquad \text{Eq. 3.4}$$

where m_w is the characteristic mass of a 1.0 m high segment of the physical wall (203.9 kg/m, Section 4.7.5), and $\Psi(y)$ is the defined mode shape of the wall. Since the mode shape is multiplied by itself within the integrated expression, the resulting integration produced a value of unity. Therefore the generalized system mass was found to be 203.9 kg.

3.9.4 Applied Force

Lastly, since the load was applied at two locations, the forces were converted to a generalized force given by:

$$\mathrm{F}_{sys}(t) = \frac{F(t)}{2} \cdot \Psi(1.1\ \mathrm{m}) + \frac{F(t)}{2} \cdot \Psi(1.9\ \mathrm{m}) \qquad \textbf{Eq. 3.5}$$

where t is the elapsed time of the trial, $F(t)$ is the total instantaneous force at time t which is divided evenly between the two load locations; $\Psi(1.1\ \mathrm{m})$ and $\Psi(1.9\ \mathrm{m})$ are the mode shape amplitudes at the locations of the applied load.

Chapter 4: Results

4.1 Introduction

This chapter presents the results of twenty out-of-plane wall tests, and their companion specimens, that were tested at the University of Saskatchewan in the Structures laboratory. This chapter contains the results and observations that were obtained from physical testing that was completed between February and July 2012.

The four test series described in Chapter 3 were tested to determine the differences in behaviour of the walls due to the different support and load types. Each of the twenty walls has been assigned a three digit designation based on the test series and numbered in the order in which the tests were done. The first digit is "I" or "R" (denoting "ideal" or "realistic," respectively) describing the type of support connection, followed by an "S" or "D" for the type of loading, either static or dynamic, respectively. Finally, a number from "1" to "5" is included to show the order of the tested wall within a test series. A sample designation is: "ID2", which represents the second ideally-pinned dynamic test that was performed.

Additionally, when the term "series" is used to describe the testing methodology, it is referring to the series of similar walls that were to be tested (i.e. real-static (RS) series, or ideal-dynamic (ID) series). The term "test" is used to describe a specific wall test within a test series (i.e. the first real-static (RS1) test). Lastly, for the dynamic tests on each wall, the individual applied wind speed time histories are referred to as a "trial" (i.e. the 14 m/s trial for wall the first ideal-dynamic (ID1) test).

4.2 Companion Specimen Tests

4.2.1 Block Tests

In addition to the companion tests that were completed in parallel with each individual wall specimen, six concrete masonry blocks were tested in compression, including three blocks from each batch of blocks that were used in the wall specimens. The compression tests on the blocks were done using a similar methodology to the prism tests which is described in Section 3.6.1.2.

The compression tests of the blocks were done to determine if the material properties of the blocks were significantly different between the two batches of blocks. The results of the six compression tests are shown in Table 4.1. As noted in Section 3.3.1, the nominal compressive strength of the masonry blocks was 15 MPa.

Table 4.1: Summary results of compressive block tests

Batch	Test Number	Compressive Strength (MPa)	Mean (MPa)	C.O.V. (%)
1	1	22.8	23.7	8.8
	2	21.8		
	3	26.6		
2	1	17.2	18.8	26.0
	2	13.7		
	3	25.4		

The results show that the average compressive strength of the first batch of block was 26% larger than the second batch. However, due to the large variation of the compressive strengths of the second batch, there is no statistical difference between the two batches of blocks at the 90% confidence level. This suggests that there is little difference of the material properties of the masonry block. Similar findings were found from the prism tests presented in the next section.

4.2.2 Prism and Mortar

With each wall test that was conducted, a three course masonry prism was tested in compression, along with multiple mortar cubes. The data from the compression tests are shown in Table 4.2. The coefficient of variation that accompanies each set of mortar cube tests refers to the variation of strength of the mortar cubes that were tested from the same batch of mortar. The prism data for the first ideal-dynamic test (ID1) was lost shortly after the test was completed and, therefore, was unable to be included in Table 4.2.

Table 4.2: Summary of companion prism and mortar test results

Specimen			Prism			Mortar Cube			
			Compressive Strength			Compressive Strength			
Support Type	Load Type	Test Number	Individual Test (MPa)	Mean (MPa)	C.O.V. (%)	Batch Mean (MPa)	Batch C.O.V. (%)	Mean (MPa)	C.O.V. (%)
Realistic	Dynamic	1	17.6	15.9	10.9	20.9	1.3	17.6	22.3
		2	16.0			20.2	9.1		
		3	16.7			18.3	5.6		
		4	13.0			17.6	9.3		
		5	16.0			11.0	7.9		
	Static	1	16.9	16.8	13.4	18.3	8.6	17.9	16.0
		2	15.3			17.3	8.5		
		3	18.8			22.6	7.5		
		4	19.0			16.5	3.6		
		5	13.8			15.0	14.7		
Ideal	Dynamic	1	-	16.4	16.6	13.4	3.1	15.7	16.8
		2	19.9			12.6	11.1		
		3	16.0			17.9	16.0		
		4	16.2			18.5	3.1		
		5	13.3			16.2	5.8		
	Static	1	18.4	17.0	9.5	13.4	3.1	14.3	19.3
		2	15.6			11.2	5.7		
		3	18.7			17.9	16.0		
		4	17.3			12.6	12.3		
		5	15.1			16.3	4.6		

When the walls were constructed, two batches of frog-ended blocks were needed. All of the ideally-pinned walls and three realistically pinned walls were constructed with the first batch of block; the remaining seven walls were constructed with the second batch. The average compressive strength of the prisms from the two different batches of blocks was 16.5 MPa for both groups, with a C.O.V. of 13% and 9% for the first and second batches, respectively. There was no statistical difference between the two different groups at the 90% confidence level, suggesting that the material properties of the masonry blocks did not affect the strength of the masonry assemblage noticeably. The total average prism compressive strength for all walls was 16.5 MPa, with an overall C.O.V. of 12%

Due to the progression of construction, some specimens were constructed from up to three different batches of mortar. The mortar cube test results shown in Table 4.2 correspond to the batch of mortar that

was used when constructing the mid-height portion of the wall since that was where the walls failed during flexural testing. The average compressive strength of the mortar batches ranged from 11.0 MPa to 22.6 MPa, while the coefficient of variation ranged from 1.3% to 16.0%.

For Walls IS3 and ID3, which had a C.O.V. of 16% for the mortar, the variation that is shown is misleading. For each batch of mortar, six mortar cubes were cast. The cube molds that were used were able to cast three cubes per mold. The average compressive strength of the cubes from the first mold was 15.1 MPa with a C.O.V. of 7.0%; the second mold gave an average compressive strength of 20.6 MPa with a C.O.V. of 1.5%. The mortar that was used to cast the mortar cube was the same, and the casting procedure was constant for all of the mortar cubes. It is not known why there was a difference between the two molds that were used.

Though many walls where constructed with multiple batches of mortar; only two mortar batches were used near mid-height in more than one wall. The first ideal-dynamic (ID1) and ideal-static (IS1) walls had mortar from the same batch placed near mid-height. Similarly, the third ideal-dynamic (ID3) and ideal-static (IS3) had the same mortar at mid-height.

4.2.3 Bond Wrench Tests

Like the other companion specimens, bond wrench tests were performed in parallel with the wall tests, for which two bond wrench specimens were tested per wall. The bond wrench tests were done to characterize the bond strength between mortar and masonry block. In total 38 bond wrench specimens were tested; two specimens were damaged prior to testing, resulting in the first and fourth ideal-static (IS1 and IS4) test having only a single companion bond wrench specimen.

The resulting bond strengths are shown in Figure 4.1, where the strength was calculated in accordance with Annex E of S304.1 (CSA 2004); in this figure, the values are shown in the order in which they were tested. It can be seen that there is a significant amount of scatter in the test results. The average calculated bond strength was 0.04 MPa, with a C.O.V. of over 1000%.

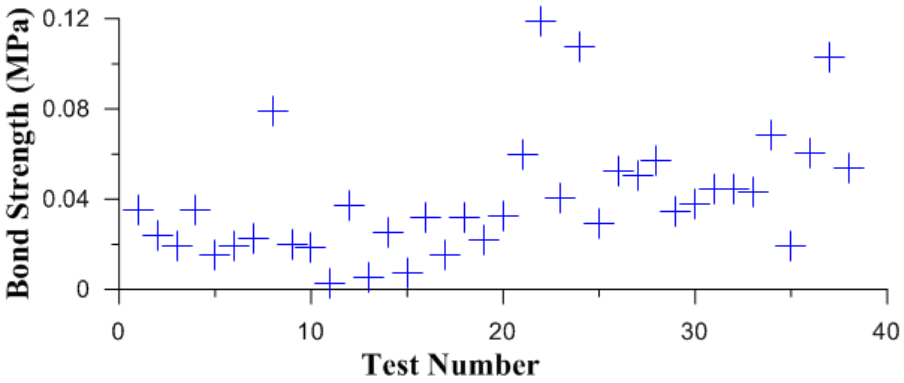

Figure 4.1: Plot of calculated bond strength from bond wrench tests

In attempt to evaluate the distribution of the bond wrench data, the results were plotted as a histogram shown in Figure 4.2. The histogram suggests that there is some grouping of the data. Additionally, to verify that the results from the bond wrench tests were acceptable, the apparent mortar/block bond strength was estimated from the calculated modulus of rupture values from the ideal-static (IS) test series. The calculations took into account the location of the mortar failure; for this calculation, a simple span was assumed. The average calculated bond strength from the ideal-static (IS) walls was 0.07 MPa, with a coefficient of variation of 8%. The resultant bond strength indicates that the bond wrench test approximated the bond strength found in the walls, since both were in the same order of magnitude and the amount of variability was large.

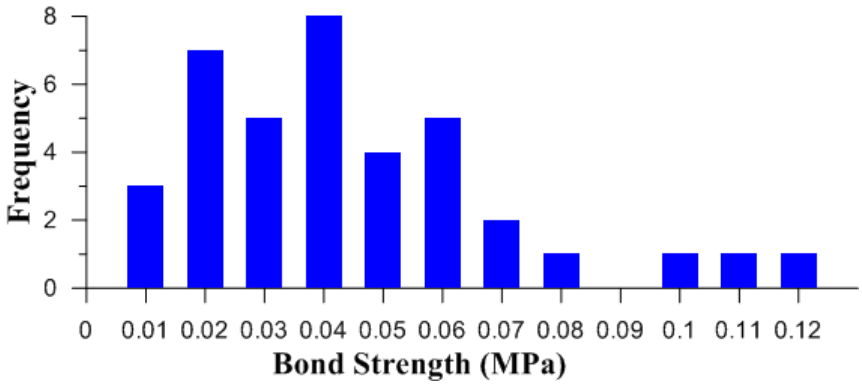

Figure 4.2: Histogram of calculated bond strength from bond wrench tests

The histogram of the calculated bond strengths suggests that the bond wrench testing was performed in a consistent manner such that the calculated bond strength can be considered representative of the bond strength within the wall tests; the large C.O.V. was influenced largely by the small values of the bond strength. The calculated bond strength was an order of magnitude lower than the specified value given in Table 4 of S304.1 (CSA, 2004) at 0.4 MPa. However, as described by Laird (2013), the specified bond strength values in the Canadian masonry code are not representative of the mortars that are commonly in

use today. Additionally, the air curing of the wall specimens in the Structures lab can cause a lower bond strength than if the wall specimens where cured under moist conditions.

4.2.4 Vibration testing

Vibration testing was carried out on the undamaged masonry walls prior to the application of any lateral loads. The purpose of the vibration tests was to determine the dynamic characteristics of the undamaged wall specimens. The natural frequency of the walls was of the highest interest since a dynamic load applied at the natural frequency of the structure can cause a resonant response which, in turn, would cause large response amplitudes and possible failure at a load level that would not normally cause damage.

For the vibration tests, the walls were divided into two groups, separating the walls by their support conditions. During each test, data was collected from seven accelerometers, placed on the wall as shown in Figure 3.19. A sample record for an ambient vibration test is shown for a 10 minute period in Figure 4.3, where the accelerometer associated with the plot shown was placed on the center of the ideal-dynamic (ID1) specimen. The ambient time history contained the accelerations of the wall specimen when it was not being actively exited.

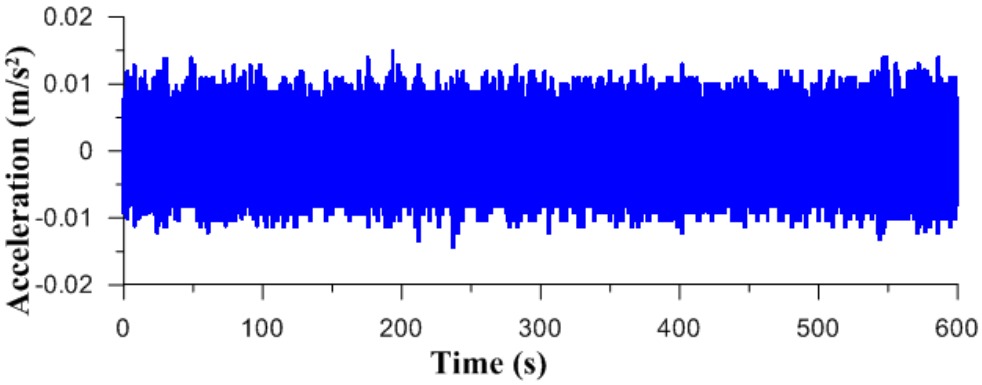

Figure 4.3: Ambient acceleration time history for the first ideal-dynamic Specimen

To determine the response of the walls to excitation, the time histories were converted to a frequency domain representation through the use of the Fast Fourier Transform (FFT). The FFT converts the time history to show how the energy of the response is distributed with frequency. The results from the FFT are shown as a normalized Power Spectral Density (PSD) plot shown in Figure 4.3. The normalized spectrum is given by the semi-logarithmic form of $\frac{f \cdot S(f)}{\sigma^2}$ versus $\ln(f)$, where $S(f)$ is the PSD (with units of $m^4/s^2/Hz$), f is the frequency increment (Hz) and σ^2 is the variance of the original time history (m^2).

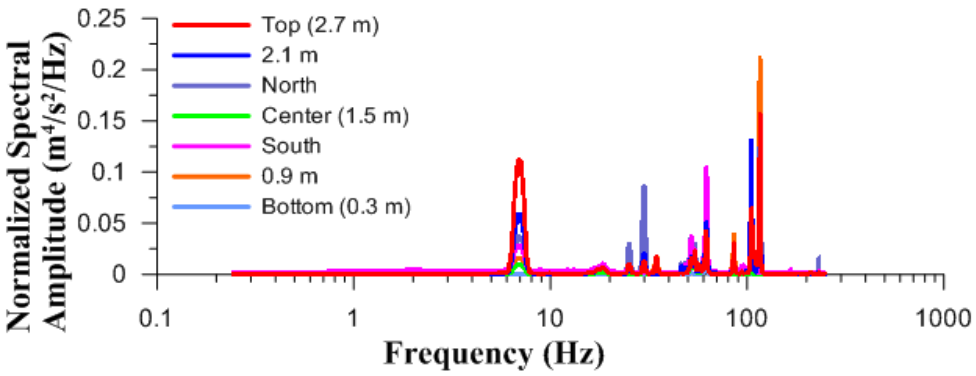

Figure 4.4: Power spectrum density plot of ambient acceleration

Generally the peaks in the PSD plot correspond to the frequencies at which the tested wall is most easily excited. Typically these frequencies correspond to the natural frequency of the wall, where a resonant response can be obtained if the wall was subjected to a load applied at that frequency. However, not all peaks correspond to the response of the wall, but are a result of the noise in the recorded signal. Peaks that correspond to a frequency of 60 Hz, and its harmonics, are typically due to the noise generated from the electrical equipment (eg, lights) in the surrounding area to the test specimens.

The first peak that is seen in Figure 4.4 is located at approximately 7 Hz, which represents the first natural frequency of the wall. The remaining peaks at approximately 30 and 120 Hz are thought to be caused, not from vibrations of the wall, but from interference within the Structures lab and do not relate to the actual response of the wall. A summary of the natural frequencies for the two different wall types is shown in Table 4.3, where results for both impact and ambient tests are shown. The reduced number of specimens reported for the impact test results was due to high amounts of noise through all of the frequency ranges in some of the impact tests, making the peaks indistinguishable within the PSD's; therefore, the natural frequencies from those tests could not be determined. Additionally, the remaining PSD's from the testing can be seen in Appendix B.

Table 4.3: Natural frequencies of walls from vibration tests

Connection Type	Test	Number of Specimens	Mean Natural Frequency (Hz)	Max. Natural Frequency (Hz)	Min. Natural Frequency (Hz)	C.O.V. (%)
Ideal	Impact	7	6.73	6.84	6.35	3.0
	Ambient	10	6.93	6.96	6.84	0.8
Real	Impact	5	7.57	9.03	6.96	12.1
	Ambient	10	7.14	7.32	6.96	2.1

Since the first natural frequency of the walls was approximately 7 Hz, the high frequency cut-off for the wind time history generation was chosen so that there would be energy in the wind that corresponded to

the natural frequency of the walls. However, the majority of the wind's energy would be contained within the lower frequencies.

Having the majority of the winds energy being contained within lower frequencies may allow for a greater resonant response of the walls when they became damaged, since the natural frequency of the walls decreased with increasing damage. A damaged wall will have a decreased stiffness compared to the original undamaged wall. The relationship between the stiffness of the wall and its natural frequency is described by:

$$f_n = \frac{1}{2\pi}\sqrt{\frac{k}{m}} \qquad \text{Eq. 4.1}$$

where f_n is the natural frequency, k is the stiffness and m is the mass of the wall. Since the stiffness of the wall is in the numerator in the equation and directly related to the damaged state of the wall, and since there is a constant mass, a reduced stiffness will result in a lower natural frequency.

At the natural frequencies, the walls will vibrate primarily in a specific shape (mode). When the wall is vibrating at a non-natural frequency, the displacement pattern of the vibration is a combination of all the mode shapes and is often described as an "operational deflected shape." An averaged mode shape that corresponds to the first natural frequency of the test ideally-pinned specimens is shown in Figure 4.5 (a), while an averaged mode shape of the realistically-pinned walls is show in Figure 4.5 (b). The mode shapes where extracted from the FFTs using the Peak Picking Method, were the amplitudes of the extracted mode shapes where normalized by the amplitude corresponding to the mid-height accelerometer. The first mode was found to have a nearly linear form, where rotation occurred at the bottom of the walls, suggesting that lateral flexibility of the top support was a major factor for this mode.

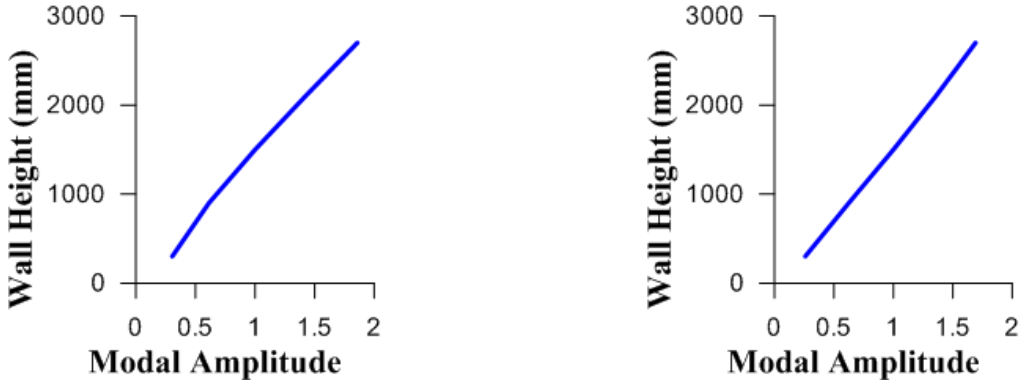

(a) (b)

Figure 4.5: Averaged first mode shape of: (a) Ideal; and (b) Real walls

In addition to the apparent rigid-body rotation that corresponded to the first natural frequency, additional modes were detected at higher frequencies. Unlike the first mode where the first natural frequency of the all the walls was approximately 7 Hz, the frequencies corresponding to the second mode ranged from 13 Hz to 29 Hz. The second mode shape appeared as a combination of the rigid body rotation in addition to the first flexural mode, with inflection points located at the top and bottom of the wall. An averaged mode shape for the ideally-pinned walls is shown in Figure 4.6 (a), while an averaged mode shape for realistically-pinned walls is shown in Figure 4.6 (b).

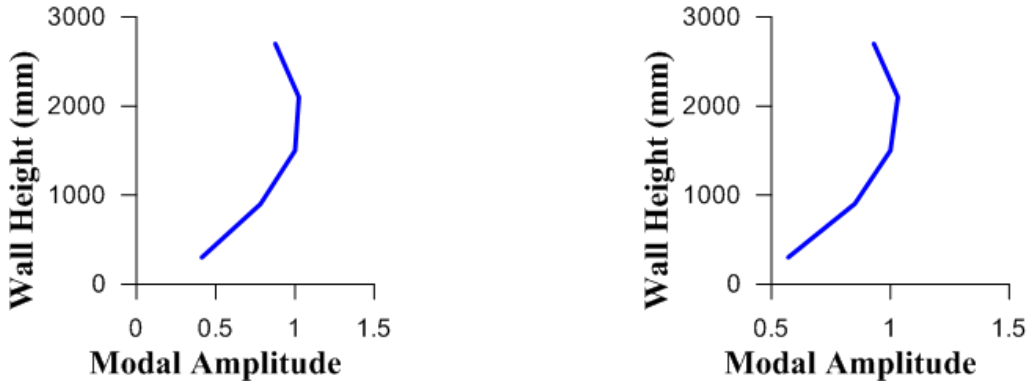

(a) (b)

Figure 4.6: Averaged second mode shape: (a) Ideal walls; and (b) Real walls

4.3 Acceptability of applied wind loads

4.3.1 Generated wind profiles

In Chapter 2, the theory for a 4th order autoregressive process was presented; and in Chapter 3, the application method used in this study was presented. Since the autoregressive process is random, the verification of the time histories such that they give a good representation of real wind is important. Therefore, the spectrum of the generated wind time histories was compared to the theoretical spectrum that was adopted by the National Building Code (NBCC 2010). Figure 4.7 shows a comparison of the spectrum of a sample time history and the theoretical spectrum, indicating acceptable agreement.

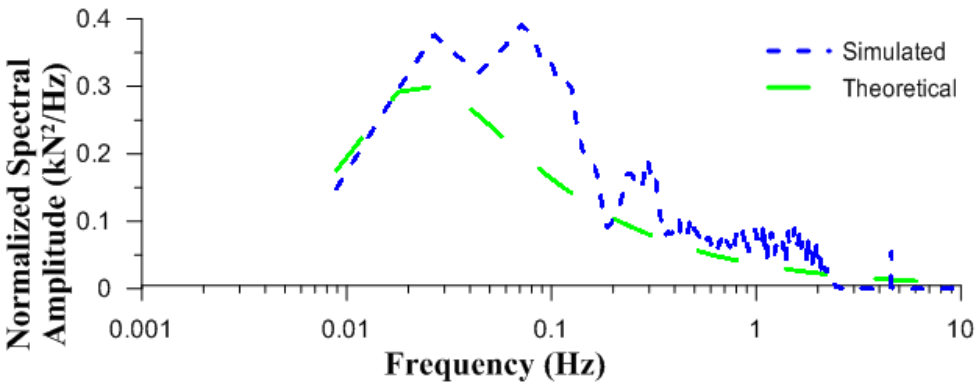

Figure 4.7: PSD of generated and theoretical wind spectrum for a 16 m/s reference wind speed trial

For this comparison between the theoretical (target) and the spectrum of the generated wind, the agreement between the two spectrums is considered to be reasonable. Although there is variation in the energy distribution throughout all of the frequency ranges, the general shape of the generated wind spectrum is similar to the target spectrum, indicating that the proportion of "gusts" of various durations in the simulated wind is similar to that of natural wind.

All of the time histories that were selected for use agreed with target spectrum in a similar manner. Efforts were made to select time histories that exhibited acceptable agreement with the target; if a time history was judged to have poor agreement, a new time history was generated. Power spectral density plots for all of the time histories used in this study are shown in Appendix C.

4.3.2 Applied loads

It has been shown that the generated wind time histories contained acceptable energy distributions, capable of representing real wind. However, the ability of the physical load system to apply to loads to the wall in a way that replicates actual wind needed to be confirmed. Figure 4.8 depicts a sample PSD containing the spectrum of the generated wind (set-point), the spectrum obtained from the measured load that was applied to the wall (applied) and the theoretical spectrum that is described by the National building code (NBCC 2010).

It is apparent that there is acceptable agreement between the measured and target power spectra, particularly in the lower frequency range. This was found to be typical for all of the dynamic wall tests in that, prior to wall cracking, the load system is able to reproduce the set-point quite accurately, with only small errors observed in reaching some instantaneous peaks.

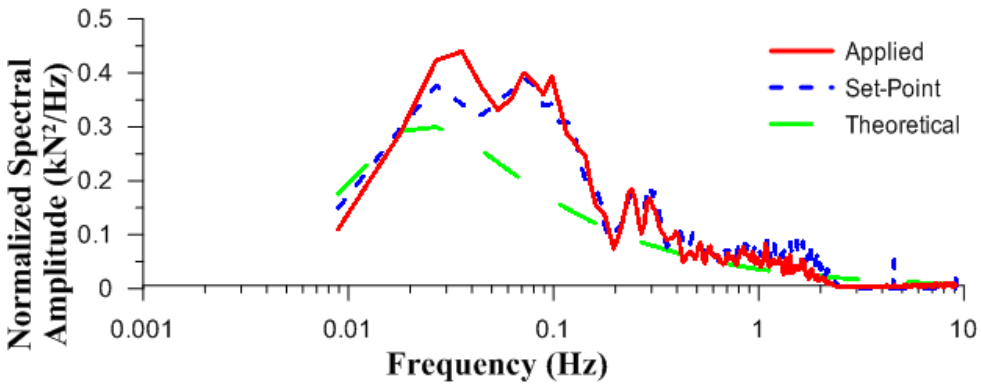

Figure 4.8: Comparison of applied and set-point spectrum for Real-Dynamic Specimen One (RD1) at 16 m/s mean wind speed

However, after the mid-span crack had formed in the dynamic wall specimens, the similarity between the target and measured load histories deteriorated. As the lateral stiffness of the post-cracking walls decreased, it became increasingly difficult for the hydraulic actuator to achieve the desired load fluctuations. This behaviour is illustrated in Figure 4.9, which compares the target and measured load histories for the third real-dynamic (RD3) wall specimen, both before and after cracking (where cracking occured at an elapsed time of approximately 375 s) during a wind storm characterized by a nominal mean wind speed of 20 m/s (0.26 kPa). While the two plots are nearly coincident prior to cracking, it is apparent that the measured force continues to follow the general trend of the target force time history after cracking, but is unable to reach the desired peak vales.

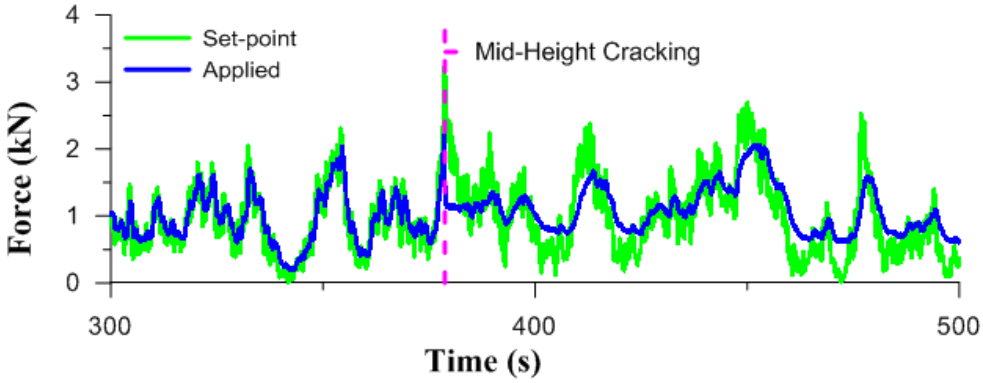

Figure 4.9: Sample force time history of wall RD3 before and after cracking

At higher load levels, when the walls were more severely cracked, and thus even more compliant, the load control feedback mechanism became somewhat unstable, resulting in a noticeable “chattering” behaviour as the actuator attempted, unsuccessfully, to find the target load level; this chattering was manifest in spurious high frequency load fluctuations that occurred at a frequencies between approximately 3 to 5 Hz. An example of the chattering is shown in Figure 4.10, where a comparison of the theoretical and the

applied load spectra is shown. It is apparent that there is large amount of energy content centered at approximately 5 Hz, corresponding to the chattering.

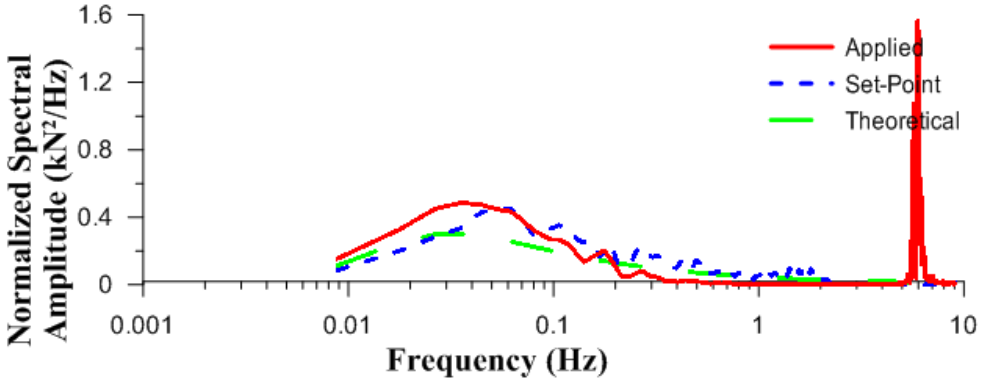

Figure 4.10: PSD plot of the 22 m/s trial of specimen RD1 showing the effect of chattering

As a result, the applied load on several damaged walls typically featured excessive high frequency fluctuations and a deficit of low frequency fluctuations compared to the target wind. The influence of this loading behaviour on the ultimate capacity of the walls is not known precisely.

4.4 General behaviour of masonry walls

Since all of the walls were unreinforced, the strength of the bond between mortar and masonry block played a significant role in the overall strength of the wall specimens. A crack was formed when there was a failure of the bond between masonry block and mortar. An example crack that formed during testing is shown in Figure 4.11. Typically, the crack did not occur within the mortar, but at the interface between mortar and block. It was also noted that the crack did not occur along a single mortar/block interface within a given mortar bed joint, but rather tended to fail on the interface that was furthest from successive head joints between the blocks. The bond failure, therefore, followed a wave-like pattern across the width of the wall.

Figure 4.11: Typical cracking pattern for all wall specimens

For both the ideally-pinned and realistically-pinned walls to collapse, a failure mechanism had to be formed. The failure mechanism formed quickly in the ideally-pinned walls, where only a single crack at mid-height had to form. On the other hand, the realistically-pinned walls required the formation of three cracks: at mid-height, at the base of the wall, and at the top of the wall.

The probable location for the first crack formation for the realistically pinned walls was at the base of the wall; indication of this behaviour was found in a few of the real-dynamic test specimens. This crack typically occurred in either mortar joint 0 (between the concrete beam and masonry block) or in the 1st mortar joint (between the first and second course of masonry). When the wall was uncracked, it would tend to act similar to a "propped cantilever" where the largest moment occurs near the base of the wall. Although not visually observable in most cases, the initial bottom cracking was inferred from marked changes in the slope of load-deflection curves at load levels below those that caused mid-height cracking.

The crack at mid-height was the second crack to form for the realistically pinned walls and the first, and only, crack to form for the ideally pinned walls. The formation of this crack governed the strength of the ideally pinned walls. When this crack formed, there was a significant drop in the applied load, coupled with a large deflection occurring simultaneously. The location of the mid-height crack was not as consistent as for those near the top or bottom cracks, ranging from the 6th mortar joint to the 10th mortar joint due to the presence of a constant moment region between the load points. The last crack to form for the realistic walls was at the top of the wall, where the crack always appeared in the 14th mortar joint, immediately bellow the top course of masonry.

The displacement of the walls occurred primarily by rigid-body movement throughout all the tests of a given wall specimen. Lateral displacements in the wall were almost entirely attributed to rotation of the wall segments from the crack at mid-height to the locations of support cracking (or at pinned supports for the ideally-pinned walls), with the remainder of the wall being uncracked and displacing linearly. Figure 4.12 depicts a real-static wall prior to collapse, where the bi-linear mechanism can be clearly seen. In all cases, large lateral displacements were required for collapse of the walls to be initiated, such that the walls were displaced to the point of geometric instability. The required movement of the wall to reach geometric instability appeared to be largely independent of the type of loading, but rather depending mostly on the support conditions, with the realistically supported walls sustaining more displacement prior to collapse.

Figure 4.12: Geometric configuration of realistically-pinned wall just prior to collapse

4.5 Realistic-Static test series

4.5.1 Overview

The results of the static test series conducted on the walls with realistic support conditions are presented in this section. Numerical results are presented for two critical loading conditions (damage states), denoted as cracking and ultimate. For the purpose of this discussion, the cracking condition is defined as the instant when the mid-height crack was formed, as indicated by observable cracking and movement of the wall specimen during the test; in addition, the load applied to the wall reached an observable local peak in the load-deflection plots at this point. On the other hand, the ultimate condition is defined as the instant at which the maximum load was found to occur within the test. After the ultimate load point, the applied load on the wall decreased until collapse occurred.

For each critical loading condition, the mid-height moment and displacement for the Realistic-Static (RS) test series are presented in Table 4.4. The moments were calculated at mid-height of the wall based on the measured loads, assuming that the wall was simply supported at its top and bottom edges. The displacement measurements represent an average of the mid-height displacement measurements for all available sensors. The displacement measurements were obtained from LVDT's attached to the wall up to the stage of mid-height cracking. However, since the attached LVDT's were removed prior to collapse, the ultimate displacements were extrapolated using the measured displacement of the load actuator (which was measured throughout the entirety of the test), and assuming that the relationship between the

displacements at the load actuator and the pre-cracking displacement behaviour of the wall at mid-height remained the same. The locations of the center and bottom cracks are provided in Table 4.4 since there was variation in the location of those cracks, unlike the top crack that always formed in the 14th mortar joint.

Table 4.4: Summary of realistic-static (RS) test results

		RS1	RS2	RS3	RS4	RS5	Mean	C.O.V. (%)
Cracking	Moment (kN·m)	-	-	0.92*	1.39	1.69	1.3	29.1
	Displacement (mm)	-	-	0.80	1.64	0.23	0.9	79.7
Ultimate	Moment (kN·m)	1.57	1.45	2.26	1.65	1.93	1.8	18.3
	Displacement (mm)	42.8	78.2	69.2	86.7	61.6	67.7	24.8
Crack location†	Mid-height	8	8	9	9	6	-	-
	Bottom	0	1	0	1	1	-	-

***The cracking moment was calculated using load measurement from the center load cell (Section 4.5.4). †Mortar joint counting up from the base, with "0" representing the bed joint between the first course and concrete beam.**

The response of each individual realistically supported statically loaded specimen test is presented in the following sections. Each load-displacement plot presented in the following sections is shown in Appendix D; additionally, the displacements of the vertical and horizontal centerlines of the wall are shown in Appendix E.

4.5.2 Wall Specimen RS1

Real-Static-1 (RS1) was the first wall test to be conducted. Some errors were discovered during the set-up and testing of this wall. These errors were rectified for the remaining tests. The first error that was encountered occurred during setup. The concrete beam that the wall was built on had been bolted to the floor and needed readjustment so that the wall would be vertical. When the readjustment was done, the top supports were already put in place, causing the mid-height crack to form in the 8th mortar joint prior to the application of lateral loading. This prevented measurement of the loads and displacements at cracking. A photograph of the crack prior to testing is shown in Figure 4.13.

Figure 4.13: Cracking of wall prior to testing

The second error was that the connections within the load spreader system were inadvertently partially restrained rotationally, resulting in the spreader system being statically indeterminate; that, in turn, caused a non-symmetrical load distribution between the top and bottom location of load application. Binding within the spreader system caused irregular shifts throughout the load-displacement profile, as seen in Figure 4.14. As the wall was cracked prior to the test, a measurement for the cracking load was not possible. However, the ultimate load, corresponding to the peak moment (1.57 kN·m), was found at a mid-height displacement of 42 mm.

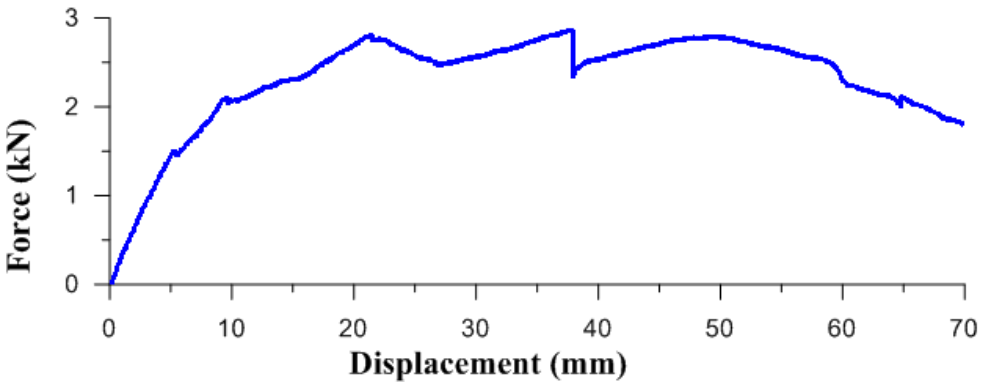

Figure 4.14: Load-displacement plot of Specimen RS1

Cracking at the bottom of the wall was observed in the first mortar joint (between the lowest two courses of block). As the test progressed, the bond in mortar joint 0 (below the lowest course) failed, with an audible sound, simultaneously causing the crack in the 1st mortar joint to close, resulting in the cracking shown in Figure 4.15.

Figure 4.15: Base cracking in mortar joint 0 in Specimen RS1

Finally, the method for attaching the LVDT's to the wall was found to be inappropriate because the LVDT's could not be removed from the wall in a safe manner while the test was running. Therefore, the test was terminated prior to the collapse of the wall so that the LVDT's could be removed. In the remaining tests a new LVDT support system was implemented that enabled safe removal of the LVDT's while the test was being conducted.

Additionally, as this was the first test to be conducted, an initial load rate of 1 mm/min was chosen since the behaviour of the wall was unknown. However, after the test of Specimen RS1 was completed, the load rate was increased to 3 mm/min in subsequent tests, as described in Section 3.7.4.

Once the LVDT's were removed, there was an opportunity to test the residual capacity of the wall by reloading it to failure. In the interests of time, the resilience (residual capacity) test was performed with a higher loading rate of 5 mm/min. The resulting load-displacement curve is presented in Figure 4.16. From the resilience test, the calculated maximum moment was 0.90 kN·m at a displacement of 62.8 mm. The resilience test showed that, even though the wall had been severely damaged by the previous test, there was reserve capacity left in the wall (57% of the original ultimate capacity.)

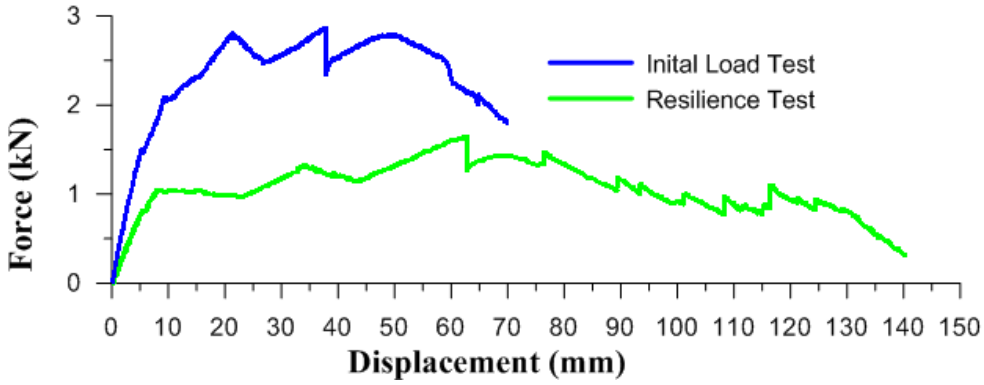

Figure 4.16: Comparison of the initial and resilience load-displacement plots for Specimen RS1

The displacement of wall RS1 at the ultimate load was approximately half the magnitude of that found in all of the other realistically pinned wall tests. In addition, the statically indeterminate spreader system caused a somewhat different behaviour compared to the other walls. Therefore, it was deemed that the behaviour of this wall was significantly different from the other walls; as a result, the measured data was not included in the data set used to compute the average response of the real-static (RS) test series.

4.5.3 Wall Specimen RS2

This wall test was conducted after RS1, and was the first wall test to use the updated load spreader and LVDT support systems. Unfortunately, two new complications occurred during set-up of the load cells. Firstly, the two load cells that were within the spreader system were improperly connected so that applied load could not be recorded. Secondly, the physical characteristics of the load cell allowed it to become pinched in the load spreader system in such a way that the load was able to be passed though the spreader system load cells without load being measured.

Two unsuccessful attempts were made at loading the wall before the problem could be rectified satisfactorily. With both unsuccessful attempts, testing was halted before visible cracking was observed. However, the load-displacement plot (Figure 4.17) of this test specimen has similar characteristics to those of Specimen RS1. At the start of the test, in particular, it is evident that the load-deflection behaviour is similar to RS1, indicating that the wall had, in fact, been cracked, even though the cracking was not observable. When the center crack became visible, that crack had formed in the 8th mortar joint, as it had in Specimen RS1, and the bottom crack formed in the 1st mortar joint.

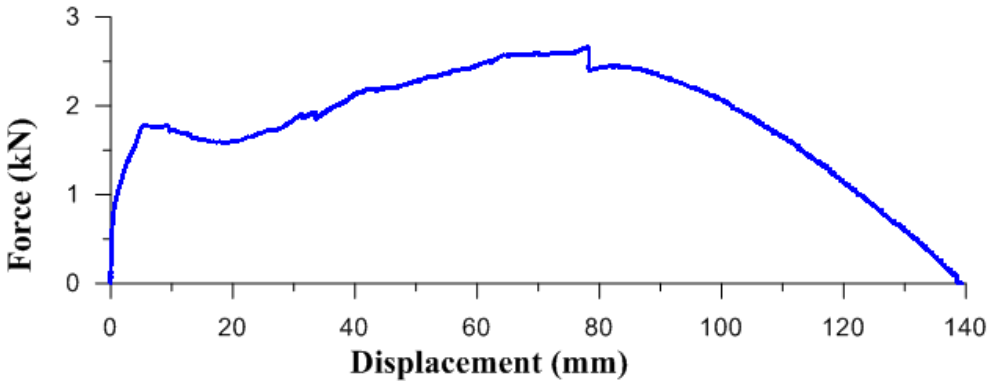

Figure 4.17: Load-displacement plot of Specimen RS2

After the mid-height cracking became visually observable (at a displacement of approximately 5 mm) there was an apparent post-crack strengthening phase. The load-deflection behaviour during this strengthening is seen to be similar to the behaviour of steel undergoing strain hardening in that the applied load increased with increasing deflection. This post-cracking behaviour is thought to be caused by the

top-most course of masonry block binding in its support. The binding does not allow the unloaded face of the wall to move vertically with increasing deflection, generating an axial compressive force that allows for arching action to occur within the wall. The arching is thought to increase the overall strength of the wall past its initial pre-cracking strength.

As the test progressed, the ultimate load was found to coincide with the sharp decrease in load at approximately 78 mm of mid-height deflection, with the calculated peak moment being 1.46 kN·m. The observation that the ultimate moment occurred just before a drop in load was a characteristic also seen in Specimens RS1 and RS4. It is possible that the instantaneous drop in load corresponded to cracking of the top most mortar joint.

4.5.4 Wall Specimen RS3

Specimen RS3 was the fifth wall specimen to be tested, and the third static test. Similar to the RS2 test, the top and bottom load cells were not properly installed initially and they were unable to properly read load. This error was not observed until after the wall specimen had been loaded well past mid-height cracking, where the test was ended when the wall had been displaced approximately 55 mm at mid-height. The center load cell, which was functioning properly (Figure 4.18), was therefore used as the sole source for providing the measured load for calculating the cracking moment of 0.92 kN·m at a displacement of 0.80 mm. The load is denoted with an asterisk (*) in Table 4.4 because the load cell that recorded the load was not in direct contact with the walls and therefore differed from what was used for the other wall tests.

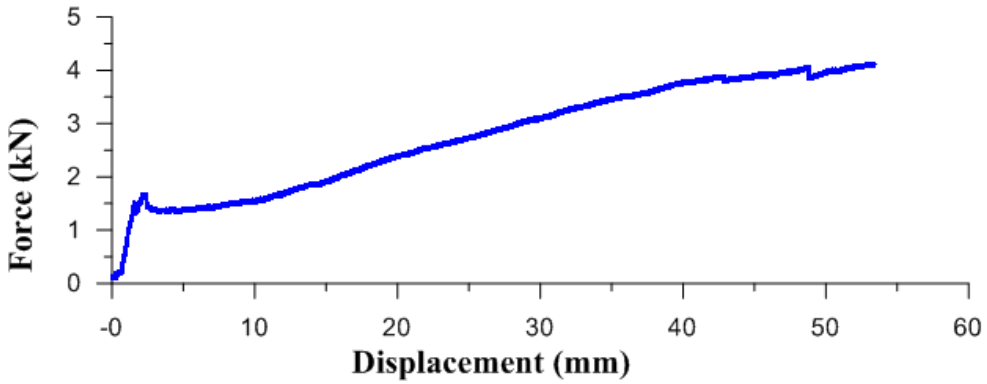

Figure 4.18: Load-displacement plot of Specimen RS3

The mid-span crack for this wall was located at the 9th mortar joint, with the bottom crack forming in mortar joint zero. Similar to Specimen RS2, post-cracking behaviour with large strength gains is apparent. Additionally, the post-cracking strength gain was accompanied by increased wall ductility, with large deflections observed at ultimate conditions. The test was then terminated prior to the collapse of the wall.

Like Specimen RS2, the increased strength and ductility of the wall in its cracked state is thought to occur from the masonry binding in the top support, thereby causing arching action. The binding of the top course of masonry could be seen when the wall was unloaded, when cracking formed along the compression face of the 14th joint as the wall was unloaded and returned to a less deflected position, as shown in Figure 4.19.

Figure 4.19: Crack formation from unloading of the wall

After the wall was unloaded, and the load cells were reconnected, the wall was reloaded. The reloading caused the cracks at the top of the wall to close, re-engaging the compression face of the joint. When the load was reapplied to the wall, the load path did not follow the initial load path that was measured during the initial loading. At the beginning of the test, instead of a quick increase in load, the softer, cracked, wall reached a constant load value as the wall displaced until the crack at the top of the wall closed, restoring the axial compressive force mechanism in the wall (at approximately 25 mm). After the top support began to reapply the axial force and arching action could be initiated, however, the load path approached a similar ultimate load, although at a steeper slope than that of the initial test. The high ultimate load reached during the re-loading phase was surprising in that a failure mechanism (cracking at the bottom, mid-height, and at the top of the wall) had already formed. This reinforces the conclusion that arching, rather than flexure, was the primary load resisting mechanism at this stage.

The ultimate condition found during this reloading phase of the wall was characterized by a calculated moment of 2.26 kN·m at a displacement of 69.2 mm. The load-deflection plot of the reloading phase is shown in Figure 4.20 and compared to the plot from initial first load trial.

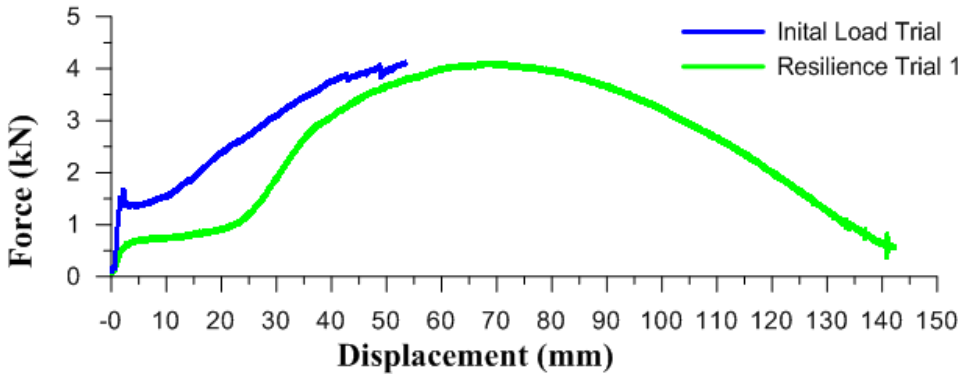

Figure 4.20: Load-deflection plot for the reloading of Specimen RS3

As wall was nearing collapse, the spreader system shifted as the frictional force holding it in place was reduced as the applied load decreased near the end of the trial. After the spreader system moved, the trial was terminated and reset. The wall was loaded again at a rate of 25 mm/min until collapse was reached. A plot of the three load-displacement curves is shown in Figure 4.21.

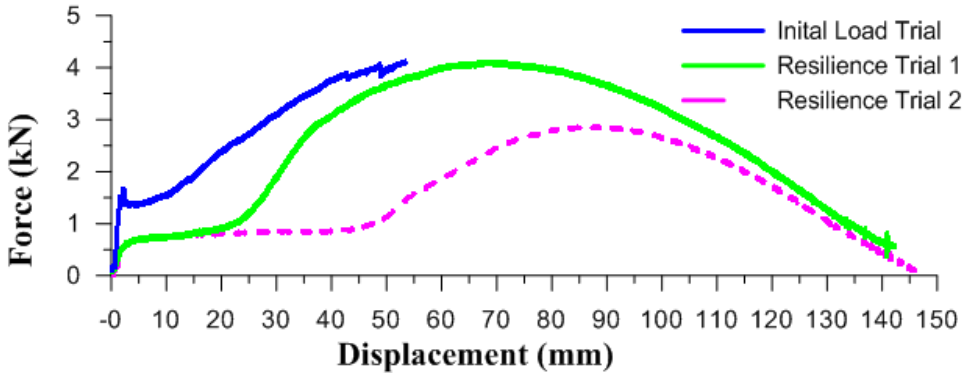

Figure 4.21: Load-displacement plot of the residual capacities of Specimen RS3

For the first resilience trial, the wall was cracked, but had not necessarily reached its ultimate load state during the initial load trial; the wall was therefore able to be reloaded to a similar level of load as the initial load trial. After the first resilience trial, the second resilience trial shows that there was still load capacity in the wall even after it had been severely damaged, and considered failed by engineering standards (i.e. post-ultimate behaviour). The second and third tests were similar in nature to the resilience test which was performed on Specimen RD1 (discussed below).

It should be noted that the load measured for the first trial was exclusively taken from the single central load cell placed on the load actuator, whereas the load-deflection plots for the first and second resilience trial use the data collected from the load cells placed on the top and bottom of the load spreader system similar to all of the other tested specimens.

4.5.5 Wall Specimen RS4

The load-displacement curve for Specimen RS4 is shown in Figure 4.22. It is evident that the load initially increased rapidly with small displacements. The first and second peaks correspond to cracking at the base of the wall and at mid-height, respectively. The calculated moment at mid-height cracking was 1.39 kN·m with a displacement of 1.64 mm. The mid-height crack formed in the 9th mortar joint with the bottom crack forming in the 1st joint. The ultimate load corresponds to cracking at the top of the wall, where the calculated ultimate moment was 1.65 kN·m at a displacement of 86.70 mm.

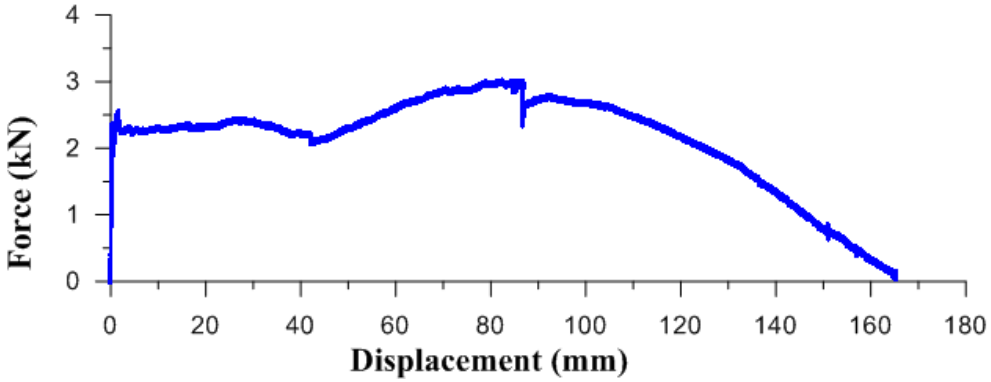

Figure 4.22: Load-displacement plot of Specimen RS4

4.5.6 Wall Specimen RS5

Similar to Specimen RS4 the location of cracking on the load-deflection curve for Specimen RS5 was well defined, and is shown in Figure 4.23. The mid-height crack formed lower than in the other walls, along the 6th mortar joint, placing it below the constant moment region; the bottom crack formed in mortar joint zero. The calculated cracking moment was 1.69 kN·m at a mid-height displacement of 0.23 mm. However, unlike the other walls, the location of the ultimate load did not correspond to an immediate drop in load; instead, a smooth, gradual decrease was observed. The ultimate load corresponded to a maximum calculated moment of 1.92 kN·m after a displacement of 61.6 mm at mid-height. The location of the top crack was unable to be seen, most likely because the upper portion of the wall was taller than for other wall specimens (since mid-height cracking occurred at the 6th mortar joint). This appeared to result in a failure of the top joint that was less violent.

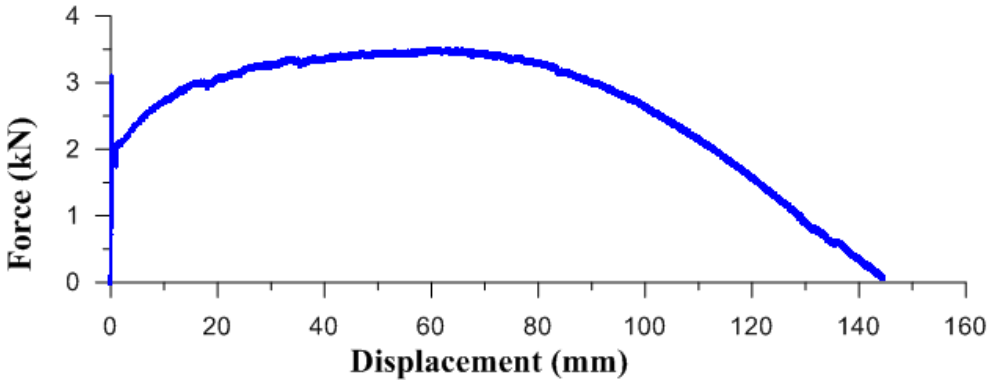

Figure 4.23: Load-displacement plot of Specimen RS5

4.6 Realistic-Dynamic test series

4.6.1 Overview

The dynamic tests conducted on the walls with realistic supports were done in alternating order with the corresponding static tests. A unique set of wind time histories was generated for each wall, with each wall test starting with the 14 m/s trial where the simulated wind "storm" (i.e. a 10 minute time history) had a mean wind speed of 14 m/s. The mean wind speed value of each successive trial was increased by 2 m/s until failure was achieved. Visible damage was not observed in any of the walls as a result of the wind histories with a mean speed of 14, 16, or 18 m/s (0.13, 0.17, 0.21 kPa, respectively). Cracking at mid-height generally occurred during the 20 m/s trial (corresponding to a mean pressure of 0.26 kPa), while collapse of the walls was initiated during storms with wind speeds equal to, or larger than 30 m/s (0.58 kPa).

The dynamic test series were conducted under load control, rather than displacement control as used in the static tests. As a result of the fluctuating load cycles, there was no longer a unique relationship between displacement and applied load; therefore, the definitions of critical states had to be modified for the dynamic tests.

The mid-height cracking load condition was defined as the instant at which there was a sudden, significant increase in the measured displacements, with observable cracking; this state was generally accompanied by a decreased level of agreement between the applied and set-point (target) loads, as depicted in Figure 4.9. As a consequence of the load-control system, once the stiffness of the wall had been substantially decreased by the formation of an unstable mechanism as a result of cracking at the top of the wall, the system would push the wall continuously towards collapse. Therefore, the measured load prior to the initiation of collapse defined the ultimate load condition.

As the walls became more compliant with increasing damage, unintentional high-frequency content was introduced into the dynamic load applied to the walls (chattering, as described in Section 4.3.2). In an attempt to remove the influence of the load chattering, a smoothed response was generated by applying a digital filter to the data. The filtered load time history was determined using a 1st order Butterworth filter applied in a forward-backward method (Mathworks, 2002) with a cut-off frequency of 1 Hz. The filtered data shows the long wave length response of the wall subjected to the wind load. Both unfiltered and filtered moments are provided for the ultimate condition in Table 4.5.

In the following sections, observations from multiple wind speed trials are described for the different walls in the realistic-dynamic test series. A summary of the results are presented in Table 4.5. The table presents the same type of data that was described for the static test, in addition to moments corresponding to digitally filtered data at the ultimate condition state. All of the load-time histories of each trial are presented in Appendix F, with displacement time histories of the horizontal and vertical centerlines shown in Appendix G.

Table 4.5: Summary of real-dynamic (RD) test results

Wall			RS1	RS2	RS3	RS4	RS5	Mean	C.O.V. (%)
Bottom Cracking	Moment (kN·m)		1.00	0.39	1.21	1.00	1.09	0.94	33.9
	Displacement (mm)		0.15	0.17	0.25	0.27	0.15	0.20	29.1
Center Cracking	Moment (kN·m)		1.20	1.02	1.21	1.09	1.40	1.18	12.2
	Displacement (mm)		0.97	1.98	0.25	3.61	1.22	1.61	79.7
Ultimate	Moment (kN·m)	Unfiltered	2.36	1.89	2.15	1.62	1.90	1.98	14.2
		1 Hz filter	1.36	1.24	2.01	1.01	1.39	1.40	26.5
	Displacement (mm)		91.1	90.5	87.0	94.7	94.8	91.6	3.6
Crack location†	Center		9	9	10	8	7	-	-
	Bottom		0	1	0	1	1	-	-

†Mortar joint counting up from the base, with "0" representing the bed joint between the first course and concrete beam.

4.6.2 Wall Specimen RD1

Specimen RD1 was loaded successively with load time histories corresponding to mean wind speeds of 14, 16, and 18 m/s (0.13, 0.17, 0.21 kPa, respectively), without any observable damage. The response of the 16 m/s trial is depicted in Figure 4.24; based on visual examination, the wall was undamaged as a result of this trial. Figure 4.24 indicates that the applied load followed the set-point accurately throughout the trial. However, there did appear to be a small, constant offset between the set-point and the applied load, with the applied load being somewhat lower.

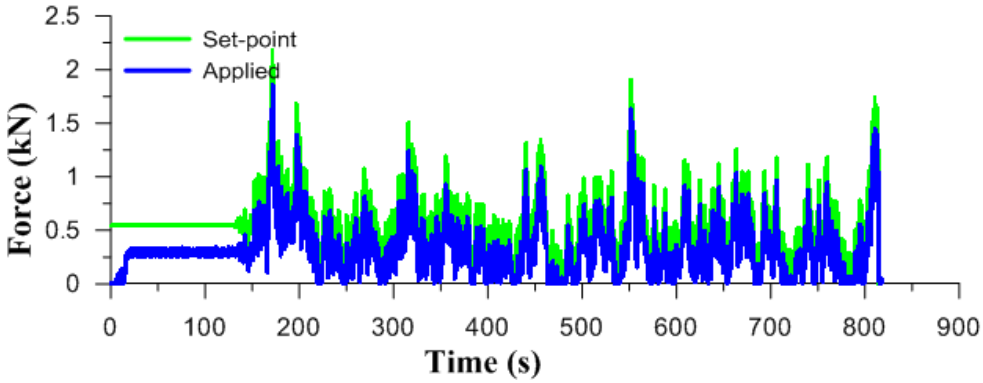

Figure 4.24: 16 m/s load time history plot for Specimen RD1

It is thought that the difference between the applied load and the set-point load may be attributed primarily to friction in the roller used to support the horizontal hydraulic actuator. Figure 4.25 shows the trial of the controlling (center) load cell at a 16 m/s reference wind speed. Here the agreement between the set-point and the measured load is better. However, because the measured response of this load cell is not being directly applied to the wall it was not an accurate representation of the applied load on the wall.

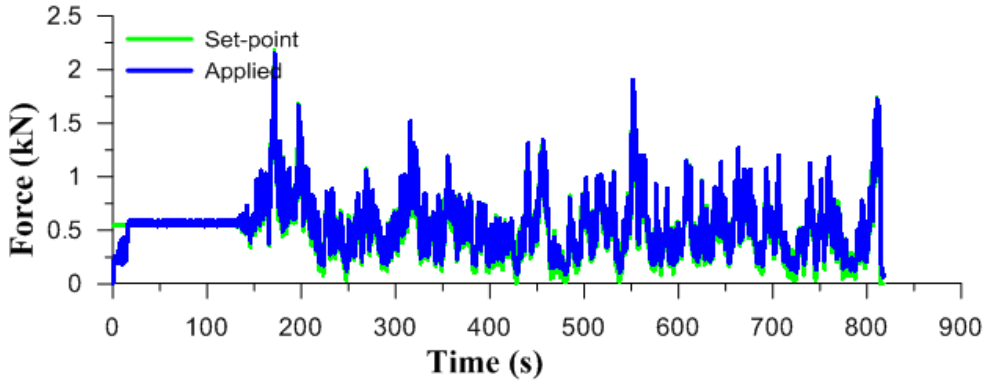

Figure 4.25: Comparison of the applied load measured from the control load cell and the set-point for Specimen RD1 and the 16 m/s trial

After the 16 m/s trial, the first indication of damage found in this wall test occurred during the 18 m/s trial. Under small deflections, the wall behaved as a "propped" cantilever, in which the top support had enough "play" that the base of the wall was relatively much stiffer in rotation prior to cracking. Figure 4.26 shows the load time history of the 18 m/s trial. Cracking at the bottom of the wall appeared to occur at a calculated moment of 1 kN·m.

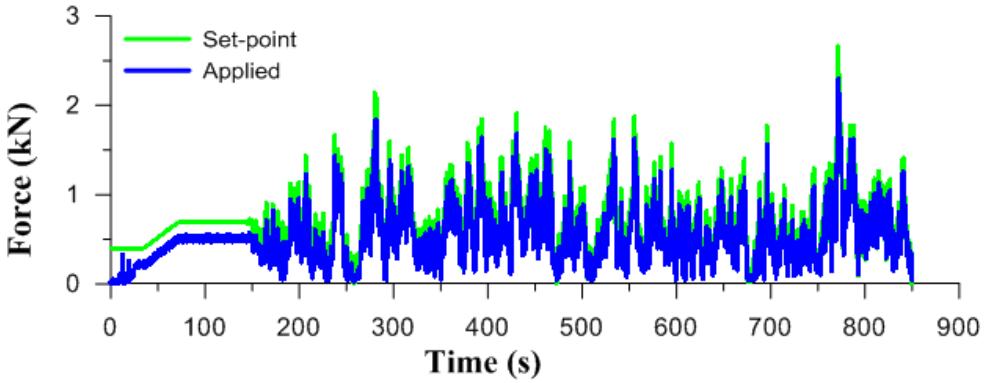

Figure 4.26: 18 m/s load time history plot for Specimen RD1

When the bottom crack formed, the agreement between the measured and set-point load time histories did not change in any observable manner. The bottom of the wall cracked at approximately 280 s into the trial. This is indicated by a large change of the mean displacements of the wall at that time. The displacement time history of the wall during the 18 m/s trial is shown in Figure 4.27. The mean displacement of the wall pre- and post-cracking at the bottom of the wall is indicated by horizontal dashed lines. When cracking at the base of the wall occurred, the mean displacement of the wall at mid-height increased by 0.2 mm. Prior to cracking (at 280 s), the instantaneous displacement of the wall was 0.15 mm at mid-height; once the crack had formed, the wall displacement increased to 0.38 mm. However, these small displacements were too small to be observed visually. Therefore, mid-height cracking was the first crack that was visually observable.

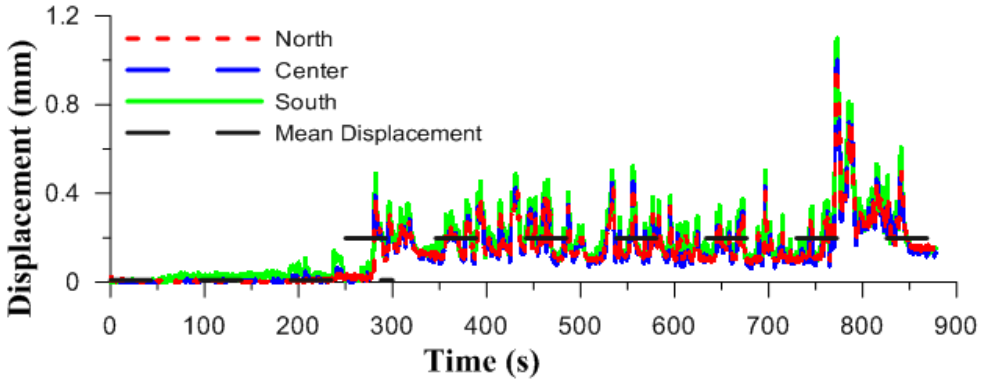

Figure 4.27: 18 m/s displacement time history of Specimen RD1

Cracking at mid-height of the wall was observed during the 20 m/s trial at approximately 355 s, as shown in Figure 4.28. The calculated moment applied by the gust that cracked the wall was 1.20 kN·m at a displacement of 0.97 mm. The mid-height crack formed in the 9th course, while the bottom crack formed in the 0th course.

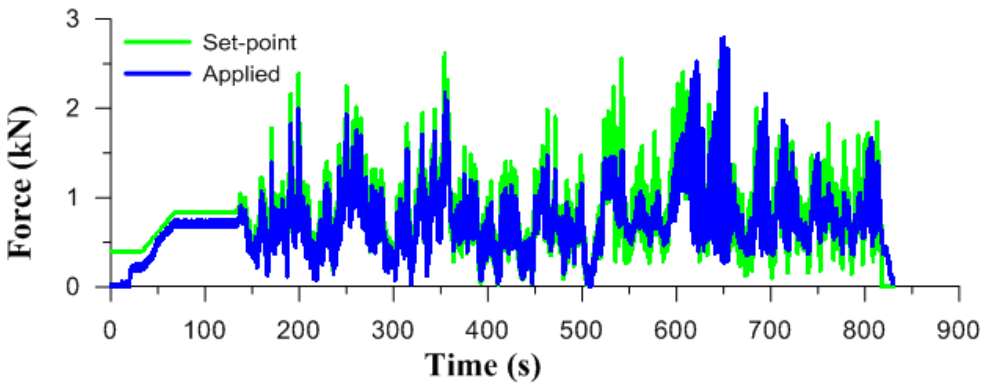

Figure 4.28: 20 m/s load time history plot of Specimen RD1

After the wall was cracked at mid-height, the agreement between the set-point and measured loads decreased. This can be seen in Figure 4.28 where, after cracking, the difference between the measured and the applied loads increased. This was coupled with an overall increase in mid-height deflection after that time, as shown in Figure 4.29. As the loading of the wall progressed, large deflections started to occur at approximately 520 s; the large deflection coincided with a large decrease in the stiffness of the wall. This large decrease in stiffness caused the agreement between the applied and set-point load to significantly decrease, and the introduction of high-frequency loading content to be applied to the wall. For the remaining time histories, the agreement between the set-point and applied loads was consistently decreased.

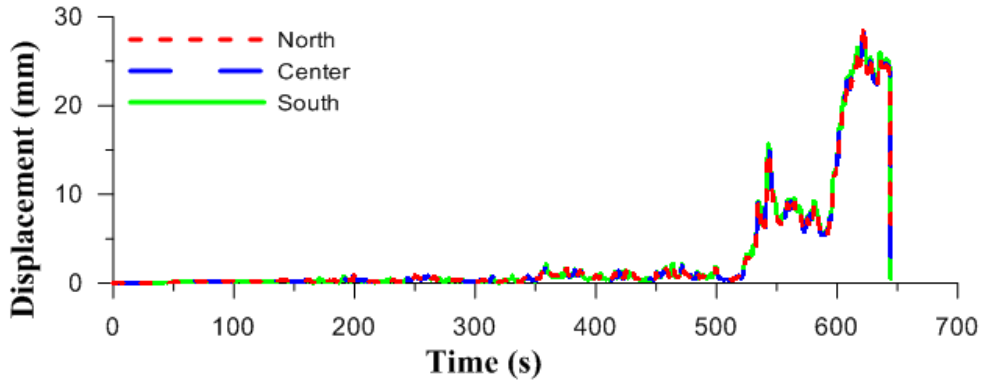

Figure 4.29: 20 m/s displacement time history of RD1 measured until LVDT's were removed

Cracking at the top of the wall formed during the 28 m/s trial. As the wall was deflected, the rotation at the top of the wall would cause the top course of masonry to become bound in the support. When the wall was unloaded between trials, a crack would open on the compression face of the joint, as shown in Figure 4.30. However, once the wall was reloaded, the crack would close and rotation would occur along that joint.

Figure 4.30: Cracking below the top course of block in Specimen RD1

Lastly, the collapse of the wall occurred during the 30 m/s trial. As the wall was severely damaged at this stage, large amounts of high frequency loading content was introduced into the wall because the load control system was unable to find the requested load before the next value was needed. This is shown in Figure 4.31, where a large amount of "chattering" is seen. The largest instantaneous load occurred prior to collapse initiation, for which the calculated moment was 2.36 kN·m. However, the filtered moment (see Section 4.6.1) of 1.36 kN·m may better represent the quasi-static behaviour of the extremely damaged wall specimen. Finally, the collapse of the wall was initiated by a large gust occurring in the set-point data with a mean value that exceeded the quasi-static load that was being applied to the wall. This suggests that a sustained loading peak was required to allow the wall to displace to a geometrically unstable position.

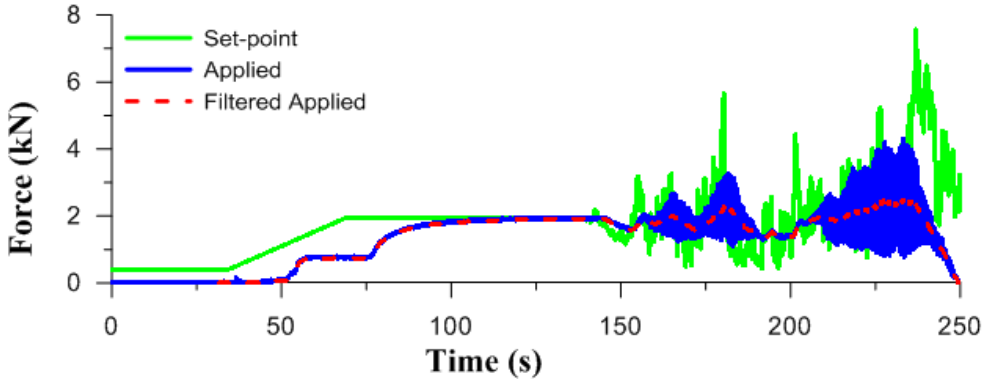

Figure 4.31: 30 m/s load time history plot of Specimen RD1

4.6.3 Wall Specimen RD2

Similar to Wall RD1, there was no observable damage on the wall before the center crack formed. Of the real-dynamic (RD) wall tests, the agreement between the set-point and the applied load was the lowest for this wall. The 14 m/s trial is shown in Figure 4.32. In this case, the load system was seemingly unable to reach the peaks that were requested, and was likewise unable to correspond to the requested values when the load had decreased substantially.

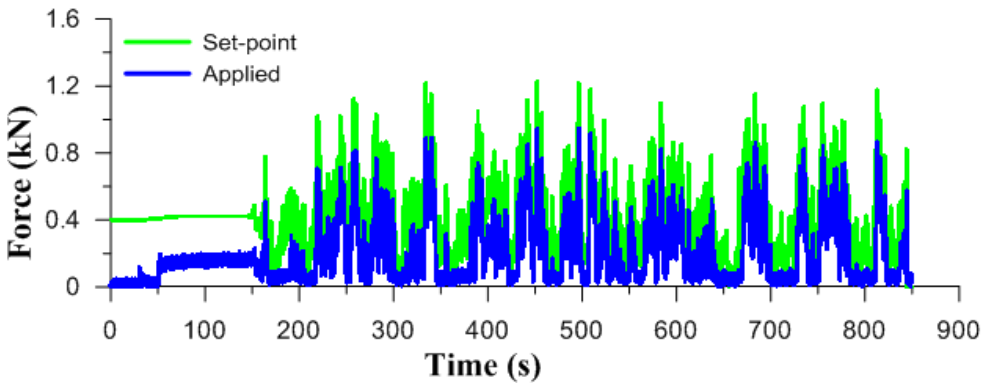

Figure 4.32: 14 m/s load time history plot of Specimen RD2

A normalized PSD of the 14 m/s trial is shown in Figure 4.33, where the applied and set-point data are plotted. The applied load record had approximately 68% of its available energy contained in the frequency ranges below 0.1 Hz, while the set-point load had approximately 72% of the total energy contained below 0.1 Hz. Additionally, the energy content of the applied load between 0.1 Hz to 1 Hz and 1 Hz to 8.7 Hz was 28% and 4%, respectively, compared to 24% and 4% over the same frequency bands for the set-point record. This shows that the applied load had some shifts in frequency content; however, the overall shapes of the PSD's are similar, showing that the load apparatus approximated the wind load.

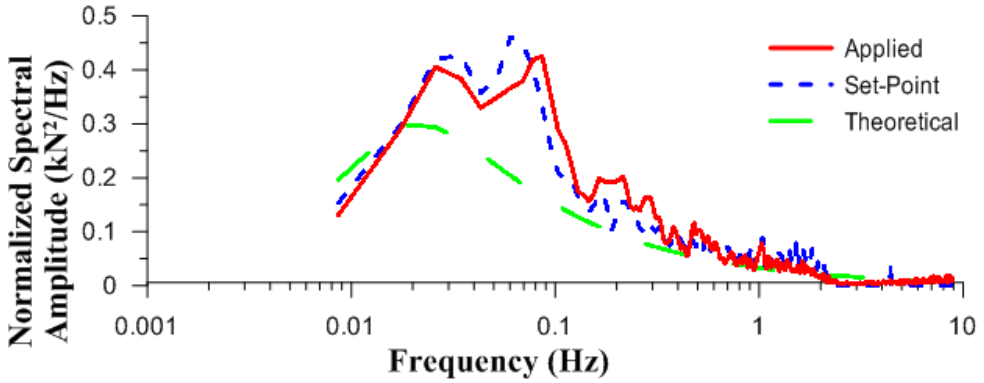

Figure 4.33: PSD of set-point and applied load for the 14 m/s mean wind speed of Specimen RD2

Similar to Specimen RD1, visually unobservable base-cracking occurred in a trial prior to the observed mid-height cracking. For Specimen RD2, the bottom crack occurred during the 14 m/s trial, as shown in Figure 4.34. The crack at the base of the wall formed at an elapsed time of approximately 225 s, with a calculated moment when the crack formed was 0.39 kN·m, significantly lower than what was found for the other walls. However, the displacement at cracking was 0.17 mm, consistent with the results from the other specimens. Like Wall RD1, the base-crack was indicated by a change to the mean displacement at the time of the crack.

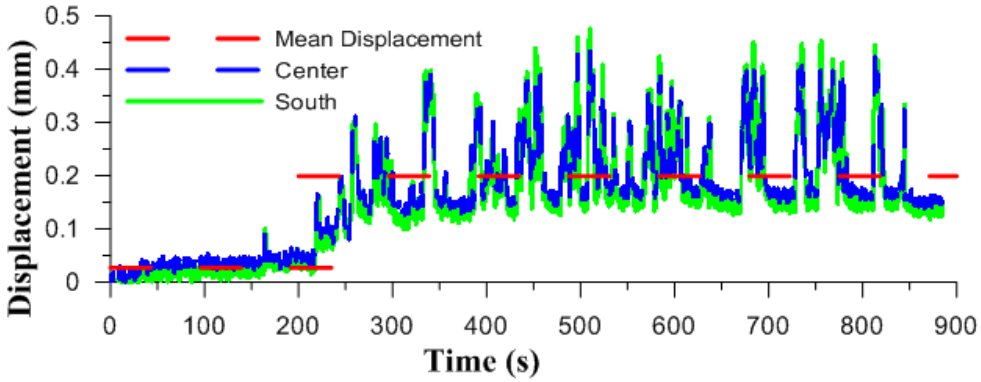

Figure 4.34: Displacement time history plot of the 14 m/s mean wind speed of Specimen RD2

Prior to the mid-height crack forming, the wall experienced a time of induced high-frequency content. The time history for the 18 m/s trial is shown in Figure 4.35. This type of vibration usually occurred when a wall became more damaged.

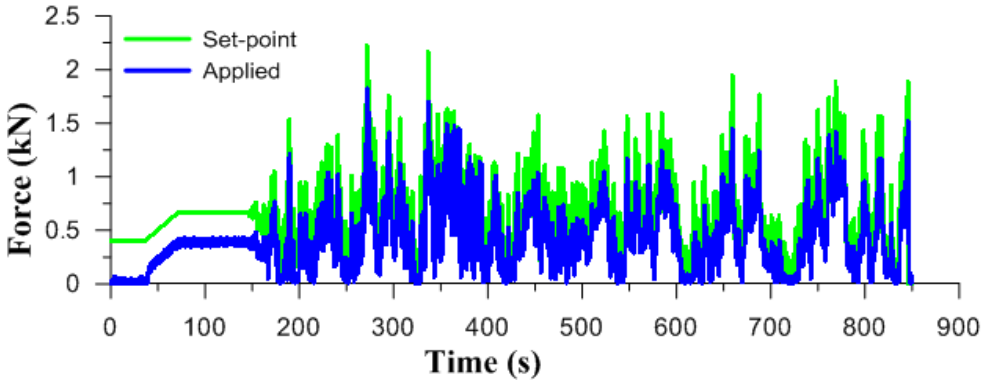

Figure 4.35: 18 m/s load time history plot of Specimen RD2

Mid-height cracking of this wall specimen occurred during the 20 m/s trail, as is shown in Figure 4.36. Cracking of the wall corresponded to the gust occurring at approximately 250 s into the test. The crack formed in the 9th mortar joint, with the calculated mid-height moment being 1.02 kN·m at a displacement of 1.98 mm. The crack at the bottom of the wall became visible in the 1st mortar joint during the 22 m/s trial.

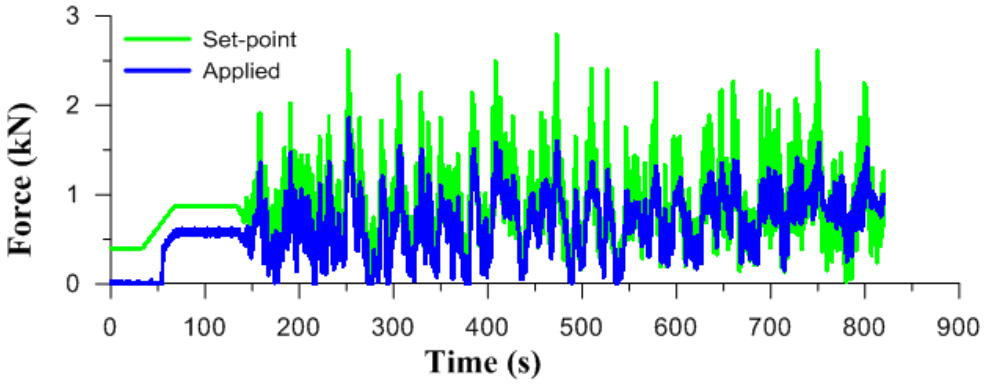

Figure 4.36: 20 m/s load time history plot of Specimen RD2

Cracking at the top of the wall did not occur during the application of a wind record, but during the unloading of the wall after the 26 m/s trial. At this stage, the top course of block had become bound in the support, and initial top course cracking was noted on the compression face of the wall, as shown in Figure 4.37. Additionally, the cracking at the top of the wall was accompanied with the failure of the head joint between the half-block at one end of the wall and the center block.

Figure 4.37: Photograph of the debonded half-block in the top course of Specimen RD2

Lastly, the wall collapsed during the 34 m/s trial. Non-specified high-frequency vibrations were experienced throughout this wind record, as illustrated in Figure 4.38. Collapse of the wall began at approximately 430 s, at an unfiltered moment of 1.89 kN·m, and a filtered moment of 1.24 kN·m. Like wall RD1, the collapse of this wall coincided with a large gust in the set-point data that was larger than the filtered (quasi-static) component of the load.

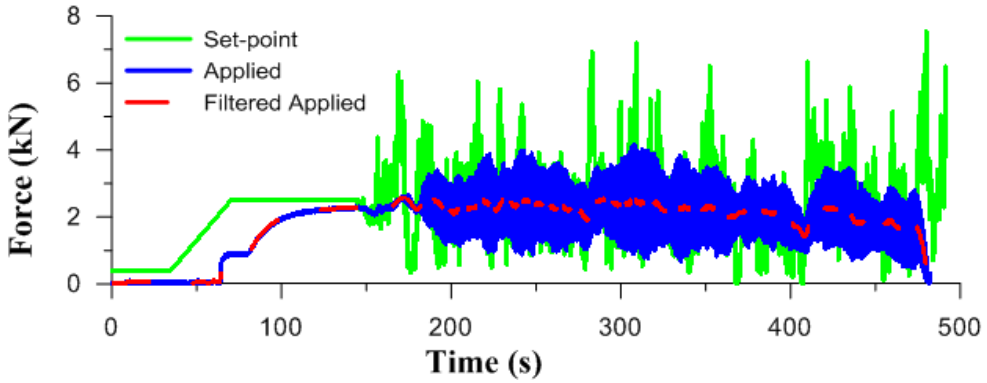

Figure 4.38: 34 m/s load time history plot of Specimen RD2

4.6.4 Wall Specimen RD3

Unlike the first two dynamic tests, there was no observable change in the deflection response that would indicate initial cracking at the base of the wall. The first change in deflection characteristics occurred with cracking at the mid-height of the wall. Therefore, the formation of the mid-height crack and the crack at the bottom of the wall appeared to happen simultaneously. The simultaneous cracking occurred during the 20 m/s trial, as shown in Figure 4.39. The mid-height crack formed at the 10th mortar joint (at approximately 375 s), outside the constant moment region, while the bottom crack formed at mortar joint zero. The moment at mid-height cracking was 1.21 kN·m, when the wall was displaced by 0.25 mm. Like wall RD2, the largest wind gust during the record was the gust that caused cracking within the wall. Also like wall RD2, the top crack formed during unloading of the wall after the 24 m/s trial.

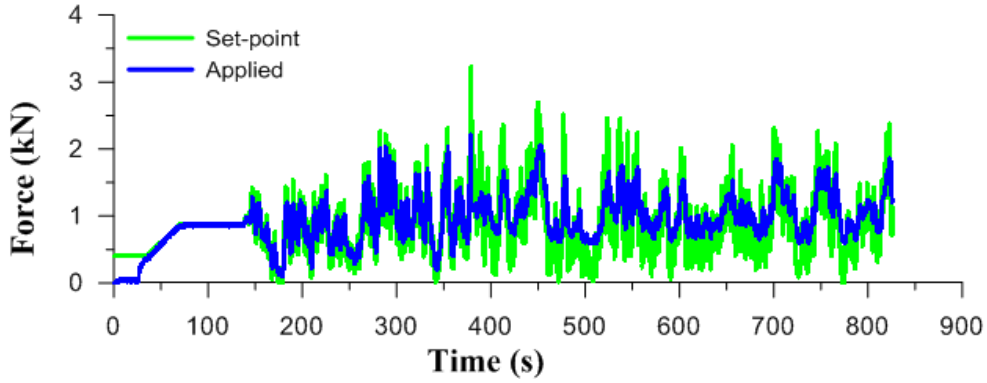

Figure 4.39: 20 m/s load time history plot of Specimen RD3

Vibrations were induced into the wall starting during the 26 m/s wind record, with more vibrations present as the wall was progressively more damaged. However, during the 36 m/s wind record (Figure 4.40), although high-frequency content was induced, it was less prevalent compared to walls RD1 and RD2. Again, similar to walls RD1 and RD2, a large gust in the set-point data caused the collapse of the wall; the calculated moment at the ultimate condition was 2.15 kN·m at a displacement of 87.0 mm. This

wall specimen was able to withstand a wind time history with the highest mean wind speed as compared to any other dynamic test.

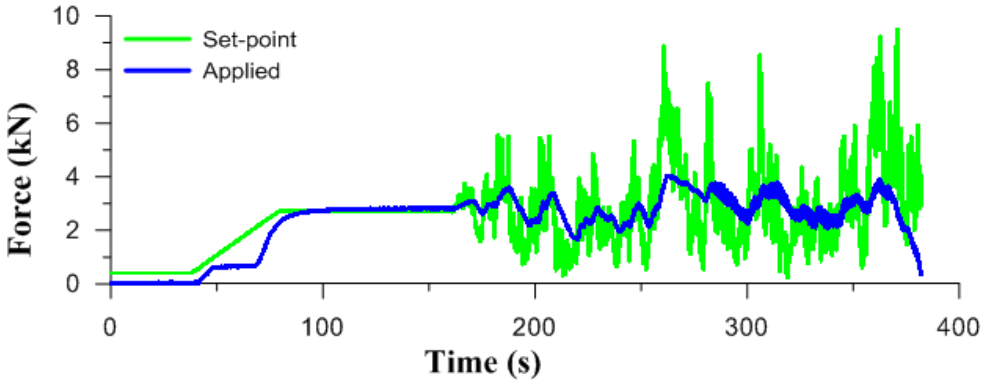

Figure 4.40: 36 m/s load time history plot of Specimen RD3

4.6.5 Wall Specimen RD4

Like the other tests, the bottom cracking was observed in the data prior to the mid-height cracking of the wall. The displacement time history for the 18 m/trial is shown in Figure 4.41, where the crack at the base of the wall formed at approximately 410 s. like Specimens RD1 and RD2, the base-crack was indicated by a large change in mean displacements of the wall at mid-height. Additionally, similar to wall RD1, the 18 m/s trial contained the largest wind gust found in any of the wind records used in this wall test.

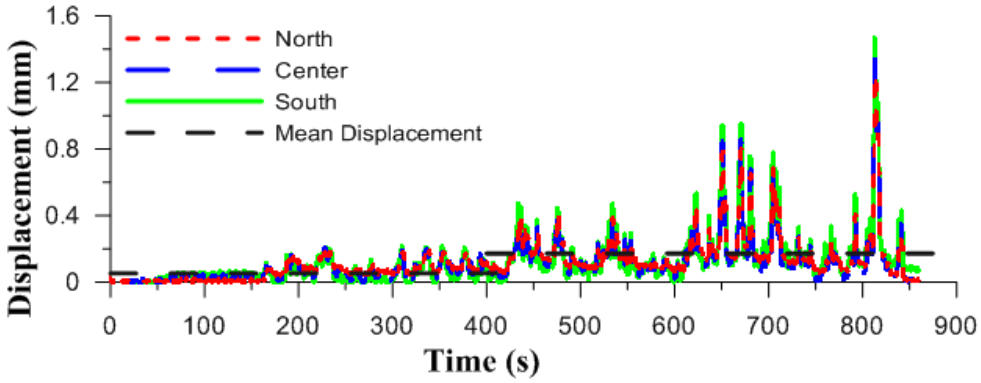

Figure 4.41: Displacement time history plot of the 18 m/s mean wind speed of Specimen RD4

Unlike the other wall tests, observable cracking occurred during the 22 m/s trial. However, like the other wall specimens, the collected data indicated that the crack first formed near the end of the 20 m/s trial (Figure 4.42). The mid-height cracking formed at approximately 750 s. There was acceptable agreement between the set-point data and the applied load until the wall became increasingly damaged, after which the agreement decreased. The moment at cracking was found to be 1.09 kN·m, with a deflection of 3.61 mm.

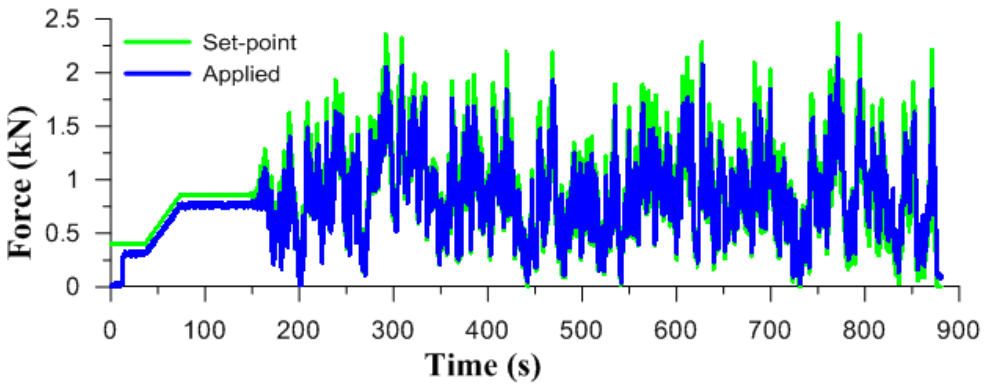

Figure 4.42: 20 m/s load time history plot of Specimen RD4

When the mid-height crack formed in the 8th mortar joint and the bottom crack formed in the 1st mortar joint during the 22 m/s trial, as shown in Figure 4.43, the agreement between the set-point and the applied load deteriorated badly. Additionally, high frequency content in the applied load was introduced immediately after the crack formed.

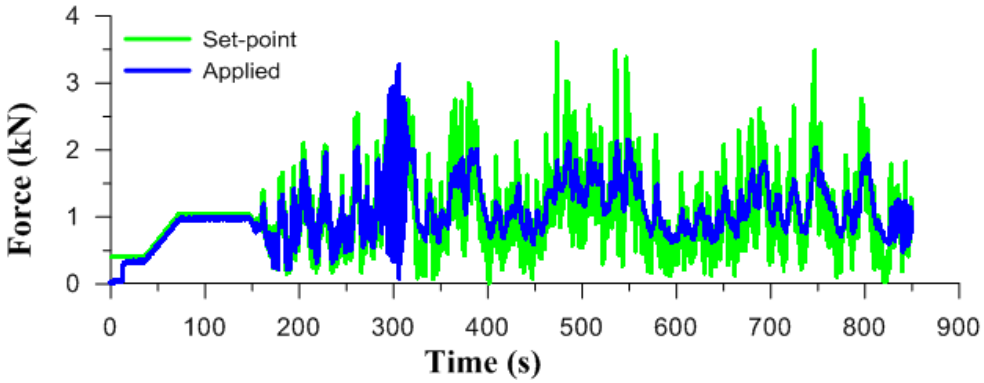

Figure 4.43: 22 m/s load time history plot of Specimen RD4

Lastly, the wall collapsed during the 32 m/s trial, as shown in Figure 4.44. The ultimate calculated moment at that instant was 1.62 kN·m, with a displacement of 94.7 mm. Unlike the previous tests where a single large gust in the set-point data caused the collapse of the wall, a series of gusts preceded the collapse. The first gust that occurred at approximately 300 s, did not cause collapse of the wall; however, it did cause a drop in the applied load that the wall could sustain. Following that, the next gust again increased the resulting deflection, while lowering the load resistance. Finally, a lower intensity gust was able to collapse the wall.

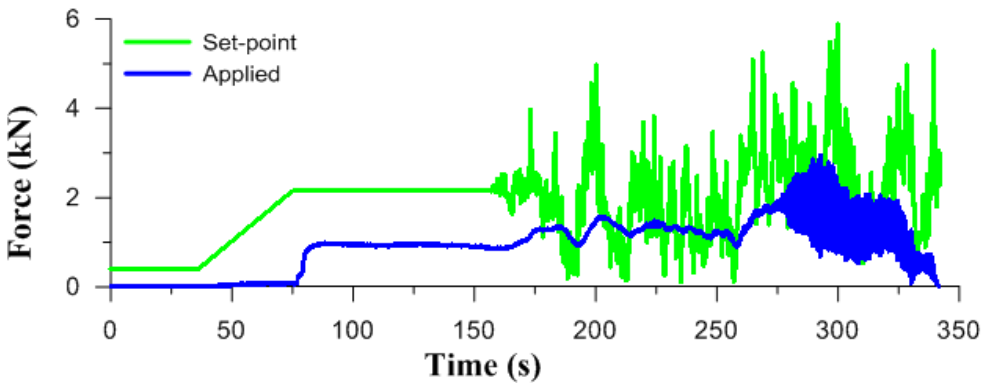

Figure 4.44: 32 m/s load time history plot of Specimen RD4

4.6.6 Wall Specimen RD5

Like the other walls, bottom cracking was detected in Wall RD5 prior to mid-height cracking during the 18 m/s trial, as shown in Figure 4.45. The large increase in deflection at 305 s indicates the instant at which the wall was initially damaged.

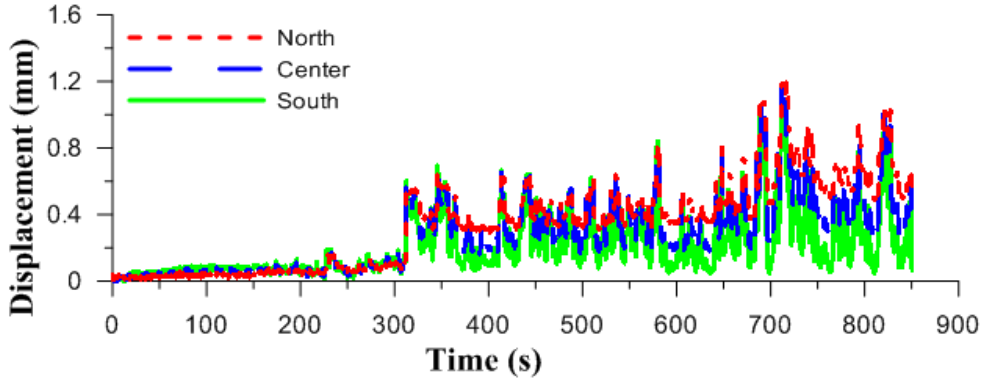

Figure 4.45: 18 m/s displacement time history plot for Specimen RD5

The mid-height crack occurred during the 20 m/s trial, at approximately 630 s, with the crack forming within the 7th mortar joint, and the bottom crack forming in the 1st mortar joint. The load time history plot of the 20 m/s trial is shown in Figure 4.46. The calculated moment and displacement at this stage of cracking was 1.40 kN·m and 1.2 mm, respectively.

Additionally, like Specimen RD4 there was acceptable agreement between the set-point and the applied load prior to mid-height cracking. However, once mid-height cracking had occurred, the wall became unstable and a short period of the high frequency "chattering" was applied to the wall. Similar to Wall RD4, the agreement between the set-point and applied load was reduced after the cracking even when the chattering was no longer being applied.

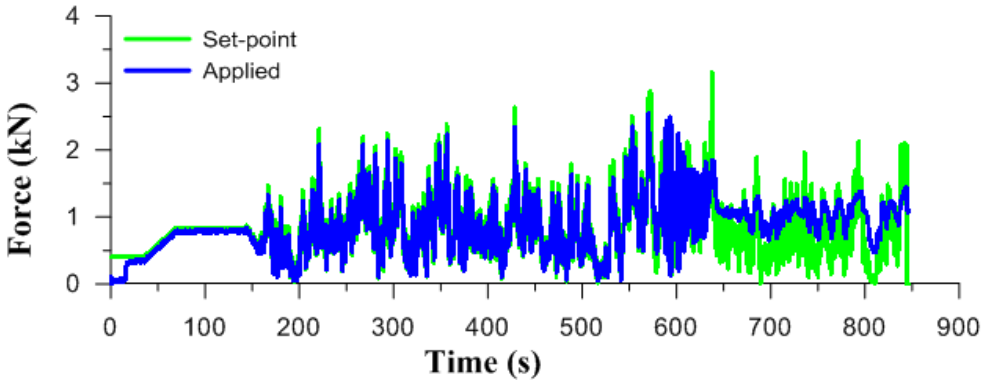

Figure 4.46: 20 m/s load time history plot for Specimen RD5

The top crack formed during the 26 m/s trial, with collapse occurring at the end of the 30 m/s trial, which is shown in Figure 4.47. This time history is similar to the failure time history of the RD2 wall test, with the ultimate calculated moment being 1.98 kN·m, at a displacement of 91.6 mm. The collapse of the wall occurred in a similar manner to Wall RD4, where multiple successive gusts were needed to push the wall to failure.

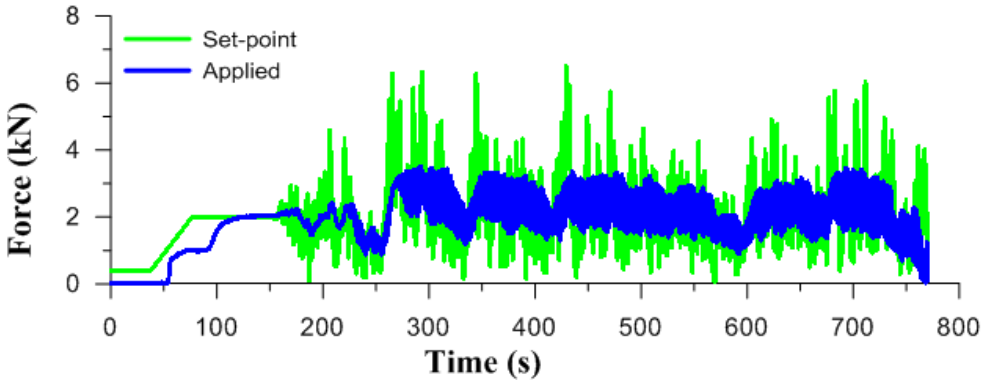

Figure 4.47: 30 m/s time history for Specimen RD5

4.7 Ideal-Static tests series

4.7.1 Overview

The results of the ideally pinned walls subjected to static loads are presented here. The pre-cracking response of these walls was similar to the pre-cracking behaviour of the realistically pinned walls. At the beginning of the tests, the applied load increased quickly to the peak value, and then dropped with the formation of the crack near mid-height. The mid-height crack typically formed when the mid-height displacements were generally less than 1 mm. Once the mid-height crack had formed, the load capacity of the walls was significantly decreased, after which the applied load decreased in a nearly linear manner with increasing displacement. Observations and results relating to each wall are given in the following

sections. A summary of calculated moments, mid-height displacements and the location of mid-height crack are presented in Table 4.6.

Table 4.6: Summary of ideal-static (IS) test results

Wall	IS1	IS2	IS3	IS4	IS5	Mean	C.O.V. (%)
Moment (kN·m)	0.66	0.95	0.71	0.70	0.68	0.74	16.1
Displacement (mm)	1.0	0.4	0.4	0.3	0.9	0.60	54.0
Crack location	8	10	9	8	8	-	-

4.7.2 Wall Specimen IS1

When an ideal wall was set onto the knife-edge in the test frame, the base of the wall was blocked and leveled to ensure that the wall was vertical. The blocking prevented the walls from collapsing while the top connection was being put into place. Prior to testing, the blocking was removed and the wall was completely supported by the top and bottom pin connections. During this time, some of the walls rotated out-of-plane, and began to lean towards the loading frame, which placed the horizontal rods in the top support into compression.

The first ideal-static (IS1) wall behaved in this way. At the start of the test, as the load spreader system came into contact with the wall, the load system would slowly push the wall back into a vertical position, at a small applied load. However, the initial flatter portion of the load-deflection curve, as seen in Figure 4.48, indicates that it took relatively more applied load to return wall IS1 to its vertical position, as compared to the other walls in this series.

Wall tests IS2 and IS4 had the expected load-deflection path, in which there was no initial out-of-vertical behaviour, featuring an almost-vertical slope at the beginning of the test. Likewise, wall IS3 which started out being out-of-vertical in a manner similar to wall IS1, was brought back into a vertical orientation before significant loading took place, which resulted, again, and almost-vertical slope indicated on the load-deflection plots.

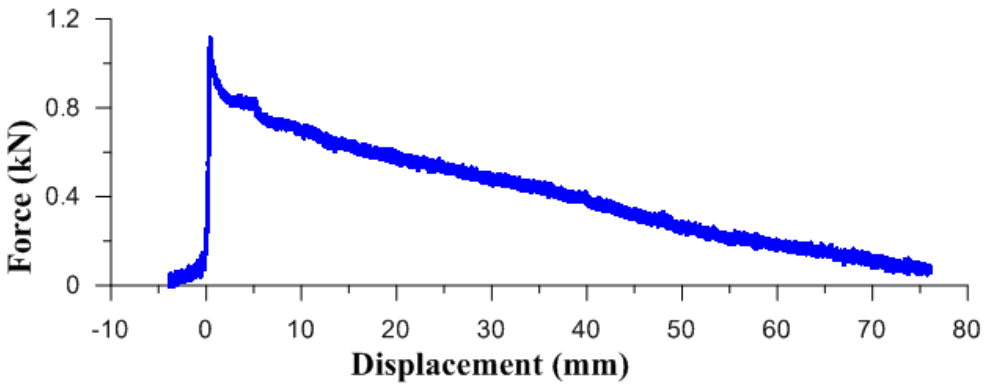

Figure 4.48: Load-displacement plot for Specimen IS1

For this first wall test, the slope of the force-displacement plot prior to cracking was not as steep as seen in the other specimens, resulting in a displacement at cracking that was larger than for the other wall specimens. This indicates that the initial out-of-plane movement of the wall when it rotated towards the load frame was not completely removed prior to the cracking of the wall. Therefore, the measured displacements at cracking for Wall IS1 are not comparable to the deflections of other walls. However, the calculated moment that was found to be 0.66 kN·m when the center line crack formed in the 8th mortar joint was comparable to results from the other walls.

4.7.3 Wall Specimen IS2

The load-displacement plot for the test of Wall IS2 is shown in Figure 4.49. The moment at cracking (at the 10th mortar joint) was 0.95 kN·m, approximately 0.26 kN·m larger than for the other wall tests. The displacement at this load was similar to the other walls at 0.36 mm. The small drop of applied load at a deflection of approximately 35 mm coincides with the removal of the LVDTs from the wall (i.e. the point at which displacements where estimated using only the LVDT attached to the load actuator).

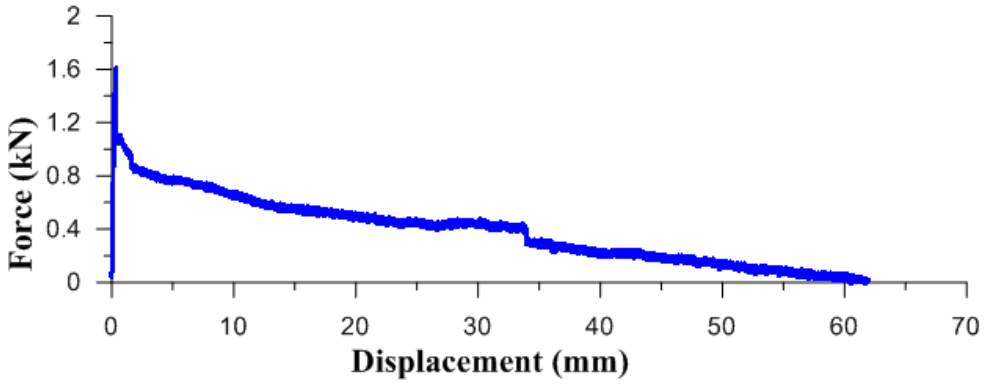

Figure 4.49: Load-displacement plot for Specimen IS2

A possible reason for the larger calculated moment could be attributed to the construction of the wall. This wall specimen was the first to be constructed, and the plaster that was placed between the first course of block and the steel angles hardened too quickly. This resulted in non-uniform contact between the block and angles, as seen in Figure 4.50. As a result, the center line of the wall was slightly shifted off the intended center line. This would have the effect of generating a counter-balancing bending moment about the knife-edge due to the self-weight of the wall. Removing this physical outlier from the data set reduced the C.O.V. from 16.1% to 3.4%.

Figure 4.50: Photo of the base connection of Specimen IS1 showing non-uniform contact between the steel angle and first course of the wall

4.7.4 Wall Specimen IS3

Wall IS3 behaved in a similar manner to Wall IS1, where the wall began with initial out-of-plane displacement. However, unlike Wall IS1, Wall IS3 returned to its vertical position during the initial application of load prior to cracking. This is shown in Figure 4.51, where the initial measured load remained constant for a displacement range of approximately 3 mm until the load quickly increased with further displacement, from which point the plot looks similar to the pre-cracking plot seen for Walls IS2 and IS4. Therefore, by removing the initial displacement associated with the initial out-of-verticality the wall cracked at a displacement of 0.5 mm, and a calculated moment of 0.71 kN·m, with a crack forming at the 9th mortar joint. Additionally, like Wall IS2, the removal of the LVDTs can be seen to result in a small jog in the load-deflection plot at approximately 11 mm of displacement.

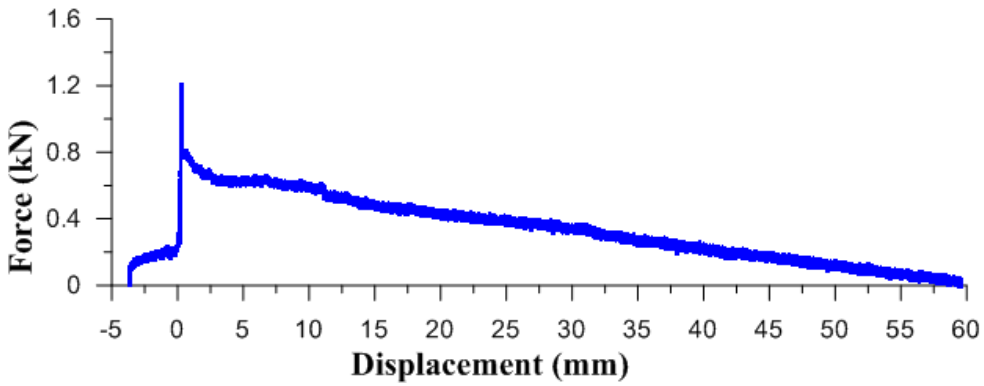

Figure 4.51: Load-displacement plot for Specimen IS3

4.7.5 Wall Specimen IS4

The load-displacement plot for wall IS4 is shown in Figure 4.52. This wall behaved similar to Wall IS2, with a mid-height cracking moment of 0.70 kN·m and a displacement of 0.25 mm, and a crack forming in the 8th mortar joint. Prior to the collapse of the wall, the test was terminated, shown by the non-zero load reading at the end of the load-deflection plot.

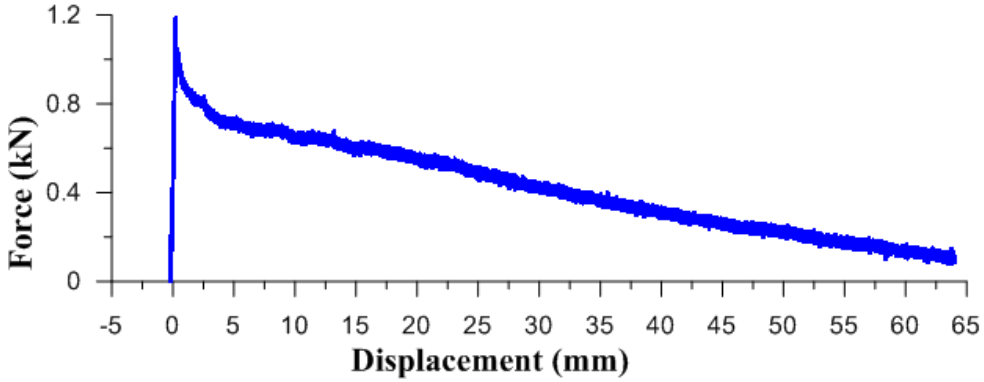

Figure 4.52: Load-deflection plot for Specimen IS4

The test was ended prematurely to ensure that a controlled collapse of the wall could be obtained. An undamaged section of the wall was extracted and used to obtain the characteristic unit weight of the wall of 1.95 kN/m^2; this was then assumed to be representative for all of the walls. Figure 4.53 shows the wall section being weighed.

Figure 4.53: Weighing of wall section extracted from Specimen IS4

4.7.6 Wall Specimen IS5

Again, the behaviour of this Wall Specimen IS5 was similar to that of Wall IS1, in that there was initial out-of-plane displacement that was not completely removed prior to the cracking of the wall. The load-displacement plot shown in Figure 4.54 reveals that the displacement at cracking is significantly larger than the displacements found in Walls IS2 and IS4. Therefore, the measured displacement for this wall cannot be compared directly with that of the other walls; however, when the wall did crack in the 8th mortar joint, the calculated moment was 0.68 kN·m. As seen in previous wall test plots, the removal of the LVDTs from the unloaded wall face can be seen by the slight jog in the plot at approximately 25 mm.

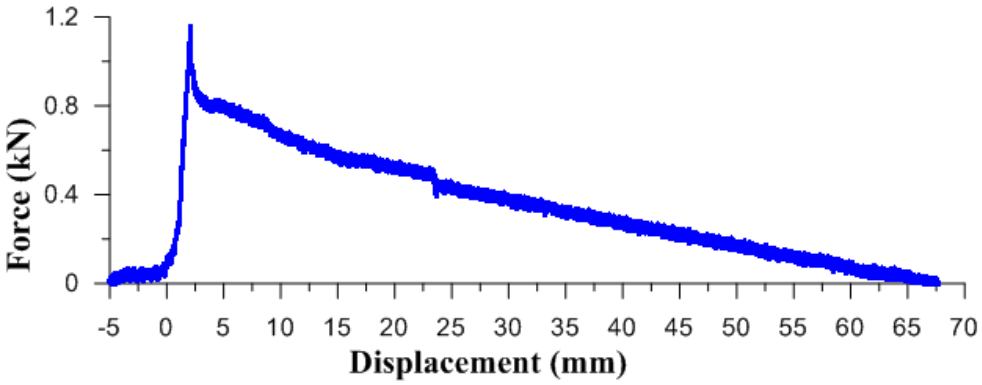

Figure 4.54: Load-displacement plot for Specimen IS5

4.8 Ideal-Dynamic test series

4.8.1 Overview

Similar to the behaviour of the static tests, failure of the ideal-dynamic walls was initiated with a mid-height crack forming across the width of the wall. Unlike the dynamic tests conducted on the realistic walls, collapse of the wall occurred quickly after the formation of the mid-height crack. A summary of the results from the dynamic tests is shown in Table 4.7; here the calculated moment, displacements and crack location refer to the first and only crack to form in the walls. Unlike the realistically-pinned walls,

the ideally-pinned walls do not have an additional post-cracking strength gain; therefore, the ultimate load occurs at the same point as the cracking load.

Table 4.7: Summary of ideal-dynamic (ID) tests

Wall	ID1	ID2	ID3	ID4	ID5	Mean	C.O.V. (%)
Moment (kN·m)	0.74	0.75	0.37	0.69	0.85	0.68	26.9
Displacement (mm)	0.3	0.2	0.5	0.4	0.2	0.32	40.7
Crack Location	10	9	12	7	10	-	-

4.8.2 Wall Specimen ID1

Common to most of the walls in this series, both mid-height cracking and collapse occurred within the same trial. The failure of the Wall ID1 was initiated during a wind record with a reference wind speed of 14 m/s. The moment at cracking was found to be 0.74 kN·m at a displacement of 0.3 mm. Like Wall IS2, the crack formed in the 10th mortar joint, outside of the constant moment region.

A load versus time plot of the 14 m/s trial is shown in Figure 4.55. The agreement between the set-point and the applied load was acceptable while the wall remained uncracked, which can be seen between 120 and 530 s. However, even during this period, the applied loads did not accurately reproduce the valleys of the set-point data, a feature that was not observed in the other wall tests.

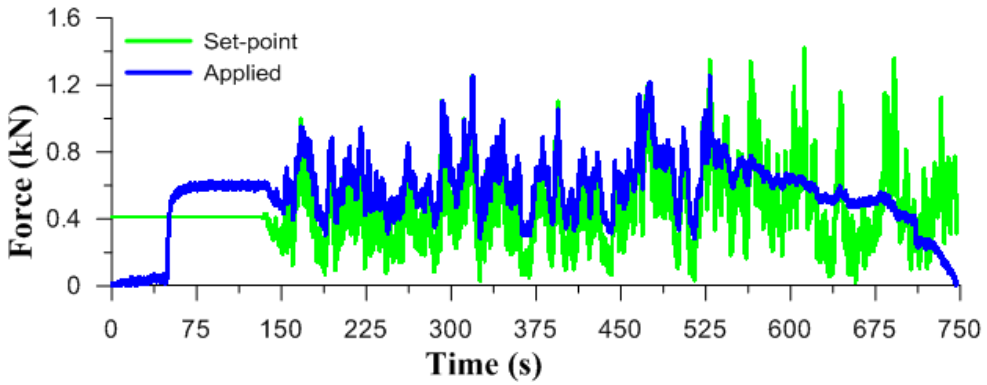

Figure 4.55: 14 m/s load time history plot for Specimen ID1

Once the wall became cracked, at approximately 530 s, the applied load did not resemble to set-point load time history. Rather, after the crack formed, the wall became too compliant and was unable to respond to the changes in force. This can be seen in Figure 4.56 where, once the crack had formed, the displacement started to increase. Similar to the results from the RD walls, sustained gusts in the set-point load which had a larger magnitude than the mean applied load began to initiate the collapse of the wall.

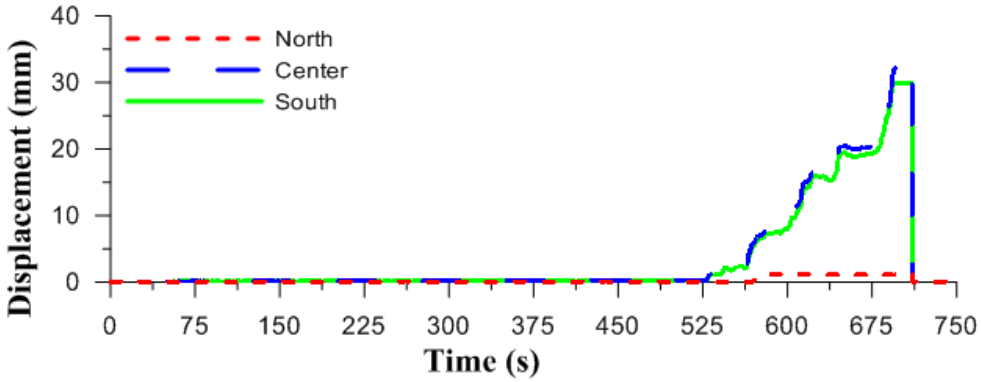

Figure 4.56: 14 m/s displacement time history plot for Specimen ID1 until LVDT's were removed

4.8.3 Wall Specimen ID2

Similar to Wall ID1, cracking and failure of the wall occurred within the same trial. However, for this test, the wall remained undamaged throughout the 14 m/s trial. The crack opened in the 9th mortar joint during the 16 m/s trial. A plot of the time history of this trial is shown in Figure 4.57.

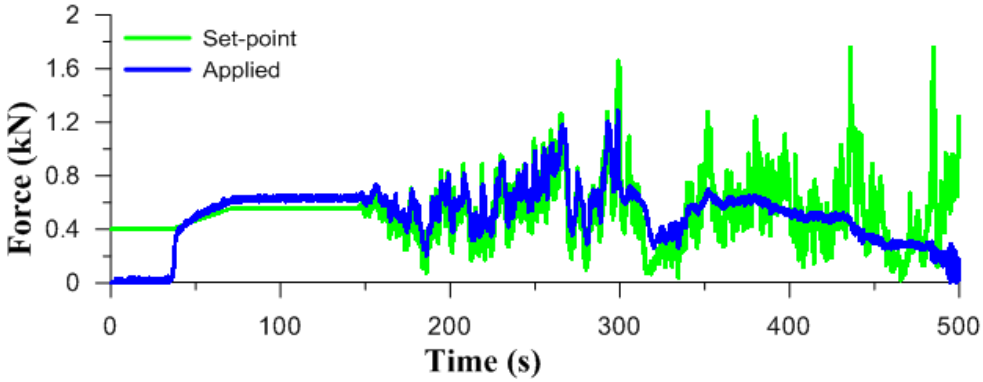

Figure 4.57: 16 m/s load time history plot for Specimen ID2

The agreement between the set-point and the applied load was better than for Wall ID1. The mid-height crack formed with an applied moment of 0.75 kN·m at a displacement of 0.2 mm. Again, the collapse of the wall was governed by a sustained gust that caused large deflections.

4.8.4 Wall Specimen ID3

Similar to wall ID2, cracking and collapse occurred during the 16 m/s trial, which is shown in Figure 4.58. The wall cracked shortly after the dynamic loads began, at an elapsed time of approximately 175 s. The calculated moment at cracking was found to be 0.37 kN·m at a displacement of 0.5 mm. This moment is approximately 50% smaller than any of the other moments found in the other tests. Once the wall had cracked, high-frequency content in the applied loading was greatly enhanced. This was the only ideally-pinned wall specimen to be subjected to a substantial amount of high-frequency content.

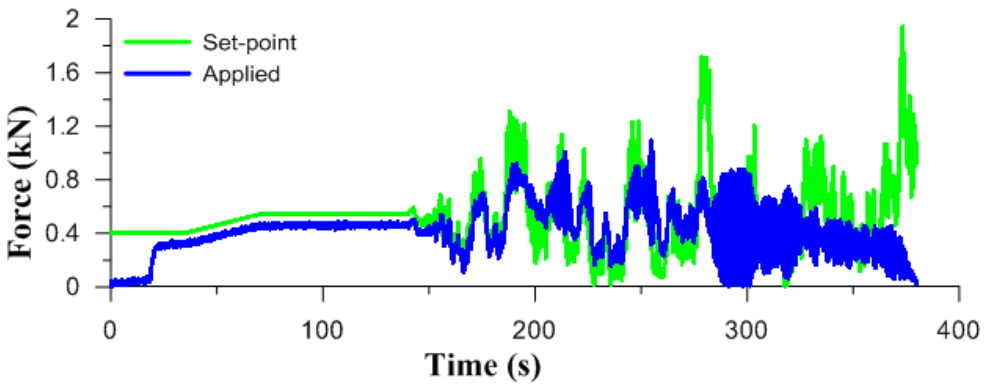

Figure 4.58: 16 m/s load time history plot for Specimen ID3

The most probable cause for the loss of strength in this wall was that the crack formed in the 12th mortar joint, as shown in Figure 4.59. The location of the crack was approximately 500 mm above the constant moment region. The mortar batch that was used this joint had the second largest compressive strength C.O.V. based on the strength of the mortar cubes tests, compared to the other mortar batches that were made. Therefore, it is assumed the bond strength between the block and the mortar was likely weaker than expected, causing the crack to form at a location that did not coincide with the largest bending moment. When this wall specimen was ignored, the wall strength C.O.V. for the ideal-dynamic series was reduced from 26.5% to 8.5%.

Figure 4.59: Crack position of ID3

4.8.5 Wall Specimen ID4

Unlike the other walls, Wall ID4 developed a mid-height crack at the 7th mortar joint during the 14 m/s trial. However, the wall collapsed during the 16 m/s trial. Figure 4.60 displays the time history for the 14 m/s trial. At approximately 250 s in this trial the wall became cracked, as indicated by the peak gust followed by the decreased agreement between the applied and set-point time histories. The moment at cracking was 0.69 kN·m, with a displacement of 0.4 mm. After the crack formed, the applied load

remained fairly stable and consistently above the mean value of the set-point time history; as a result, the wall did not collapse during this wind record.

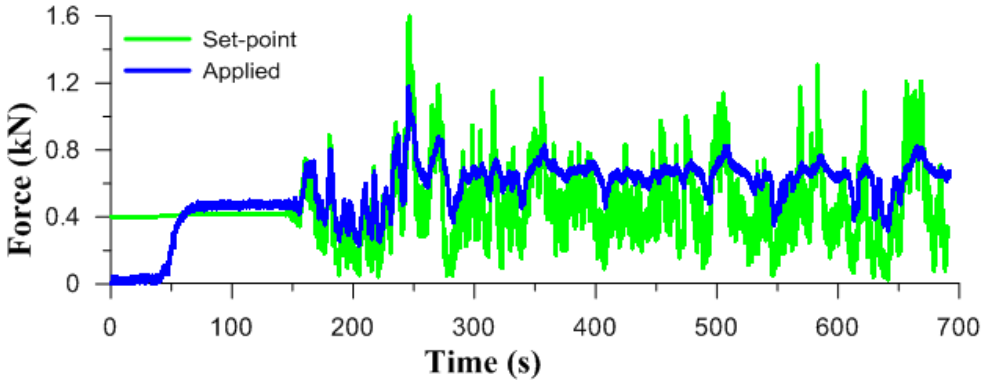

Figure 4.60: 14 m/s load time history plot for Specimen ID4

However, once a sustained gust in the set-point data in the subsequent 16 m/s trial exceeded the apparent resistance level of the wall, the wall was quickly pushed to failure, as seen in Figure 4.61.

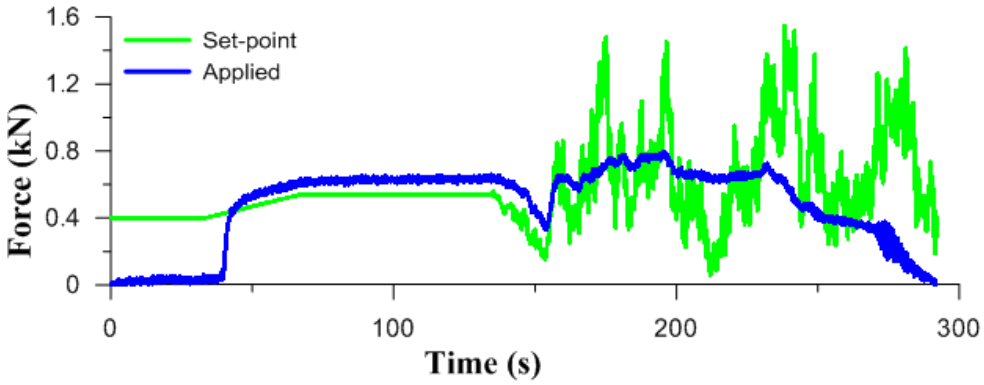

Figure 4.61: 16 m/s load time history plot for Specimen ID4

4.8.6 Wall Specimen ID5

Similar to Walls ID2 and ID3, cracking and collapse of Wall ID5 test happened during the 16 m/s trial, which is shown in Figure 4.62. The mid span crack formed in the 7th mortar joint at an applied moment of 0.85 kN·m and a displacement of 0.2 mm.

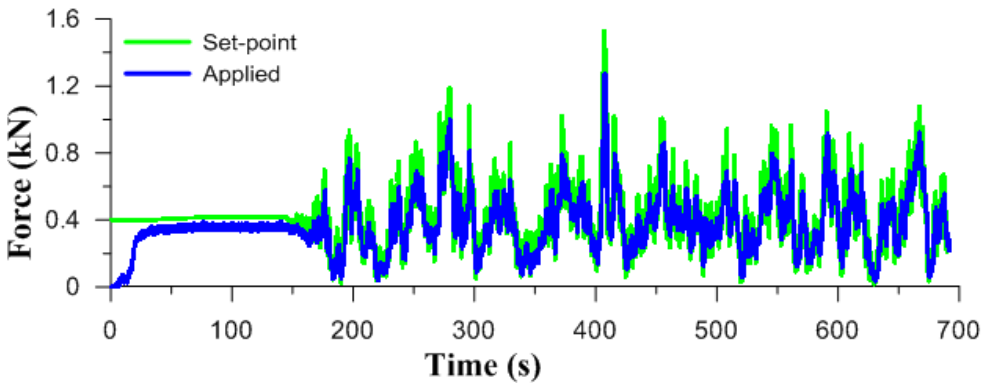

Figure 4.62: 16 m/s load time history of ID5

4.9 Deflection Behaviour of Physical Test Specimens

The primary objectives of this study were to compare the behavioral differences of the wall specimens with different supports and different forms of applied load. In this section, the deflection characteristics of the walls are discussed. Specifically, the deflections of the ideal pinned walls are compared to the realistic walls to determine the effect of the support conditions on the deflection, and walls with the same support condition are compared to determine the effect of the loading method. Table 4.8 summarizes the mean mid-height deflection values that were obtained from the tests at various loading stages. The number of specimens indicated in the table shows how many replicates were used in computing response statistics since some values were excluded if they were deemed to be unrepresentative. These results are discussed in the following sections.

Table 4.8: Summary of displacement results from wall tests

Loading Stage	Test Series	Number of Specimens	Average Displacement (mm)	C.O.V. (%)
Mid-Height Cracking	IS	3	0.3	19.3
	ID	5	0.3	51.4
	RS	3	0.9	79.7
	RD	4	1.6	79.7
Ultimate	RS	4	73.9	14.7
	RD	5	91.6	3.6
Collapse	IS	5	66.8	10.0
	ID	5	60.7	13.6
	RS	5	147.2	7.2
	RD	5	151.9	8.3

The mid-height displacements presented in Table 4.8 represent an average of the walls within each test series. The displacements for each wall, at mid-height, were calculated as the average reading of three

LVDT's that were positioned across the horizontal center line of each wall. These measurements were taken directly for the mid-height cracking; on the other hand, the displacement for the ultimate and collapse conditions were interpolated using the relationship between the three mid-height LVDTs prior to their removal from the wall and the measured displacements of the load actuator that were recorded throughout the entirety of the wall tests.

4.9.1 Deflection behaviour at Mid-Height Cracking

When cracking occurred at mid-height within the walls, the mid-height displacement was typically less than 1 mm, with the exception of the walls in the realistic-dynamic (RD) test series. Within both the ideal and realistically pinned wall series, the differences between measured cracking deflections of the statically and dynamically loaded walls were not statistically significant. These results correlate with the observations obtained by Griffith et al. (2004) where it was found that the deflection behaviour of the static tests were a good indicator of the deflection response of the walls loaded dynamically. From these results, it appears that the ultimate displacements were not strongly influenced by the form of loading (static or dynamic) for either the ideal or realistic support conditions. This suggests that collapse was initiated when the walls reached a limiting displacement.

Unlike the loading type, the support conditions appear to have a greater effect on the displacement behaviour of the walls. The average cracking displacement of the ideally pinned wall was found to be 0.3 mm, whereas the corresponding value for the realistically pinned walls was 1.0 mm, an increased deflection at cracking of 223%. However, with the large coefficient of variation for these tests, the difference in deflections were not statistically significant at the 90% confidence level.

4.9.2 Deflection Behaviour at Ultimate loading

The ultimate deflection of the ideally pinned walls were 0.3 mm, the same as at cracking since the ideal walls had no post-cracking capacity. However, the ultimate deflection behaviour differed from that seen at cracking and collapse, as well as from observations from Griffith et al. (2004) in regard to the influence of the loading type. Unlike at first cracking and collapse, there was a statistically significant difference between the deflections of dynamic (RD) and static (RS) test series, for which the displacements of the dynamic series were 24% larger than in the static series. However, the difference in ultimate displacements may be related to the methodology employed in identifying the deflection at the ultimate condition. For one thing, the location of the ultimate load in the dynamic test series was less well defined, being chosen as the initiation of movement leading to collapse. As a result, the ultimate displacement did not necessarily coincide with the peak load in the dynamic tests.

Also, the displacement behaviour resulting from the different support conditions showed large differences between the ideal and realistically pinned walls. Specifically, the realistic walls exhibited substantially increased deflections at the ultimate load condition, as compared to that at mid-height cracking, with an average ultimate displacement of 82.8 mm. This resulted in an average increased displacement of over 53,000% as compared to the ideally pinned walls.

4.9.3 Deflection Behaviour of Walls Nearing Collapse

In all the wall specimens, the out-of-plane load-carrying capacity of the walls was reduced to near-zero as the walls were pushed to an unstable geometrical configuration at collapse. Similar to the behaviour at cracking, there was not a statistically significant difference in the measured displacements at collapse resulting from the different load types of the walls having similar support types. This is consistent with earlier findings that suggest the displacement behaviour and the displaced geometry of the walls was significant in determining the ultimate behaviour of the walls.

Additionally, the realistically pinned walls consistently achieved increased deflections at collapse as compared to the ideally pinned walls. In this respect, the realistic walls had deflections at collapse that were 120% and 150% greater than the ideal-static (IS) and ideal-dynamic (ID) tests, respectively. This shows, again, that the increased restraint provided by the realistic supports increased the deflection capacity of the walls at all critical loading stages.

4.9.4 Ductility of the Wall Specimens

From the displacement results at the different critical loading conditions, conclusions regarding the ductility of the walls can be made. For this purpose, ductility is defined as the ratio of the displacement at the ultimate load condition to the displacement when mid-height cracking occurred. As a first observation, the ductility of the walls was found to be largely independent of the method of loading. As noted previously, the critical loading conditions were reached at similar displacements on both the dynamic and static tests.

However, the ductility of the walls was influenced by the rotational stiffness of the wall supports. The ductility of the ideally pinned (IS and ID) test specimens was identically equal to unity since the cracking and ultimate load condition were coincident for these walls. However, the ductility of the realistically pinned (RS and RD) walls was 70, on average.

In general the displacement behaviour of the walls was independent of the method of loading, but dependant on the support conditions. Similar loading stages developed at similar displacements

throughout all test series. Collapse of the walls appeared to be initiated when the test specimens were deflected to an unstable geometric configuration.

4.10 Summary of Calculated Moments for Physical Wall Tests

Averaged calculated mid-height moments that were determined from the twenty wall tests are summarised in Table 4.9. For each test series and loading stage, the number of specimens that were included in the average is shown, indicating instances where data was not available (due to technical difficulties in the test) or where it was excluded when a significant improvement to the series C.O.V. was found when a data point was excluded.

Table 4.9: Summary of moments from physical tests

Loading Stage	Test Series	Number of Specimens	Filter cut-off	Mean (kN·m)	C.O.V. (%)	Normalized Moment
Mid-Height Cracking	IS	4	-	0.69	3.4	0.65
	ID	4	-	0.76	8.5	0.72
			1 Hz	0.71	8.2	0.68
	RS	3	-	1.34	29.2	1.17
	RD	5	-	1.19	12.0	1.05
			1 Hz	1.08	13.2	0.95
Ultimate	RS	5	-	1.77	18.1	1.55
	RD	5	-	1.98	14.2	1.74
			1 Hz	1.40	26.5	1.23

The measured forces found in the ideal tests (IS and ID) could not be compared directly to the forces measured in the realistic tests (series RS and RD) due to the difference in effective wall height. The ideal walls were 76.2 mm (3") taller than the realistic specimens as a result of the support details, as described in Section 3.7. Therefore, calculated moments at the different load stages had to account for the difference in height; as a result, these calculated moments were normalized by the theoretical cracking moment of the ideal and realistic walls to get a better understanding of the relative severity of the loading on the walls.

The moments were normalized by dividing the calculated moment by the theoretical moment required to cause mid-height cracking. The calculation for the theoretical moments assumed linear stress-strain behaviour and the specified bond strength of 0.40 MPa, as indicated in S304.1 (CSA 2004). The analysis also assumed idealized pins at the top and bottom of the wall for both the realistic and ideal walls, and

that the mid-height crack formed at the 8th mortar joint. The theoretical 1st cracking moments that were calculated were 1.05 kN·m and 1.14 kN·m for the ideal and realistic walls, respectively.

Similar assumptions were made when calculating the moment for the physical tests. The cracking locations were not taken into account when calculating the mid-height moments, which may cause a slight over- or under-estimation of the moment, depending on the actual position of the crack. The assumption of a fixed crack location worked well for the mid-height moments when the wall was became cracked at mid-height. The largest moment occurred near mid-height of the wall, with symmetrical loading of the "simply" supported wall, when the wall remained undamaged. For consistency, though, even once cracking had occurred, the same assumptions were carried through to the other load conditions in terms of how the mid-height moments were calculated.

4.11 Ideal versus Realistic Supports

4.11.1 Summary of Moment Results from Physical Testing

Comparing the differences in strength resulting from the different support conditions was one of the objectives of this study. To determine the effects that may be attributed to the support conditions, test series having the same load type were compared; specifically, the ideal-static (IS) series was compared to the realistic-static (RS) series and the ideal-dynamic (ID) series was compared to the realistic-dynamic (RD) series. The numerical results are tabulated in Table 4.9, while a visual representation of the results is shown in Figure 4.63; in this figure, the average calculated moments at cracking are overlain onto the calculated ultimate moments. The cracking and ultimate moments coincide for the ideal test walls.

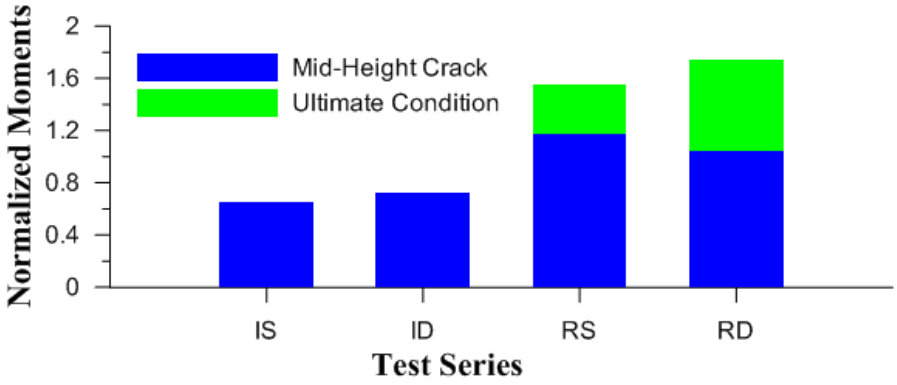

Figure 4.63: Graphical summary of moment results at mid-height cracking and ultimate condition

4.11.2 Comparison of Moments at Mid-Height Cracking

Comparing the calculated moments at mid-height corresponding to the formation of the mid-height crack, it is found that there was an 80% increase in strength of the realistic-static (RS) test over the ideal-static (IS) tests. Similarly, the real-dynamic (RD) walls were 46% stronger than the ideal-dynamic (ID) walls.

The strength gained by the realistic test series over the ideal test series was determined to be statistically significant at a 90% confidence interval.

For the ideal walls, the cracking strength of the wall was completely dependent on the mortar/block bond strength. This was seen in the static wall tests for the ideal walls, where, once the center crack formed, there was no residual strength left within the wall specimen. Furthermore, the calculated normalizing moment was larger than the measured capacity of the walls (i.e. the normalized moments were less than unity), since the bond strength cited in S304.1 which was used to determine the normalized moment was an order of magnitude larger than the measured bond strength.

The realistic walls, on the other hand, featured additional mechanisms that allowed for these walls to obtain higher strengths. First of all, as the realistic walls were displaced, the walls rotated about one edge of the masonry block (see Figure 4.64). This causes the weight of the wall, acting though the centroid of the wall, to be applied eccentrically relative to the location of resulting vertical reaction at the base of the wall. The eccentric weight creates a restoring moment within the wall (Drysdale and Hamid 2005).

However, this restoring moment due to the self-weight eccentricity does not, by itself, fully explain observed differences in the wall strengths. Using the same apparent bond strength and unit weight as found for the ideal-static specimens, and assuming that the top support acts as an ideal roller (no binding), the theoretical moment resistance for the realistic specimens calculated based on Figure 4.64 would be 0.88 kN·m, this was approximately 34% lower than the measured strength of the realistic-static walls. It is not likely that the bond strength or weight of the realistic walls was significantly different than that of the ideal walls; therefore, it is reasonable to conclude that additional restraint from the top support was responsible for the apparent increase in flexural capacity. In other word, the top support did not, in fact, act like an ideal roller. This conclusion is consistent with visual observations suggesting the existence of some binding of the wall within the top angle supports, which would have induced additional axial compression in the wall. As mentioned previously, such an axial force would counteract the flexural tension and enable arching to take place within the wall.

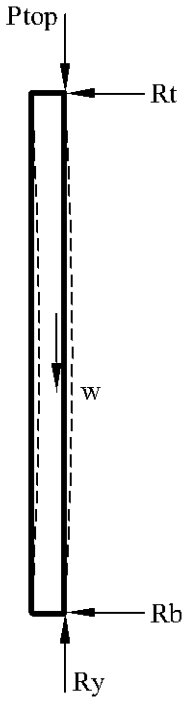

Figure 4.64: Free-body diagram of realistic support showing eccentric bottom reaction

In summary, although construction details similar to that used for the top support are generally assumed to behave as pin connections, they do add some rotational capacity. However, the support is not stiff enough to be a fixed support, but instead behaves like a rotational spring. Furthermore, the binding action at the top support permits the development of some axial force, enabling a limited degree of arching action. With the additional reaction at the top of the wall, created by the support, the system also becomes statically indeterminate. It should be noted, though, that in practice top supports are generally spaced further apart than what was used during this testing. An increased spacing of the angle supports would likely reduce the restraining effect that the support provided to the walls in this study.

4.11.3 Comparison of Moments at the Ultimate Condition

The behaviour of the wall specimens in the realistic and the ideal test series was similar until the occurrence of mid-height cracking. However, once the mid-height crack formed, the out-of-plane resistance of the ideally-pinned walls decreased while the load-carrying capacity of the realistically-pinned walls exhibited a gradual increase with increased deformation. As a result, the ultimate static strength of the realistic (RS) walls was increased by an average of 138% over the ideal (IS) series. Similarly, the average calculated moment capacity at ultimate loading for the realistic-dynamic (RD) series was 142% larger than that for the ideal (ID) series. It should be noted, that the “ultimate” strength

for the dynamic series was somewhat less well defined, corresponding to the peak value of the somewhat "noisy" measured signal.

Once the mid-height crack formed, the strength of the ideal walls was reduced since the flexural tensile strength had been reduced to near zero. The realistic walls, on the other hand, had a small drop in the resisted load observed after mid-height cracking, indicating an initial loss of strength when the crack formed. However, the increased post cracking strength suggests that another mechanism was present that supplemented the capacity of the realistic walls.

As the top course of masonry block became bound in the top support for the realistic wall series, vertical movement of the wall was impeded. This may have resulted in a resisting couple due to unbalanced vertical reaction forces on either face of the top block.

In addition, the binding of the top support may have generated a net axial force that, in turn, allowed for the wall to generate additional capacity through arching action. There are two limiting factors to the capacity that can be added to the wall. Firstly, there may be a maximum value of the axial force before it overcomes the binding of the top course of masonry. Secondly, the thrust line for the arching (Figure 4.65) must remain to the left of the vertical line that connects the pivot points at the top and bottom of the wall; as the deflection in realistic walls became larger, the arch became flatter until it ultimately reached an unstable position, resulting in a "snap-through" failure. The assumed static representation of the realistic walls after cracking is shown in Figure 4.65.

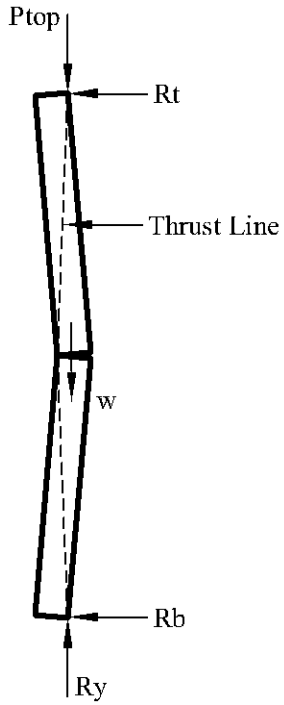

Figure 4.65: Revised static free-body diagram in the displaced position of a realistic wall.

As the realistically supported walls were displaced beyond the formation of mid-height cracking, a crack eventually formed in the top-most mortar joint. In effect, this created a new hinged location across which moments were transferred less efficiently than when the joint remained uncracked. With cracks at three elevation on the wall (top, mid-height, and bottom), increasingly large lateral displacements eventually produced an unstable configuration, overcoming the arching resistance generated by binding of the top support.

4.11.4 Resilience of Realistically-pinned walls

In the context of this study, resilience is defined as the ability to carry load once severe cracking has been sustained. During the realistic-static (RS) test series, there were two occasions (RS1 and RS3) where the test was terminated prior to the collapse of the walls, and then the wall was reloaded. Since the dynamically loaded walls were constantly unloaded, and reloaded, the resilience of these walls can give an indication of the behaviour that is seen in the dynamically loaded walls.

For the first realistic-static (RS1) test, shown in Figure 4.66, the calculated ultimate moment found in the "Initial" load trial was 1.57 kN·m, while the largest calculated moment that was found in the "Resilience" trial was only 0.90 kN·m. This results in a 43% reduction of load capacity when the wall was reloaded. Additionally, the displacement at the ultimate load, found in the Initial load trial, was 37.7 mm (piston

displacement). However, once the wall has been damaged, a 67% increase of displacement was required for the wall to reach the maximum moment found in the Resilience trial, at a displacement of 62.9 mm.

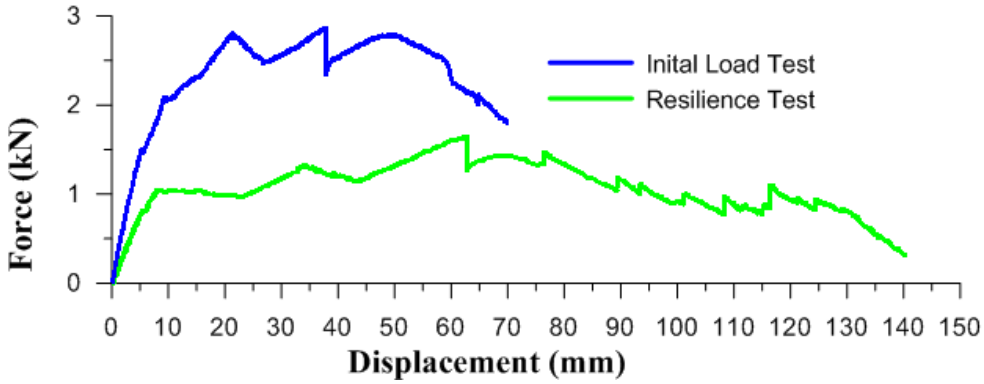

Figure 4.66: Load-deflection plots static load trials performed on RS1

For Wall RD1 the ultimate capacity of the wall was reached within the "Initial" load trial. As a result, the "Resilience" trial gives an indication of the remaining capacity of the damaged wall specimen. However, this was not the case for the third real-static (RS3) wall specimen, where the load-displacement plots from the three load trials are shown in Figure 4.67. In the "Initial" load trial, the maximum load occurred at the point when the trial was terminated, at which time there was a calculated moment of 2.26 kN·m. However, the trend of the load-deflection plot for the "Initial" trial was still increasing at that point. This suggests that the wall had not reached its ultimate capacity before the trial was terminated.

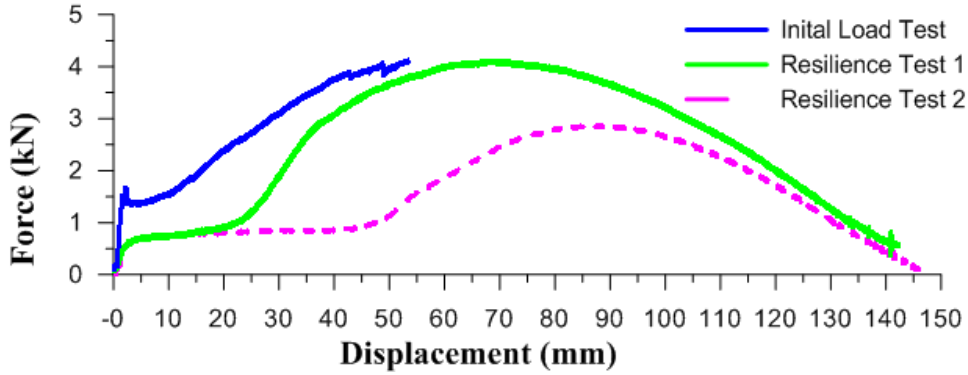

Figure 4.67: Serviceability of RS3

When the first "Resilience" trial (second trial) was conducted it was found that the calculated ultimate moment again reached 2.26 kN·m, after which the trial was continued until the wall had been displaced to the stage where it was nearing failure. For the second "Resilience" trial (third trial) the calculated ultimate moment was found to be 1.57 kN·m, indicating a 30% reduction of moment capacity as compared to the first "Resilience" trial, a similar reduction that was found in Specimen RS1. However, since the "Initial" trial was terminated before finding the true ultimate load, the comparison of strength between the "Initial"

and first “Resilience” trial is more difficult; however Figure 4.67 does suggest that the “Initial” trial was nearing its ultimate load when it was terminated.

In addition to the decreasing moments between the tests, it was found that the displacement at the ultimate load stage increased in each successive trial. For the “Initial” trial, the measured displacement at the end of the trial was 53.4 mm, while in the first “Resilience” trail the ultimate load was found at a displacement of 69.2 mm; likewise, the second “Resilience” trail the wall displaced 87.3 mm before the ultimate condition was reached, a 26% increase of the displacement between the two “Resilience” trials. Of additional note is that the load-displacement trend in the “Resilience” trials became similar at large displacements (greater than approximately 120 mm).

These “Resilience” trials on the realistically-pinned, statically loaded walls show that when a wall was reloaded it does not follow the same load path as in the previous load cycle. This indicates that, as the walls accumulate damage over each trial, they became in progressively less stiff when loaded multiple times. However, these trials also indicate a surprising level of residual strength, given the advanced stage of damage in the walls from the previous load cycle.

4.12 Comparison of Static and Dynamic Response

The second primary objective of this study was to determine the effects of the form of the loading on the behaviour and strength of the walls. Specifically, the behavioural differences were investigated when the masonry walls were subjected to dynamic loads simulating natural wind versus static loads. Therefore, in this section, walls with the same type of support conditions will be compared, so that the strength of the static walls (IS and RS) will be compared directly to the corresponding dynamically loaded walls (ID and RD).

Unlike the differences observed between wall specimens featuring ideal and realistic supports, where the strength differences were easily determined, behavioural differences between the static and dynamic loads are less clear. Since the static and dynamic tests were conducted with different control methods (displacement and load control, respectively), it was difficult to compare the results directly from the test series, as summarised in Table 4.9.

4.12.1 Comparison of Moments at Mid-Height Cracking

For the ideal pin-supported walls (IS and ID) at mid-height cracking, the average calculated mid-height moment of the Ideal-dynamic (ID) wall was 10% greater than the average calculated moment found from the static (IS) series. The differences in strength were determined to be statistically significant at a 90%

confidence level, suggesting that a wall loaded dynamically can resist larger instantaneous loads than when loaded statically.

However, for the realistic series, the average calculated moment at cracking for the static (RS) series was 13% greater than the average moment found in the dynamic series (RD), although the difference was found not to be statistically significant at the 90% confidence level. The finding that the static (RS) series was slightly stronger than the dynamic (RD) series at this stage differs from the results from the ideal support series. Since the relative first cracking strengths of the dynamic and static realistic walls appeared to be anomalous, it is possible that the walls in the dynamic (RD) series cracked earlier than what was expected.

There may be multiple mechanisms that contributed to why the dynamic series was weaker at mid-height cracking, some of which are discussed below.

For the dynamic ideally-pinned test series, because of their low strength, each wall was loaded with only one or two wind trials before mid-height cracking and collapse. In contrast, the realistically-pinned walls were each subjected to a minimum of four wind trials of increasing intensity before mid-height cracking occurred. Therefore, it is possible that the realistic-dynamic (RD) walls experienced some level of accumulated damage from the successive storms before the mid-height crack became visible, which resulted in a lower strength at cracking than was found in the static test specimens.

A mechanism to describe how incremental damage may form is presented in Zielinski and Reinhardt (1982). Here, it was observed that the tensile strength of a cementitious material is decreased when the material is subjected to an increasing number of loading cycles, since initial cracking forms along existing microcracks. As the crack lengths increase, the amount of energy required to extend the crack length also increases, since the cracks are arrested by air voids or other cracks. However, when more load cycles are applied, either existing cracks will lengthen or new macrocracks will form from other microcracks, making it easier for the microcracking to propagate under cyclic loading.

An additional mechanism that acts in conjunction with the fatigue of the mortar is dynamic amplification, which is caused by the wall resonating at its natural frequency. From the vibration tests it was found that the ideal and realistic walls have similar natural frequencies; however, at mid-height cracking the realistically-pinned walls are loaded with a larger mean wind speed (20 m/s) as compared to the ideally-pinned walls that cracked at mid-height at a lower wind speed (14 m/s). Since the wind storm on the realistically-pinned walls has a larger mean wind speed, there is an increased amount of energy contained throughout the high frequency range. Therefore, the larger storm (20 m/s) can induce a larger resonant

response than the smaller stroms (14 m/s) can. The increased resonant response can be seen in Figure 4.68, where two FFT plots of wind storms with different mean wind speeds are plotted together. The plots are modified with a dynamic amplification function, which shows that the larger (20 m/s) wind storm produced a larger response at the natural frequency (approximately 7 Hz) of the walls.

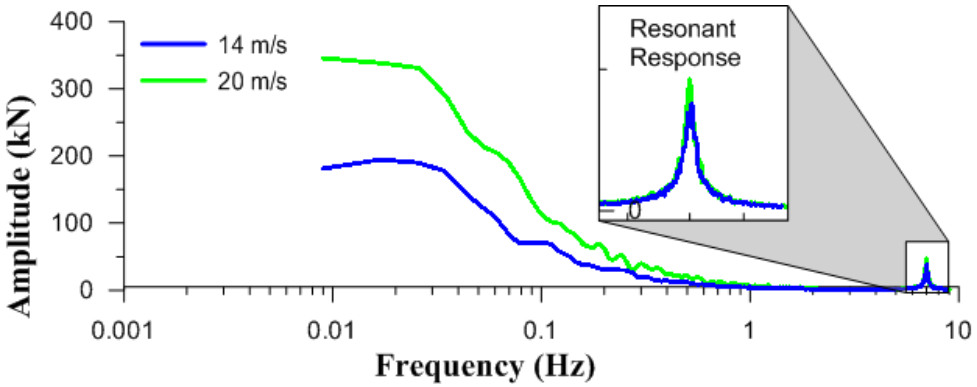

Figure 4.68: FFT comparing the resonant response of a 14 m/s and 20 m/s wind storms

4.12.2 Comparison of Moments at Ultimate Loading

Unlike at mid-height cracking, the ultimate moment for the dynamic (RD) series was larger than the ultimate strengths found from the static (RS) test series. Specifically, the ultimate dynamic moment capacity was 12% larger than the corresponding static strength. The increased capacity of the dynamic walls was not large enough to be statistically significant at the 90% confidence level, as compared with the results of the ideally pinned walls. It should be noted, though, that the high compliance of the severely damaged walls near the ultimate load prevented the loading system from applying high frequency load peaks; as a result, only the low frequency, quasi-static load fluctuations were replicated. Therefore, the applied load at this stage was not truly representative of the behaviour of natural wind.

The high frequency content that was seen in post-cracking stages of the tests was introduced spuriously into the walls due to instability in the load control algorithm as the system unsuccessfully attempted to reach rapidly changing load peaks, as discussed previously. Even though it was "artificial" in the sense of representing realistic wind loads, the observed high frequency content was still a significant source of dynamic loading. It was found that the "gusts" of the chatter were approximately 0.1 to 0.3 s in duration, whereas the gusts in the target wind time histories were typically longer than 1 s, on average.

In addition to the differences in high frequency loading, the quasi-static characteristics of both time histories were different. The quasi-static component of the measured and set-point loading data could be determined by applying a digital low-pass filter, with a 1 Hz high frequency cut off, to the measured data. Figure 4.69 shows the filtered load time history with the corresponding unfiltered and theoretical time

histories. It is apparent that the measured loading was able to follow only the long duration fluctuation trends, lasting several seconds or more, and not the shorter period loading peaks.

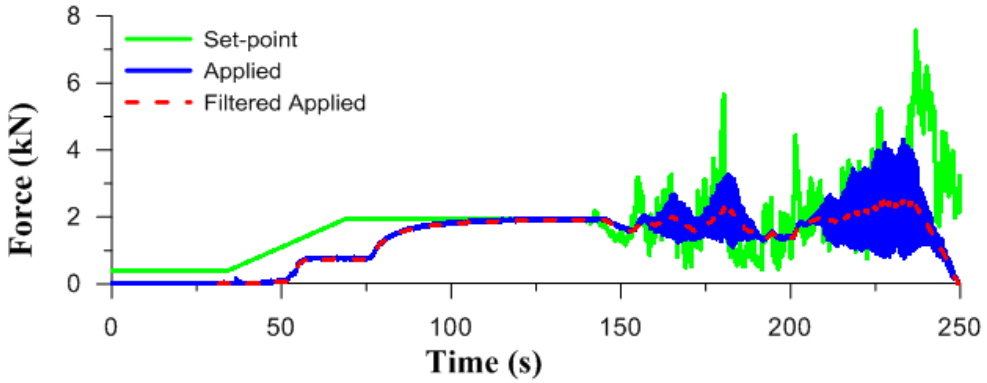

Figure 4.69: Load-deflection plot of filtered and non-filtered applied loads on Specimen RD1

The results from the ideally-pinned walls suggest that, when the masonry walls are loaded dynamically, their strength does increase. However, the results from the realistically pinned walls are less clear. The addition of the realistic supports allow for additional mechanisms to affect the behaviour of the walls, allowing for the strength to increase. Therefore, the precise behaviour of the realistically pinned walls that are dynamically loaded requires further investigation. Additionally, since the agreement between the target and measured loads decreased significantly near the ultimate load, in the realistic-dynamic (RD) test series, it is questionable as to what extent the behaviour of the walls was representative of the behaviour if the walls were to be loaded by natural wind.

4.13 Summary of Wall Tests

Comparing the behavioural response of the walls with different support conditions, it was found that the realistically pinned walls had increased strength and ductility that was not present in the ideally pinned walls. This was primarily due to the increased stiffness due to induced axial compression that allowed for arching action to increase the strength of the wall. The realistically pinned walls had an average increase in strength of 63% and 140% at mid-height cracking and the ultimate condition, respectively, as compared to the ideally-pinned walls. Additionally, it was found that the realistically pinned walls had an average ductility ratio of 70 (i.e. the ratio of the displacement at the ultimate load versus the displacement at mid-height cracking), while the ideal walls had a ductility ratio of unity.

The change in behaviour that occurred due to the method of loading the wall specimens was less clear. For the ideally pinned walls it was found that the dynamically loaded walls were able to withstand a 10% increase of load as compared to the static walls, which was determined to be statistically significant. However, there was no statistically significant difference of the deflection characteristics of the walls

throughout all of the critical load conditions due to the type of load (static or dynamic) that was applied to the wall.

For the realistically pinned walls at mid-height cracking, the statically loaded walls withstood 13% more load than the dynamically loaded walls. The increased strength of the statically loaded walls may have been due to the applied load type (static versus dynamic), because the dynamically loaded walls may have been incrementally damaged due to multiple loading cycles that the realistic wind applies to the wall. Then, at the ultimate condition, the dynamic walls withstood 12% larger loads than the statically loaded walls. However, the applied load at this stage was not truly representative of natural wind, and unintentional high frequency content was introduced because of the load control method used during the test. The displacement characteristics from these tests were similar to the results found in the ideally pinned walls. In fact, the deflections at the cracking and collapse critical loading stages were not statistically different. Therefore, deflection amplitudes appear to play significant role in determining the overall behaviour of the walls.

4.14 Numerical Model Results

4.14.1 Overview

Once the walls in the dynamic load test series (ID and RD) had become damaged by the formation of a mid-height crack, the test apparatus was unable to apply the required load to match the theoretical (set-point) loads. This behaviour occurred because the walls were too compliant, requiring large displacements to develop changes in resistance of the walls.

To investigate how these highly damaged walls might respond to dynamic loading that contained fluctuations more closely resembling natural wind, a single degree of freedom numerical model was constructed to determine the behaviour of the walls if the load system was capable of applying the required load through the life of the wall.

The numerical model used a step-by-step integration method as the time marching scheme, specifically Newark's β method. The theoretical method used by the model was presented in Chapter 2, and the modeling of physical characteristics of the wall specimens was described in Chapter 3. The model was implemented in MathCad 15©; the code for the model is provided in Appendix H, with the results from the model study presented in Appendix I.

Throughout the development of the model, the model response could not be directly compared to the recorded data from the different trials since the measured response was obtained at slightly uneven time increments due to limitations of the data acquisition system. This resulted in a phase shift between the

simulated and measured response throughout each wind trial, an example of which is shown in Figure 4.70. Since the data collected from testing had an uneven time step, the model data was generated at a time step equal to the average time step obtained from the test.

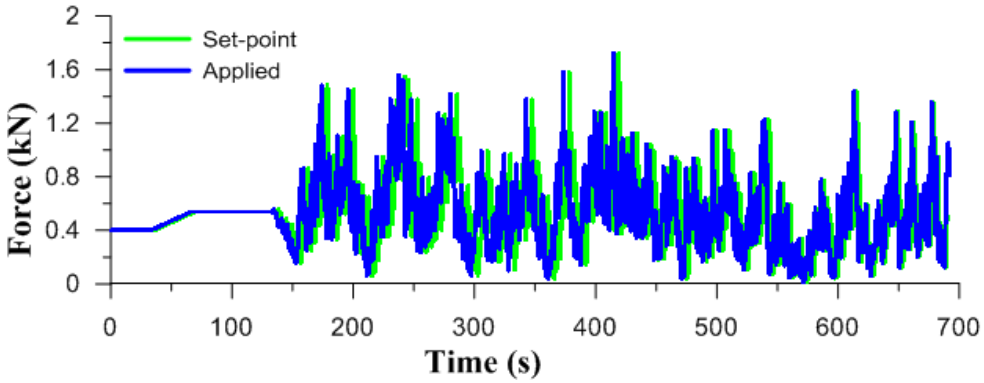

Figure 4.70: Phase shift between model and measured data sets

The model was calibrated to the response of the fourth and fifth real-dynamic walls (RD4 and RD5) because they had the best pre-damage agreement between the applied and set-point data sets, as judged visually by comparing the set-point to the measured load for all five real-dynamic (RD) walls; however, only the calibration using data from Wall RD5 will be described here; the calibration using Wall RD4 followed a similar process, and had similar characteristics.

4.14.2 Calibration of the Numerical Model

Data obtained from both static test series (IS and RS), indicated that the walls behaved approximately in a linear manner when undamaged. However, once the walls became damaged, the behaviour became non-linear. Therefore, a linear behaviour was assumed for the walls when undamaged, using a stiffness of 8.6 kN/mm, which is within the ranges of stiffness obtained from the wall specimens in the real-static (RS) series. Figure 4.71 depicts the displacements generated from the model as well as the measured data for the 16 m/s wind trial. It is apparent that the model is able to approximate the measured data quite closely. A large amount of signal noise is present in throughout the measured time history due to the small displacements that were measured at this stage of loading.

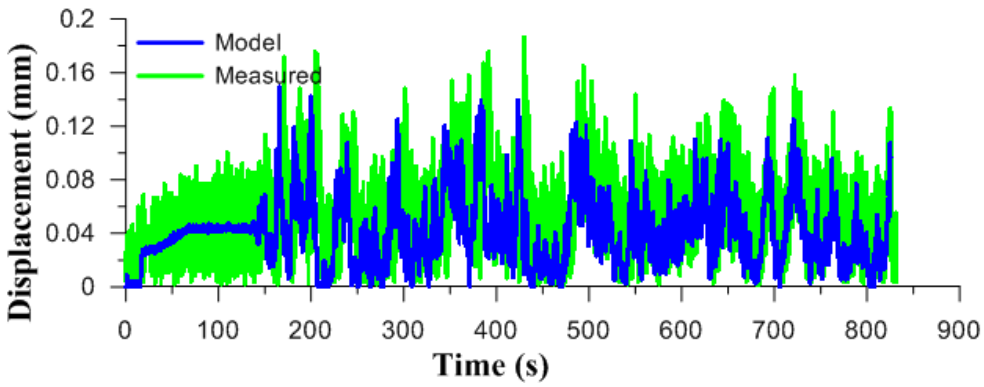

Figure 4.71: Calibration of the model to measured data using a 16 m/s mean wind speed

A Fast Fourier Transform (FFT) was performed on the displacement data, which is presented as a normalized power spectral density (PSD) plot shown in Figure 4.72. It is evident that the energy distribution of the model and the measured displacements is similar for all frequency bands to an approximate frequency of 9.3 Hz. After that point, the agreement between the model and the measured data decreases. However, since 99.9% of the energy is contained below a frequency of 9.3 Hz, the extra frequency content in the measured signal above 9.3 Hz may be attributed to the signal noise in the measured data. Within these limitations, it can be concluded that the model is able to reproduce the response of the wall in its undamaged state.

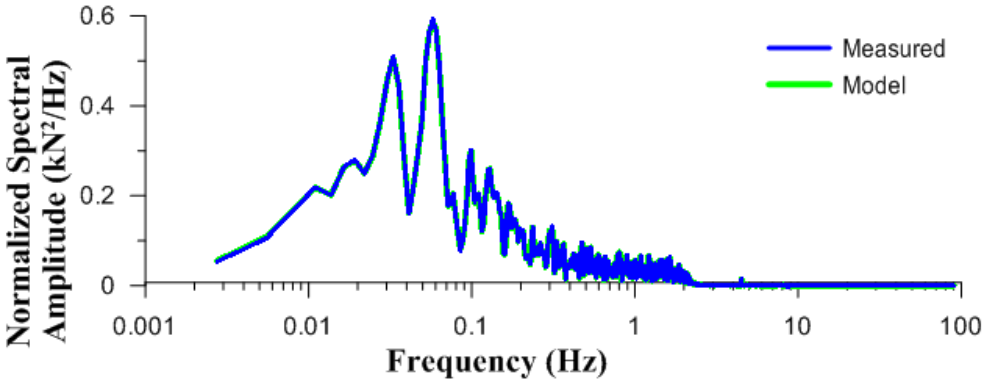

Figure 4.72: PSD of model and measured data

As the behaviour of the cracked walls was non-linear, the stiffness of the walls changed as the displacements of the walls increased. The instantaneous non-linear stiffness of the wall was determined by taking the first derivative of a representative static load-displacement curve. For modeling purposes, the load-displacement data from the third realistic-static test (RS3) was used. Since experimentally collected data is discrete and not differentiable, a cubic spline curve was fit to the experimental data.

To facilitate the definition of the cracked model stiffness, a smooth, continuously differentiable cubic spline curve was fit through the experimental quasi-static load-deflection data (see Figure 4.73). Although

unable to reproduce the pre-cracking stage, the fitted curve is seen to provide a good fit to the measured data over the cracked response region defined by mid height displacements extending from approximately 3 mm up to 40 mm; the model load-deflection curve was terminated at a displacement of 40 mm since that marked the beginning of the wall's collapse, as characterized by a descending load-deflection curve, in the static loading test in question.

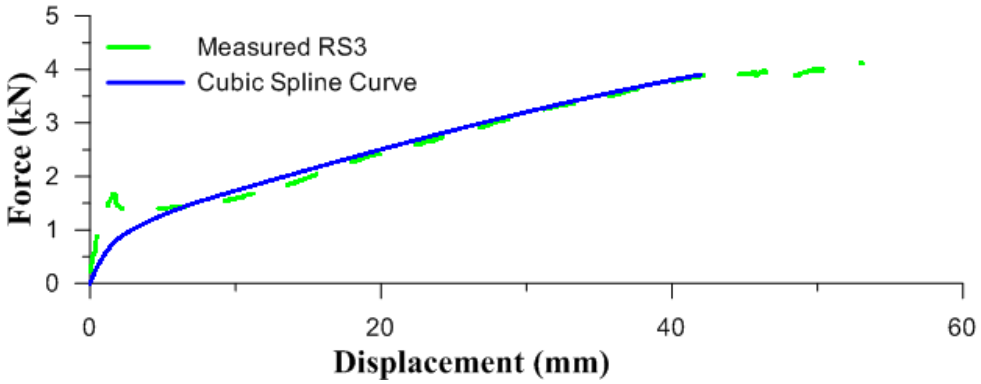

Figure 4.73: Fitted load-displacement curve used for the single degree of freedom model with Specimen RS3 used as a representative quasi-static test

During the calibration process for the cracked wall numerical model, it was found that the relationship between the apparent stiffness of the dynamically loaded walls and stiffness derived from the quasi-static data varied depending on the current state of damage in the wall. Specifically, in order for the model to reproduce the measured dynamic response, the quasi-static stiffness K_s had to be increased by some factor κ_d in order to obtain a representative dynamic stiffness K_d, or:

$$K_d = \kappa_d \cdot K_s \qquad \text{Eq. 4.2}$$

for which K_s was calculated by determining the first derivative of the fitted quasi-static load-deflection curve at the current displaced position of the wall. Different values of κ_d were found for each major damage state, as listed in Table 4.10. For the purposes of the dynamic model, the onset of each condition state was assumed to occur at specific displacements, which are also provided in Table 4.10. To avoid potential numerical instability problems due to a sudden change in stiffness, a 10 s transition period was imposed during which the stiffness modification factor κ_d was gradually changed in a linear fashion.

Table 4.10: Calibration factors for dynamic wall stiffness for numerical model

	Model Calibrated to Specimen RD4			Model Calibrated to Specimen RD5		
	Stiffness Definition			Stiffness Definition		
Condition State	Linear	κ_d	Onset Displacement (mm)	Linear	κ_d	Onset Displacement (mm)
Uncracked	7.4 kN/mm	-	0	8.6 kN/mm	-	0
Bottom cracking	-	4.1	0.2	-	4.7	0.2
Mid-height cracking	-	3.6	1.5	-	1.4	1.5
Post-cracking damage	-	1.2	4	-	0.9	14.7

To demonstrate that the results from the numerical model was acceptable, PSD functions of the displacement time history of the model and measured data is shown in Figure 4.74. For the case shown, the occurrence of the bottom cracking and the resulting transition from linear to non-linear stiffness occurred during the 18 m/s wind trial. The measured and simulated distributions of energy throughout the PSD were found to agree within 3% within each logarithmic frequency band.

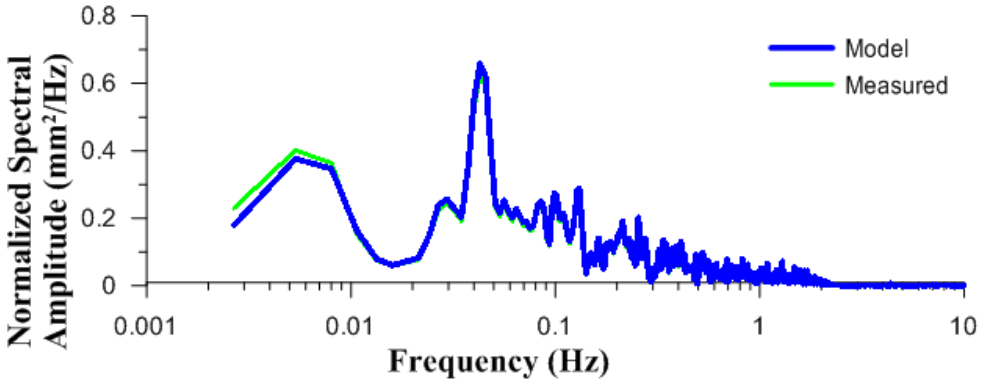

Figure 4.74: PSD of model and measured data for the 18 m/s mean wind speed test, with cracking at the base of the wall

Similarly, a comparison of the PSDs of the model and measured displacement time histories for the 22 m/s trial is shown in Figure 4.75. In this case, mid-height cracking has already occurred and the apparent dynamic stiffness value has transitioned to a κ_d value of 0.9. The PSDs show that the model had agreement with the measured displacement time history. Within this trial there is less energy contained at the higher frequency ranges as compared to lower mean wind speed trials (see Figure 4.74), the case where the wall was lightly damaged.

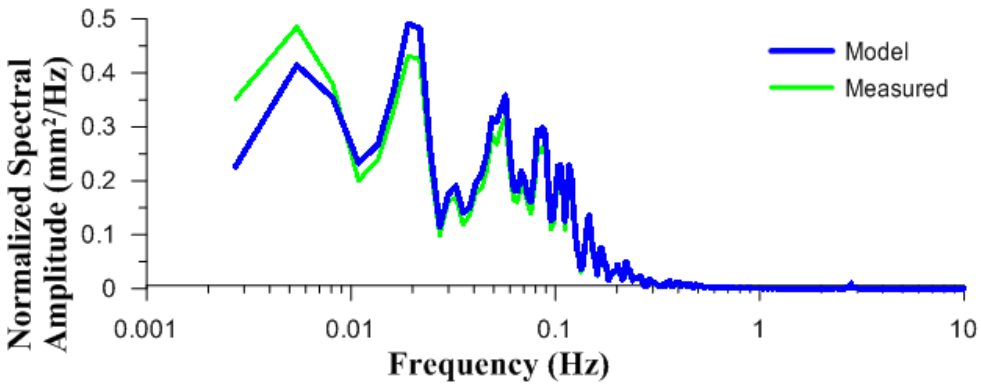

Figure 4.75: PSD comparison between model and measured response of the 22 m/s trial

In summary, as the walls became incrementally more damaged, the relative magnitudes of the static wall stiffness (used as the basis for the model) and the experimental dynamic stiffness of the walls changed. It was apparent that the dynamic stiffness of the walls was significantly larger than the static stiffness of an undamaged wall. However, as the wall becomes more damaged, the dynamic response of the wall became relatively less stiff, and the response became similar to the quasi-static stiffness, as seen by the fact that the required stiffness calibration factor gradually reduced to approximately one (i.e. the apparent dynamic stiffness eventually converges to the static stiffness values).

4.14.3 Comparison of Numerical and Measured Results

Once the calibration of the numerical model was completed, the model was subjected to the theoretical load time histories that were used on the physical test specimens. A comparison of the model trials (calibrated to Specimen RD5) and the measured response of the tests on Specimen RD4 were made. Comparisons were made at four loading states on the walls; when the walls were undamaged, when cracking occurred at the bottom of the wall, the formation of the crack at mid-height, and at the collapse of the walls.

For the first loading state, when the walls were undamaged, the displacement time histories are shown in Figure 4.76 for the 16 m/s trial. The mathematical model was able to approximate the behaviour of the physical wall at this undamaged state. However, the model was unable to reach the same magnitude of displacements for each gust as was seen in the physical tests; nonetheless, the overall behaviour of the model generally agreed with the measured data.

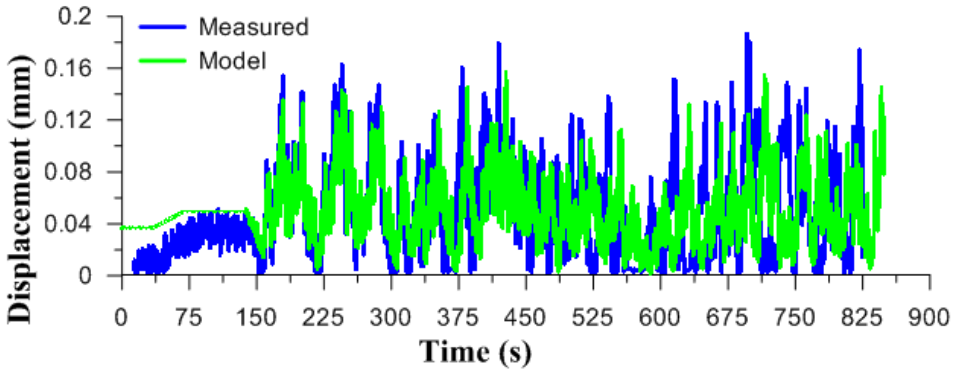

Figure 4.76: Displacement time history plot of model and measured data for the 16 m/s trial

Cracking at the bottom of the walls occurred in the 18 m/s trial, for which the displacement time histories are shown in Figure 4.77. In this case, the model was able to give a good approximation to the behaviour of the experimental wall, with this small increment of damage. When cracking at the base of the wall occurred, the stiffness behaviour of the model transitioned from a linear stiffness to non-linear stiffness with a modification value of κ_d = 4.7. This value of κ_d suggested that there was a substantial difference between the static stiffness (obtained from the experimental results of Specimen RS3) and the apparent dynamic stiffness that was needed for the model. The exact cause of the different apparent dynamic stiffness is not known, however, it is speculated that the dynamic loading of the walls caused the supports to have an increased load resistance effect that was not effective when the walls were loaded quasi-statically.

Of additional note is the displacement behaviour of the model after the formation of the bottom crack (occurring at an elapsed time of approximately 410 s), where the displacements of the model after cracking were increased as compared to the physical wall. This may be an indication that the κ_d value (calibrated to Specimen RD5) resulted in an apparent dynamic stiffness that was stiffer than the apparent dynamic stiffness that was experienced by Specimen RD4.

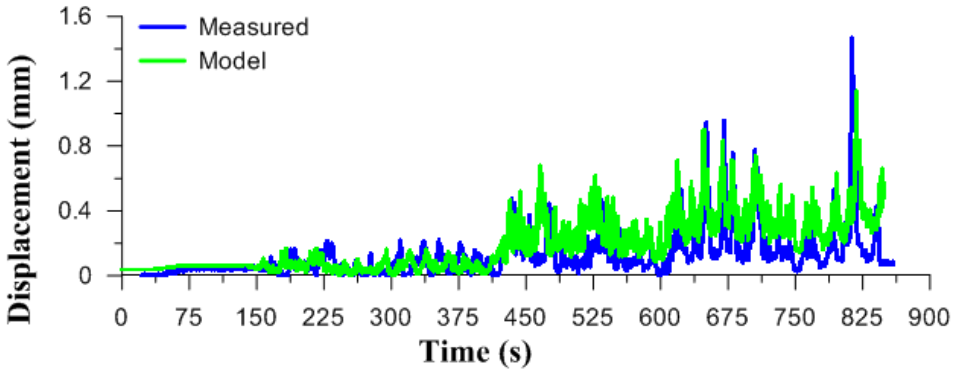

Figure 4.77: Displacement time history plot of model and measured data for the 18 m/s trial

During the 20 m/s trial, the behaviour of the model and of Specimen RD4 began to deviate. Within the displacement time histories that are shown in Figure 4.78, mid-height cracking of Specimen RD4 occurred at an elapsed time of approximately 750 s, while no additional cracking occurred in the model. The difference of the behaviour may be attributed to the model wall being stiffer than the experimental wall, resulting in the model underestimating the displacements of the physical wall.

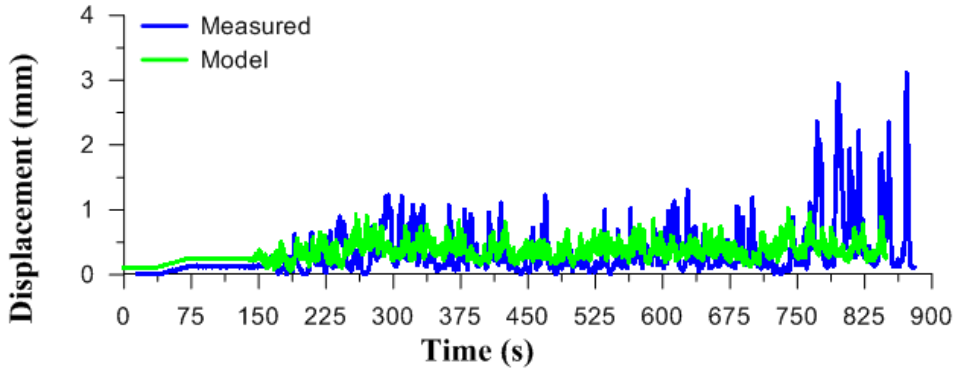

Figure 4.78: Displacement time history plot of model and measured data for the 20 m/s trial

In the 22 m/s trial, both the mid-height crack and the collapse of the wall occurred (as shown in Figure 4.79) and the model was no longer representative of the physical wall. It is important to note that the formation of the mid-height crack led directly to the collapse of the wall. This behaviour of the model is due to the wall being governed by the apparent dynamic stiffness; when the mid-height crack formed the dynamic stiffness was reduced, with the κ_d value reducing from 4.7 to 1.4.

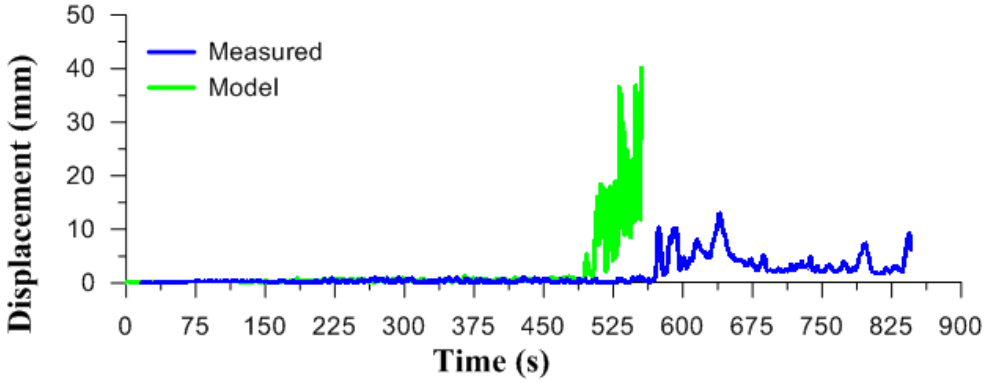

Figure 4.79: Displacement time history plot of model and measured data for the 22 m/s trial

During the calibration of the model, when the wall sustained additional damage the value κ_d was reduced. As the value of κ_d was continually reduced, it indicated that the apparent dynamic stiffness of the wall was approaching quasi-static stiffness; in other words, the properties that had given additional strength were now too damaged to supply additional resistance.

Additionally, the behaviour of the experimental walls during testing was responsible for some of the differences observed between the model and the physical test. As described in previous sections (Section 4.6 and Section 4.8), once the walls became severely damaged the applied load was reduced due to the compliancy of the walls, since the applied load was not able to reach its intended value, resulting in the experimental walls having a longer life span. However, the model applied the theoretical load without any reductions due to damage. The non-reduced loading, coupled with the reduced apparent dynamic stiffness of the wall, combined to cause the model wall to collapse when the mid-height crack formed.

Of additional interest was the effect of resonance on the behaviour of the walls, which was previously described in Section 4.12.1. The resonant response may have allowed for additional damage to be introduced into the walls. The model displacements were analysed using an FFT to determine the extent of the resonant response. It was determined that, when the walls were undamaged, there was no indication of resonance. When the wall became damaged, though, there may be resonance occurring at approximately 2.5 Hz, as suggested in Figure 4.80. However, the trial that exhibited the possible resonance also caused the "collapse" of the wall; therefore, the evaluated response levels near 2.5 Hz may represent motion associated with the collapse, rather than resonance of the wall.

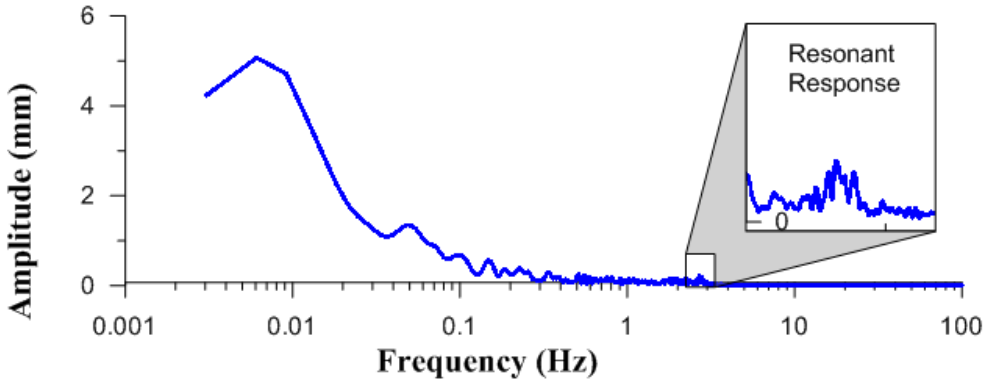

Figure 4.80: FFT of 20 m/s trial using the RD5 calibrated model depicting possible resonance

4.14.4 Summary of Results from Numerical Model

From the development of the mathematical model it was found that the dynamic stiffness of the realistically-pinned walls was greater than the static stiffness of the similar realistically-pinned walls at low levels of damage. This stiffer behaviour did not come from inertial effects within the walls, which were accounted for within the model, but more likely from loading rate-related effects on the materials and at the supports which are not well understood. Specifically, the top support may have experienced higher levels of binding under dynamic conditions than when loaded quasi-statically.

However, once the walls became cracked at mid-height, the cubic spline curve used to approximate the quasi-static load-deflection behaviour of the walls provided an increasingly good fit to the measured stiffness of the walls. Two conclusions can be made based on this observation. In the first place, the mechanisms that allowed for the apparent dynamic stiffening of the walls at the start of the test were no longer as effective at higher levels of damage so that the dynamic stiffness of the wall became similar to the static stiffness. Secondly, the general behaviour of the model when the cubic spline curve better approximated the static-stiffness of the walls may have allowed for a more representative estimation of the behaviour of unreinforced masonry walls subjected to realistic wind loads at that damaged state. The results from the model indicated that initiation of the collapse of the walls occurred shortly after cracking when loaded by large, dynamic gusts. This suggests that if the load applied to the physical walls was representative of natural wind throughout the entirety of the test sequence, the walls may have collapsed shortly after mid-height cracking.

4.15 Summary of Results

From the four physical test series that were conducted, a number of behavioural characteristics were determined. Firstly, it was found that the displacements from test series that had similar support conditions (ideal or realistic) had similar displacements at all of the critical damage states, regardless of the type of loading (quasi-static or dynamic).

The average displacements when mid-height cracking occurred for the ideally-pinned walls was 0.3 mm, whereas the realistically-pinned walls were displaced 1.3 mm before the formation of the mid-height crack. Additionally, the realistically-pinned walls, having a post mid-height cracking strength gain that was not seen in the ideally pinned walls, allowed for an average displacement of 82.8 mm at their ultimate load condition, while the ultimate condition for the ideally-pinned wall coincided with the mid-height cracking of the walls. The post cracking behaviour of the realistically-pinned walls, similar to that of strain hardening in steel, allowed the realistically-pinned walls to behave with more apparent ductility. The ductility, defined as the displacement at the ultimate load divided by the displacement at mid-height cracking, of the realistically pinned walls had an average value of 70, while the ductility for the ideally-pinned walls was unity.

One of the primary objectives of the study was to determine the differences in strength due to the support conditions of the walls. It was found that the realistically-pinned walls were stronger than the ideally-pinned walls at all loading stages, regardless of the loading method (quasi-static or dynamic). At mid-height cracking, the average normalized moments for the ideally-pinned walls were 0.65 and 0.72 for the static and dynamic tests, respectively. In comparison, the realistically-pinned walls had normalized mid-

height moments of 1.17 and 1.05, for the static and dynamic test series, respectively. The realistically-pinned walls had an average increased strength of 80% over the ideally-pinned walls for the static test series, while there was a 46% increase of strength for the dynamic test series. Additionally, the post-cracking behaviour of the realistically-pinned walls resulted in ultimate normalized moments of 1.55 and 1.74, respectively. This allowed for the realistically-pinned walls to have increased strengths of 138% and 142% over the ideally-pinned walls, in the static and dynamic tests, respectively; in this regard the ultimate strength of the ideally-pinned walls coincided with the cracking strength.

The second primary objective of the study was to determine the strength differences due to the type of loading (static or dynamic) that was applied to the walls. The ideally-pinned walls had an average series strengths of 0.65 kN·m for the static test and 0.72 kN·m for the dynamic tests, respectively. Comparing the calculated moments at mid-height, the dynamically loaded walls were able to resist 10% more load, which was a statistically significant result. However, the difference of the realistically-pinned walls at mid-height cracking showed that the statically-loaded walls were 11% larger than the dynamically loaded walls; however this result was found not to be statistically significant. Comparing the calculated moment at mid-height at the ultimate condition, it was found that the dynamically loaded walls were 12% stronger, on average, than the statically loaded walls, which again, was not statistically significant at the 90% confidence level. However, as suggested in the published literature (see Section 2.1.3), it was concluded that dynamic loading appeared to have a small beneficial effect on the strength of the walls.

Lastly, from the development of the mathematical model, it was found that the apparent stiffness and strength gain of the dynamically loaded walls did not arise from the dynamic behaviour of the walls, but rather from the behaviour of the supports when the walls were loaded dynamically. However, the increased stiffness of the walls gradually declined as the walls become more damaged; eventually, the behaviour of the dynamically loaded walls approached the stiffness behaviour of the quasi-statically loaded walls. Additionally, results from the model study also indicated that if the realistically-pinned walls experienced loads that were representative of realistic wind at all damage states, the dynamically loaded walls may have collapsed shortly after mid-height cracking, which was generally seen in the ideally-pinned walls. However, that conclusion is speculative since it could not be verified due to the limitations of the load control system.

Chapter 5: Conclusions and Recommendations

5.1 Summary

In practice, the design of unreinforced masonry to resist out-of-plane loading is conducted on the basis of several simplifying assumptions. Firstly, wind loads are modeled as non-varying static loads (whereas real wind loads vary through space and time), and supports are modeled as idealized, freely rotating pins (whereas actual supports do supply some rotational resistance). These assumptions determine the expected behaviour of the walls. For example, assuming a static pressure on a wall leads to the assumption that the wall behaves quasi-statically. Additionally, given the basic geometry of the masonry block and standard construction practice, ideally-pinned connections to supporting elements cannot be realized as some degree of rotational restraint is unavoidable. An experimental study was therefore carried out to determine how these assumptions actually affect the behaviour of unreinforced masonry walls.

Twenty full-scale masonry specimens were constructed in the Structures Laboratory at the University of Saskatchewan. The twenty walls were divided into two groups; ten walls were built on steel plates to create idealized pin connections by placing the wall on a knife edge support, while the remaining ten walls were built on concrete beams which were used to replicate realistic supports that are found in practice. Each group was then divided into groups of five, of which the first half were loaded quasi-statically, while the remaining walls were loaded dynamically in a way that the load was representative of realistic “gusty” wind.

The methodology and the results from physical tests, as well as from a numerical model study, were described in the previous chapters. The following sections present the conclusions gained from the various test series that were conducted for the study.

5.2 Conclusions

5.2.1 Wall Deflections and Ductility

From the quasi-static tests, the walls that were realistically-pinned were found to have substantially more ductility at ultimate conditions than the ideally-pinned walls. However, mid-height cracking occurred at displacements for which there was no statistical difference, at a 90% confidence level, between the realistic and the ideal walls; in this regard, cracking of the ideal and realistically pinned walls occurred at an average displacement of 0.3 mm and 1.3 mm, respectively.

After the mid-height crack formed, reserve capacity allowed the realistically-pinned walls to reach loads that exceeded the loads measured at mid-height cracking. The displacement at the ultimate load condition

for the realistically-pinned walls averaged 82.8 mm, while the ultimate load condition for the ideal walls occurred at an average deflection of 0.3 mm since the ultimate load condition for the ideally-pinned walls was coincident with the mid-height cracking stage. A measure of ductility for these walls was defined as the displacement at the ultimate load condition divided by the displacement at mid-height cracking. The realistically pinned walls had an average ductility ratio of 70, whereas the ideally-pinned walls had a ductility ratio of unity. Additionally, the displacement required to collapse the realistically pinned walls was 2.3 times larger than that of the ideally-pinned walls.

The deflection characteristics of these test series indicated that the restraint of the supports had a large influence on the deflection response of these walls. However, the different loading types (quasi-static or dynamic) had a negligible effect on the displacement behaviour of the wall specimens at both the cracking and ultimate conditions.

5.2.2 Influence of Support Conditions on Strength

The realistically-pinned walls had an average strength at mid-height cracking that was 63% higher than that of the ideally-pinned walls. Once the walls were cracked at mid-height, the realistically-pinned walls had a strength gain (similar to strain hardening in steel) that was not present in the ideally-pinned wall specimens. This reserve strength enabled the realistically-pinned walls to achieve 140% higher moment capacity than the ideally-pinned wall specimens. These results indicate that the strength of the walls is greatly influenced by the restraint provided by the supports, which parallels the conclusions made regarding the deflection behaviour of the wall specimens.

Three major factors were credited with allowing the realistically pinned walls to resist larger out-of-plane loads then the ideally-pinned walls. Firstly, rotation about the leeward bottom corner of the realistic walls in response to lateral bending resulted in a beneficial increased moment resistance due to the eccentricity of the self-weight of the wall relative to the rotation point. Secondly, the top support provided some rotational resistance. Lastly, binding of the wall occurred within the top support after significant deflection, which led to axial compressive loading and arching action.

5.2.3 Influence of Load Type on Strength

The effect of the load type on the wall strength was more difficult to determine. In the case of the ideally-pinned walls, it was found that the dynamically loaded walls were able to withstand 10% higher mid-span moments, on average, as compared to the statically loaded walls, a difference that was found to be statistically significant at the 90% confidence level. For the realistically-pinned walls, however, the

differences between static and dynamic moment capacities at both mid-height cracking and at the ultimate condition were found not to be statistically significant at the 90% confidence level.

For the realistically-pinned walls, the results of these tests differ from the results of the ideally-pinned wall tests. Specifically, the dynamically loaded walls had a 24% lower moment capacity, on average, as compared to the static series at mid-height cracking, a finding that was not consistent with results from the ideal series, or from the literature. On the other hand, at the ultimate condition, the dynamically loaded walls exhibited 12% more moment capacity, on average, than the static tests. However, at the ultimate load condition, the dynamic loads were no longer representative of real wind due to the limitation of the loading system, introducing some uncertainty into the interpretation of the dynamic results at this stage. It should be noted that these observed differences were not statistically significant at the 90% confidence level. Of additional note is that the collapse of the walls was initiated in all cases by the attainment of a geometrically unstable deflected shape, regardless of the load type.

From the numerical model study, it was found that the realistically-pinned walls had an apparent dynamic stiffness that was larger than the quasi-static stiffness. The increased apparent dynamic stiffness was inferred from the observation that the stiffness response determined from the static tests was unable to accurately predict the dynamic behaviour of the walls; as a result, the stiffness for the dynamic analysis had to be increased by a factor of up to 4.7 for largely intact walls so that the model would be able to approximate the behaviour of the dynamically loaded walls. As the walls were progressively damaged, though, the apparent dynamic stiffness of the walls decreased, eventually approaching the quasi-static stiffness near ultimate conditions. It was suggested that the increased dynamic stiffness may have been generated due to the dynamic behaviour of the wall within the supports that increased the capacity of the wall in a manner that was not seen in the statically-loaded walls; for example, increased binding at the top support may have occurred during dynamic loading.

5.3 Recommendations for future studies

From the tests that were conducted, additional gaps of knowledge were identified. The following are some recommendations for future studies that may help clarify the behaviour of unreinforced masonry that is subjected to dynamic loads.

Firstly, it was concluded that the realistic supports do increase the strength and ductility of the unreinforced masonry walls as compared to the ideally-pinned walls. It is reasonable to assume that the additional capacity of the walls is dependent, to some extent, on the stiffness of the supports. Therefore, future work could be done to better characterize the effects of specific support configurations.

Similarly, the post-cracking strength gain that was seen in the realistically-pinned test series was dependent upon an axial load that was generated when the top course of masonry became bound in the top support, allowing for additional strength from arching action. Future work could be done to better define this load bearing mechanism in unreinforced masonry walls.

Once the mid-height crack formed in the masonry walls, the stiffness of the walls was significantly reduced. The reduced stiffness of the walls resulted in the load apparatus being unable to apply the out-of-plane load such that it was representative of gusty wind. However, it is not known if the behaviour of the real wind acting on a compliant structure would be similar to the behaviour seen in the dynamic tests; for example, it is possible that the dynamic wind pressure on the wall may be partially dissipated as a result of large wall deflections. Future studies may be able to determine how real wind behaves on compliant structures.

Finally, since most masonry structures in practices are partially reinforced, future work should be done to determine the behavior of reinforced structures that are loaded both quasi-statically and with loads that are representative of realistic wind.

Chapter 6: Reference

Albert, M.L., Elwi, A.E., and Cheng, J.J.R. 2001. Strength of Unreinforced Masonry Walls Using FRPs. Journal of composites for construction, **5**(2): 76-84.

ASTM International (ASTM). 2010. ASTM C1072 – 10 Standard Test Methods for measurement of Masonry Flexural Bond Strength. ASTM, West Conshohocken, PA, United States.

ASTM International (ASTM). 2010. ASTM C1717 – 10 Standard Test Methods for Conducting Strength Tests of Masonry Wall Panels. ASTM, West Conshohocken, PA, United States.

Baker, L.R. 1972. Structural action of brickwork panels subjected to wind loads. *In* Proceedings of the Fifth Australian Ceramic Conference, Sydney, Australia, 21-23 August 1972.

Barnard, R.H. 2000. Predicting dynamic wind loading on cantilevered canopy roof structures. Journal of Wind Engineering and Industrial Aerodynamics, **85**: 47-57.

Bathe, K.J., and Wilson, E.L. 1976. Numerical Methods in Finite Element Analysis. Prentice-Hall Inc. Publishers.

Beak, M., Colwell, S.A., Crowhurst, D., and Ellis, B.R. 1994. The Behaviour of Masonry and Concrete Panels Under Explosion and Static Loading. *In* Proceedings of I Chem E Symposium Series No. 134, pp. 227-247.

Bean Popehn, J.R., Schultz, A.E., Lu, M., Stolarski, H.K., and Ojard, N.J. 2008. Influence of transverse loading on the stability of slender unreinforced masonry walls. Engineering Structures, **30**(10): 2830-2839.

Box, G.E.P., Jenkins, G.M., and Reinsel, G.C. 2008. Time series analysis: forecasting and control. John Wiley & Sons, Inc., Hoboken, N.J. USA.

Burnett, S., Gilbert, M., Molyneaux, T., Tyas, A., Hobbs, B., and Beattie, G. 2007. The response of masonry joints to dynamic tensile loading. Materials and Structures, **40**: 517-527.

Canadian Standards Association (CSA). 2004a. CAN/CSA-A179-04 – Mortar and grout for unit masonry. CSA, Rexdale, ON, Canada.

Canadian Standards Association (CSA). 2004b. CSA S304.1-04 Design of masonry structures. CSA, Rexdale, ON, Canada.

CSA. 2004. Design of masonry structures. CSA Standard S304.1-04, Canadian Standards Association, Mississauga, ON Canada

de Vekey, R.C., and West, H.W.H. 1980. The flexural strength of concrete blockwork. Magazine of Concrete Research, **32**(113): 206-218

Deodatis, G. 1996. Simulation of Ergodic Multivariate Stochastic Processes. Journal of Engineering Mechanics, **122**(8): 778-787.

Derakhshan, H., and Ingham, J.M. 2008. Out-of-Plane testing of an unreinforced masonry wall subjected to one-way bending. *In* Proceeding of the Australian Earthquake Engineering Conference, Ballarat, Victoria, Australia, 21-23 November 2008. Australian Earthquake Engineering Society.

Drysdale, R.G., and Essawy, A.S. 1988. Out-of-Plane Bending of Concrete Block Walls. Journal of Structural Engineering, **114**(1): 121-133.

Drysdale, R.G., and Hamid, A.A. 2005. Masonry Structures Behaviour and Design. Canadian Masonry Design Centre, Mississauga, Ontario.

Elsayed, M., El-Dakhakhni, W., Razavi, S., Mekky, W., and Tait, M. 2013. Response of one-way reinforced masonry walls to blast loading. *In* Proceedings of the 12th Canadian Masonry Symposium, Vancouver, British Columbia, Canada, 2-5 June 2013.

Gani, F., Legeron, F., Ashby, M. 2009. Dynamic Wind Analyses of Transmission Line Structures. *In* Proceedings of the Electrical Transmission and Substation Structures Conference, Fort Worth, TX, 8-12 November 2009. American Society of Civil Engineers, New York, 423-434.

Griffith, M.C., Lam, N.T.K., Wilson, J.L, and Doherty, K. 2004. Experimental Investigation of Unreinforced Brick Masonry Walls in Flexure. Journal of Structural Engineering, **130**(3): 423-432.

Grimm, C.T., and Tucker, R.L. 1985. Flexural Strength of Masonry Prisms versus Wall Panels. Journal of Structural Engineering, **111**(9): 2021-2032.

Henderson, D.J., and Ginger, J.D. 2011. Response of pierced fixed corrugated steel roofing systems subjected to wind loads. Engineering Structures, **33**: 3290-3298.

Hoeppner, C.R., Sparling, B.F., Wegner, L.D., and Sakr, K. 2002. CFRP reinforced masonry walls subjected to out-of-plane loading. *In* Proceedings of 4th Structural Specialty Conference of the Canadian Society for Civil Engineering, Montreal, Quebec, Canada, 5-8 June 2002.

Iannuzzi, A. 1986. Aerodynamic response of a guyed mast: A deterministic approach. IASS Bulletin, No. 89: 38-45.

Instron. 2007. Partner Operating Help. Instron. Norwood, MA, USA.

Juhásová, E. 1997. Quasi-static versus dynamic space wind response of slender structures. Journal of Wind Engineering and Industrial Aerodynamics **69-71**: 757-766.

Kaimal, J.C., Wyngaard, J.C., Izumi, Y., and Coté, O.R. 1972. Spectral characteristics of surface-layer turbulence. Quarterly Journal of the Royal Meteorological Society, **98**: 563-589.

Kopp, G.A., Morrison, M.J., and Henderson, D.J. 2012. Full-scale testing of low-rise, residential buildings with realistic wind loads. Journal of Wind Engineering and Industrial Aerodynamics, **104-106**: 25-39.

Laird D.A. 2013. The empirical design dilemma. *In* Proceedings of the 12th Canadian Masonry Symposium, Vancouver, British Columbia, Canada, 2-5 June 2013.

Morrison, M.J., and Kopp, G.A. 2010. Performance of toe-nail connections under realistic wind loading. Engineering Structures, **33**: 69-76.

National Research Council Canada (NRC). 2010. National Building Code of Canada. NRC, Ottawa, ON, Canada.

Simiu, E., and Scanlan, R.H. 1987. Wind Effects on Structures. John Wiley & Sons, Inc., Hoboken, N.J. USA.

Simonds, K., Elsayed, M., El-Dakhakhni, W., Mekky, W., and Tait, M. 2013. Testing of a resilient masonry structural wall system under blast loads. *In* Proceedings of the 12th Canadian Masonry Symposium, Vancouver, British Columbia, Canada, 2-5 June 2013.

Sparling, B.F., 1995. The dynamic behaviour of guys and guyed masts in turbulent winds. Ph.D. thesis, Deparment of Civil Engineering, The University of Western Ontario, London, Ontario.

Sparling, B.F., and Davenport A.G. 1998. Three-dimensional dynamic response of guyed towers to wind turbulence. Canadian Journal of Civil Engineering, **25**: 512-525.

Surry, D., Sinno, R.R., Nail, B., Ho, T.C.E., Farquhar, S., and Kopp, G.A. 2007. Structurally Effective Static Wind Loads for Roof Panels. Structural Engineering, **133**(6): 871-885.

Wyatt, T.A., and May, H.I. 1973. The generation of stochastic load functions to simulate wind loading on structures. Earthquake Engineering and Structural Dynamics, **1**(3): 217-224.

Zielinski, A.J., and Reinhardt, H.W. 1982. Stress-Strain behaviour of concrete and mortar at high rates of tensile loading. Cement and Concrete Research, **12**(3): 309-319.

Appendix A: Time Histories

This appendix presents the dynamic load-time histories that were generated and applied to the walls during testing.

Figures A.1 to A.9 show the trials for the first series, used on ID1 and RD1

Figures A.10 to A.20 show the trials for the second series, used on ID2 and RD2

Figures A.21 to A.32 show the trials for the third series, used on ID3 and RD3

Figures A.33 to A.42 show the trials for the fourth series, used on ID4 and RD4

Figures A.43 to A.51 show the trials for the fifth series, used on ID5 and RD5

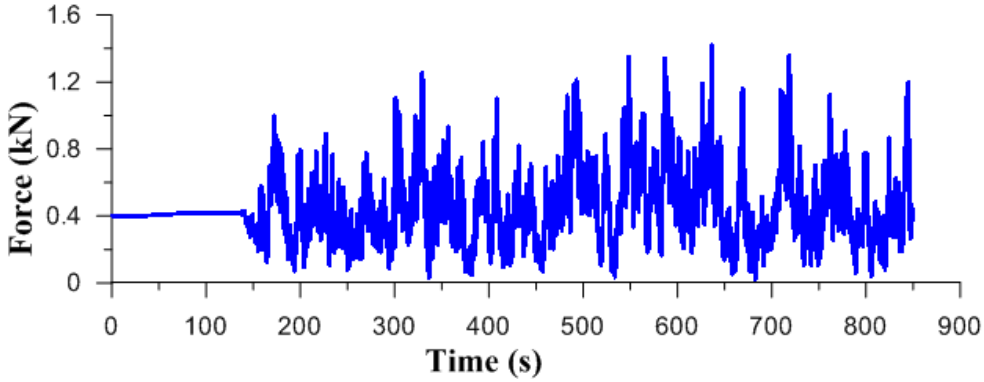

Figure A.1: 14 m/s trial for series 1

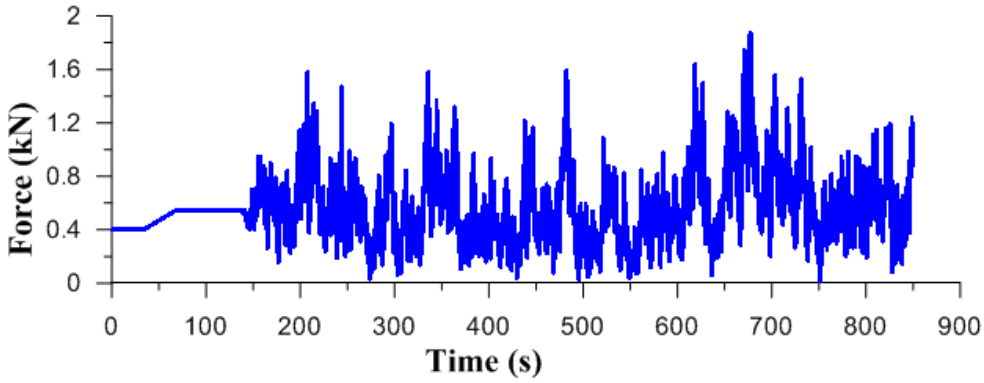

Figure A.2: 16 m/s trial for series 1

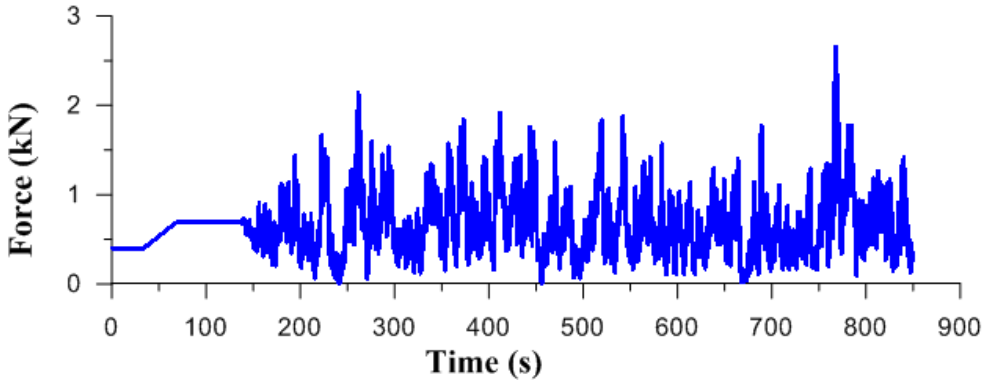

Figure A.3: 18 m/s trial for series 1

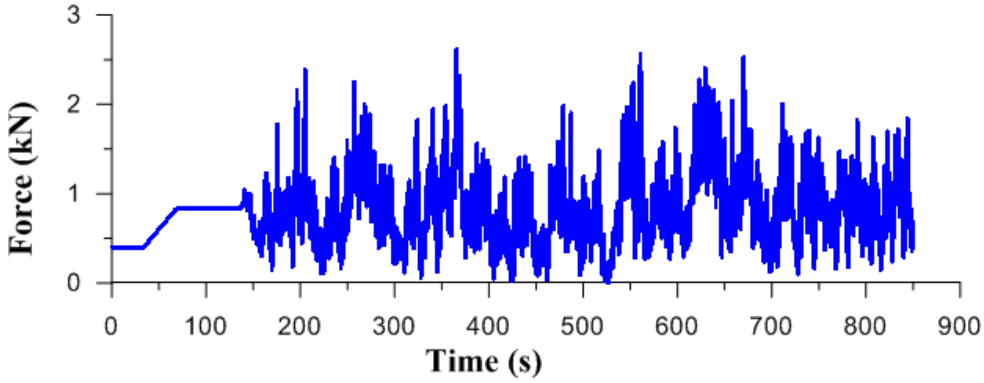

Figure A.4: 20 m/s trial for series 1

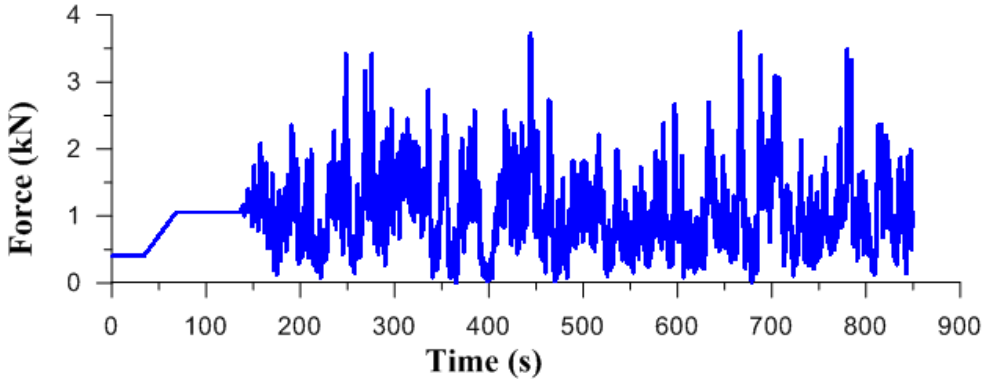

Figure A.5: 22 m/s trial for series 1

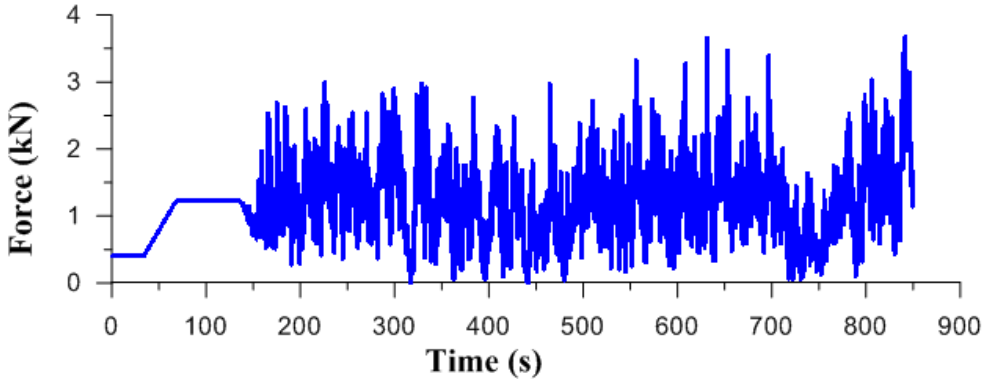

Figure A.6: 24 m/s trial for series 1

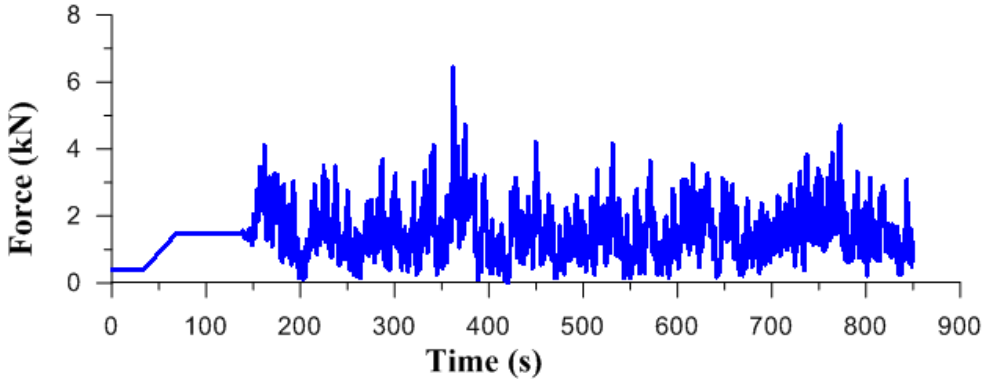

Figure A.7: 26 m/s trial for series 1

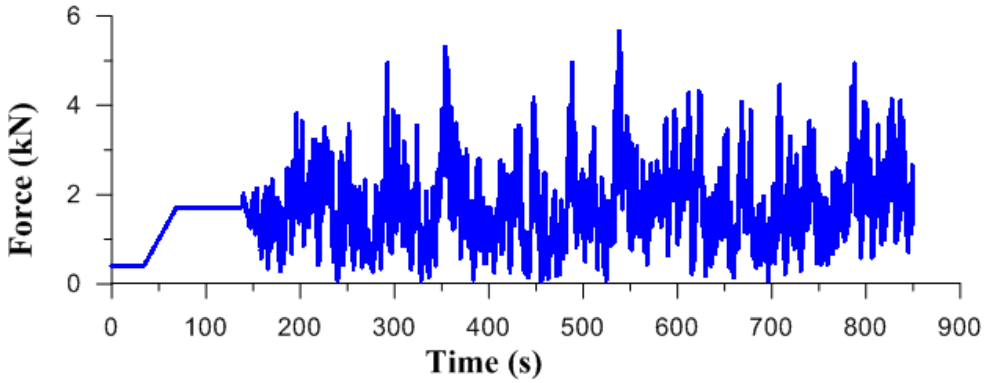

Figure A.8: 28 m/s trial for series 1

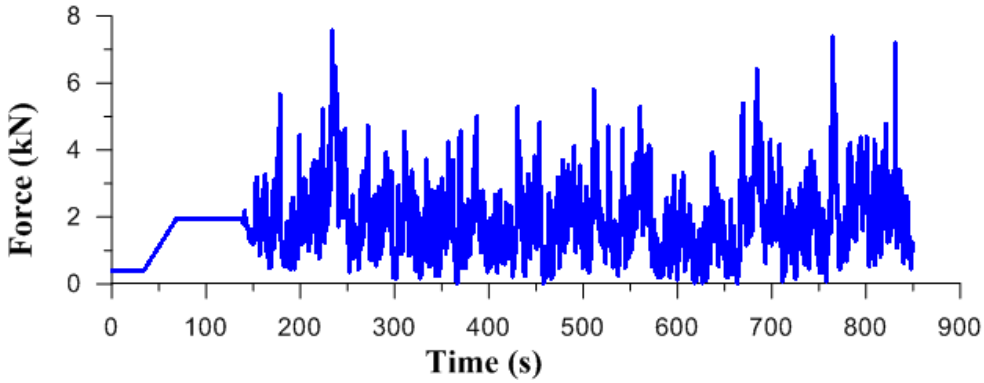

Figure A.9: 30 m/s trial for series 1

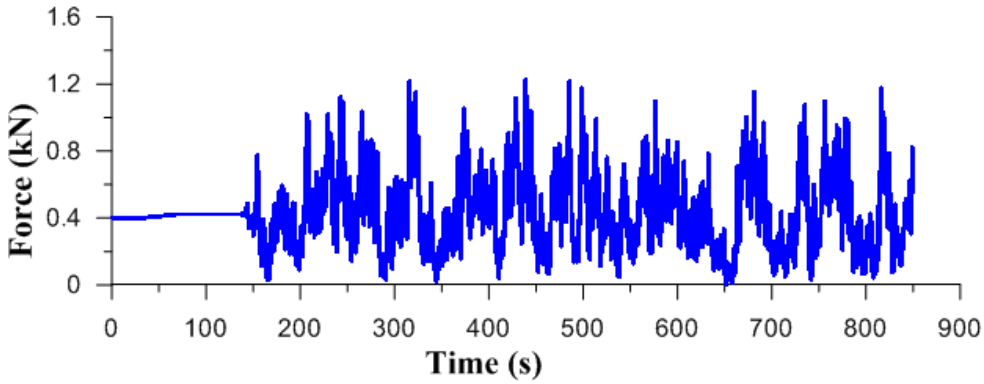

Figure A.10: 14 m/s trial for series 2

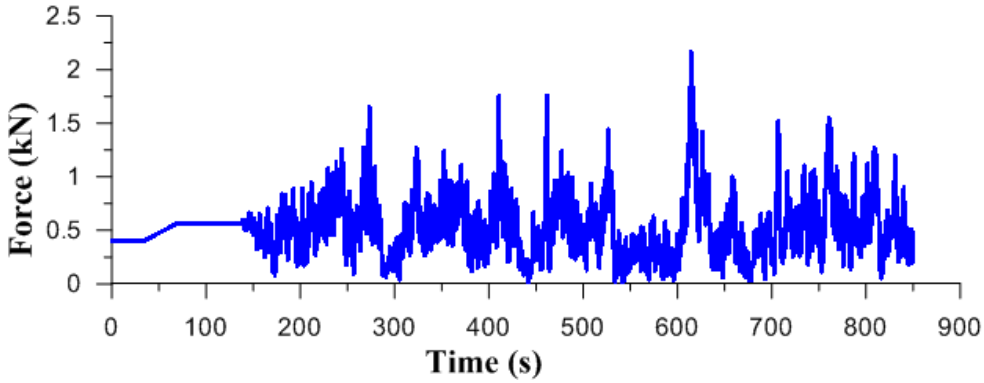

Figure A.11: 16 m/s trial for series 2

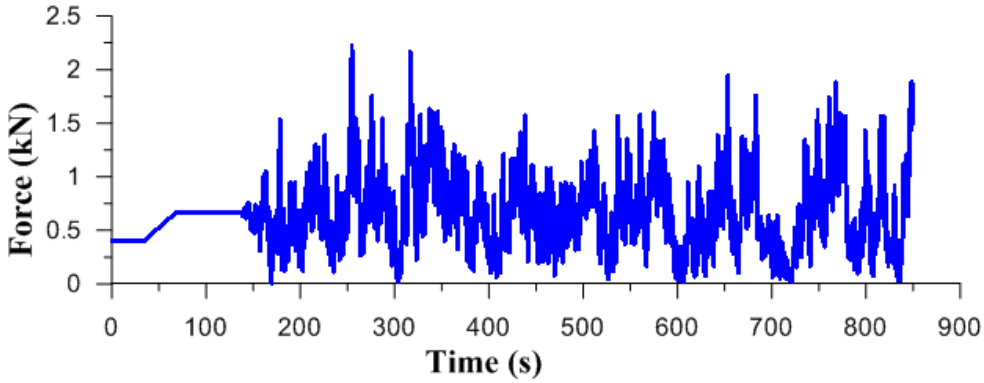

Figure A.12: 18 m/s trial for series 2

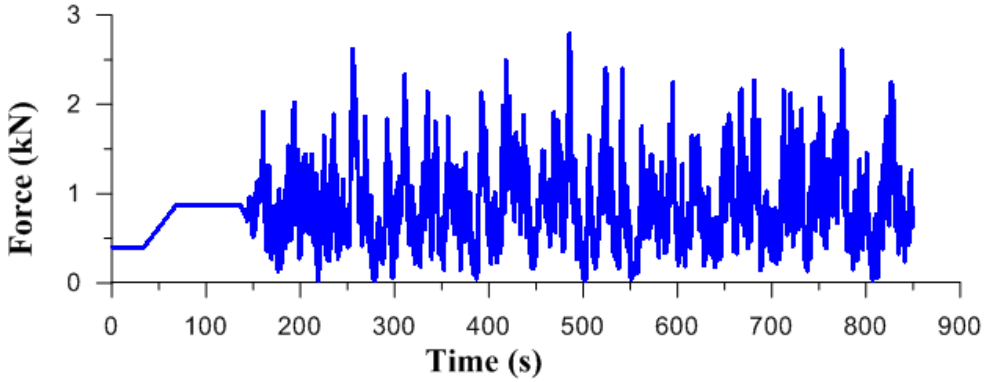

Figure A.13: 20 m/s trial for series 2

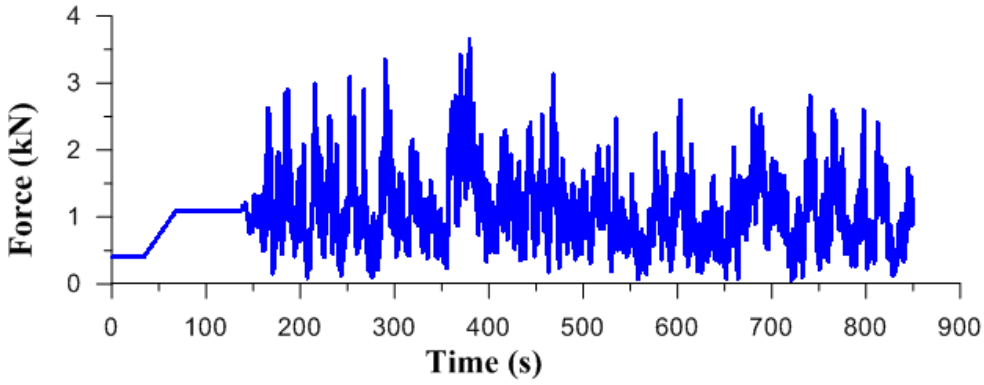

Figure A.14: 22 m/s trial for series 2

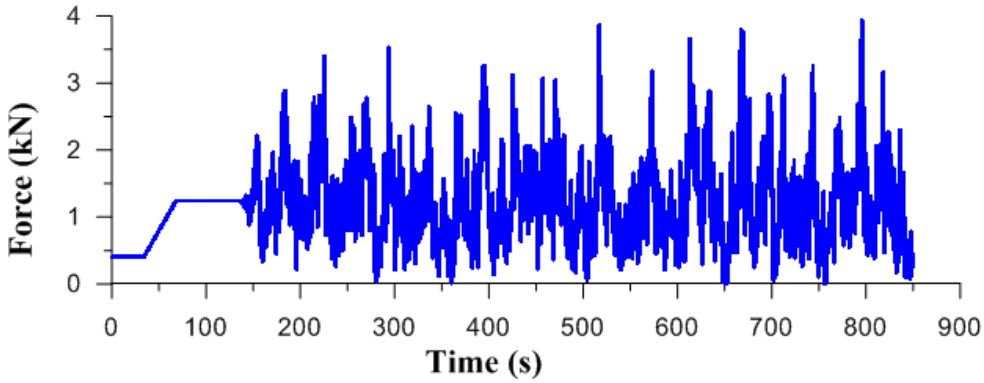

Figure A.15: 24 m/s trial for series 2

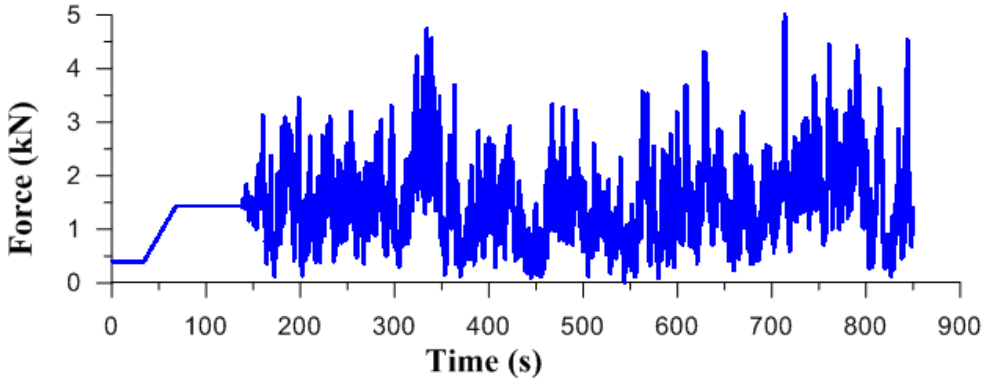

Figure A.16: 26 m/s trial for series 2

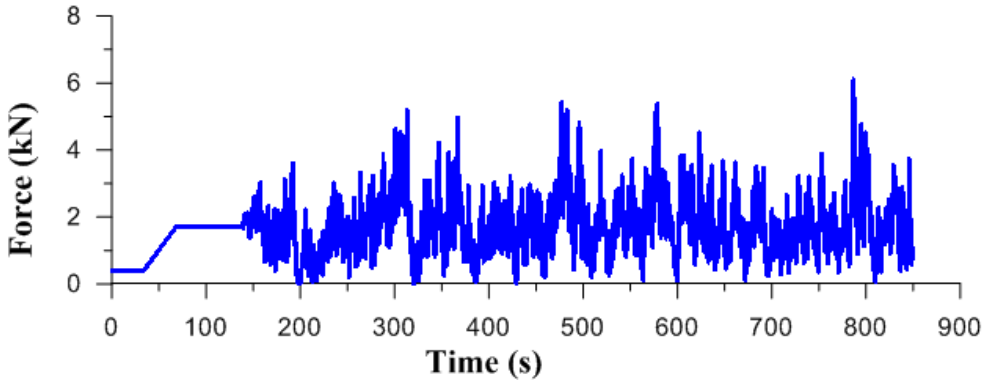

Figure A.17: 28 m/s trial for series 2

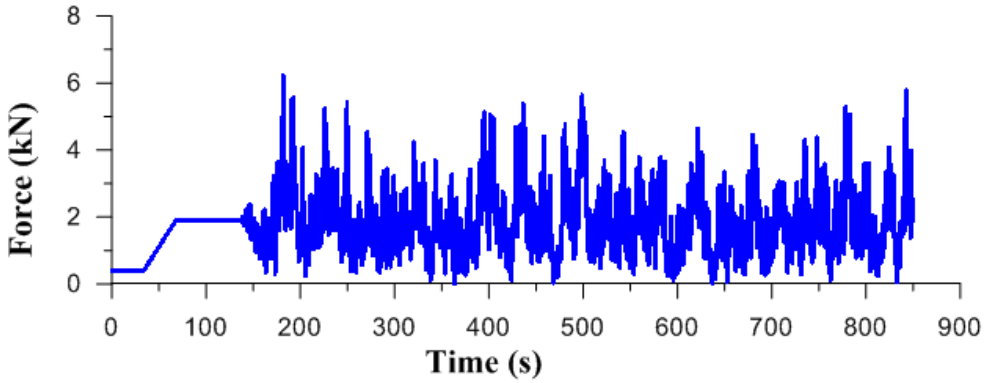

Figure A.18: 30 m/s trial for series 2

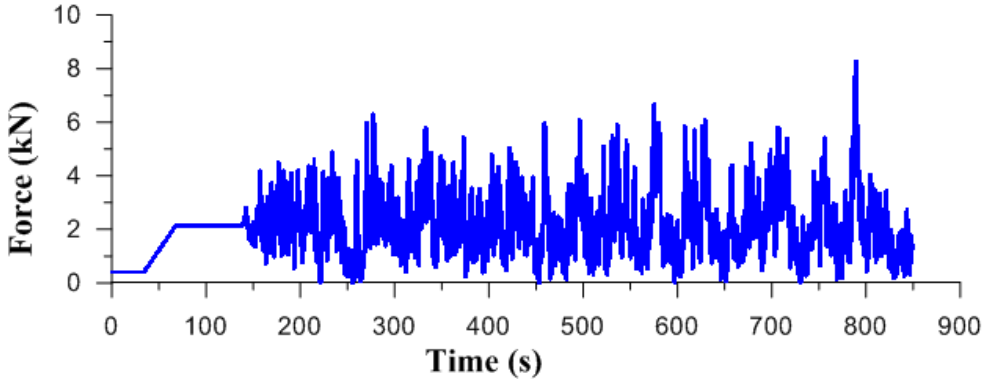

Figure A.19: 32 m/s trial for series 2

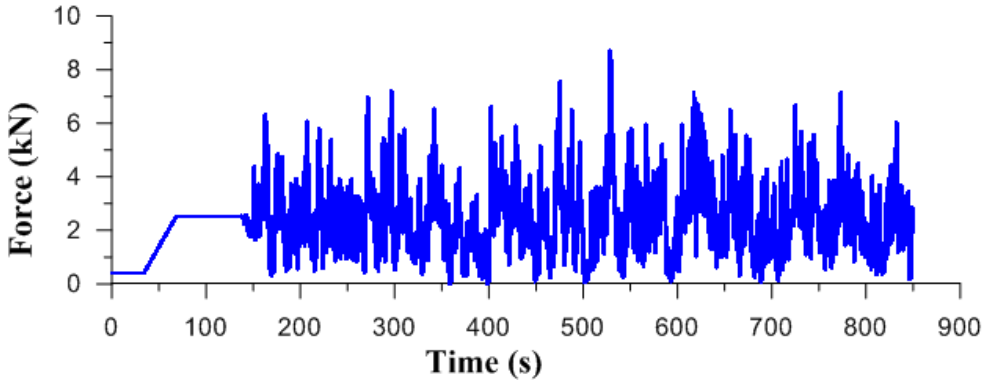

Figure A.20: 34 m/s trial for series 2

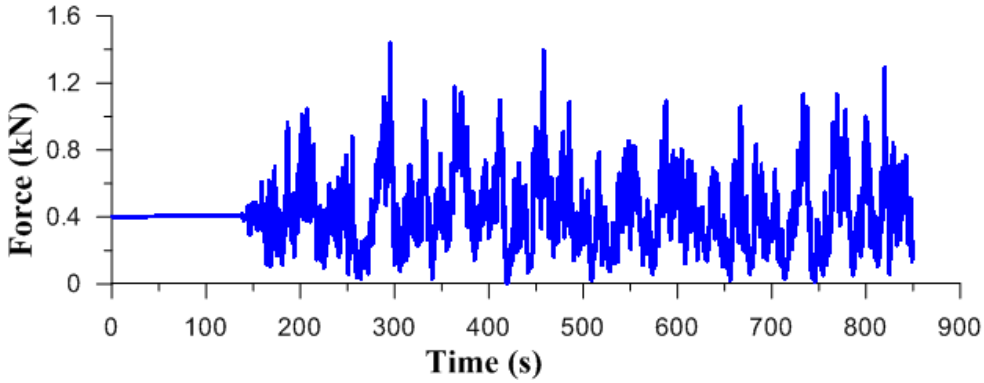

Figure A.21: 14 m/s trial for series 3

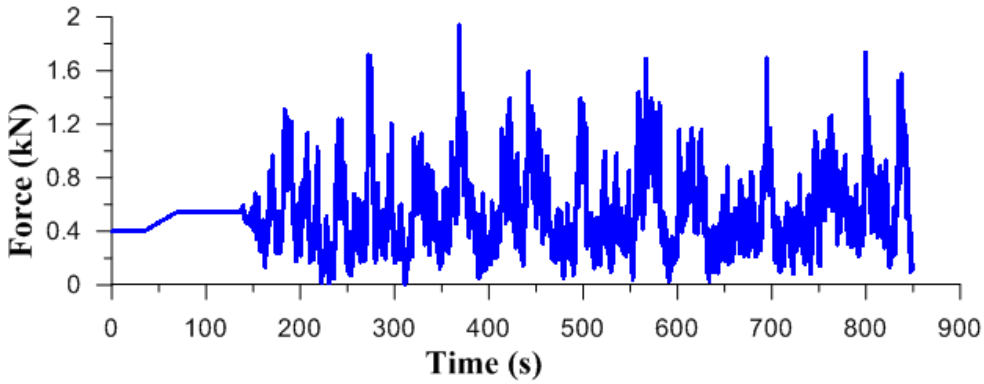

Figure A.22: 16 m/s trial for series 3

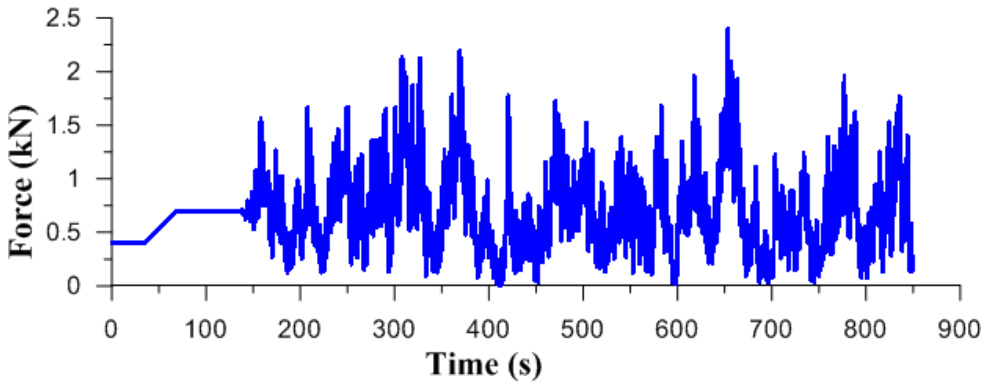

Figure A.23: 18 m/s trial for series 3

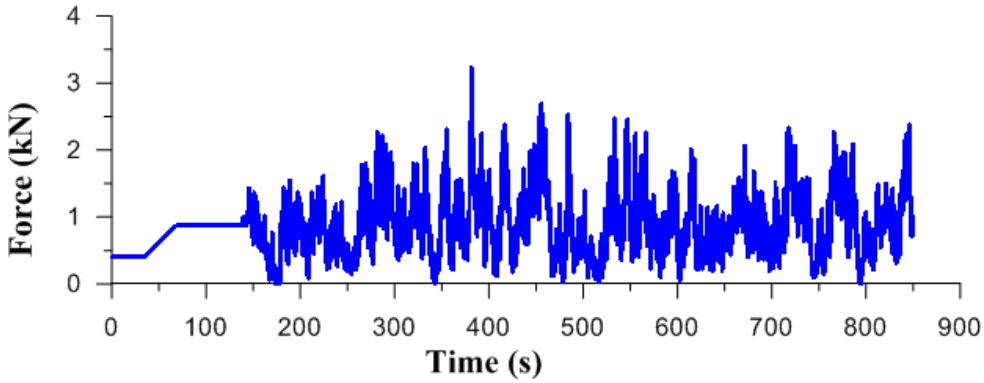

Figure A.24: 20 m/s trial for series 3

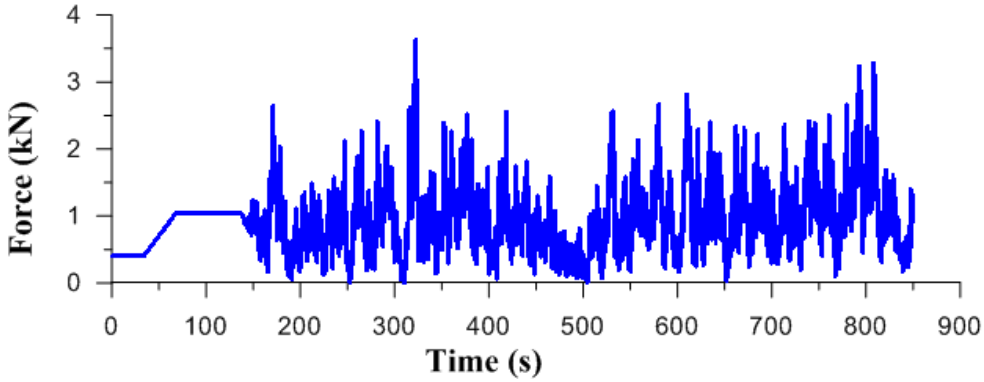

Figure A.25: 22 m/s trial for series 3

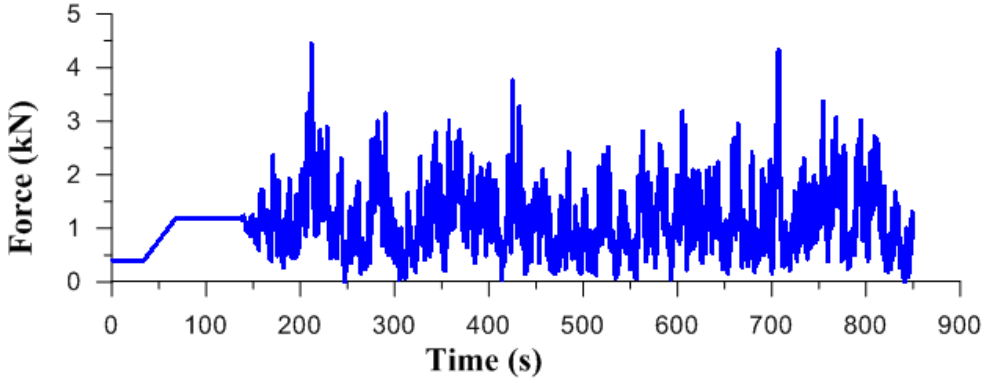

Figure A.26: 24 m/s trial for series 3

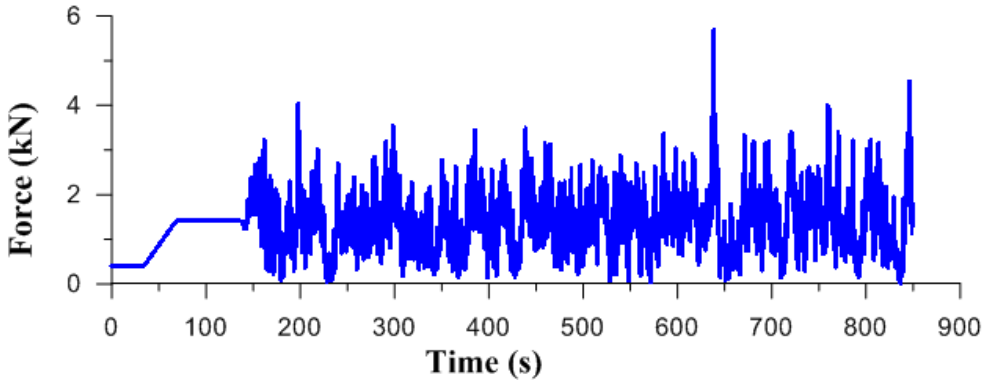

Figure A.27: 26 m/s trial for series 3

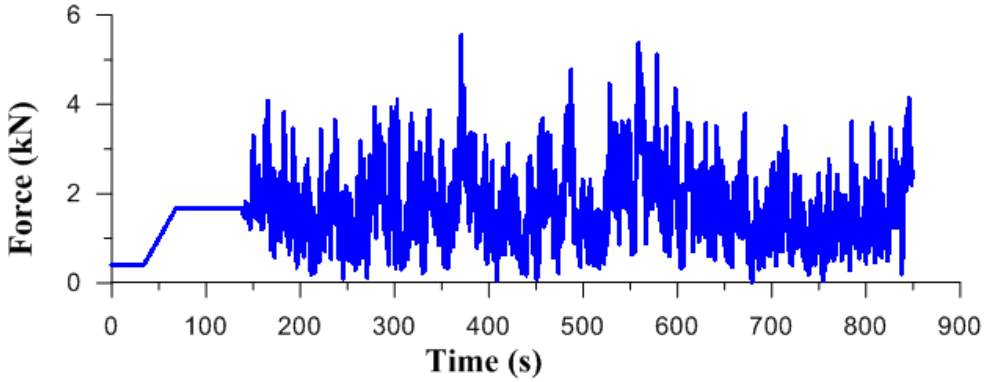

Figure A.28: 28 m/s trial for series 3

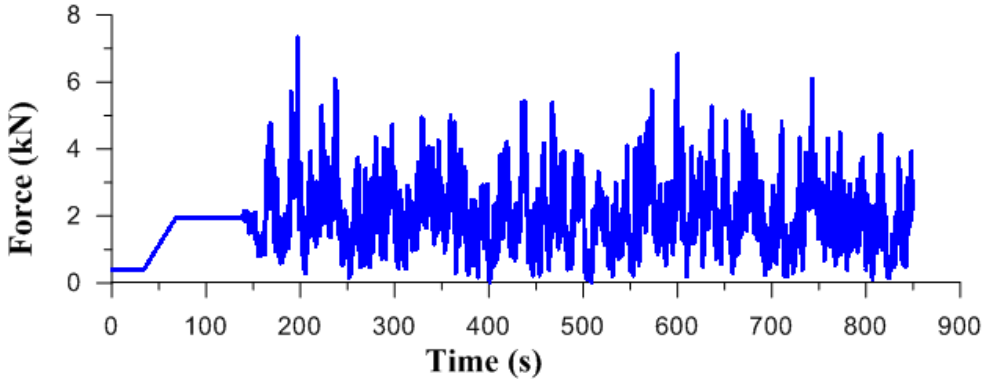

Figure A.29: 30 m/s trial for series 3

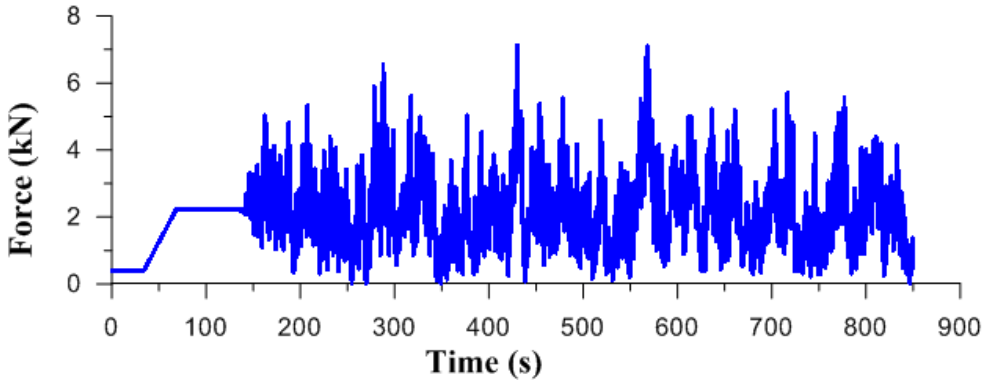

Figure A.30: 32 m/s trial for series 3

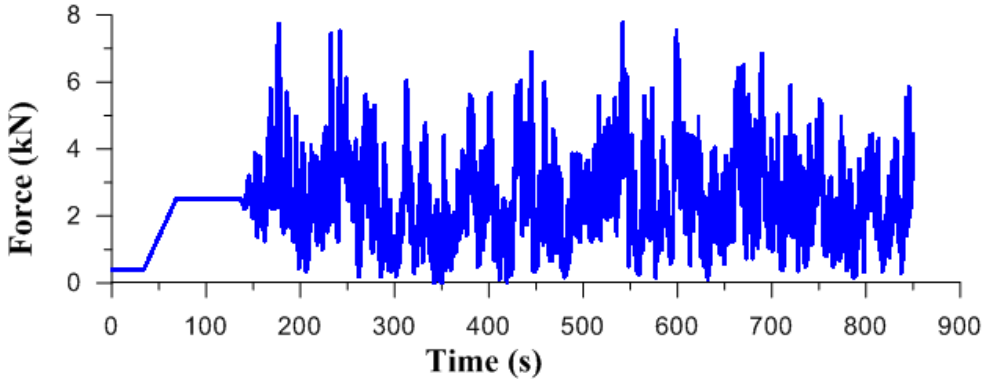

Figure A.31: 34 m/s trial for series 3

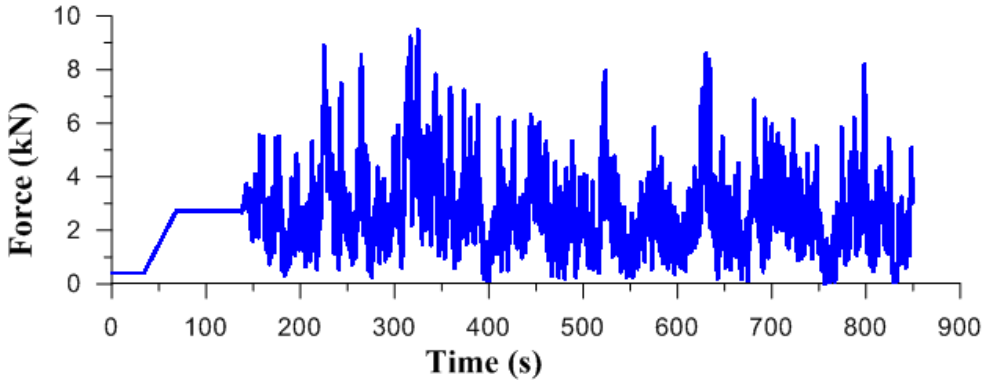

Figure A.32: 36 m/s trial for series 3

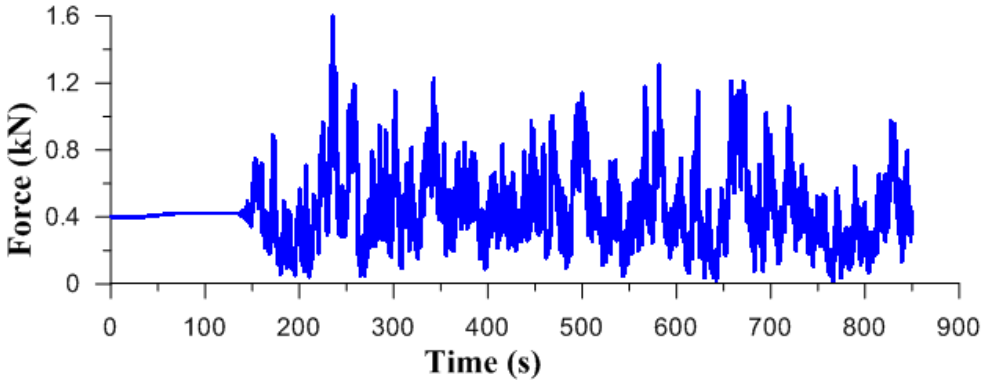

Figure A.33: 14 m/s trial for series 4

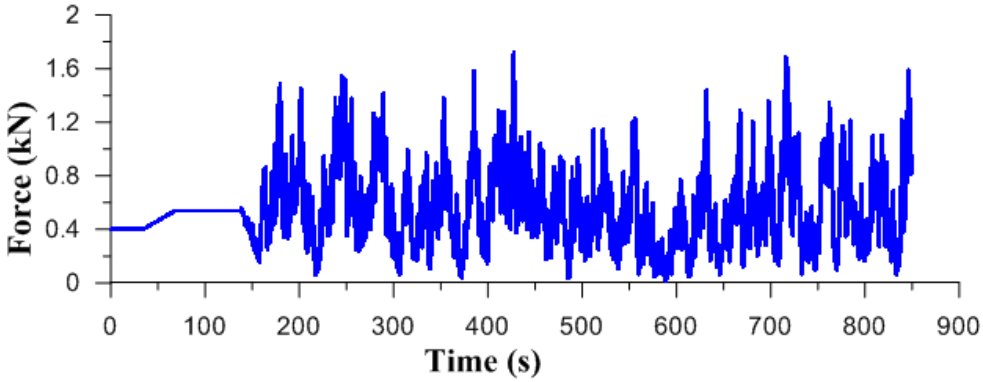

Figure A.34: 16 m/s trial for series 4

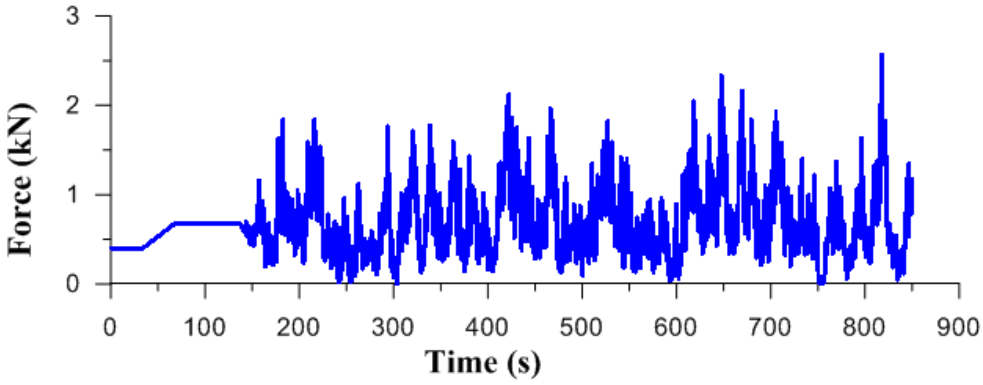

Figure A.35: 18 m/s trial for series 4

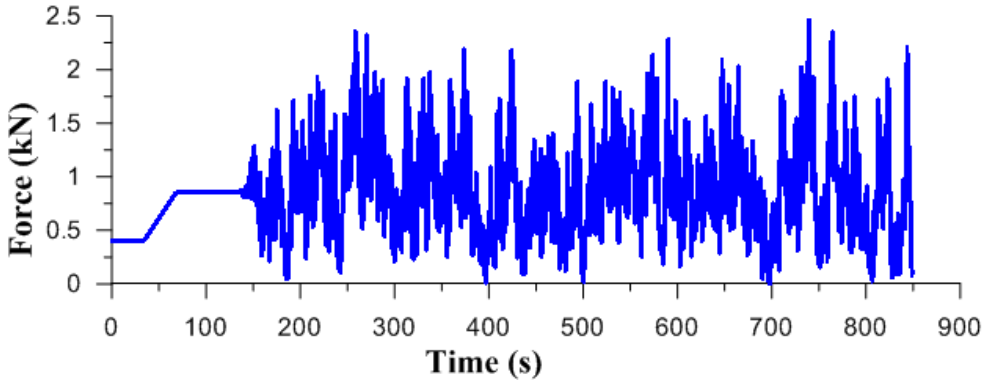

Figure A.36: 20 m/s trial for series 4

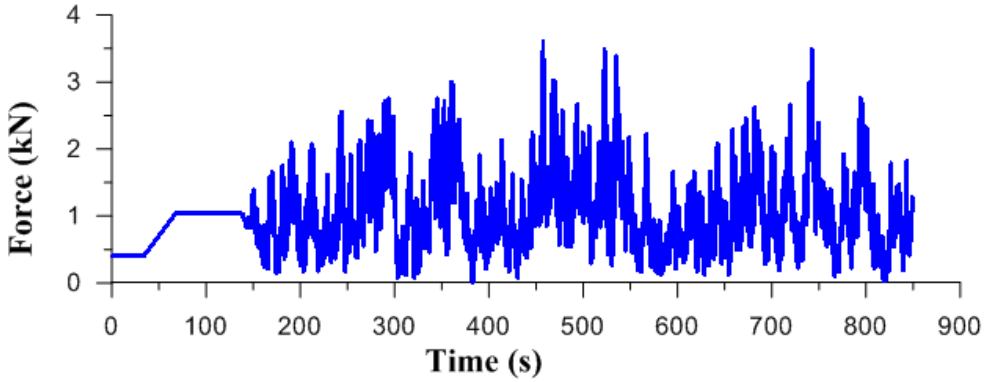

Figure A.37: 22 m/s trial for series 4

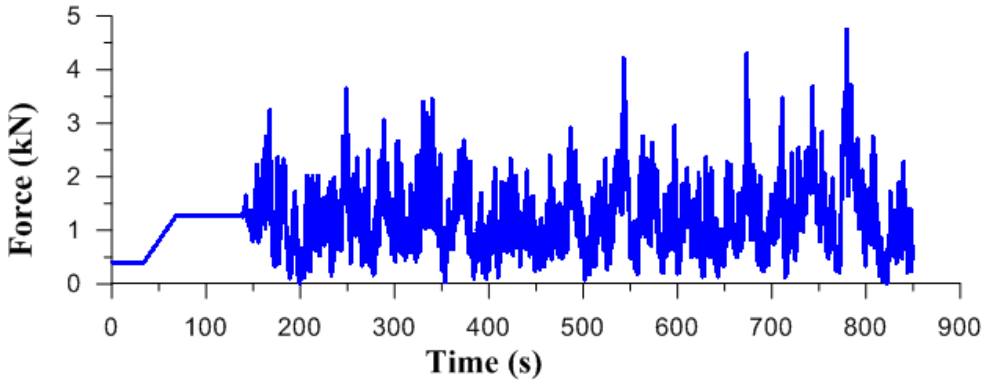

Figure A.38: 24 m/s trial for series 4

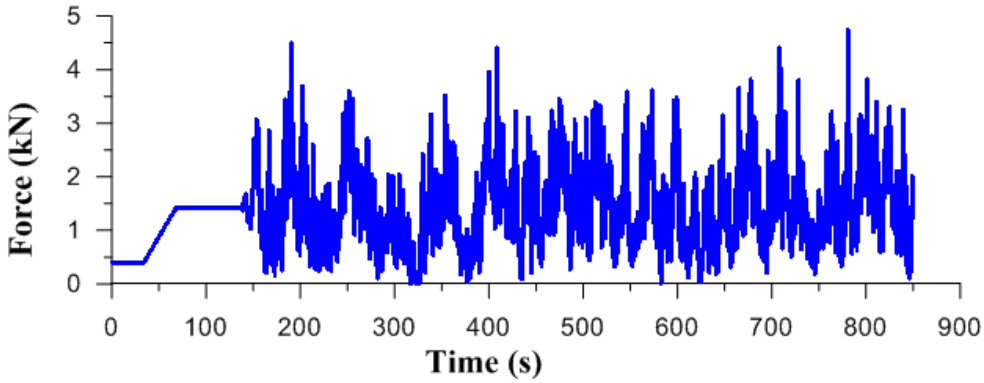

Figure A.39: 26 m/s trial for series 4

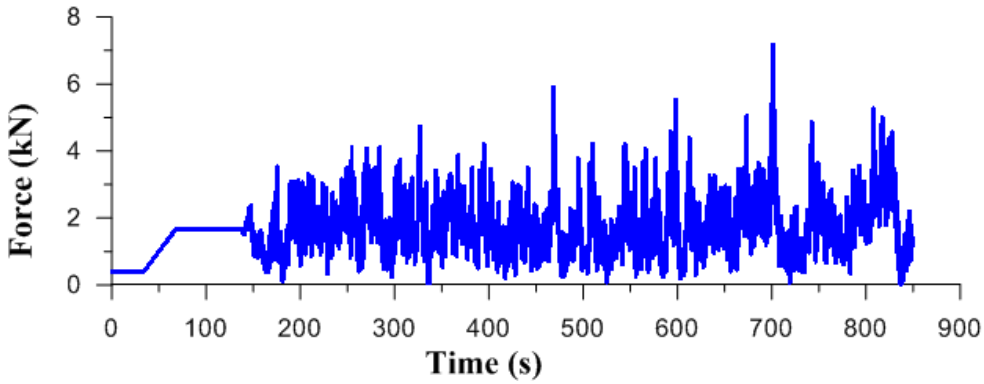

Figure A.40: 28 m/s trial for series 4

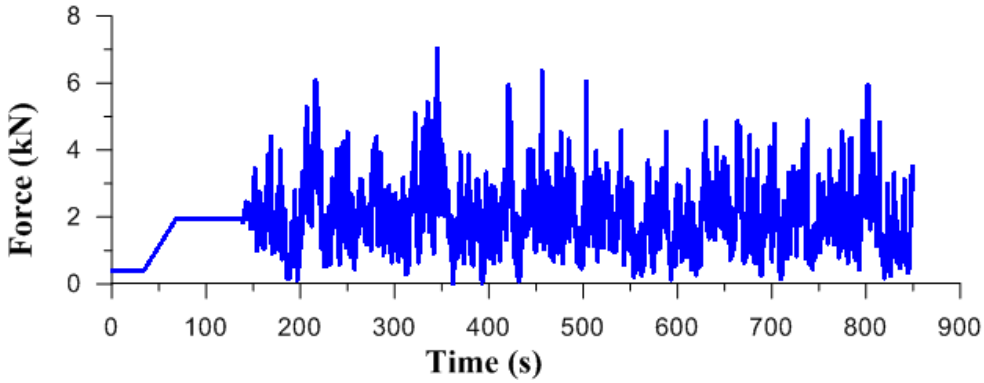

Figure A.41: 30 m/s trial for series 4

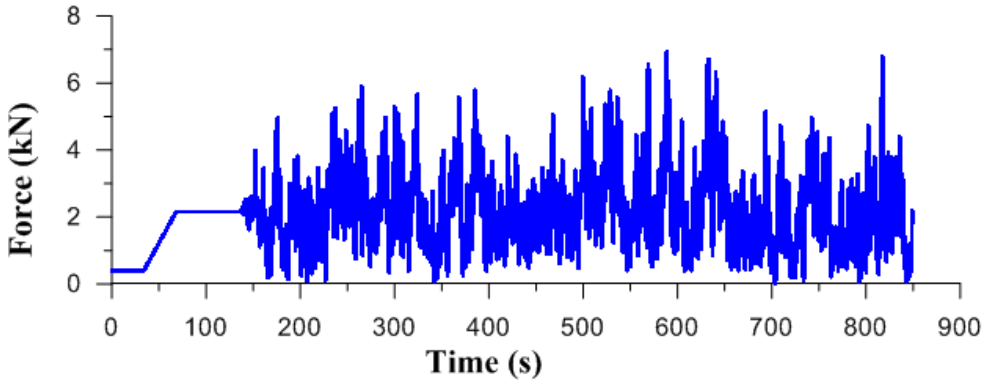

Figure A.42: 32 m/s trial for series 4

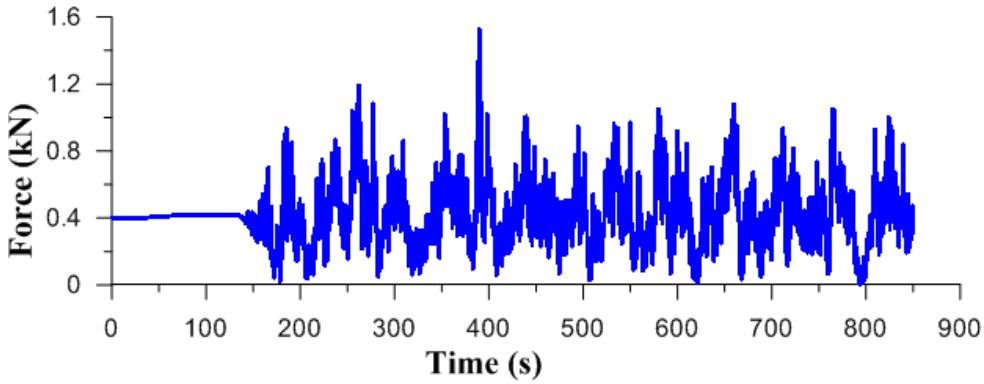

Figure A.43: 14 m/s trial for series 5

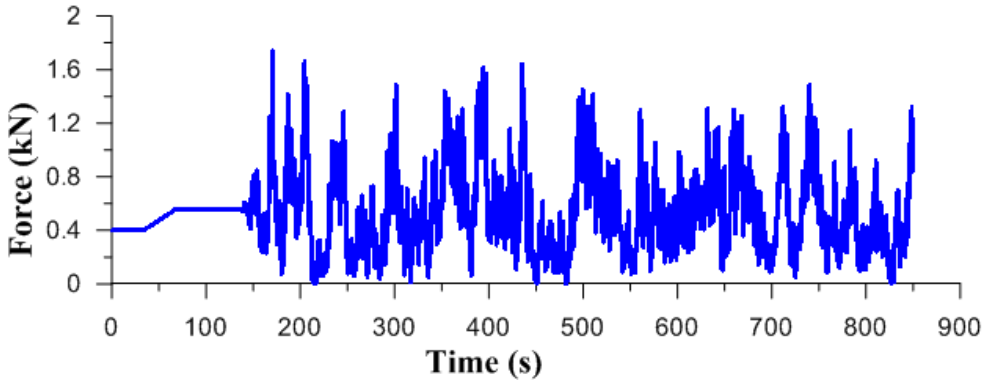

Figure A.44: 16 m/s trial for series 5

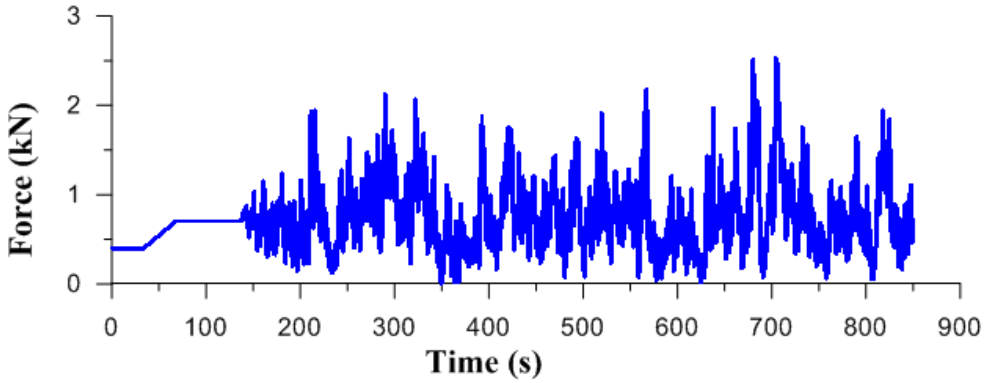

Figure A.45: 18 m/s trial for series 5

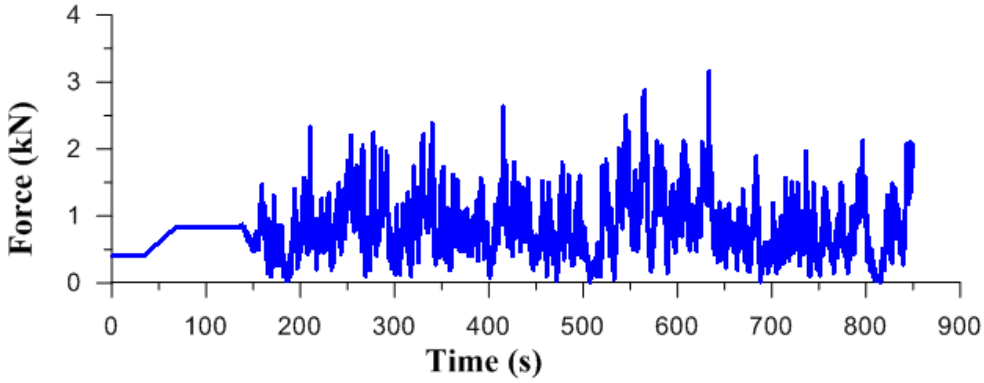

Figure A.46: 20 m/s trial for series 5

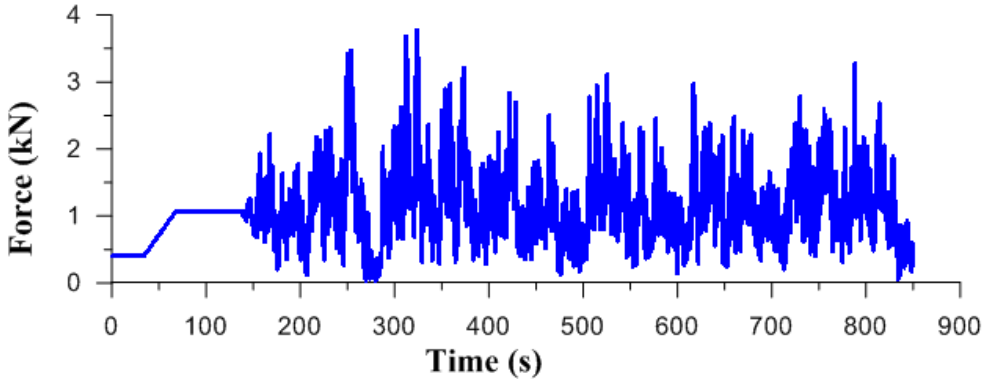

Figure A.47: 22 m/s trial for series 5

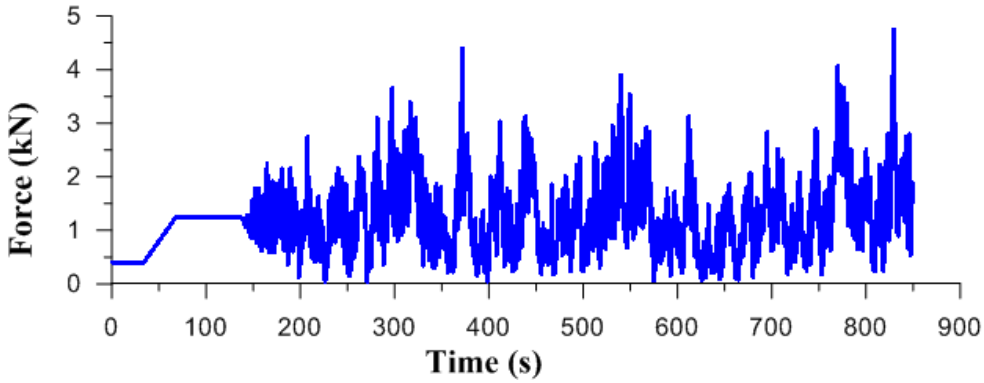

Figure A.48: 24 m/s trial for series 5

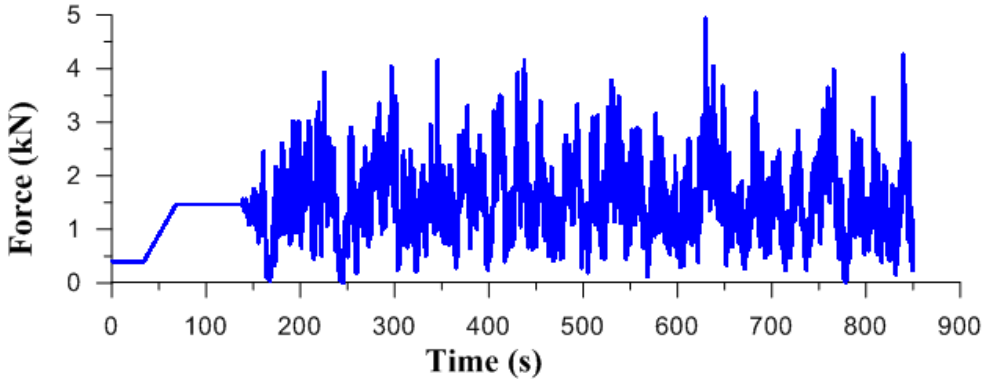

Figure A.49: 26 m/s trial for series 5

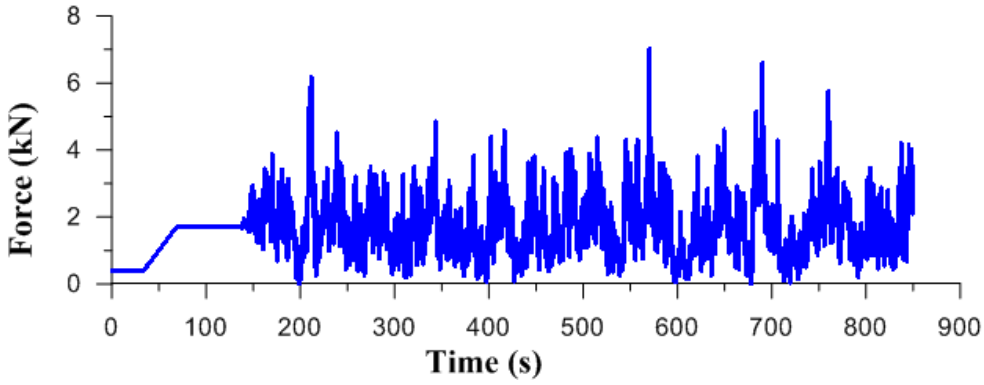

Figure A.50: 28 m/s trial for series 5

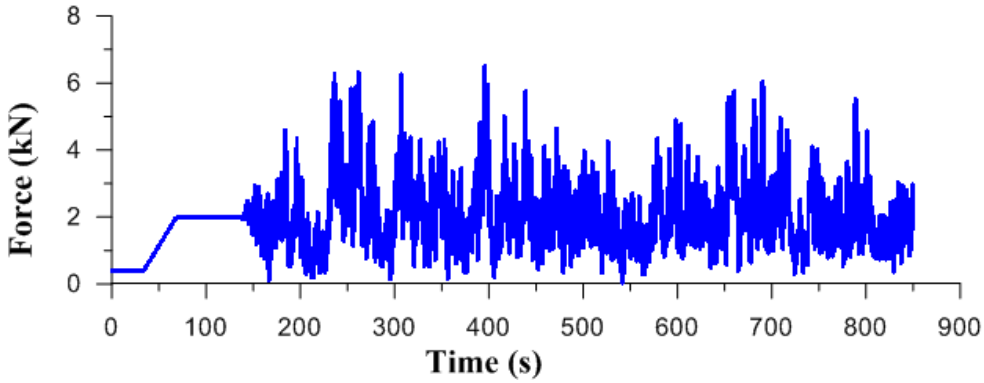

Figure A.51: 30 m/s trial for series 5

Appendix B: Vibration PSD plots

This appendix shows the PSDs of the Vibration tests conducted on the walls

Figures B.1 to B.10 show the Ambient PSDs for the ideally-pinned walls.

Figures B.11 to B.20 show the Ambient PSDs for the realistically-pinned walls.

Figures B.21 to B.30 show the PSD plots for the impact tests on the ideally-pinned walls.

Figures B.31 to B.40 show the PSD plots for the impact tests on the realistically-pinned walls.

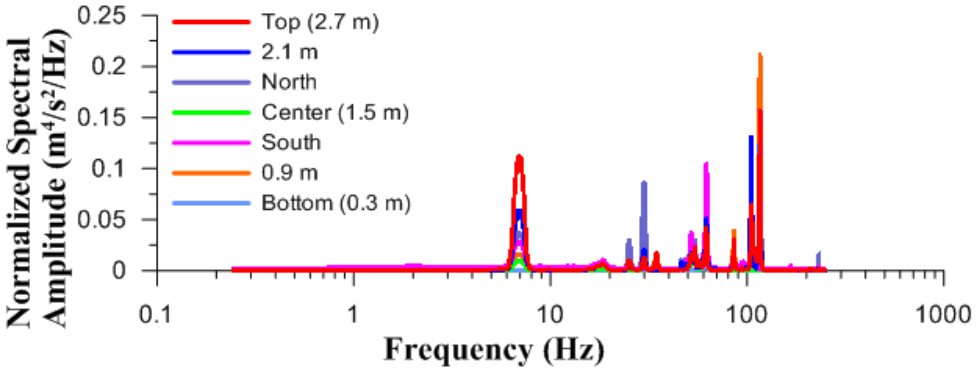

Figure B.1: PSD plot of the ambient vibration test on Specimen ID1

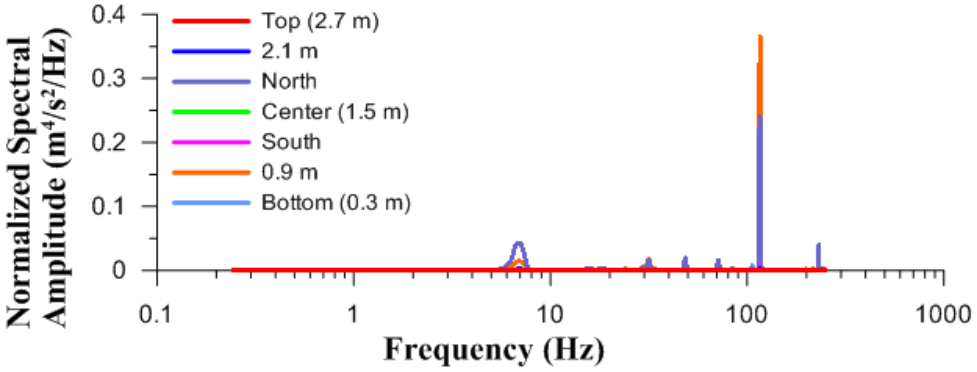

Figure B.2: PSD plot of the ambient vibration test on Specimen ID2

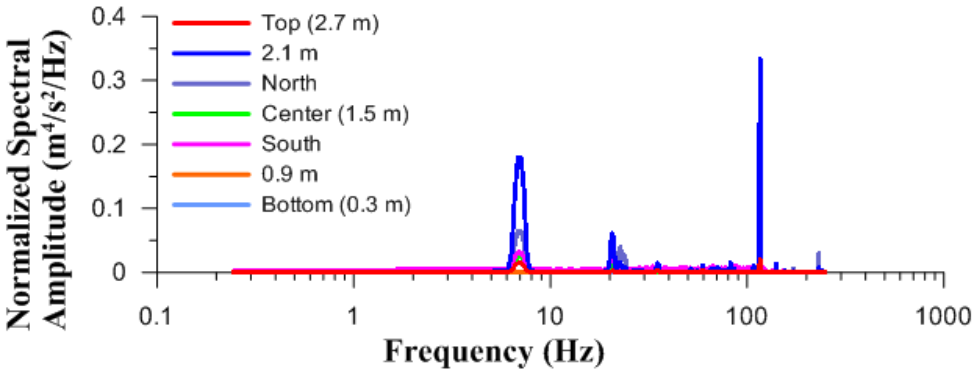

Figure B.3: PSD plot of the ambient vibration test on Specimen ID3

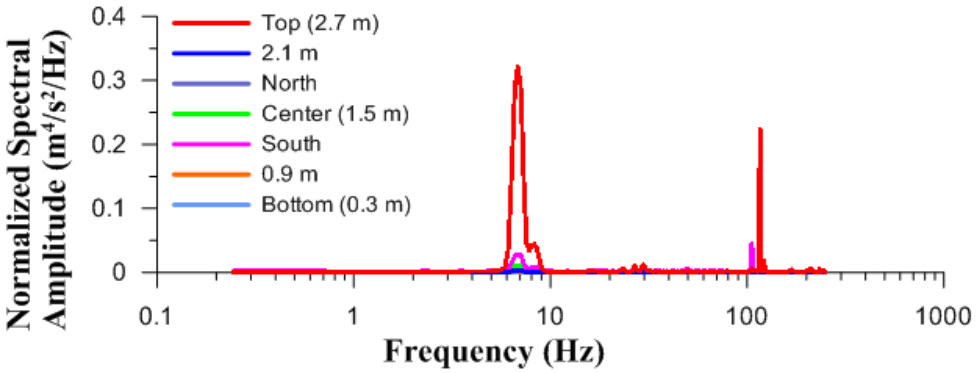

Figure B.4: PSD plot of the ambient vibration test on Specimen ID4

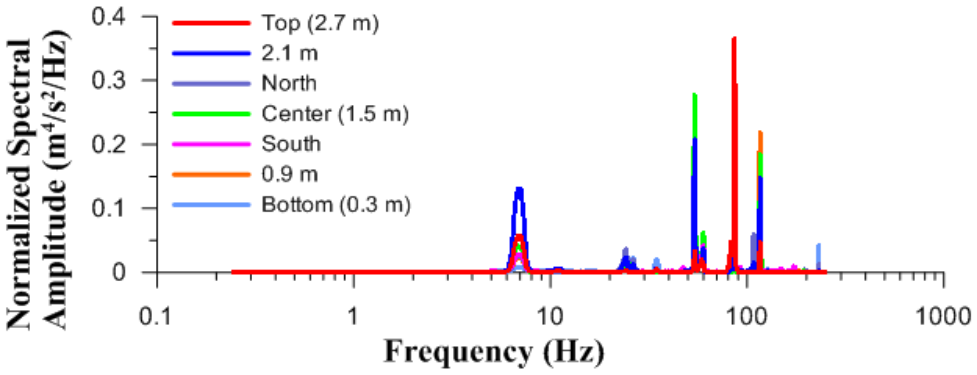

Figure B.5: PSD plot of the ambient vibration test on Specimen ID5

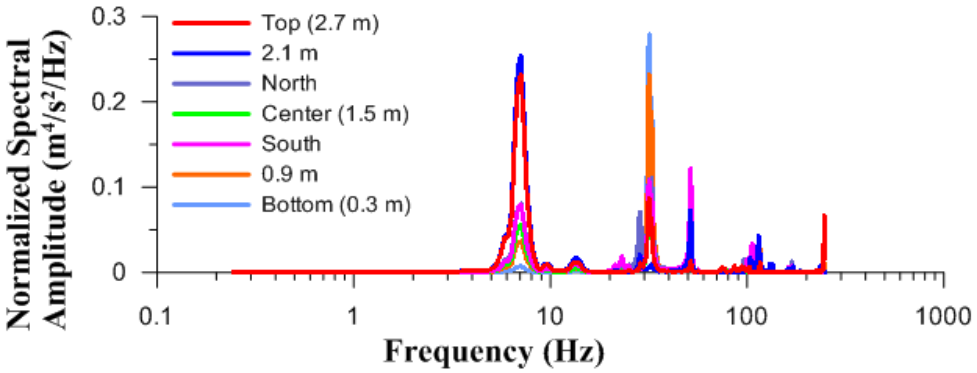

Figure B.6: PSD plot of the ambient vibration test on Specimen IS1

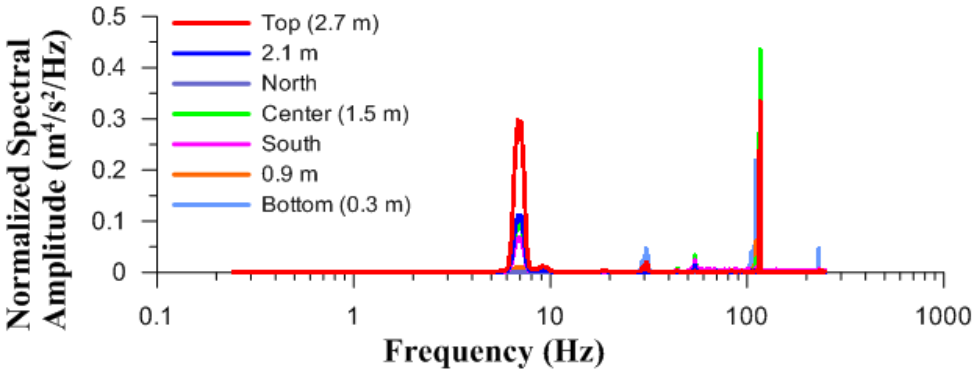

Figure B.7: PSD plot of the ambient vibration test on Specimen IS2

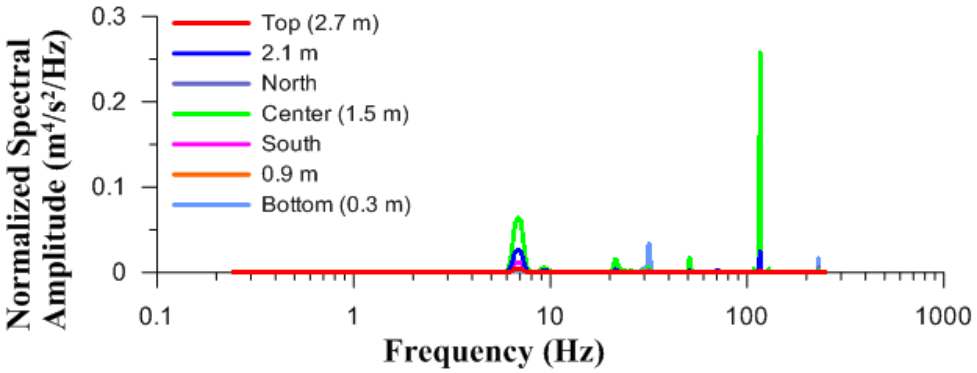

Figure B.8: PSD plot of the ambient vibration test on Specimen IS3

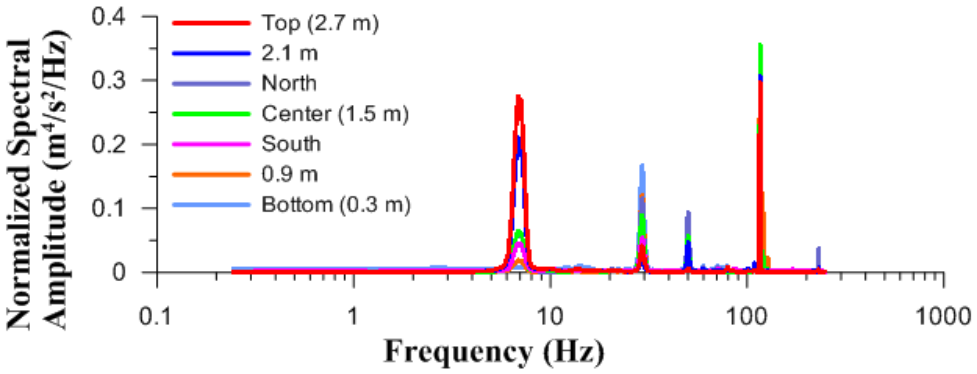

Figure B.9: PSD plot of the ambient vibration test on Specimen IS4

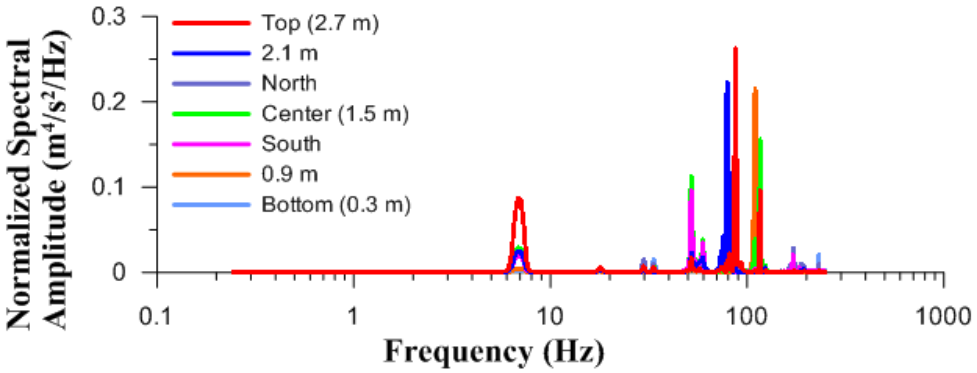

Figure B.10: PSD plot of the ambient vibration test on Specimen IS5

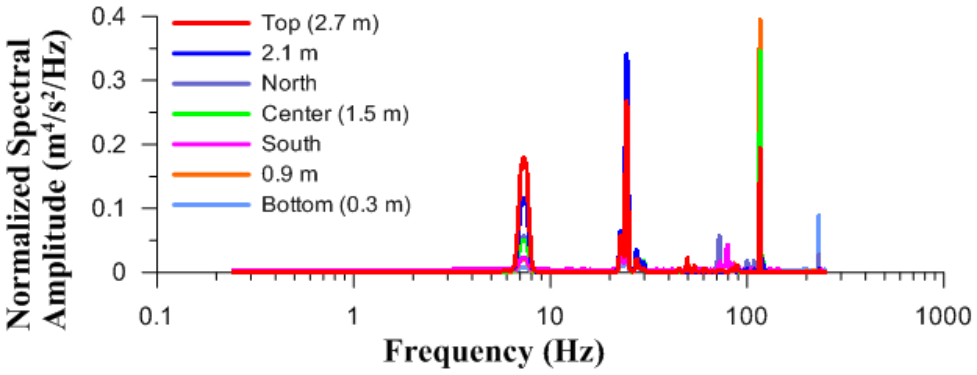

Figure B.11: PSD plot of the ambient vibration test on Specimen RD1

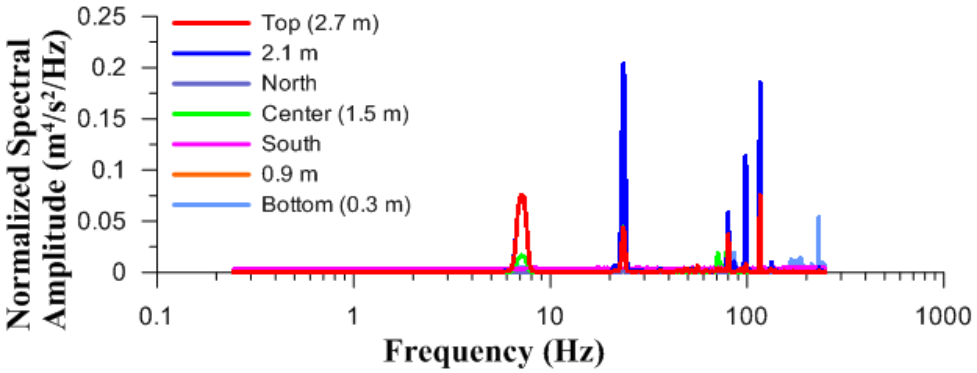

Figure B.12: PSD plot of the ambient vibration test on Specimen RD2

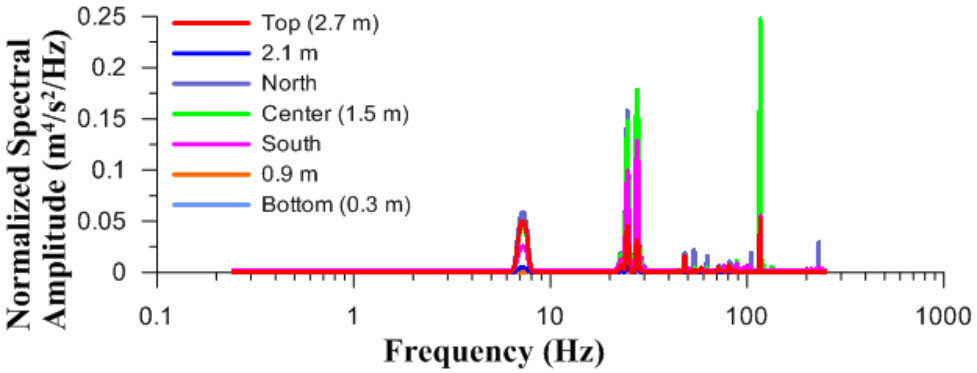

Figure B.13: PSD plot of the ambient vibration test on Specimen RD3

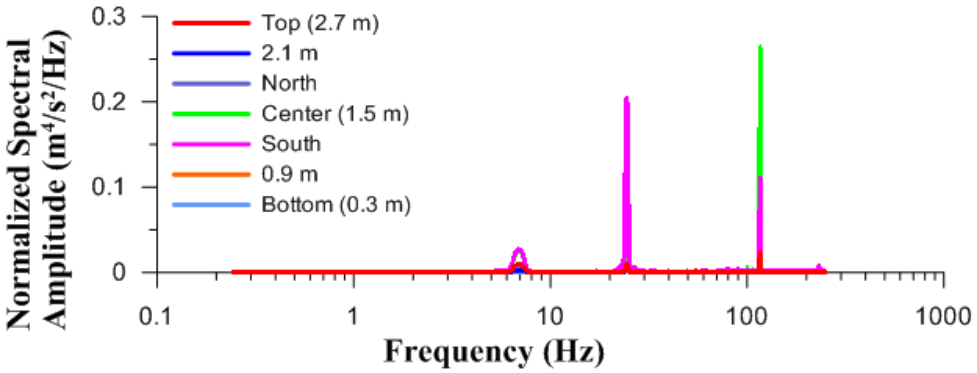

Figure B.14: PSD plot of the ambient vibration test on Specimen RD4

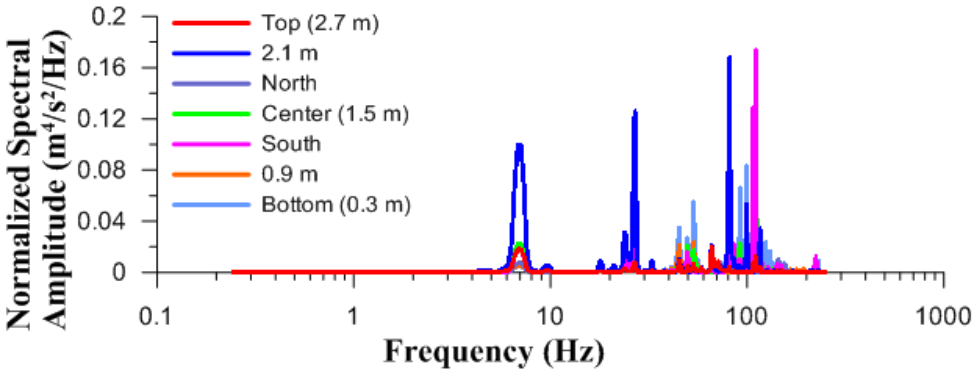

Figure B.15: PSD plot of the ambient vibration test on Specimen RD5

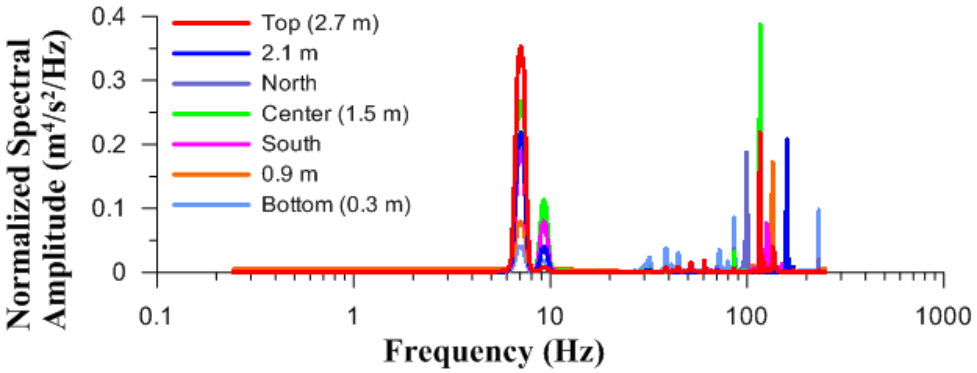

Figure B.16: PSD plot of the ambient vibration test on Specimen RS1

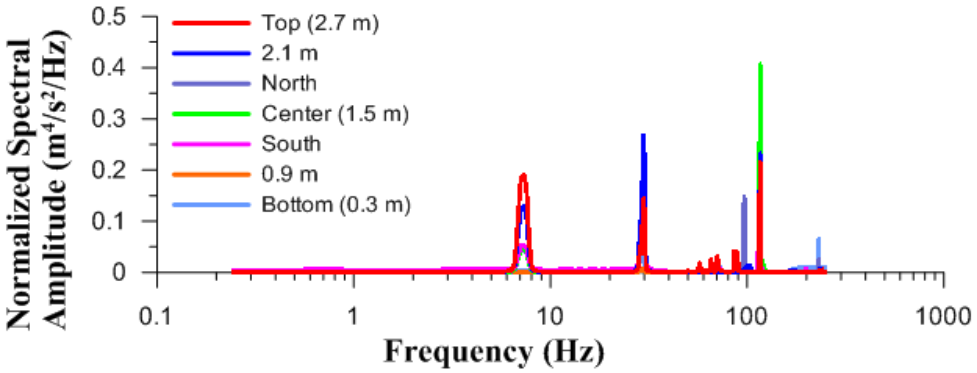

Figure B.17: PSD plot of the ambient vibration test on Specimen RS2

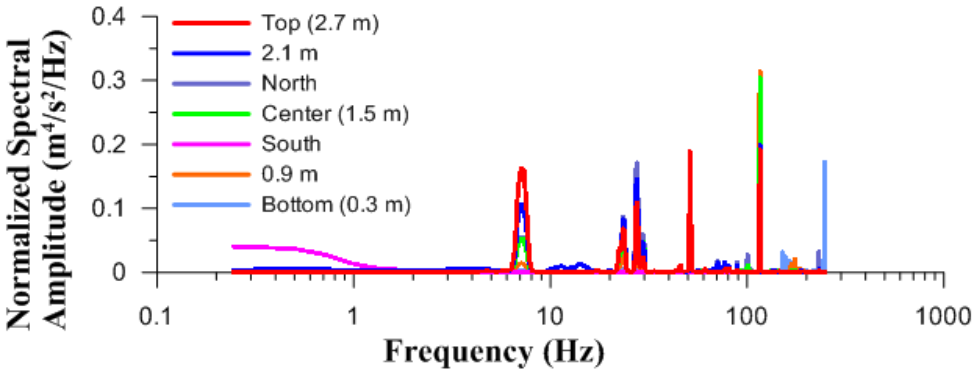

Figure B.18: PSD plot of the ambient vibration test on Specimen RS3

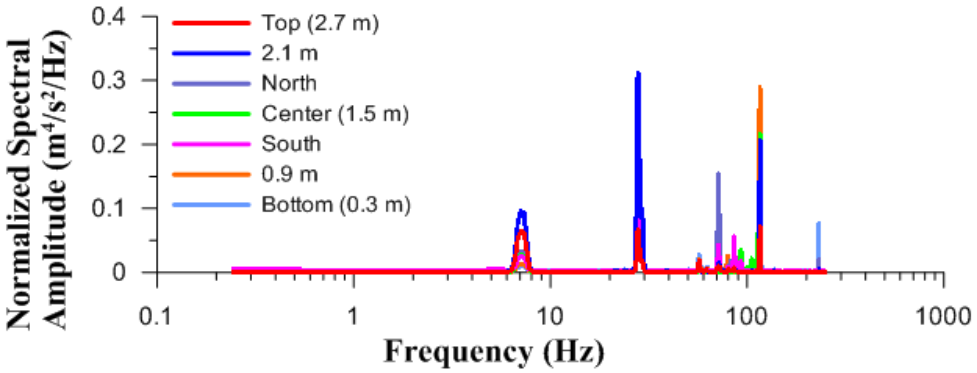

Figure B.19: PSD plot of the ambient vibration test on Specimen RS4

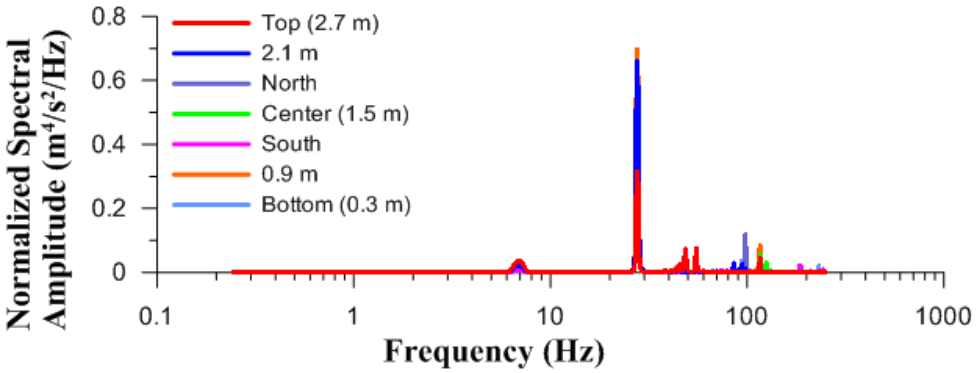

Figure B.20: PSD plot of the ambient vibration test on Specimen RS5

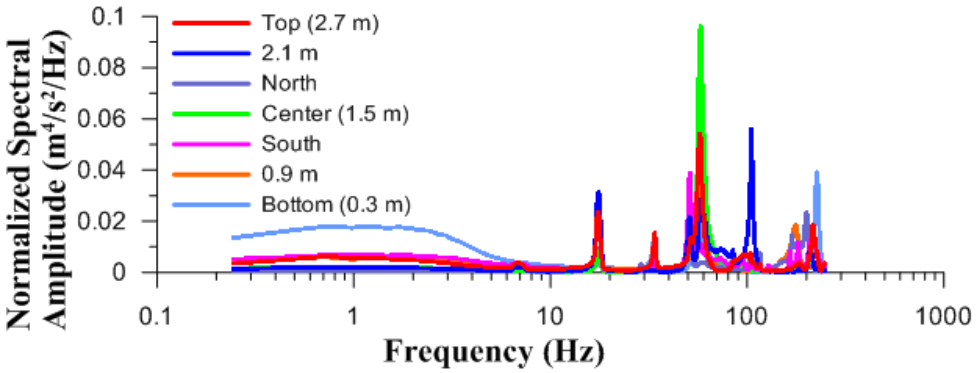

Figure B.21: PSD plot of the impact vibration test on Specimen ID1

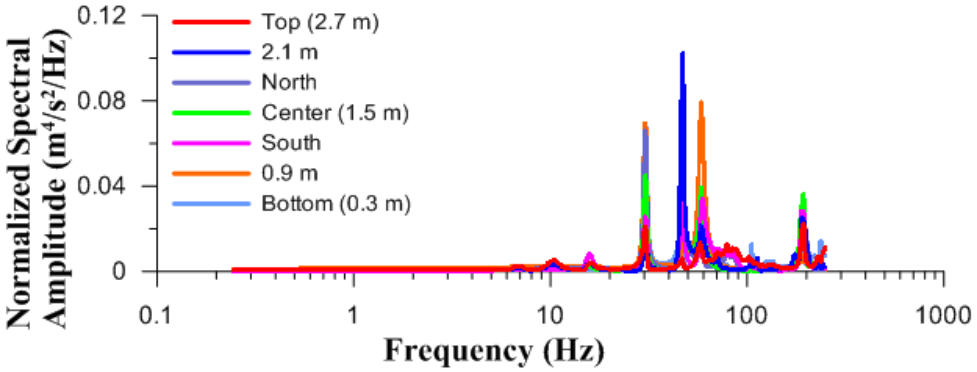

Figure B.22: PSD plot of the impact vibration test on Specimen ID2

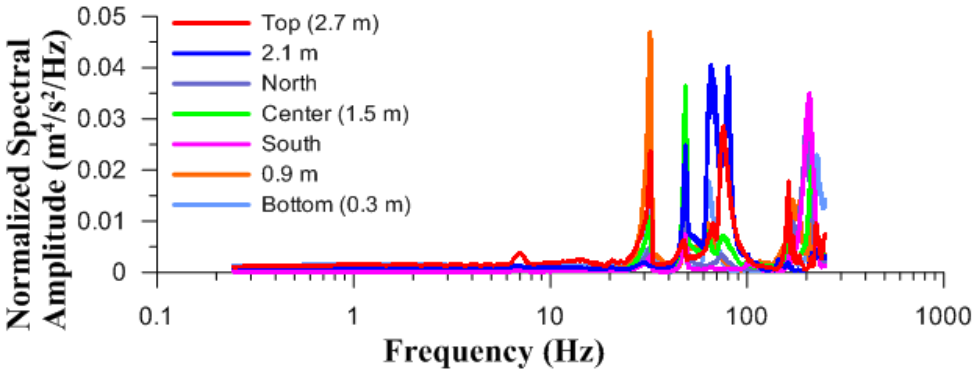

Figure B.23: PSD plot of the impact vibration test on Specimen ID3

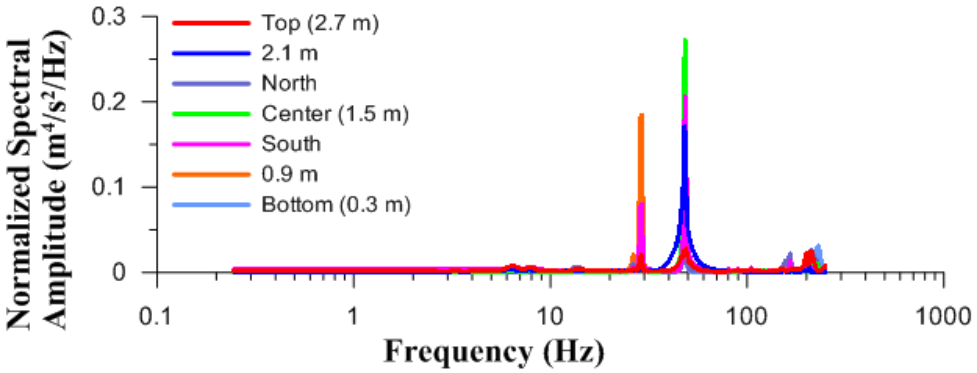

Figure B.24: PSD plot of the impact vibration test on Specimen ID4

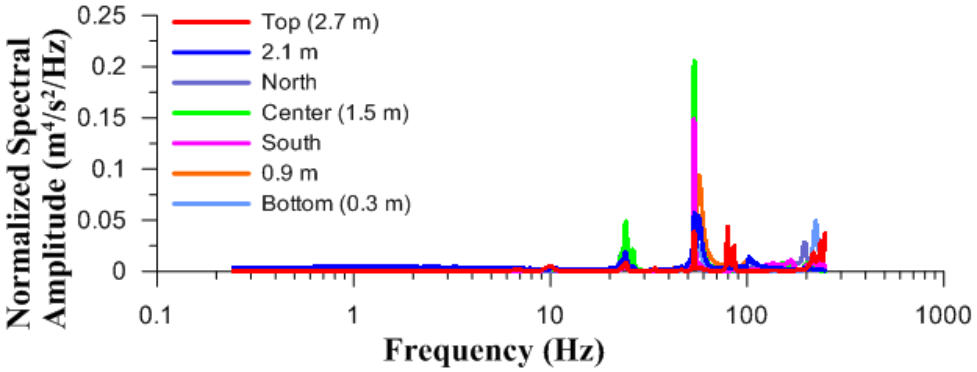

Figure B.25: PSD plot of the impact vibration test on Specimen ID5

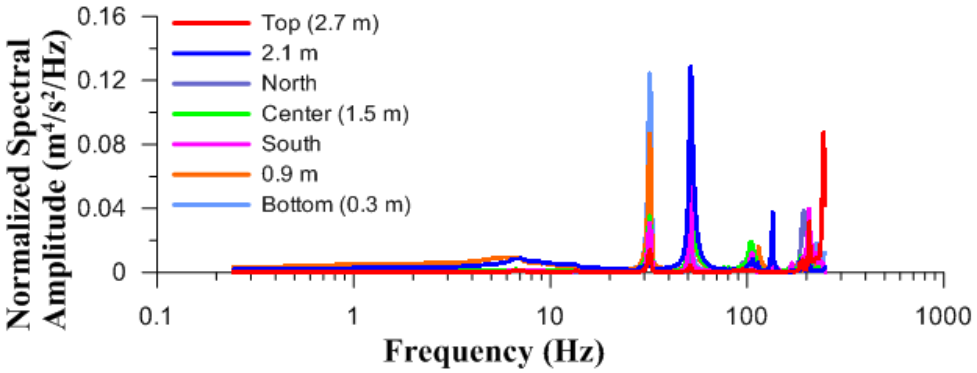

Figure B.26: PSD plot of the impact vibration test on Specimen IS1

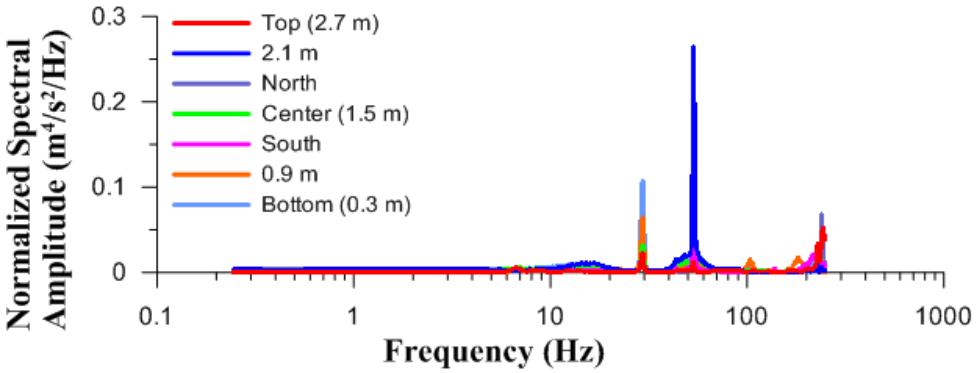

Figure B.27: PSD plot of the impact vibration test on Specimen IS2

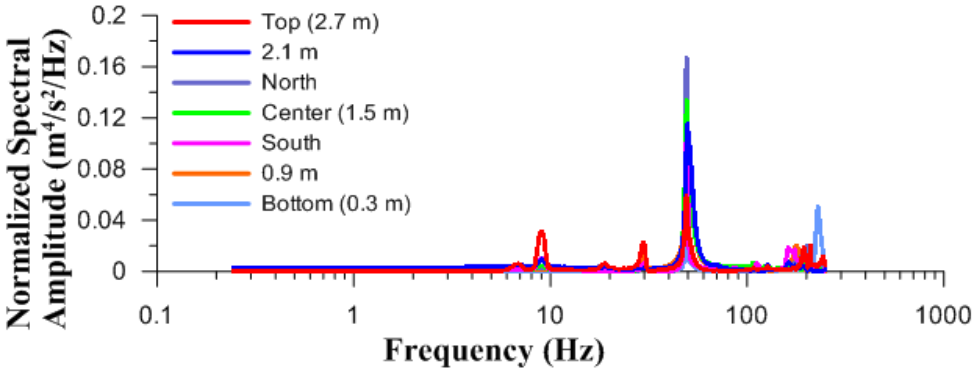

Figure B.28: PSD plot of the impact vibration test on Specimen IS3

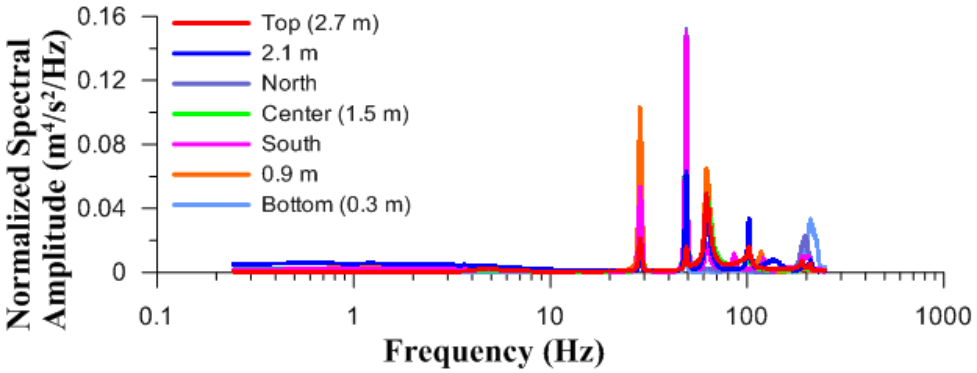

Figure B.29: PSD plot of the impact vibration test on Specimen IS4

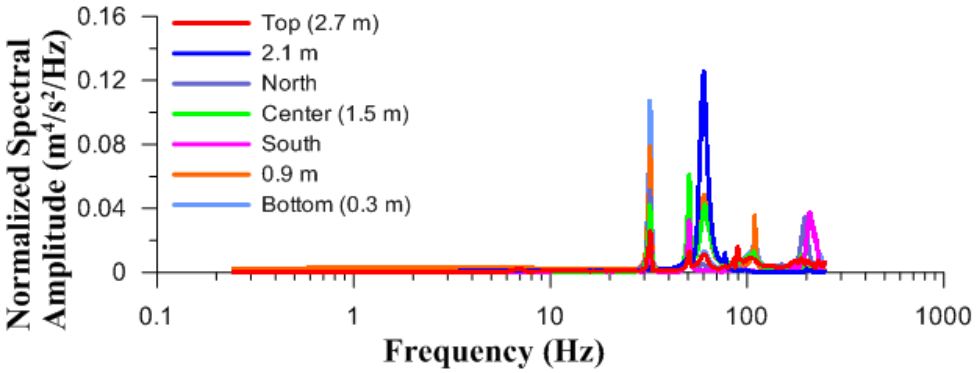

Figure B.30: PSD plot of the impact vibration test on Specimen IS5

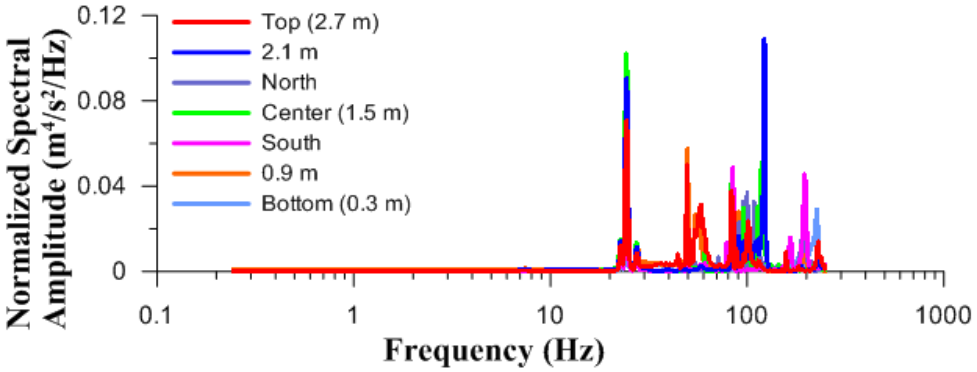

Figure B.31: PSD plot of the impact vibration test on Specimen RD1

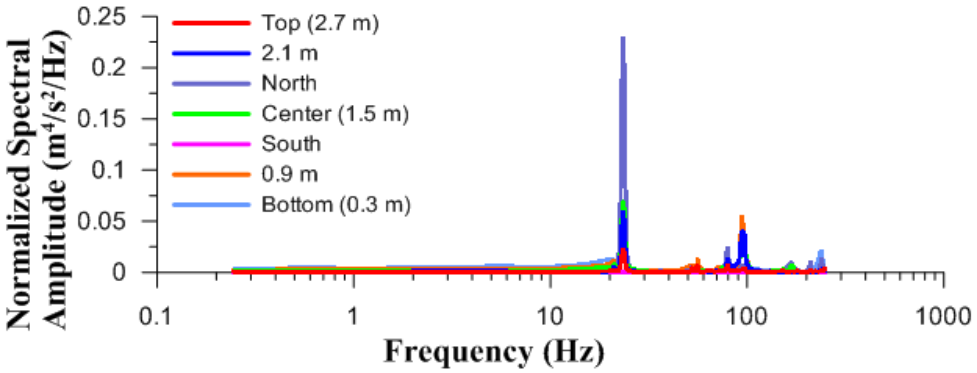

Figure B.32: PSD plot of the impact vibration test on Specimen RD2

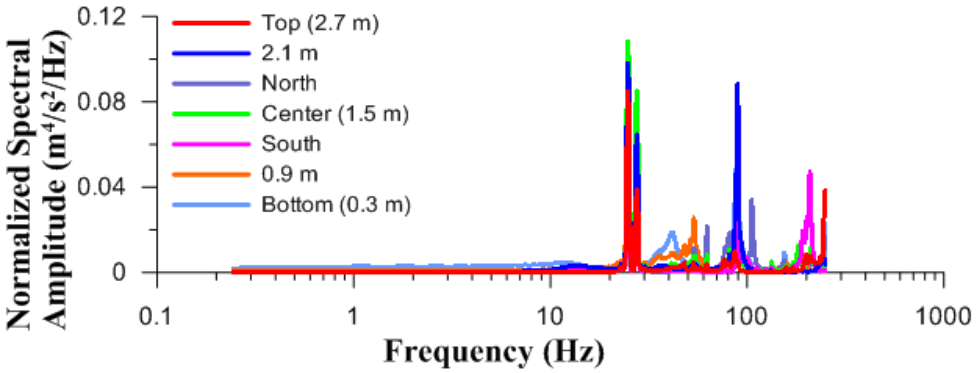

Figure B.33: PSD plot of the impact vibration test on Specimen RD3

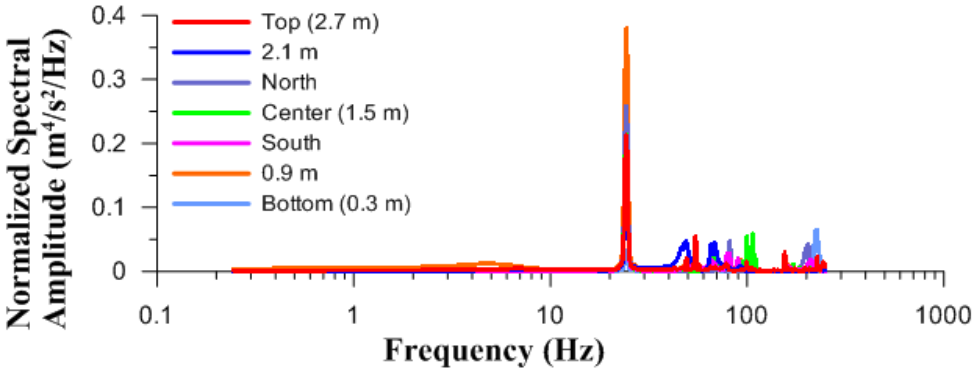

Figure B.34: PSD plot of the impact vibration test on Specimen RD4

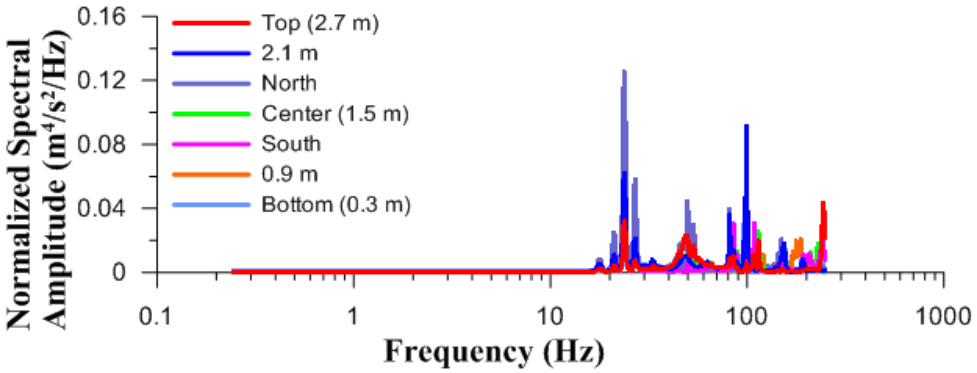

Figure B.35: PSD plot of the impact vibration test on Specimen RD5

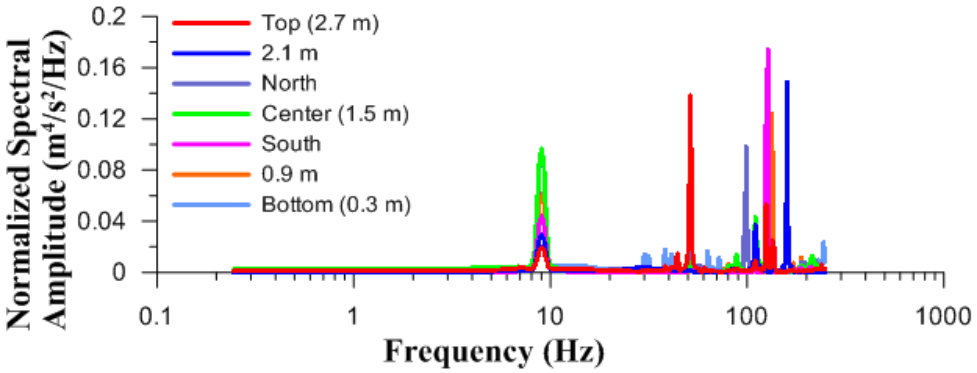

Figure B.36: PSD plot of the impact vibration test on Specimen RS1

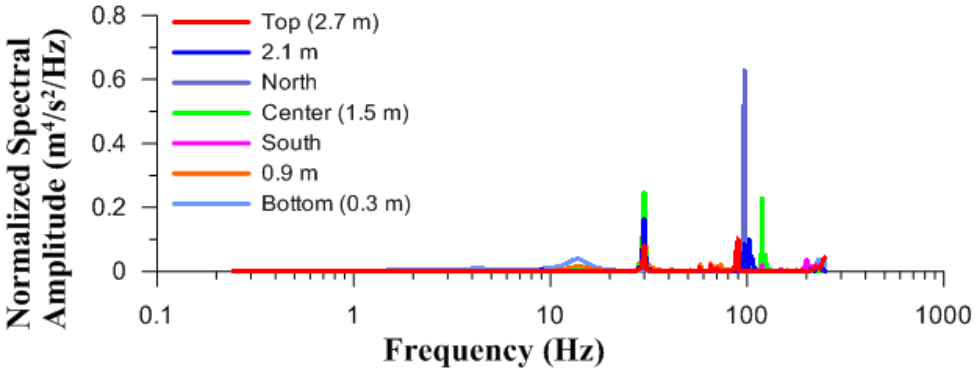

Figure B.37: PSD plot of the impact vibration test on Specimen RS2

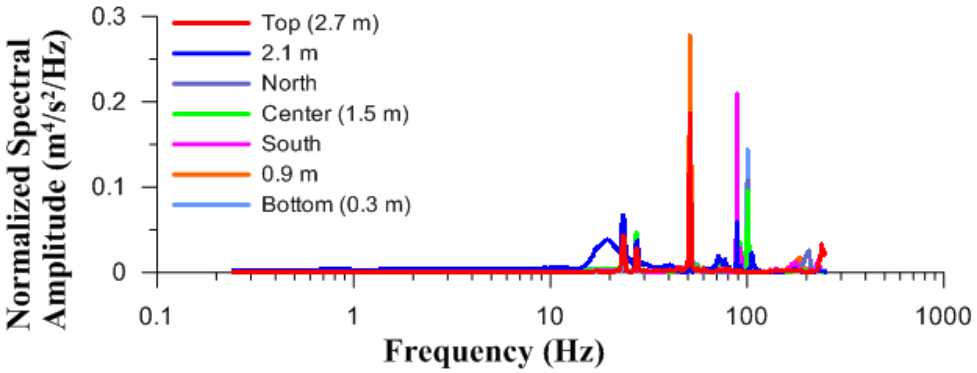

Figure B.38: PSD plot of the impact vibration test on Specimen RS3

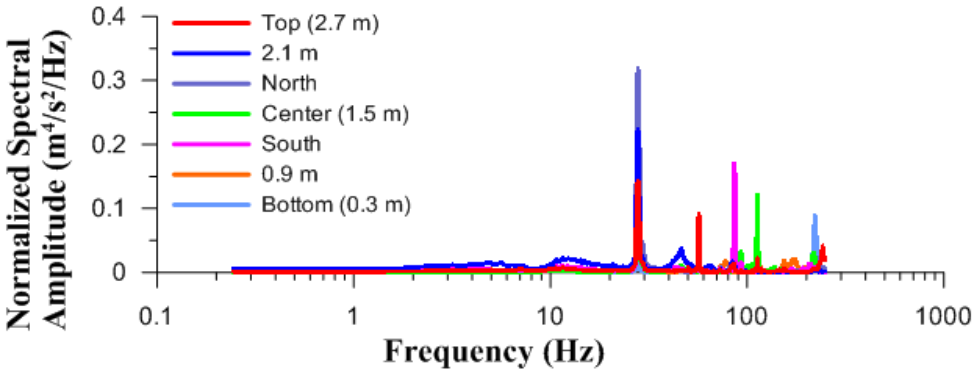

Figure B.39: PSD plot of the impact vibration test on Specimen RS4

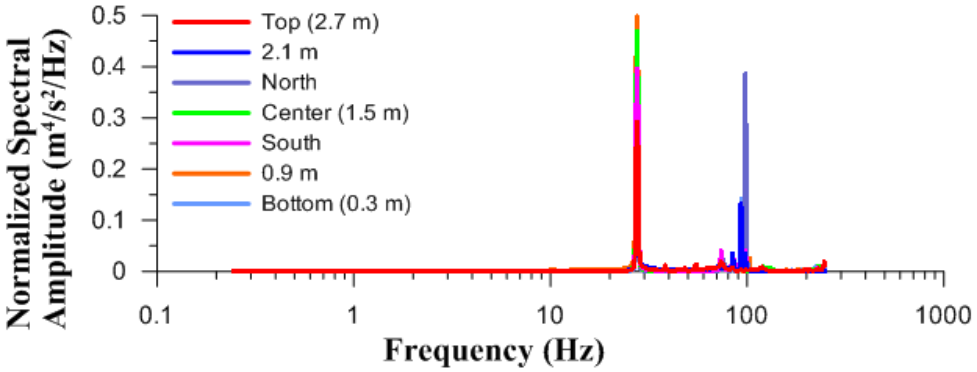

Figure B.40: PSD plot of the impact vibration test on Specimen RS5

Appendix C: PSD plot of Time Histories

This appendix contains the Power Spectral Density plots to determine the agreement between the set-point data and the theoretical energy distribution (CSA).

Figures C.1 to C.9 show the PSD plots for the trials of the first series, used on ID1 and RD1
Figures C.10 to C.20 show the PSD plots for the trials of the second series, used on ID2 and RD2
Figures C.21 to C.32 show the PSD plots for the trials of the third series, used on ID3 and RD3
Figures C.33 to C.42 show the PSD plots for the trials of the fourth series, used on ID4 and RD4
Figures C.43 to C.51 show the PSD plots for the trials of the fifth series, used on ID5 and RD5

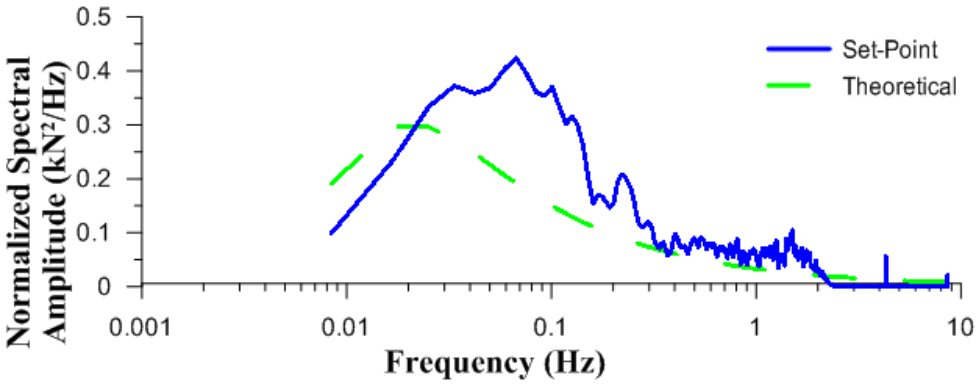

Figure C.1: PSD plot for the 14 m/s trial of dynamic test series 1

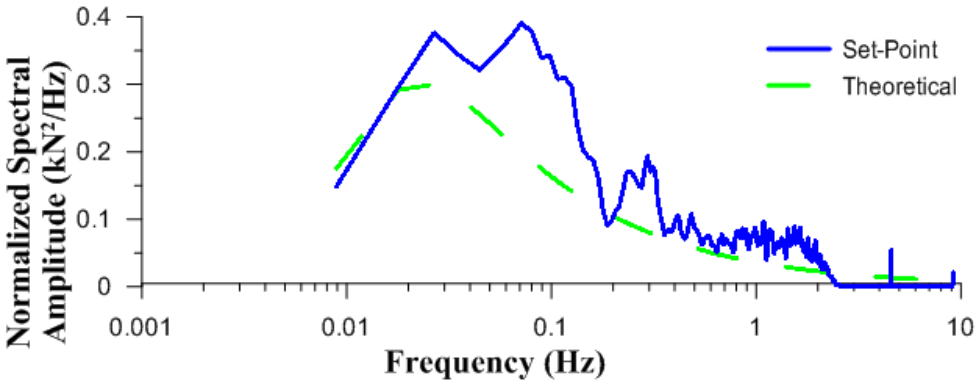

Figure C.2: PSD plot for the 16 m/s trial of dynamic test series 1

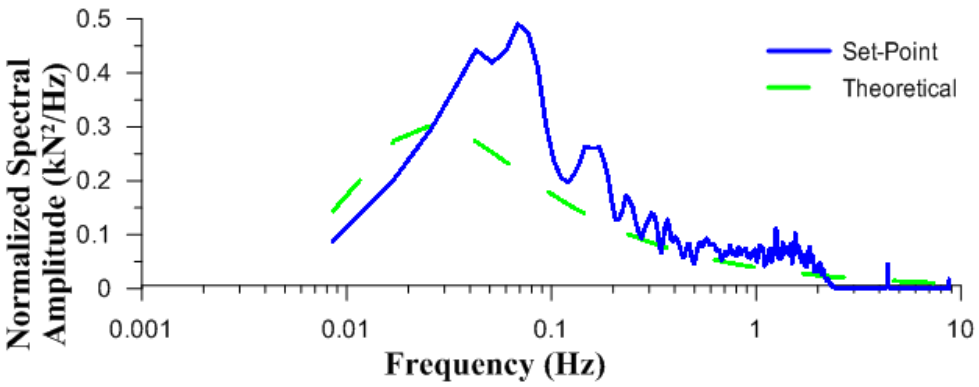

Figure C.3: PSD plot for the 18 m/s trial of dynamic test series 1

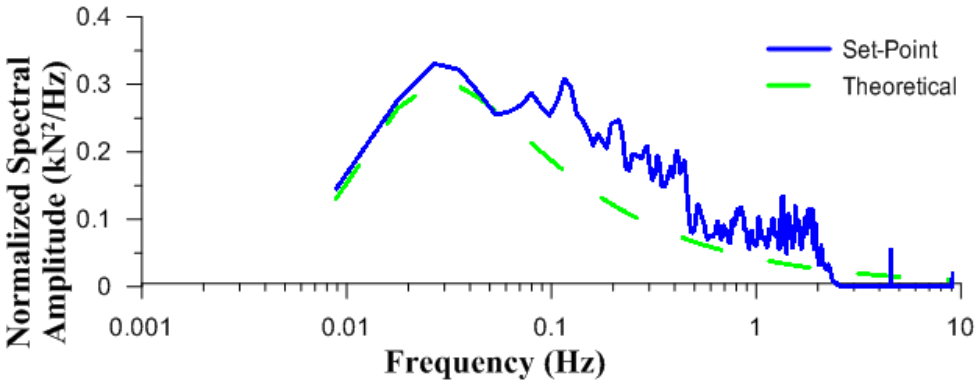

Figure C.4: PSD plot for the 20 m/s trial of dynamic test series 1

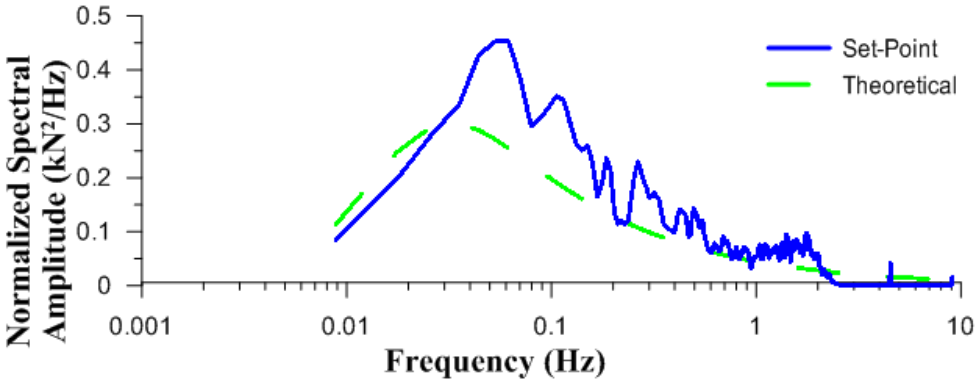

Figure C.5: PSD plot for the 22 m/s trial of dynamic test series 1

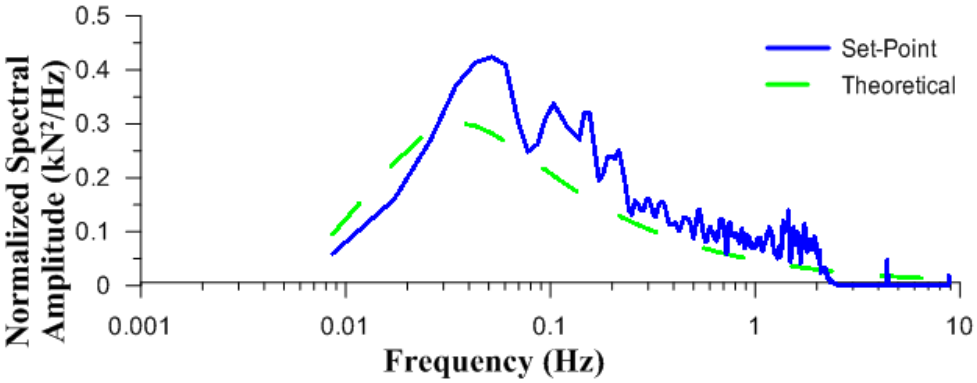

Figure C.6: PSD plot for the 24 m/s trial of dynamic test series 1

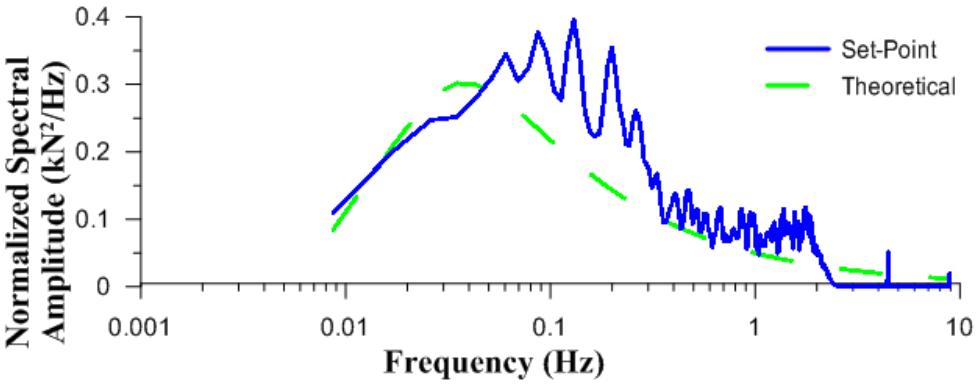

Figure C.7: PSD plot for the 26 m/s trial of dynamic test series 1

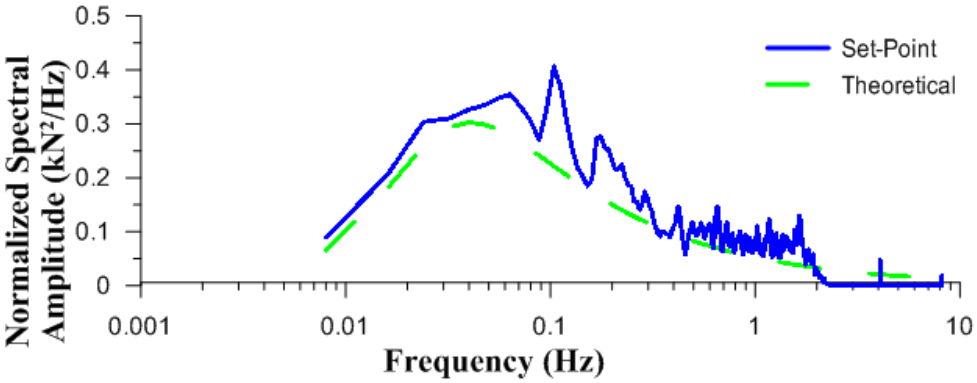

Figure C.8: PSD plot for the 28 m/s trial of dynamic test series 1

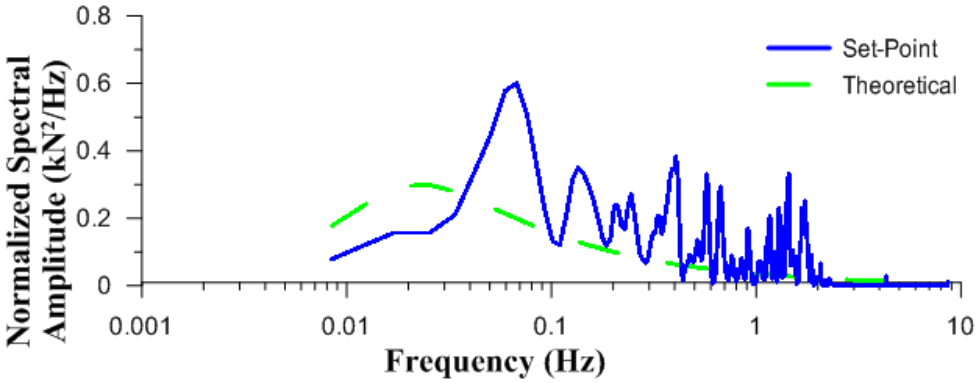

Figure C.9: PSD plot for the 30 m/s trial of dynamic test series 1

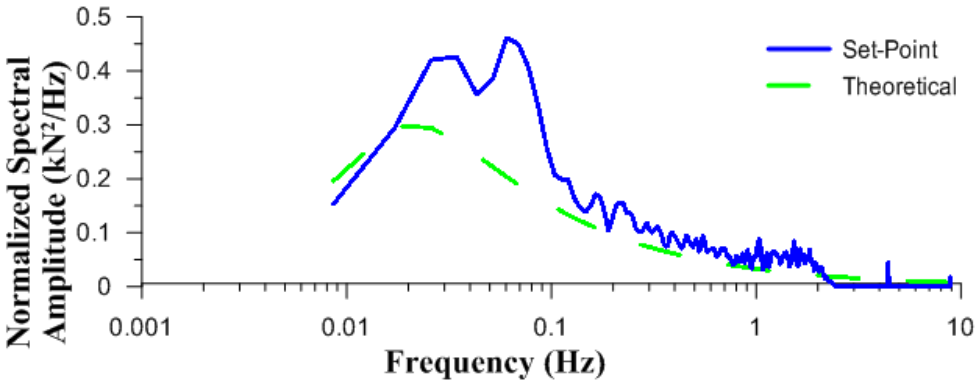

Figure C.10: PSD plot for the 14 m/s trial of dynamic test series 2

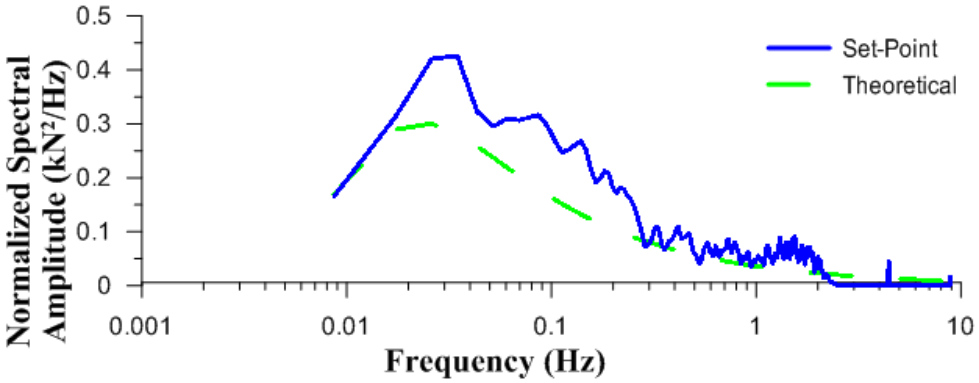

Figure C.11: PSD plot for the 16 m/s trial of dynamic test series 2

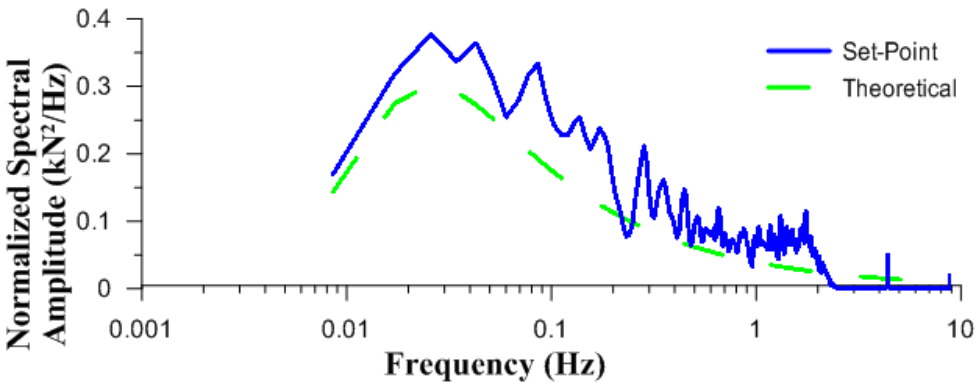

Figure C.12: PSD plot for the 18 m/s trial of dynamic test series 2

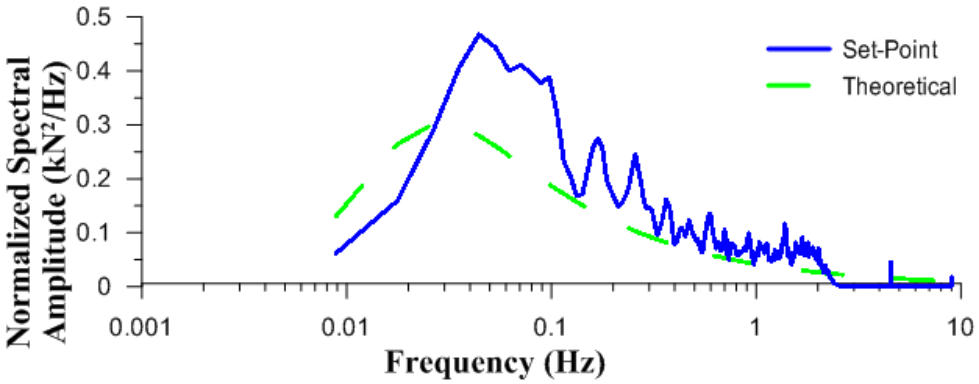

Figure C.13: PSD plot for the 20 m/s trial of dynamic test series 2

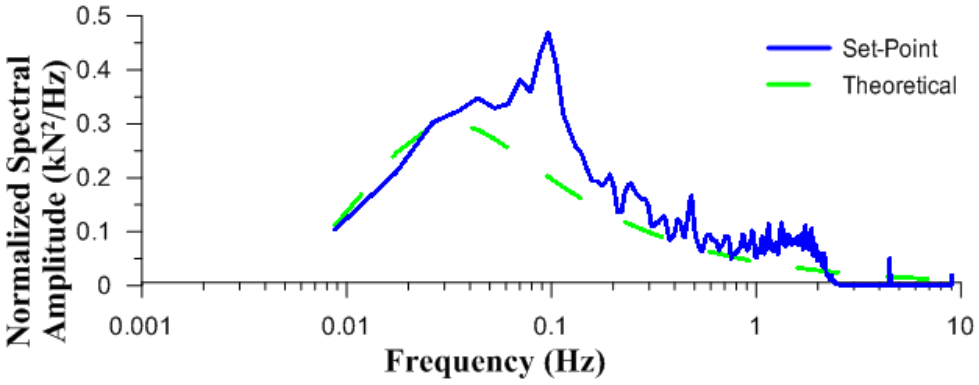

Figure C.14: PSD plot for the 22 m/s trial of dynamic test series 2

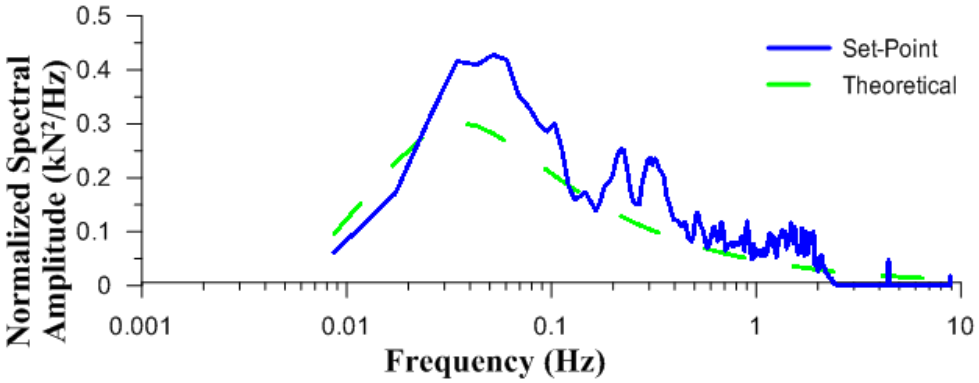

Figure C.15: PSD plot for the 24 m/s trial of dynamic test series 2

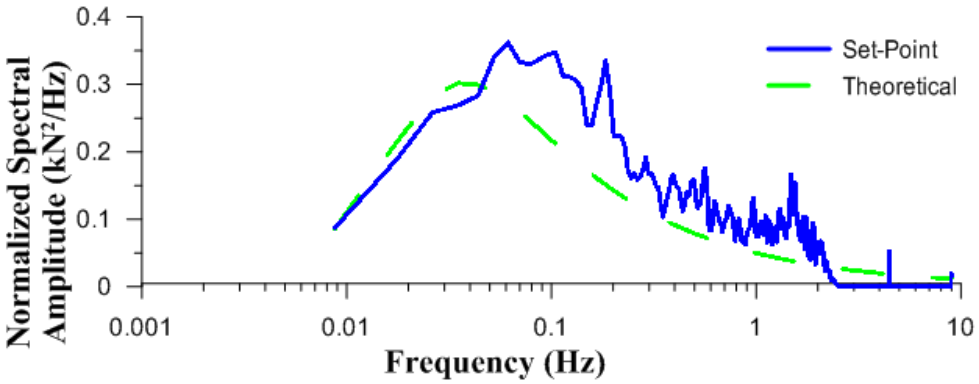

Figure C.16: PSD plot for the 26 m/s trial of dynamic test series 2

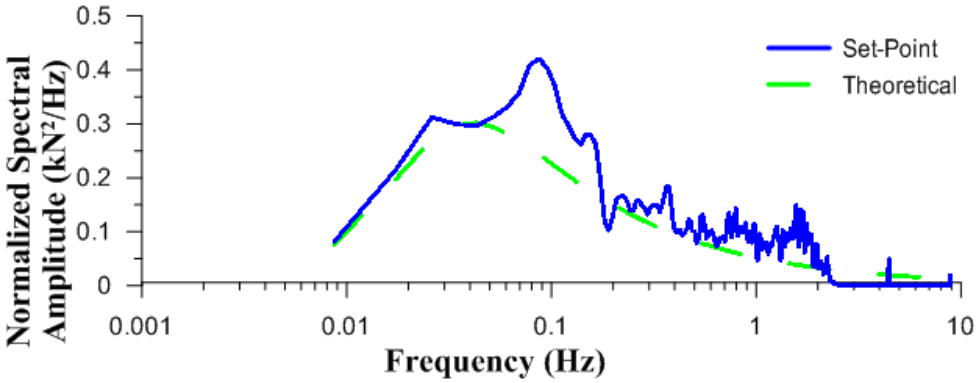

Figure C.17: PSD plot for the 28 m/s trial of dynamic test series 2

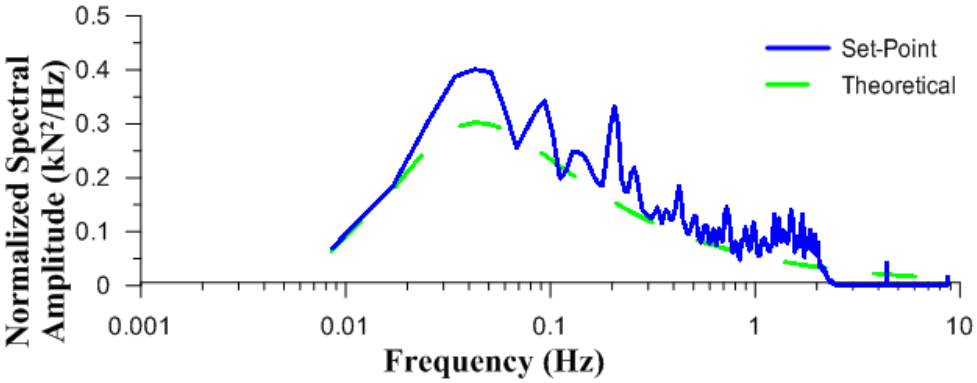

Figure C.18: PSD plot for the 30 m/s trial of dynamic test series 2

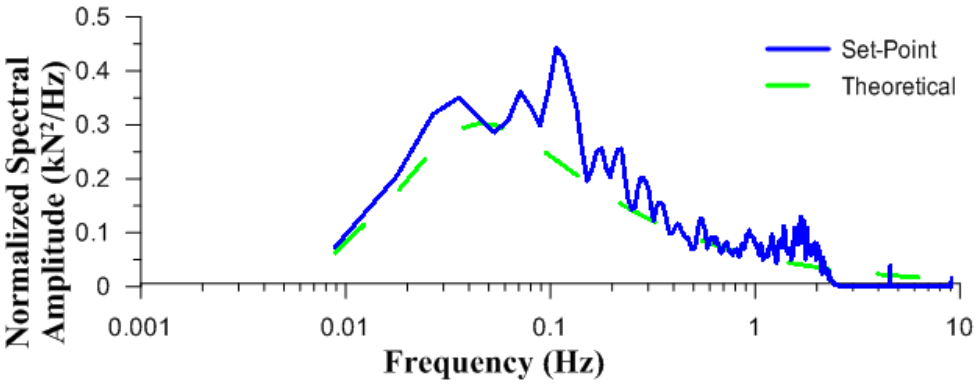

Figure C.19: PSD plot for the 32 m/s trial of dynamic test series 2

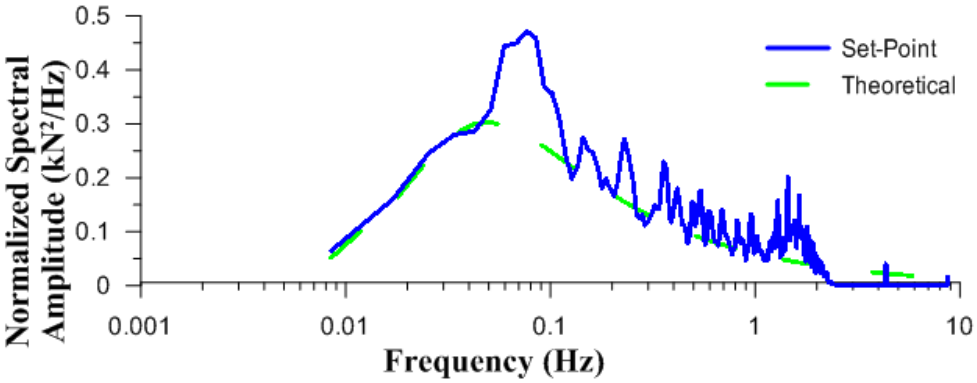

Figure C.20: PSD plot for the 34 m/s trial of dynamic test series 2

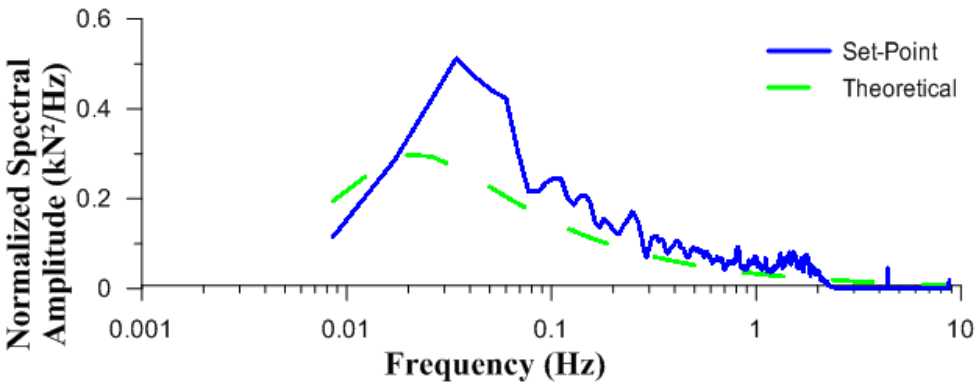

Figure C.21: PSD plot for the 14 m/s trial of dynamic test series 3

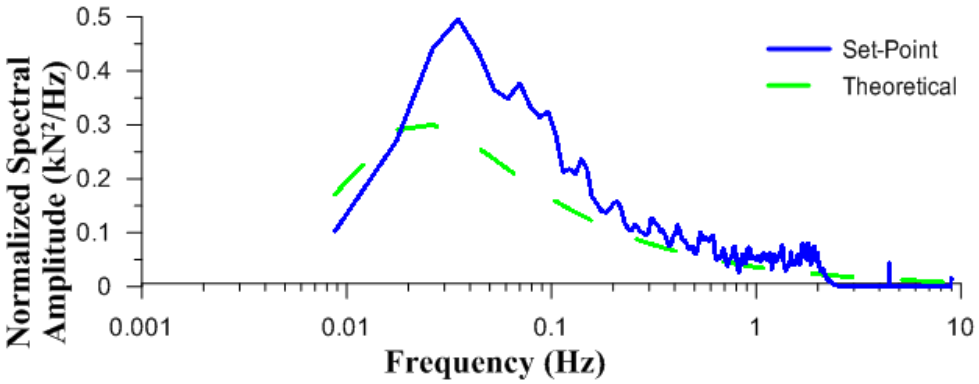

Figure C.22: PSD plot for the 16 m/s trial of dynamic test series 3

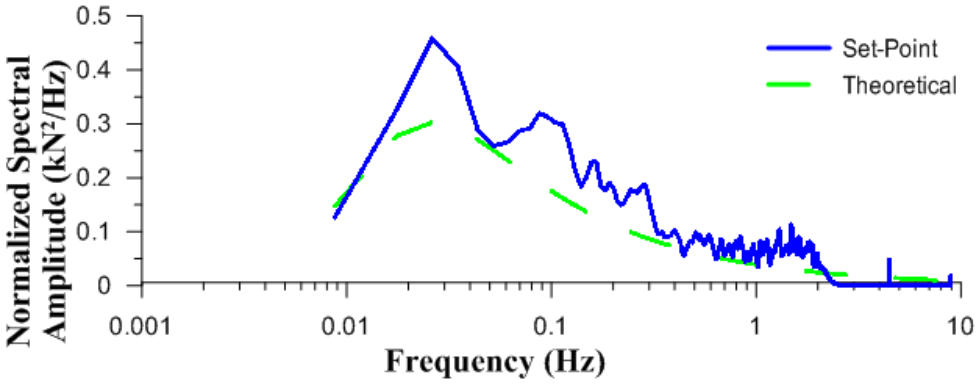

Figure C.23: PSD plot for the 18 m/s trial of dynamic test series 3

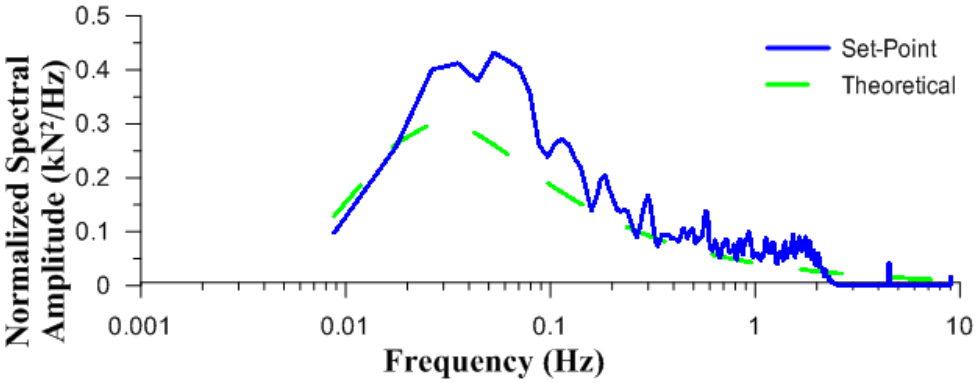

Figure C.24: PSD plot for the 20 m/s trial of dynamic test series 3

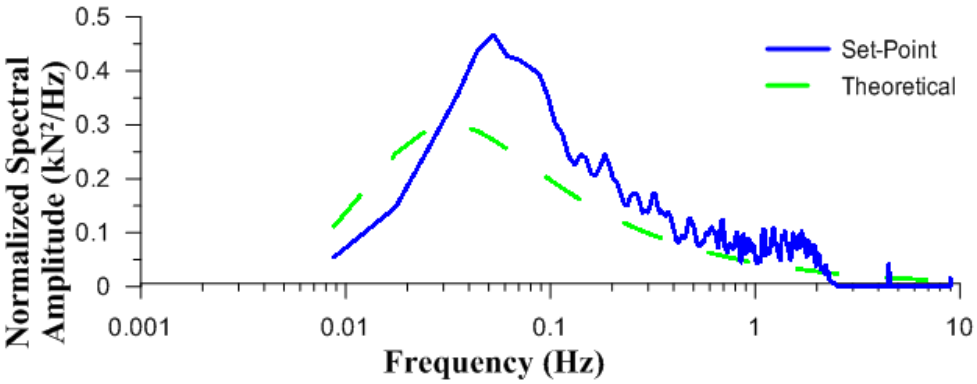

Figure C.25: PSD plot for the 22 m/s trial of dynamic test series 3

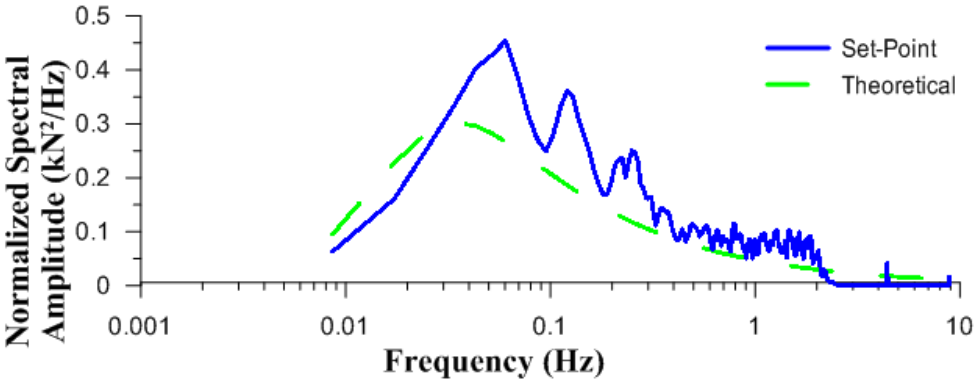

Figure C.26: PSD plot for the 24 m/s trial of dynamic test series 3

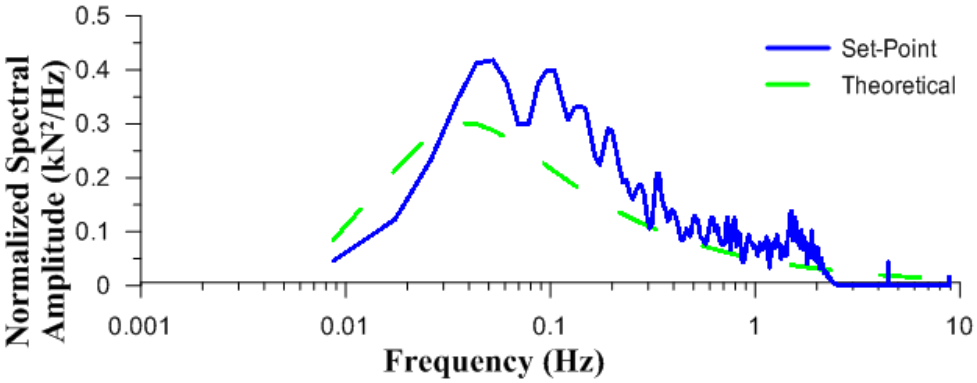

Figure C.27: PSD plot for the 26 m/s trial of dynamic test series 3

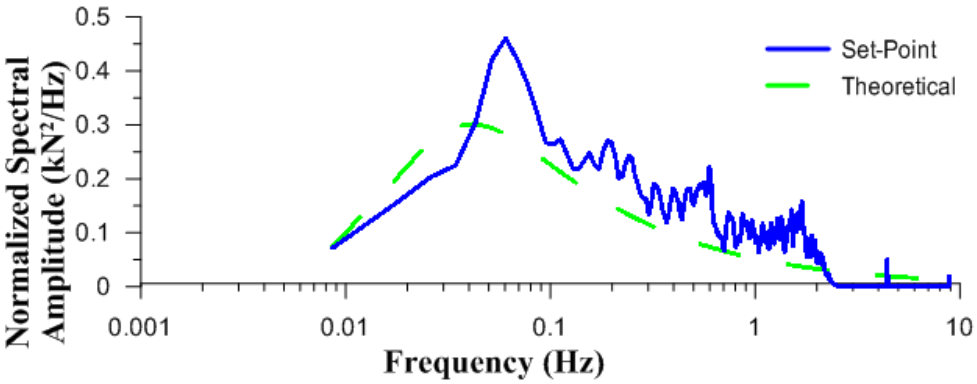

Figure C.28: PSD plot for the 28 m/s trial of dynamic test series 3

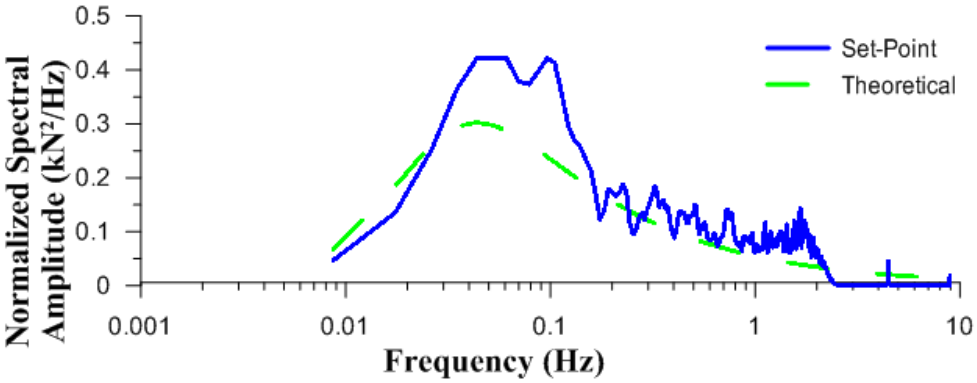

Figure C.29: PSD plot for the 30 m/s trial of dynamic test series 3

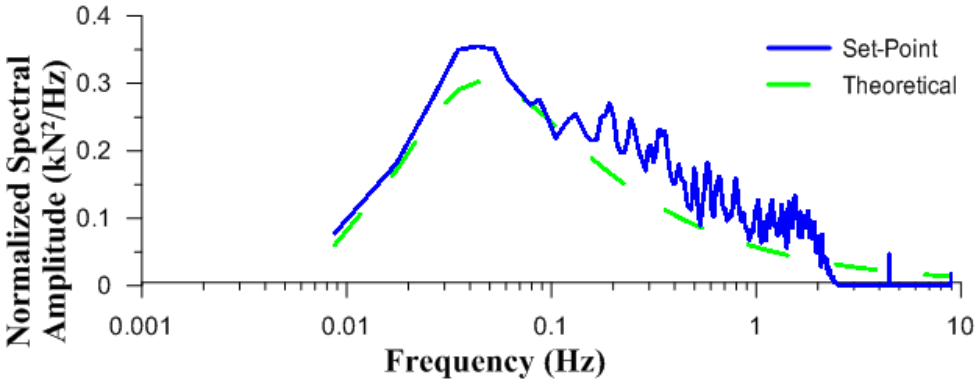

Figure C.30: PSD plot for the 32 m/s trial of dynamic test series 3

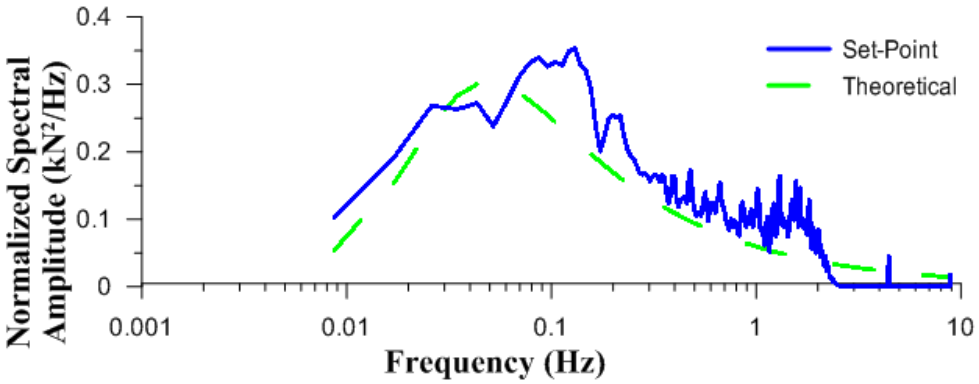

Figure C.31: PSD plot for the 34 m/s trial of dynamic test series 3

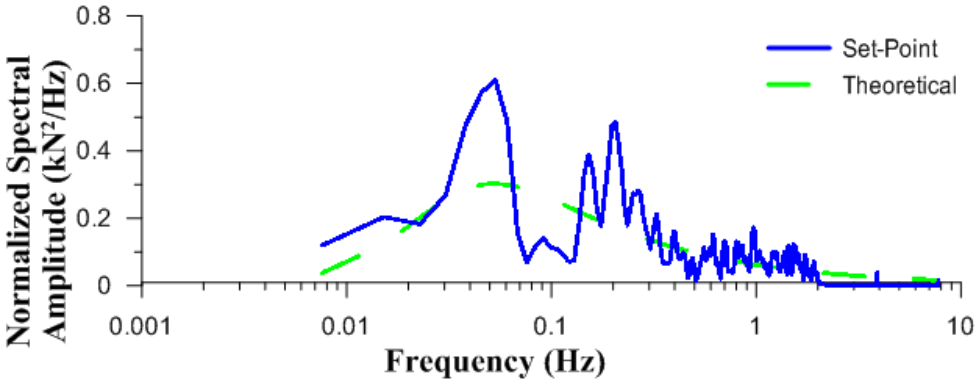

Figure C.32: PSD plot for the 36 m/s trial of dynamic test series 3

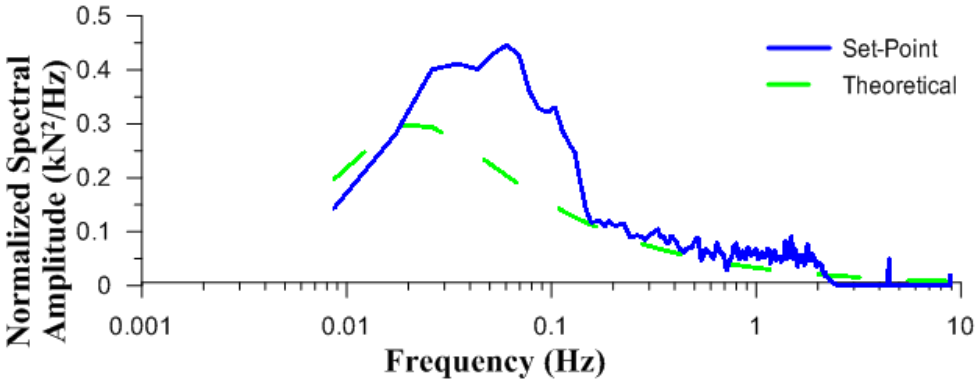

Figure C.33: PSD plot for the 14 m/s trial of dynamic test series 4

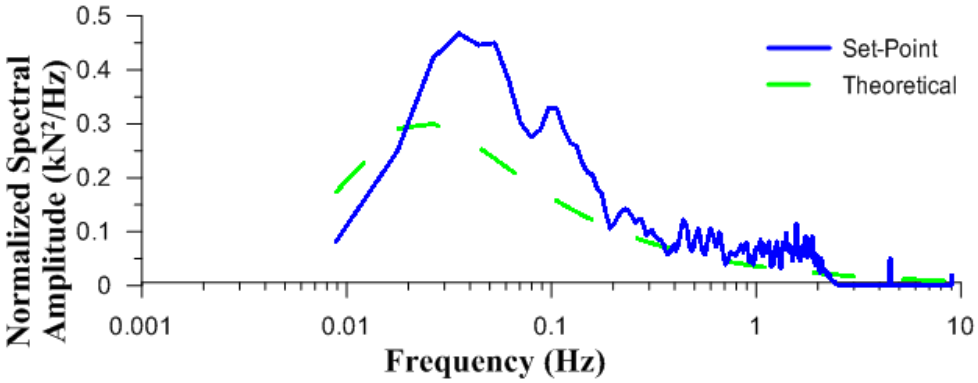

Figure C.34: PSD plot for the 16 m/s trial of dynamic test series 4

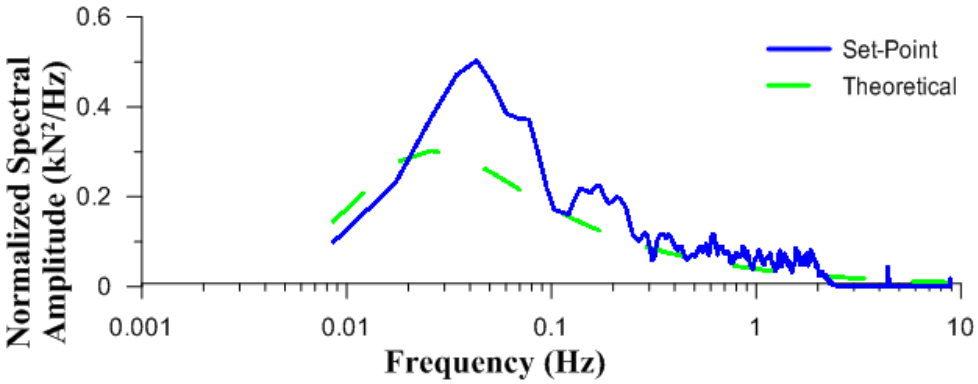

Figure C.35: PSD plot for the 18 m/s trial of dynamic test series 4

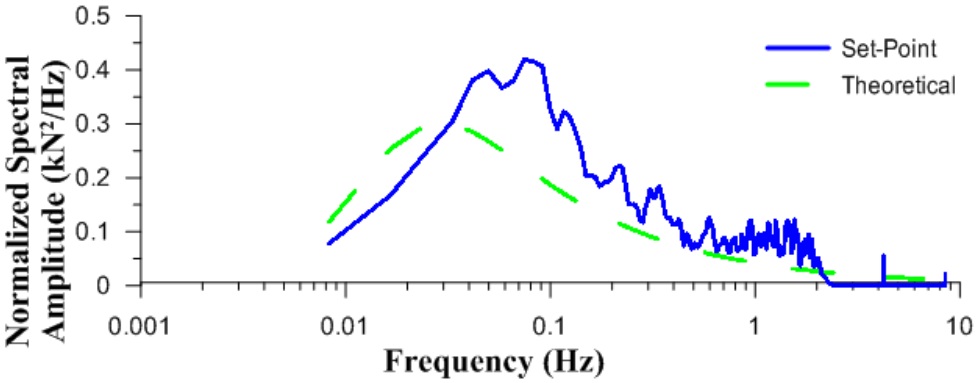

Figure C.36: PSD plot for the 20 m/s trial of dynamic test series 4

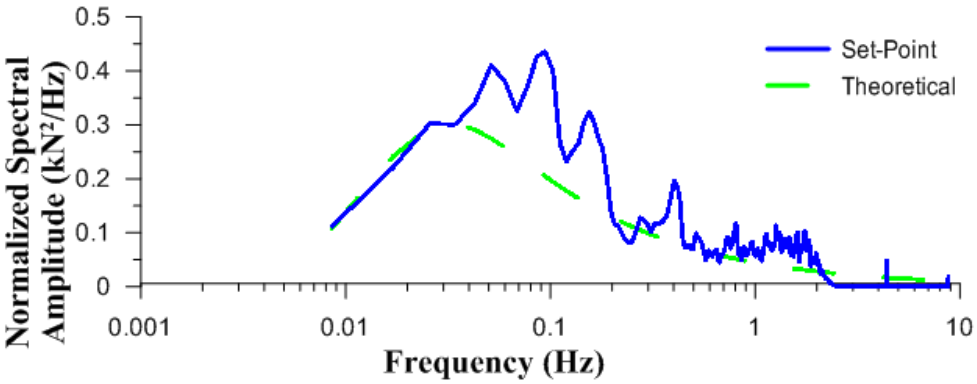

Figure C.37: PSD plot for the 22 m/s trial of dynamic test series 4

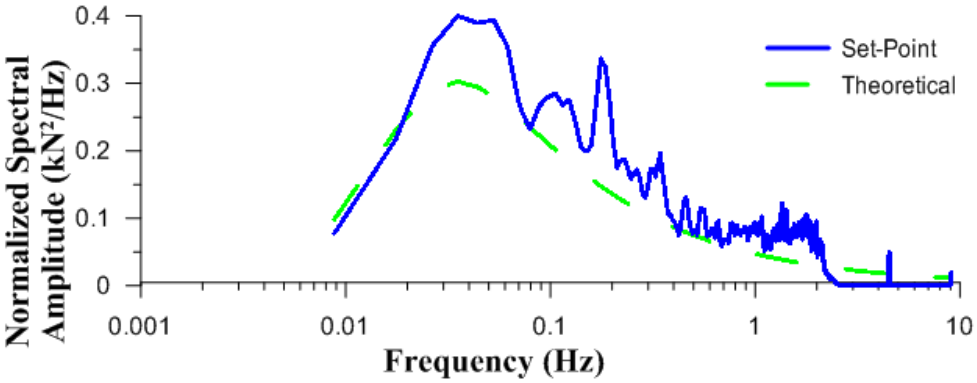

Figure C.38: PSD plot for the 24 m/s trial of dynamic test series 4

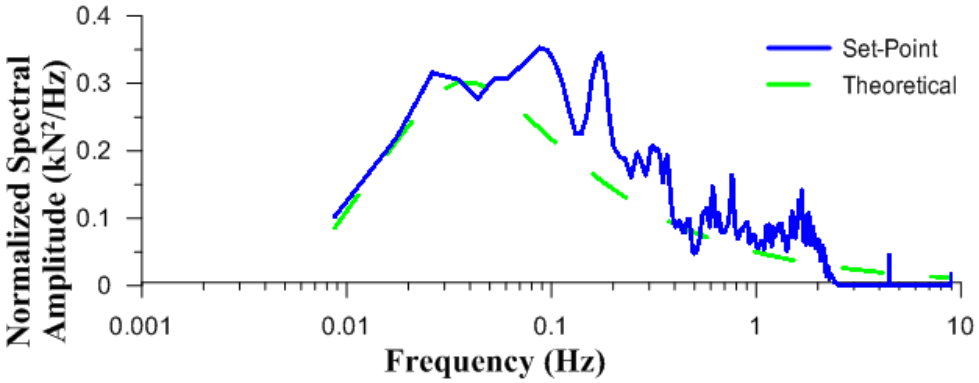

Figure C.39: PSD plot for the 26 m/s trial of dynamic test series 4

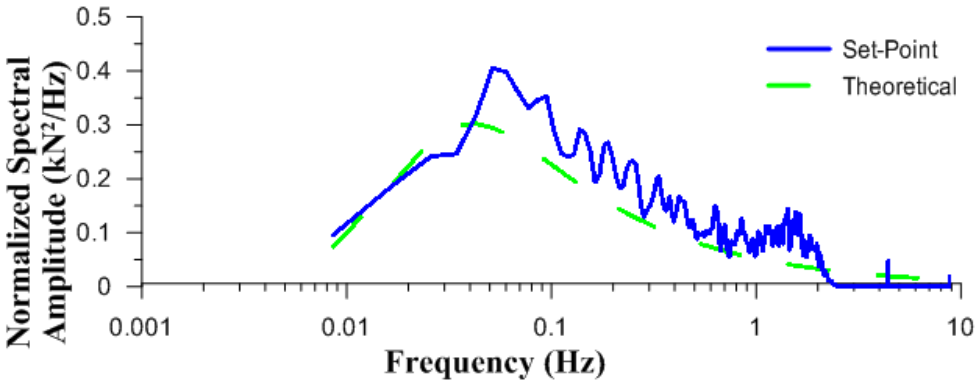

Figure C.40: PSD plot for the 28 m/s trial of dynamic test series 4

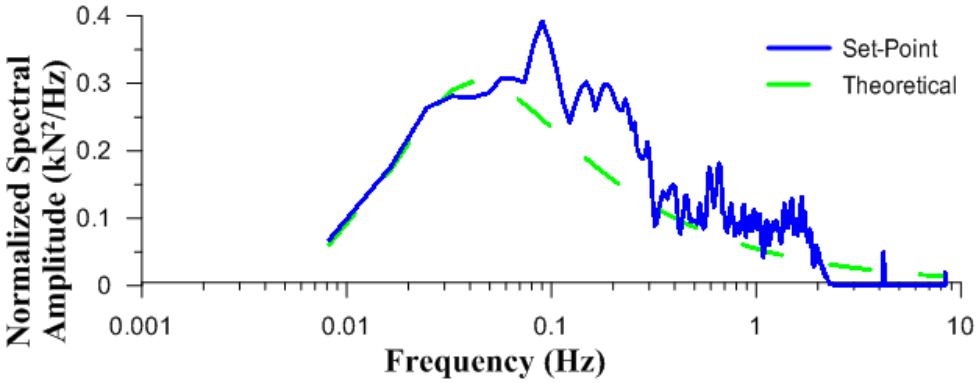

Figure C.41: PSD plot for the 30 m/s trial of dynamic test series 4

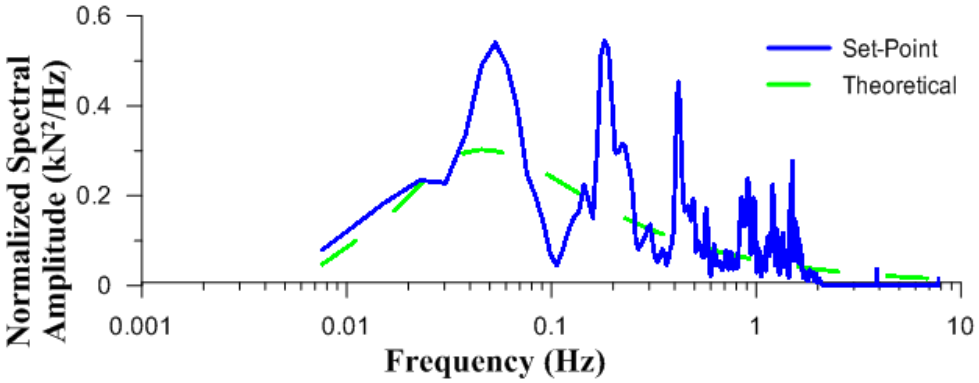

Figure C.42: PSD plot for the 32 m/s trial of dynamic test series 4

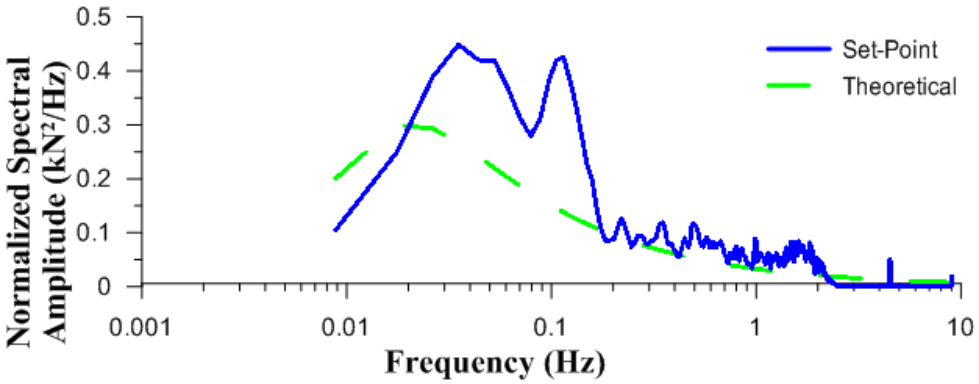

Figure C.43: PSD plot for the 14 m/s trial of dynamic test series 5

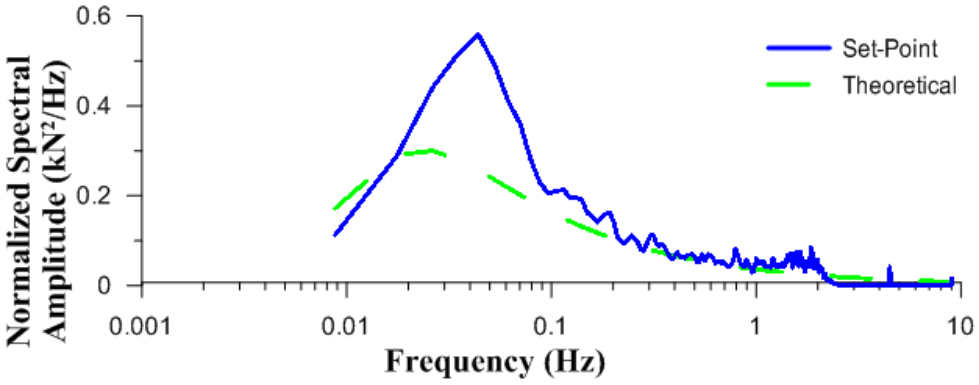

Figure C.44: PSD plot for the 16 m/s trial of dynamic test series 5

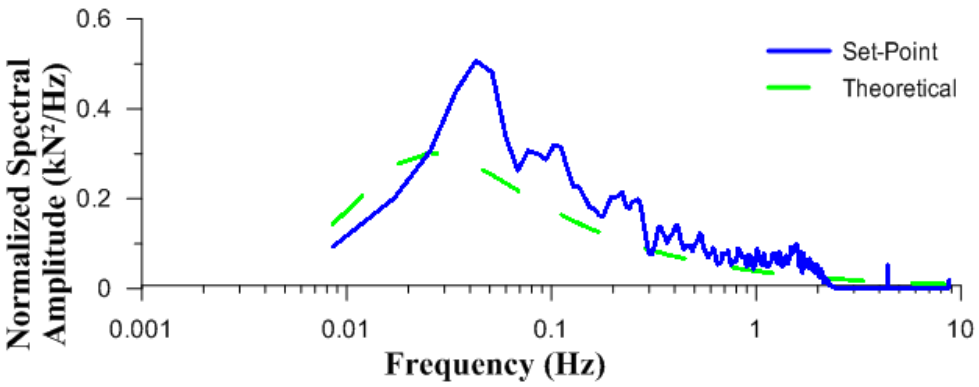

Figure C.45: PSD plot for the 18 m/s trial of dynamic test series 5

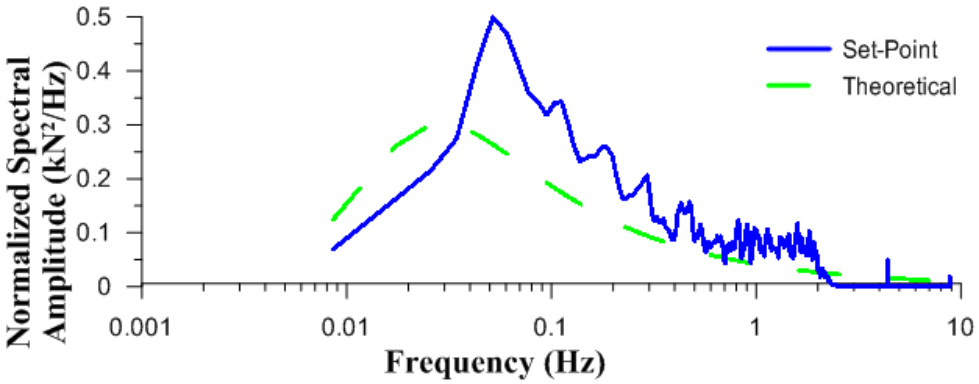

Figure C.46: PSD plot for the 20 m/s trial of dynamic test series 5

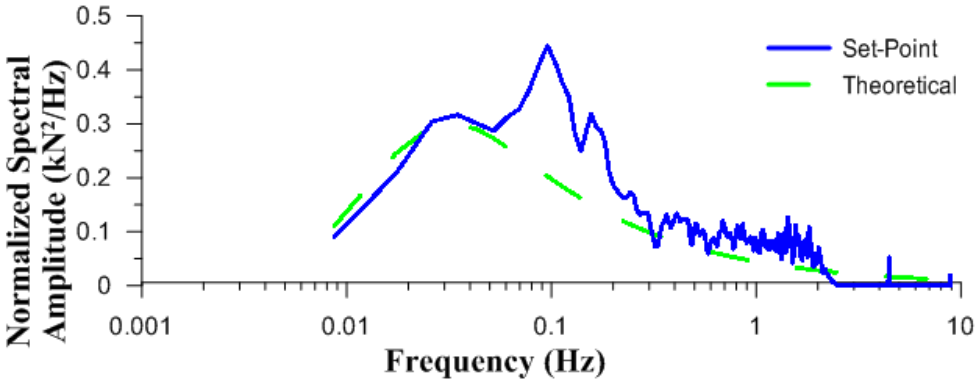

Figure C.47: PSD plot for the 22 m/s trial of dynamic test series 5

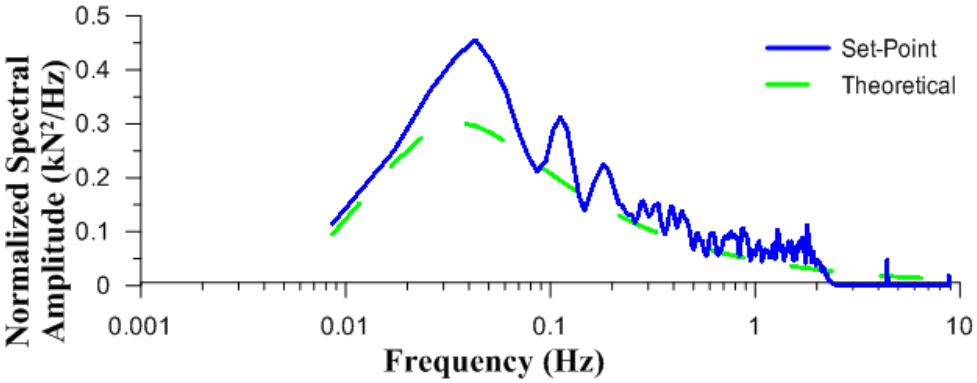

Figure C.48: PSD plot for the 24 m/s trial of dynamic test series 5

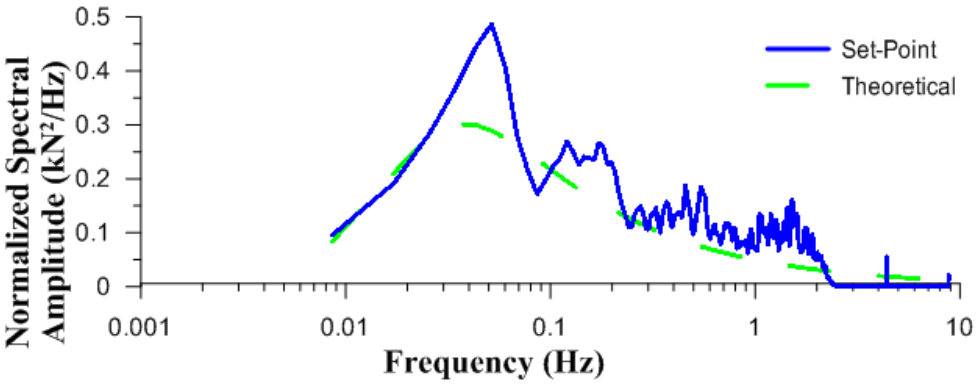

Figure C.49: PSD plot for the 26 m/s trial of dynamic test series 5

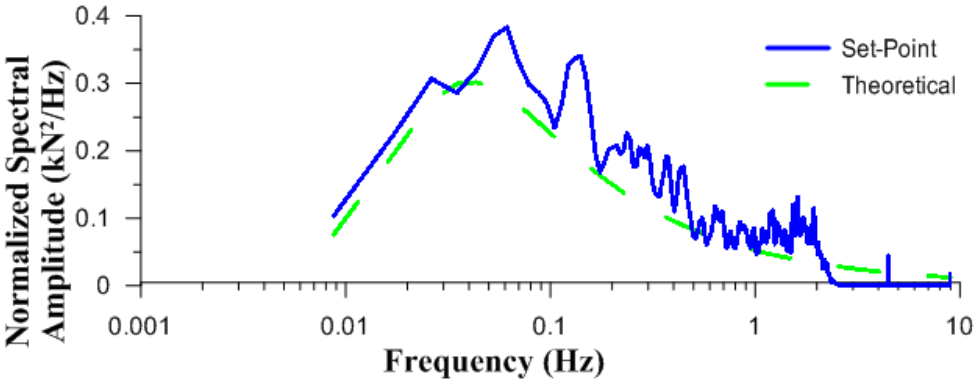

Figure C.50: PSD plot for the 28 m/s trial of dynamic test series 5

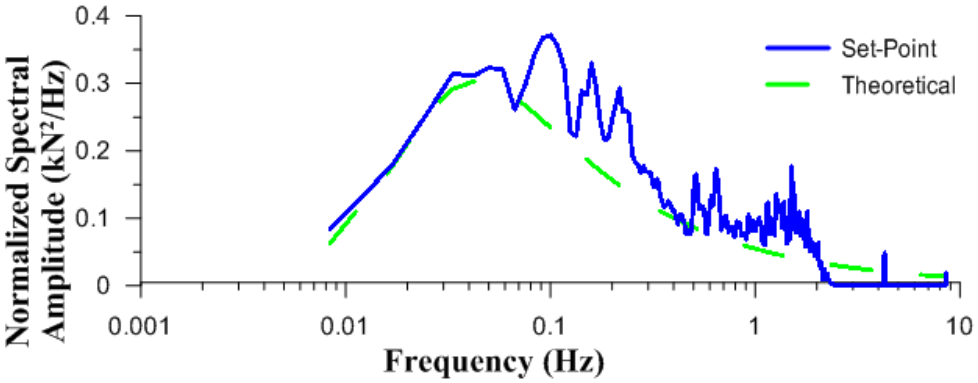

Figure C.51: PSD plot for the 30 m/s trial of dynamic test series 5

Appendix D: Load-Deflection

This appendix presents the load-deflection behaviour of the masonry wall specimens that were loaded statically.

Figure D.1 to Figure D.5 present the load-deflection plots for the ideally-pinned walls.

Figure D.6 to Figure D.13 present the load-deflection plots for the realistically-pinned walls.

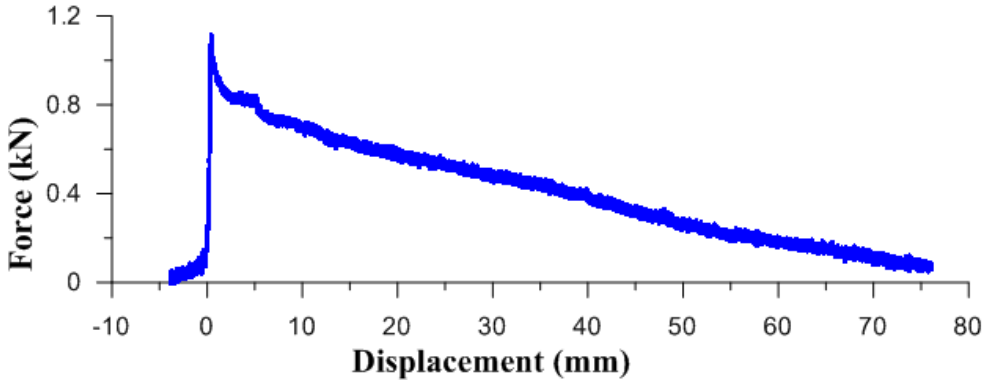

Figure D.1: Load-Displacement plot for Specimen IS1

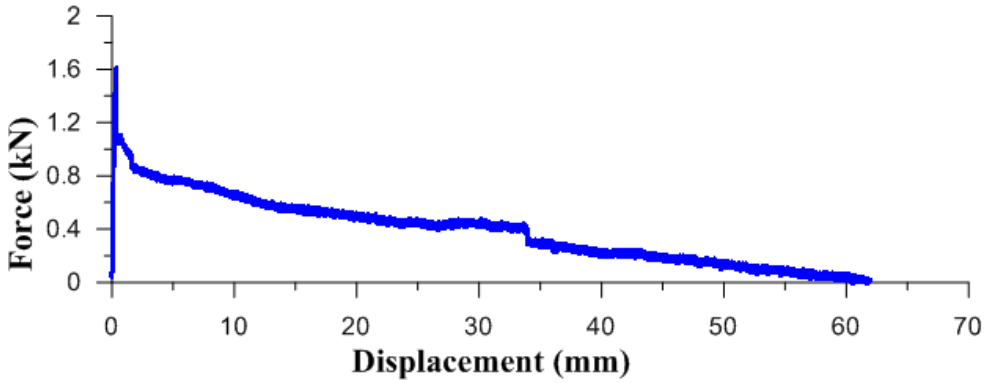

Figure D.2: Load-Displacement plot for Specimen IS2

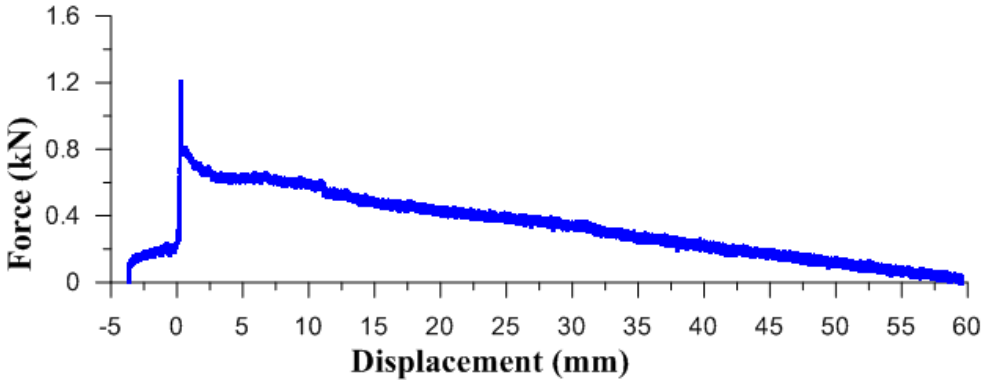

Figure D.3: Load-Displacement plot for Specimen IS3

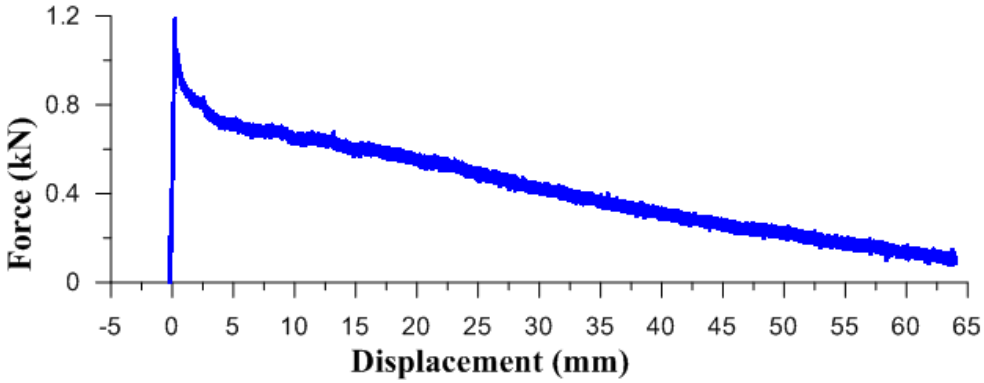

Figure D.4: Load-Displacement plot for Specimen IS4

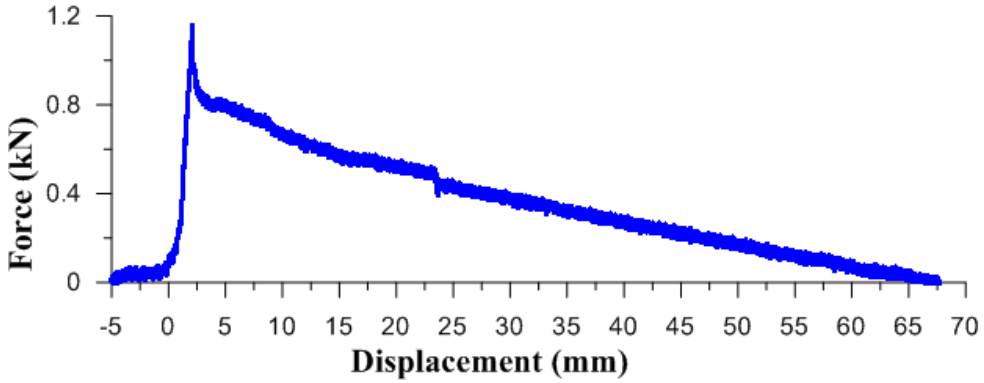

Figure D.5: Load-Displacement plot for Specimen IS5

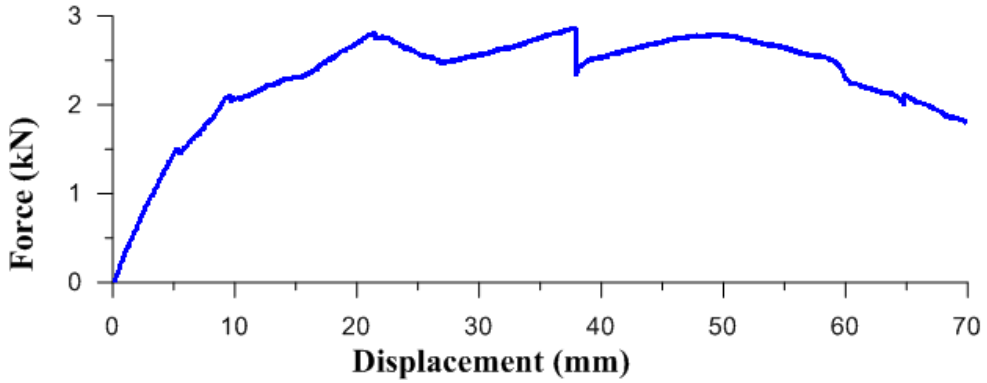

Figure D.6: Load-Displacement plot for Specimen RS1

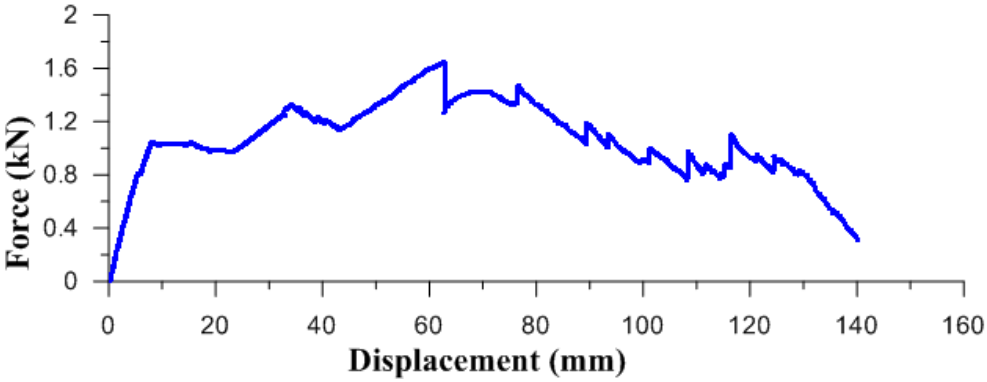

Figure D.7: Load-Displacement plot for Specimen RS1 (Resilience test)

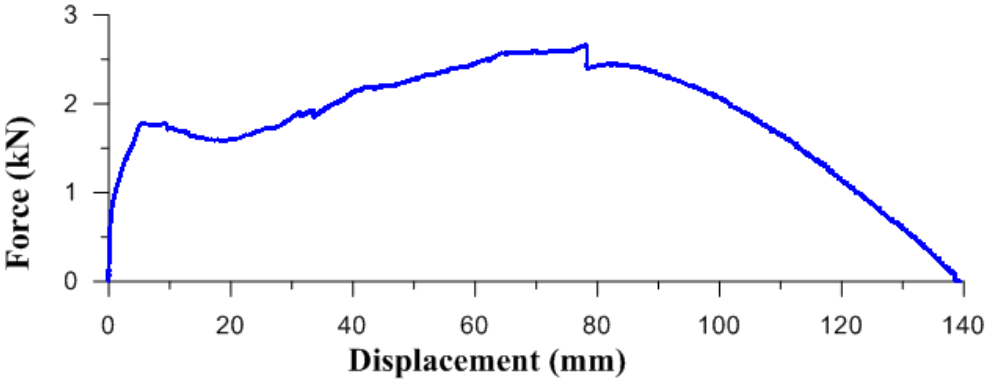

Figure D.8: Load-Displacement plot for Specimen RS2

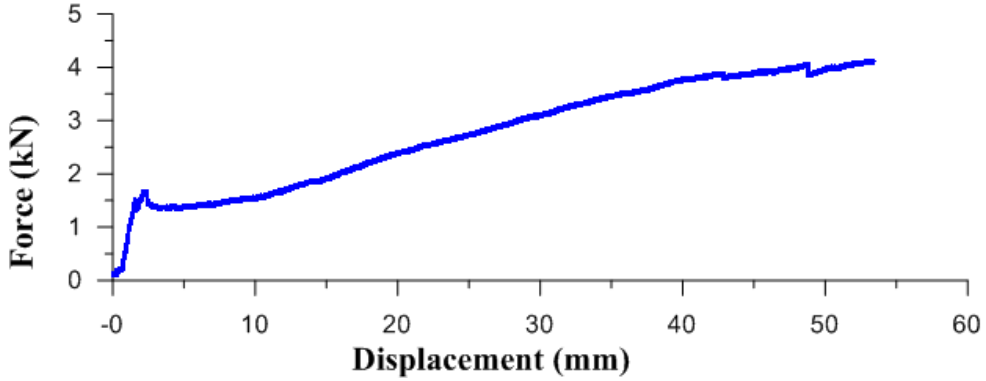

Figure D.9: Load-Displacement plot for Specimen RS3

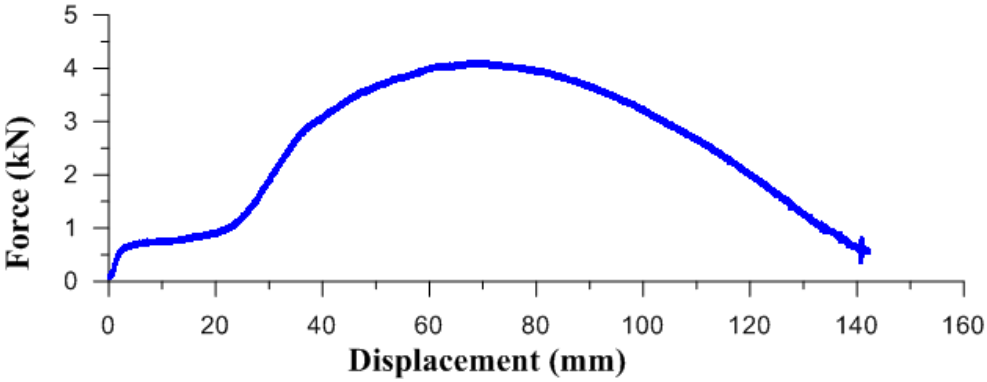

Figure D.10: Load-Displacement plot for Specimen RS3 (Resilience test 1)

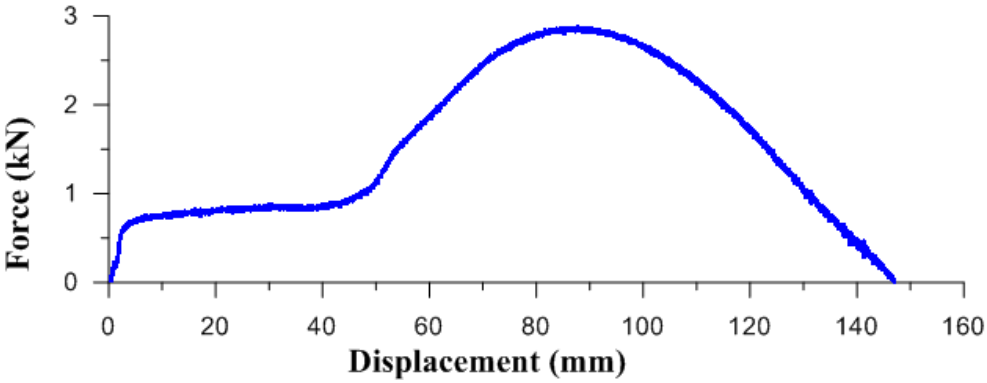

Figure D.11: Load-Displacement plot for Specimen RS3 (Resilience test 2)

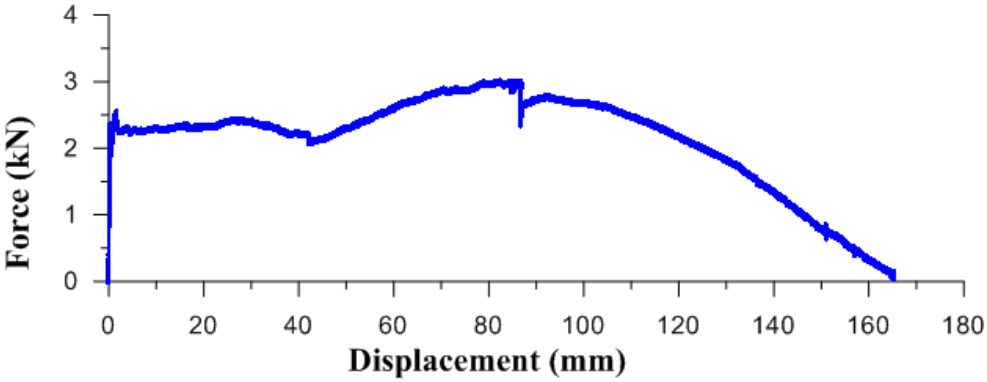

Figure D.12: Load-Displacement plot for Specimen RS4

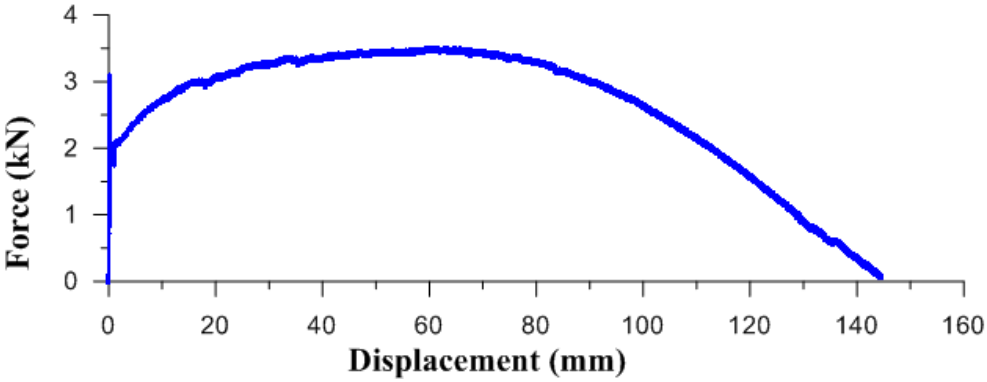

Figure D.13: Load-Displacement plot for Specimen RS5

Appendix E: Displacement versus Displacement plots

This appendix presents the displacement behaviour of the masonry wall specimens that were loaded statically. Displacement plots of the horizontal and vertical center lines are presented. For the quasi-statically loaded walls, the wall displacements are plotted against the displacements of the load actuator. While the displacement plots for the dynamically loaded walls are plotted against time. The displacement plots are shown until the LVDTs were removed from the walls.

Figure E.1 to Figure E.5 present the Horizontal center-line plots for the ideally-pinned walls.
Figure E.6 to Figure E.10 present the Horizontal center-line plots for the realistically-pinned walls.
Figure E.11 to Figure E.15 present the Vertical center-line plot for the ideally-pinned walls.
Figure E.16 to Figure E.20 present the Vertical center-line plots for the realistically-pinned walls.

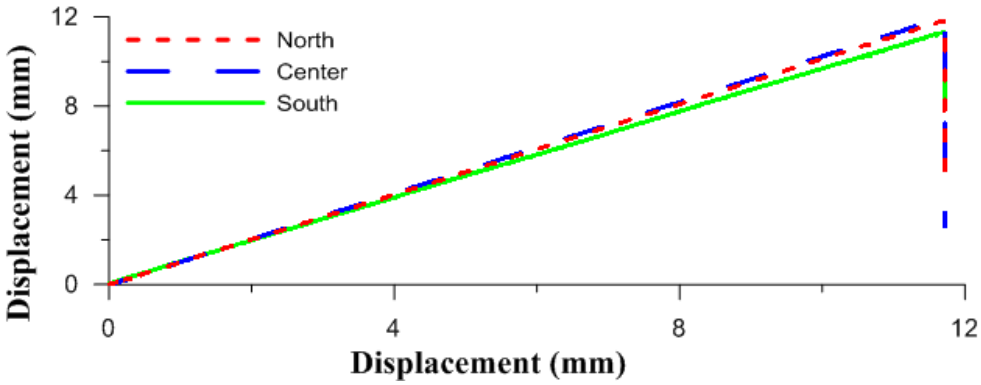

Figure E.1: Horizontal Center-line Displacement plot for Specimen IS1

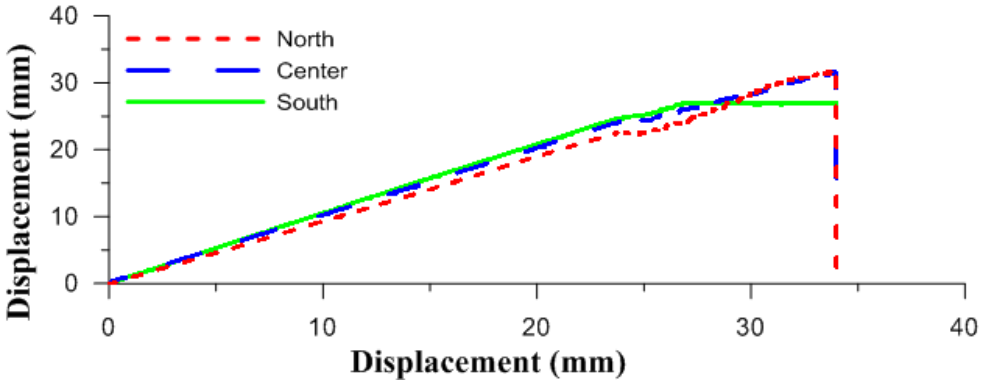

Figure E.2: Horizontal Center-line Displacement plot for Specimen IS2

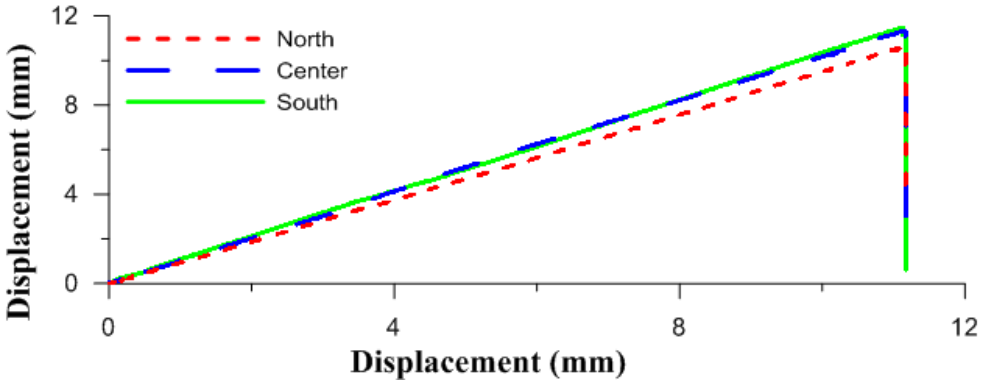

Figure E.3: Horizontal Center-line Displacement plot for Specimen IS3

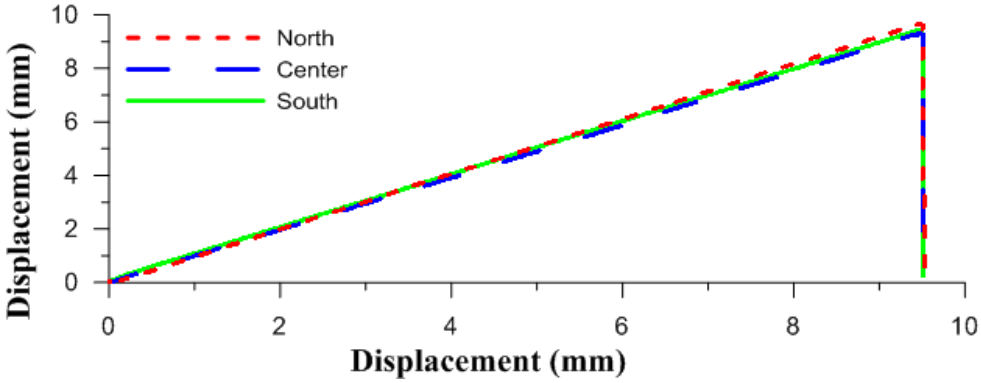

Figure E.4: Horizontal Center-line Displacement plot for Specimen IS4

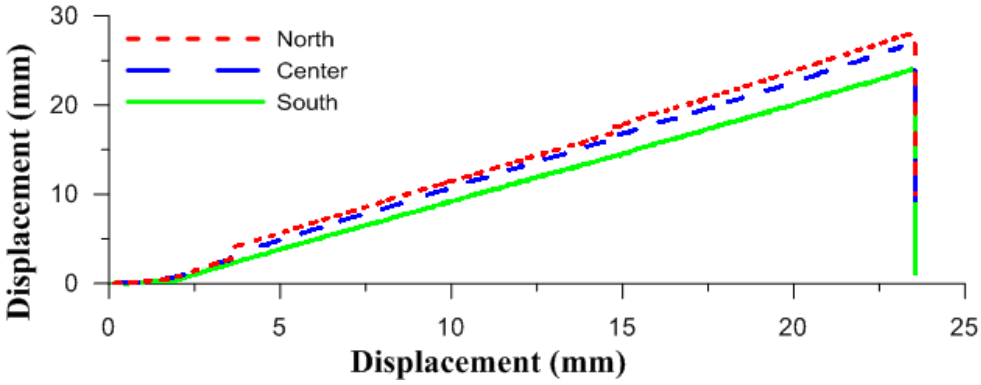

Figure E.5: Horizontal Center-line Displacement plot for Specimen IS5

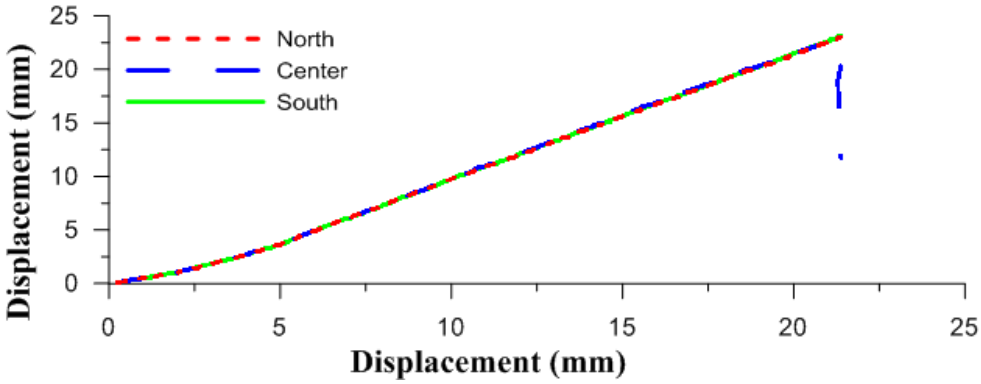

Figure E.6: Horizontal Center-line Displacement plot for Specimen RS1

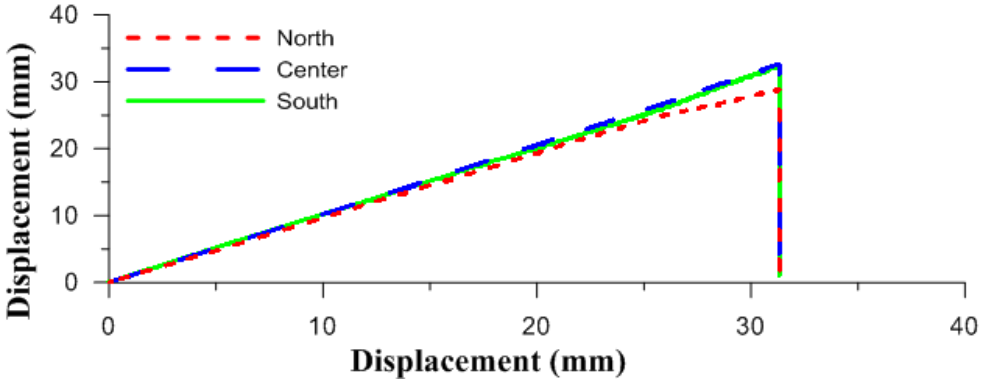

Figure E.7: Horizontal Center-line Displacement plot for Specimen RS2

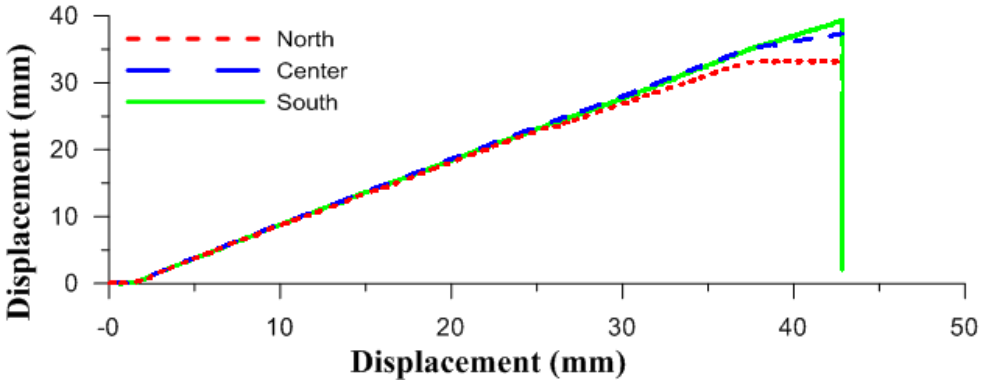

Figure E.8: Horizontal Center-line Displacement plot for Specimen RS3

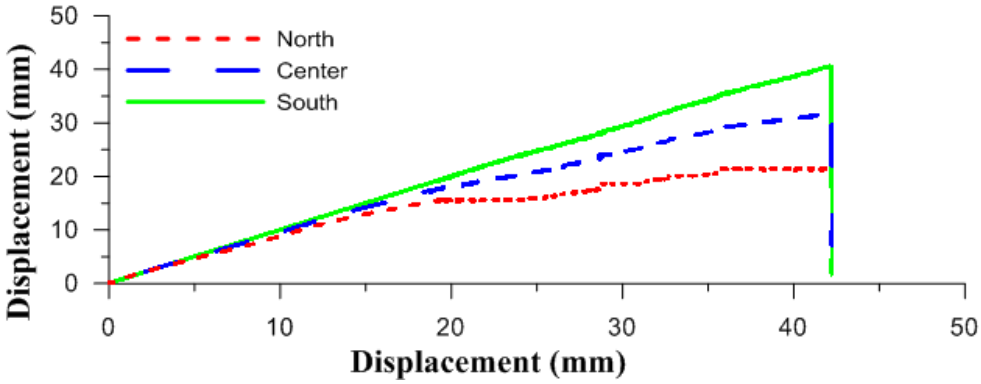

Figure E.9: Horizontal Center-line Displacement plot for Specimen RS4

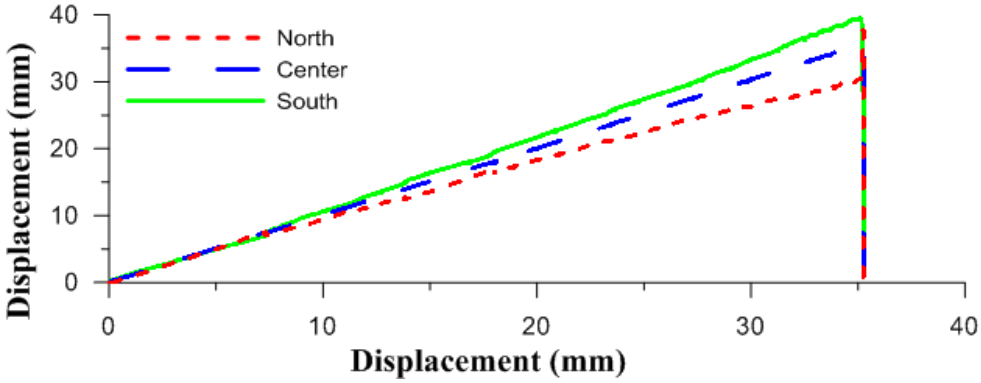

Figure E.10: Horizontal Center-line Displacement plot for Specimen RS5

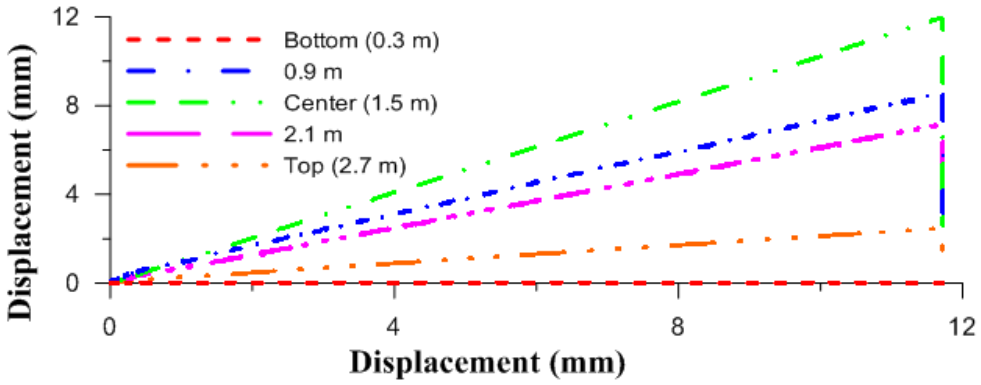

Figure E.11: Vertical Center-line Displacement plot for Specimen IS1

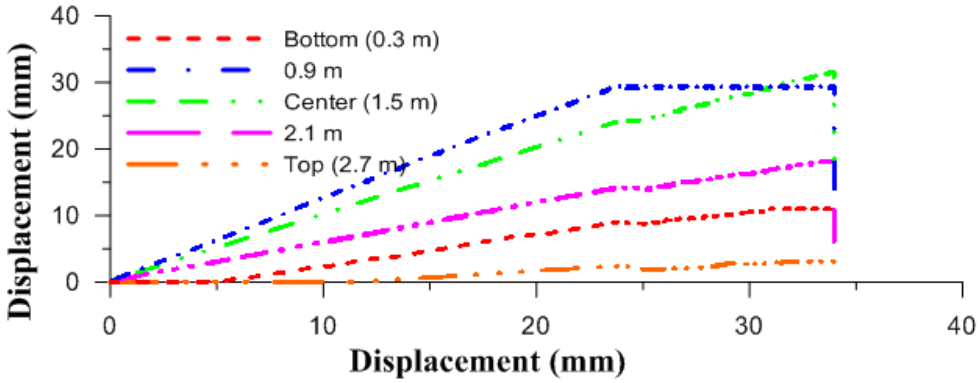

Figure E.12: Vertical Center-line Displacement plot for Specimen IS2

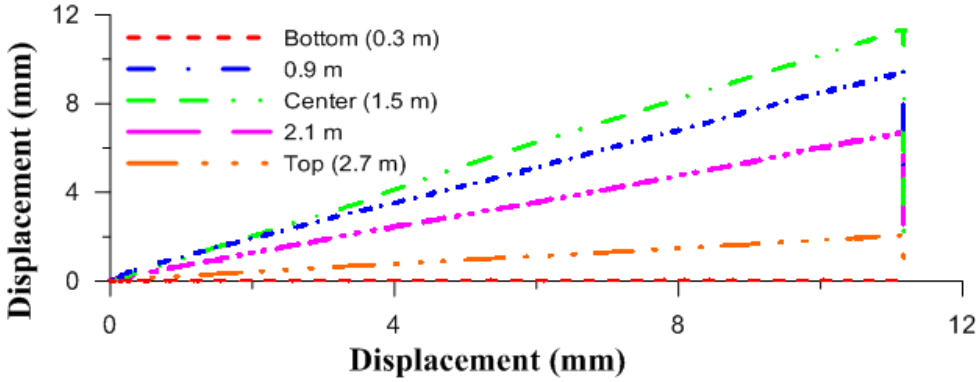

Figure E.13: Vertical Center-line Displacement plot for Specimen IS3

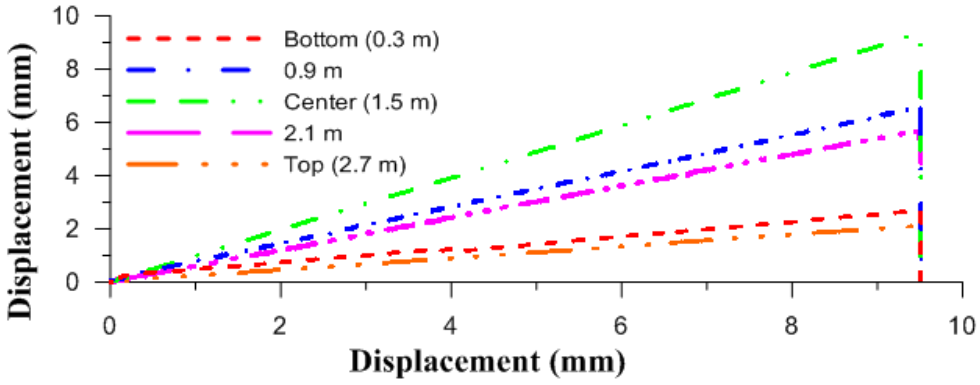

Figure E.14: Vertical Center-line Displacement plot for Specimen IS4

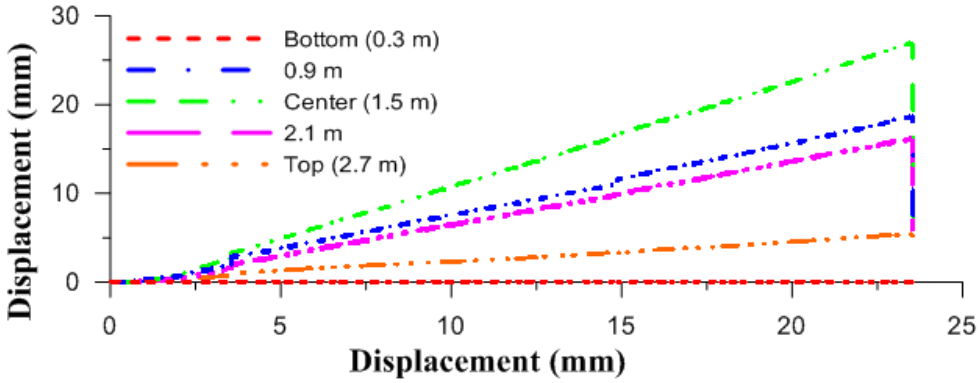

Figure E.15: Vertical Center-line Displacement plot for Specimen IS5

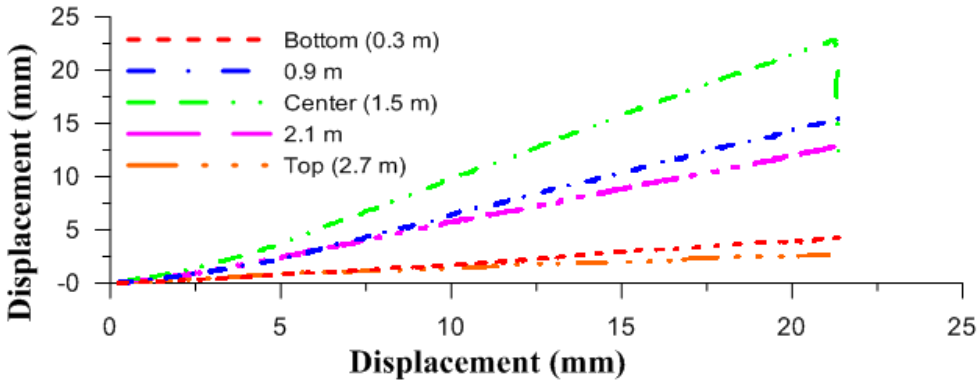

Figure E.16: Vertical Center-line Displacement plot for Specimen RS1

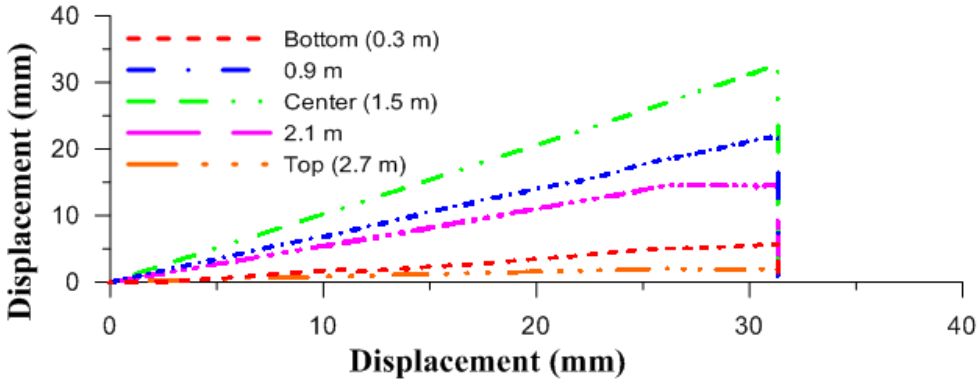

Figure E.17: Vertical Center-line Displacement plot for Specimen RS2

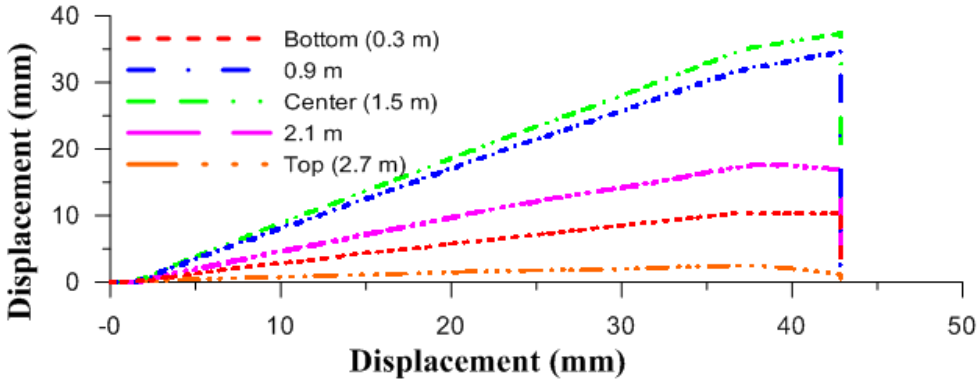

Figure E.18: Vertical Center-line Displacement plot for Specimen RS3

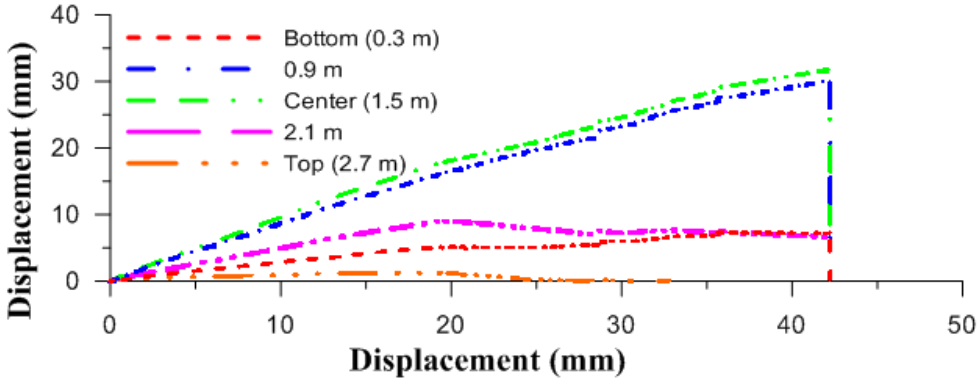

Figure E.19: Vertical Center-line Displacement plot for Specimen RS4

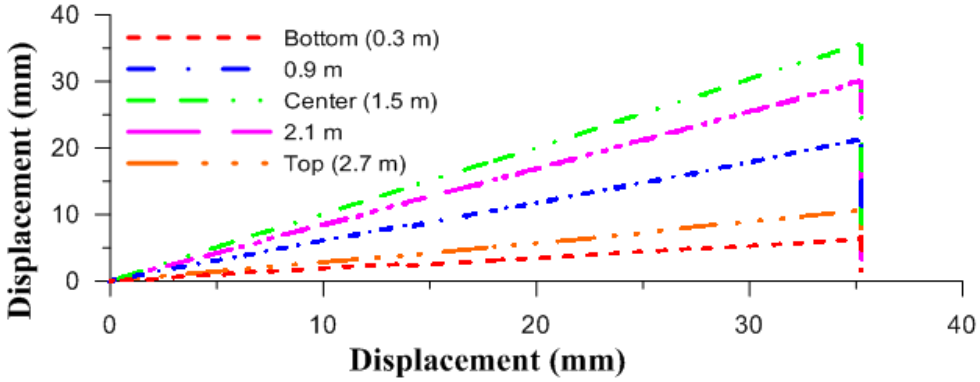

Figure E.20: Vertical Center-line Displacement plot for Specimen RS5

Appendix F: Load-Time History plots

This appendix presents the load behaviour of all of the load tests that were conducted on the masonry wall specimens. The load time histories are presented for the walls that were loaded dynamically.

Figure F.1 to Figure F.9 present the load trials for the dynamically loaded ideally-pinned walls.
Figure F.10 to Figure F.60 present the load trials for the dynamically loaded realistically-pinned walls.

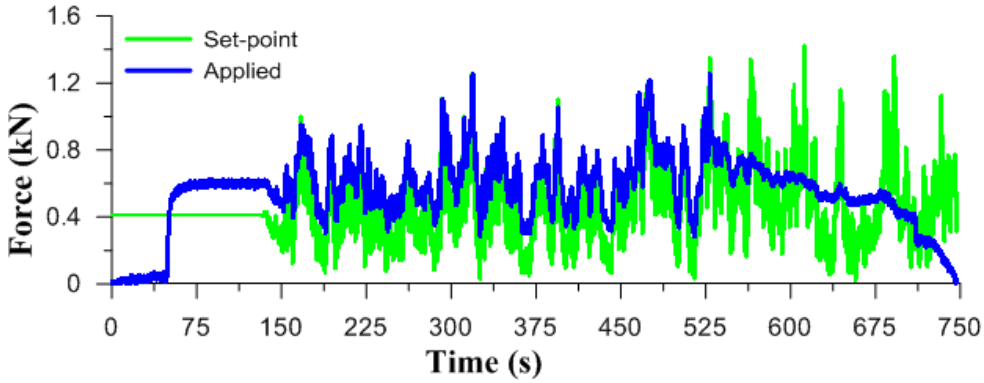

Figure F.1: 14 m/s load time history for Specimen ID1

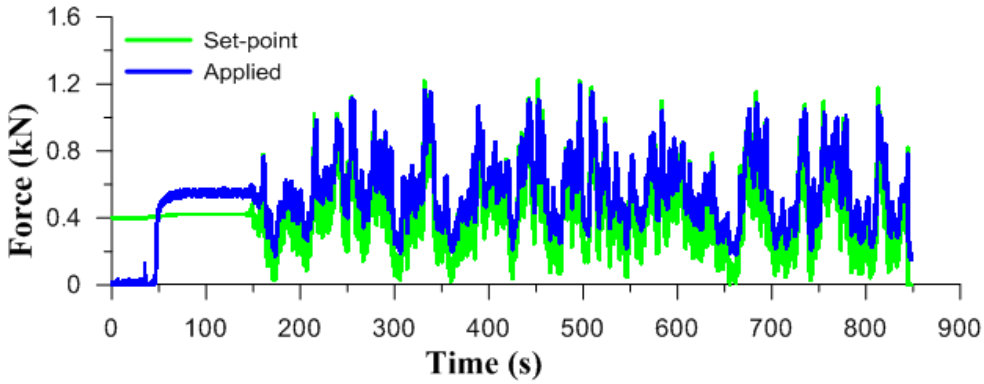

Figure F.2: 14 m/s load time history for Specimen ID2

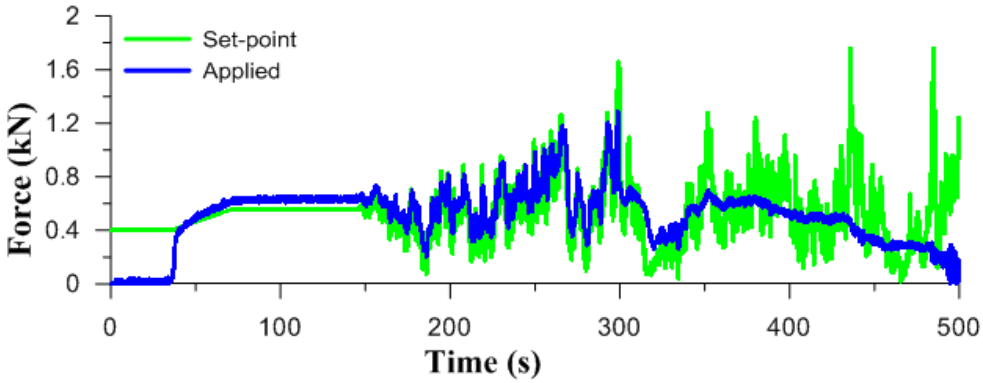

Figure F.3: 16 m/s load time history for Specimen ID2

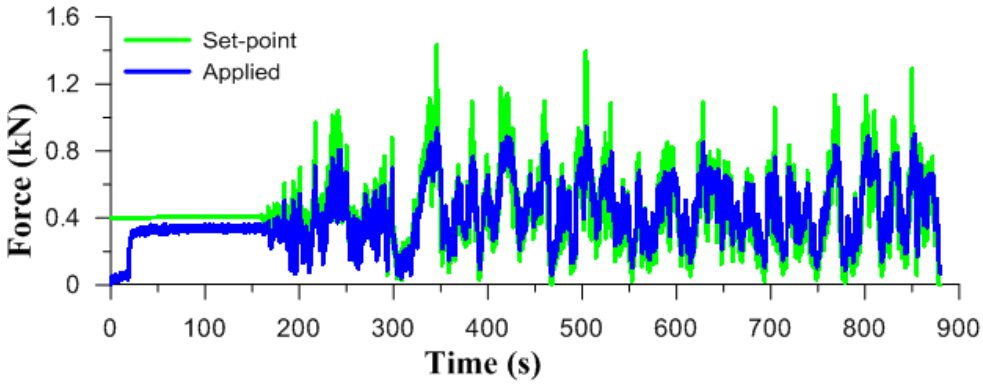

Figure F.4: 14 m/s load time history for Specimen ID3

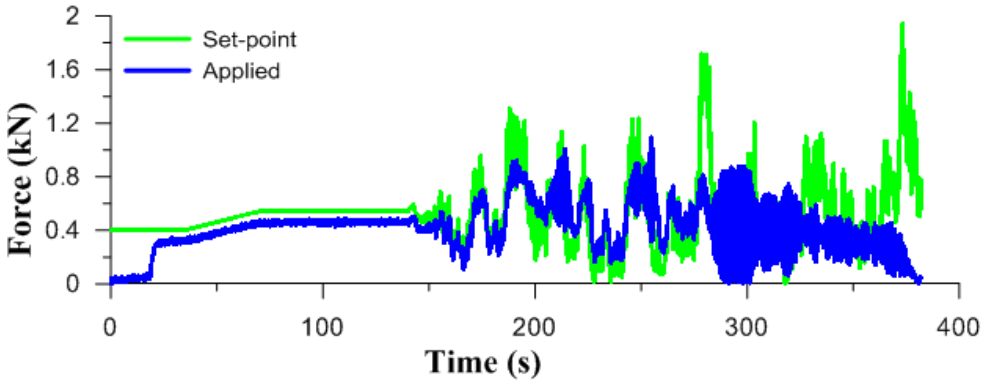

Figure F.5: 16 m/s load time history for Specimen ID3

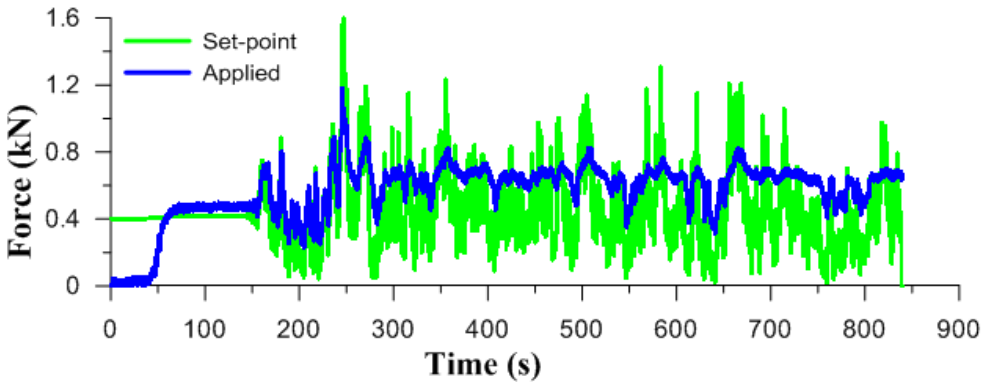

Figure F.6: 14 m/s load time history for Specimen ID4

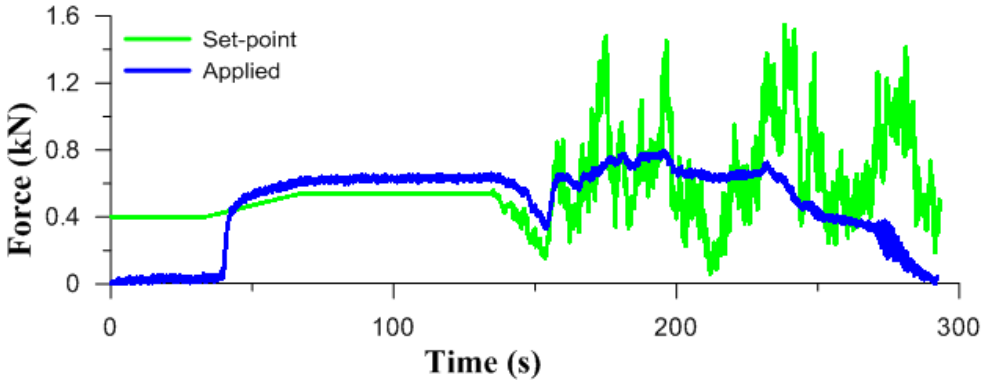

Figure F.7: 16 m/s load time history for Specimen ID4

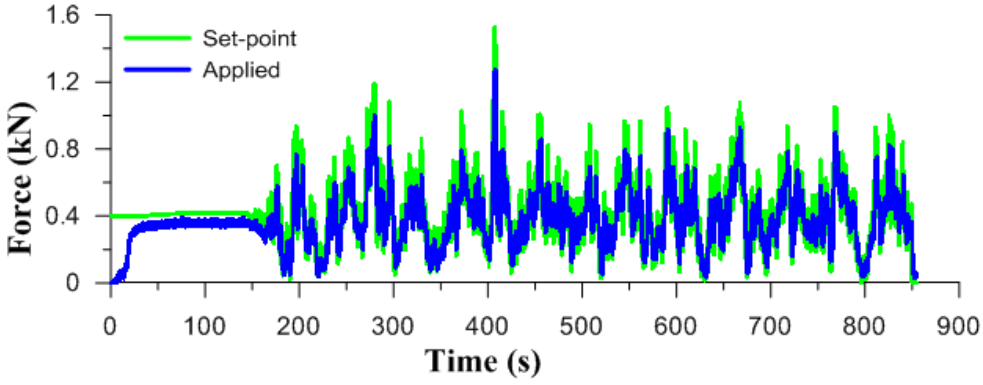

Figure F.8: 14 m/s load time history for Specimen ID5

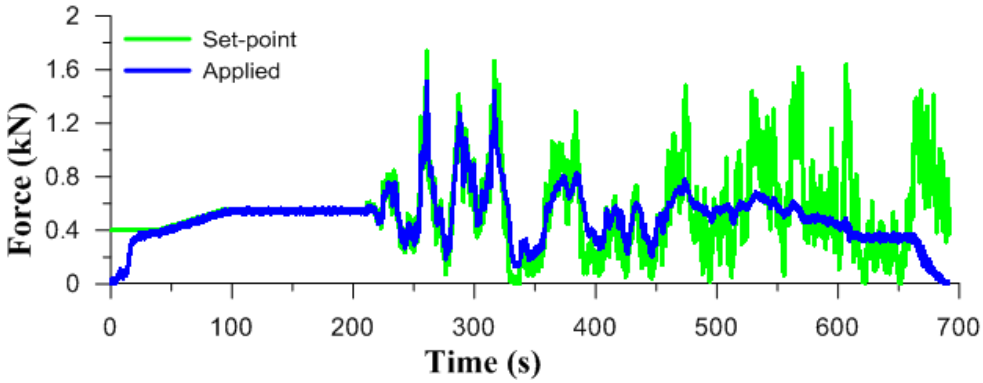

Figure F.9: 16 m/s load time history for Specimen ID5

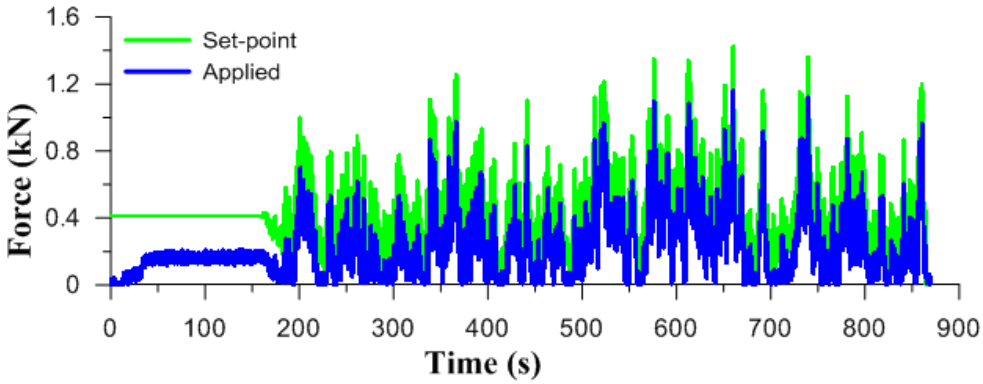

Figure F.10: 14 m/s load time history for Specimen RD1

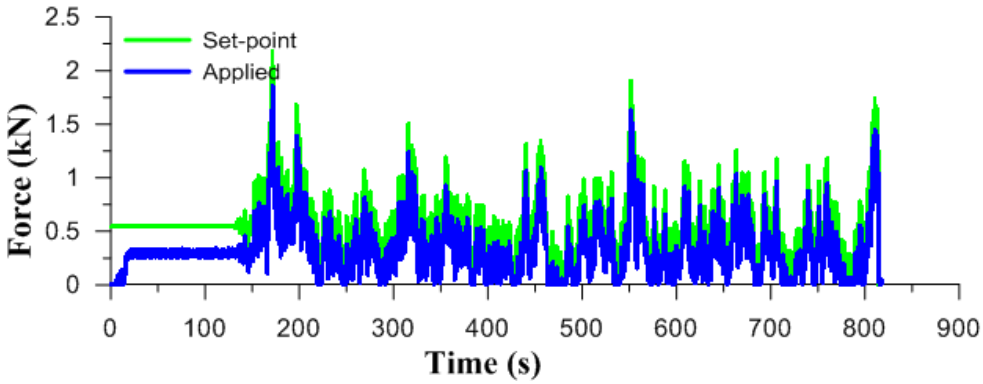

Figure F.11: 16 m/s load time history for Specimen RD1

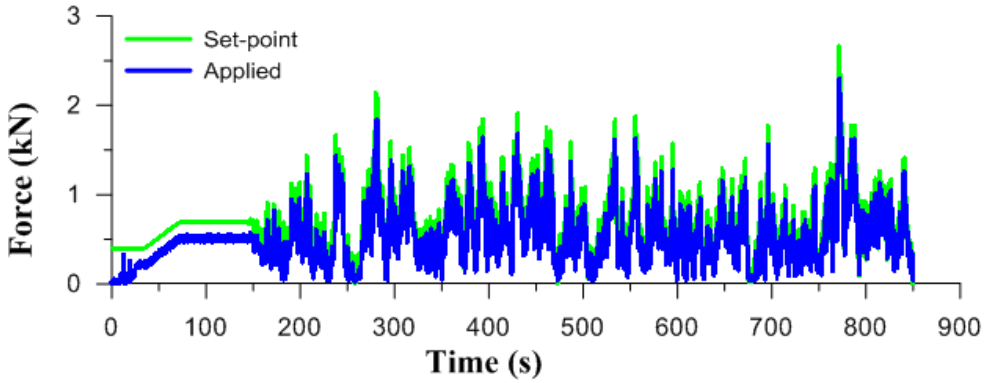

Figure F.12: 18 m/s load time history for Specimen RD1

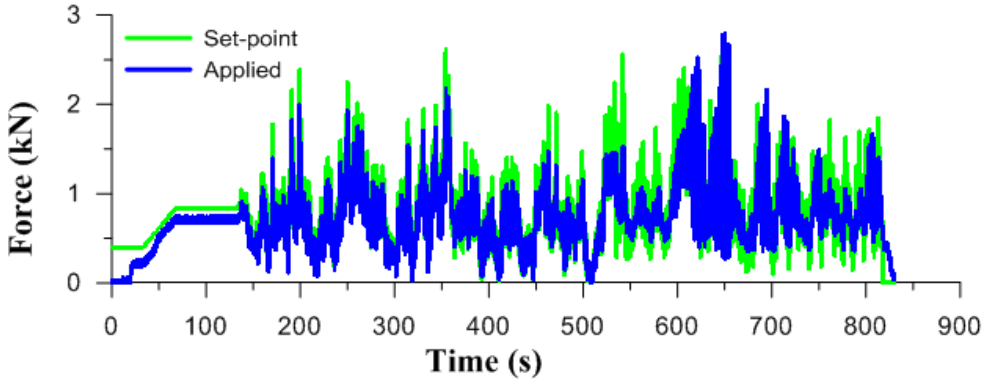

Figure F.13: 20 m/s load time history for Specimen RD1

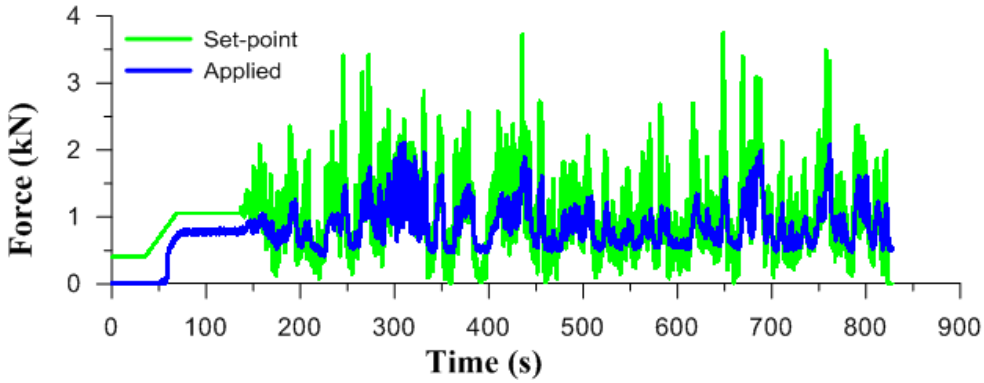

Figure F.14: 22 m/s load time history for Specimen RD1

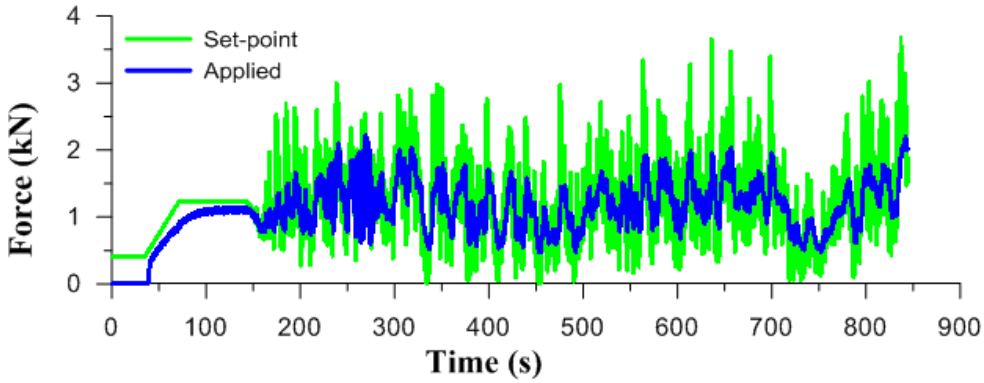

Figure F.15: 24 m/s load time history for Specimen RD1

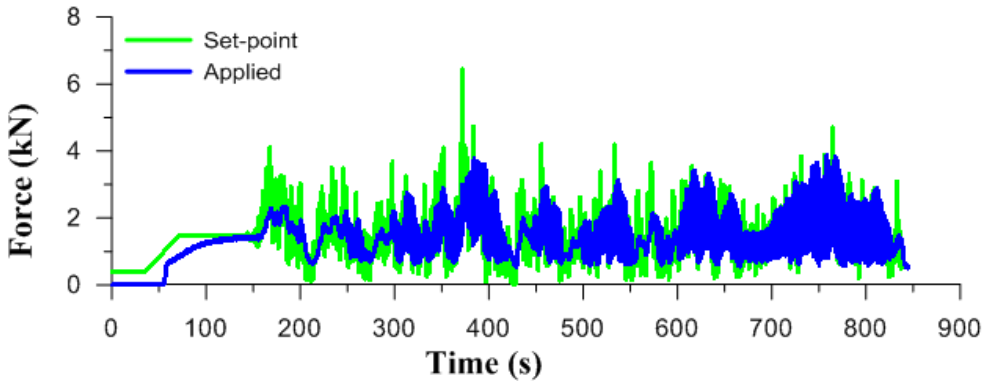

Figure F.16: 26 m/s load time history for Specimen RD1

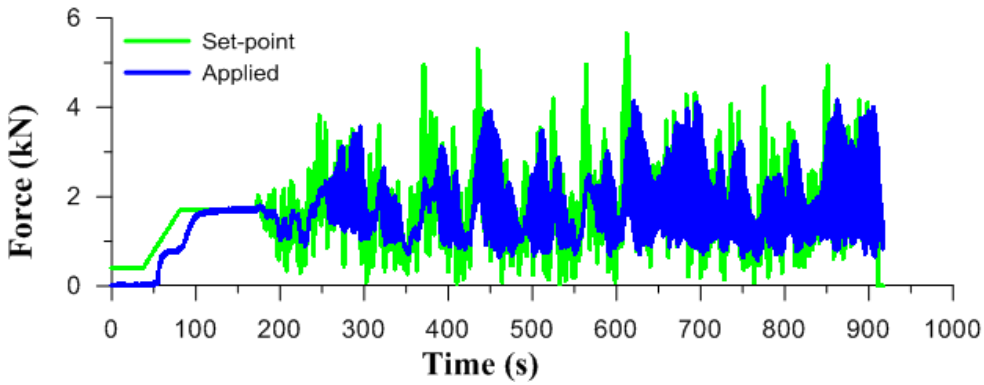

Figure F.17: 28 m/s load time history for Specimen RD1

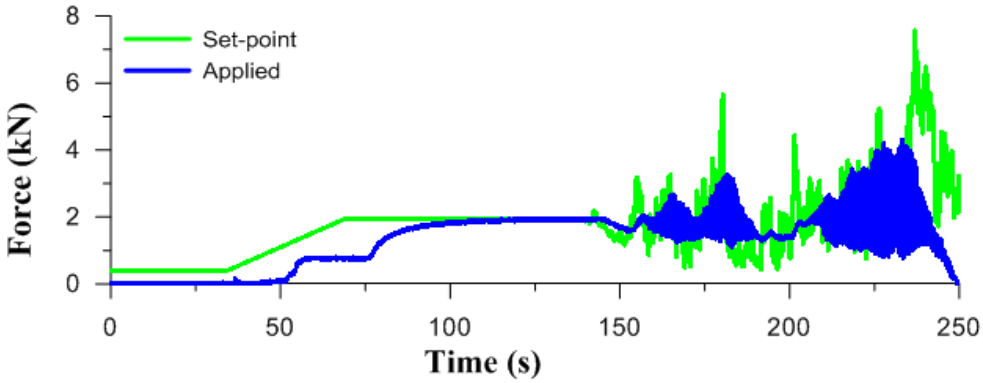

Figure F.18: 30 m/s load time history for Specimen RD1

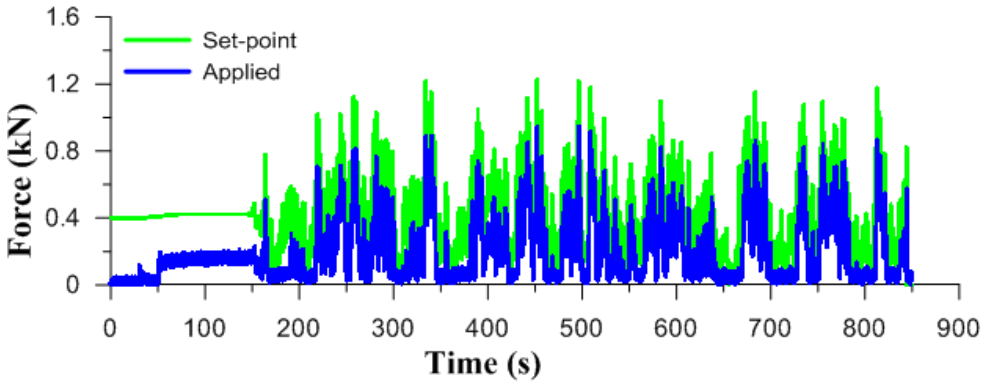

Figure F.19: 14 m/s load time history for Specimen RD2

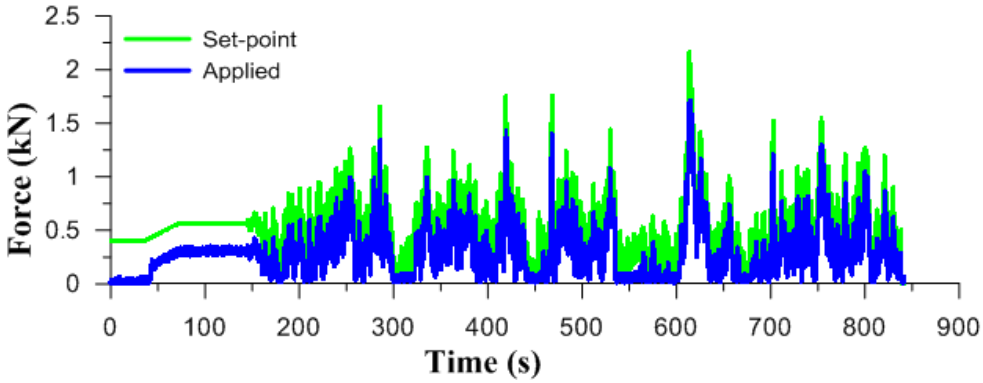

Figure F.20: 16 m/s load time history for Specimen RD2

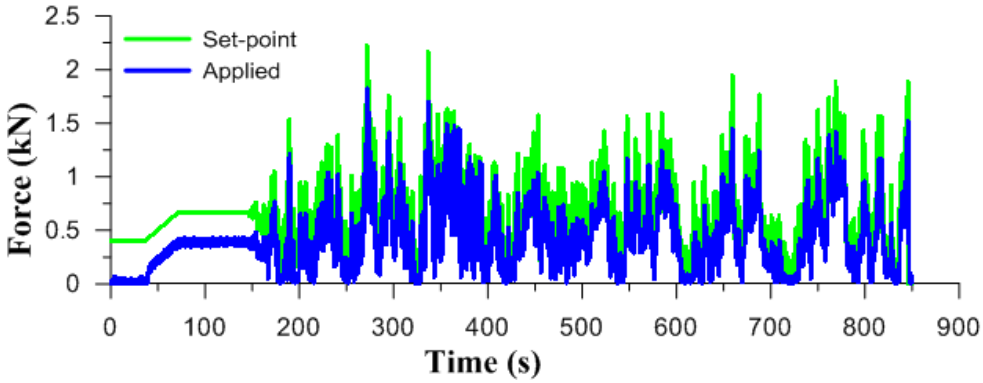

Figure F.21: 18 m/s load time history for Specimen RD2

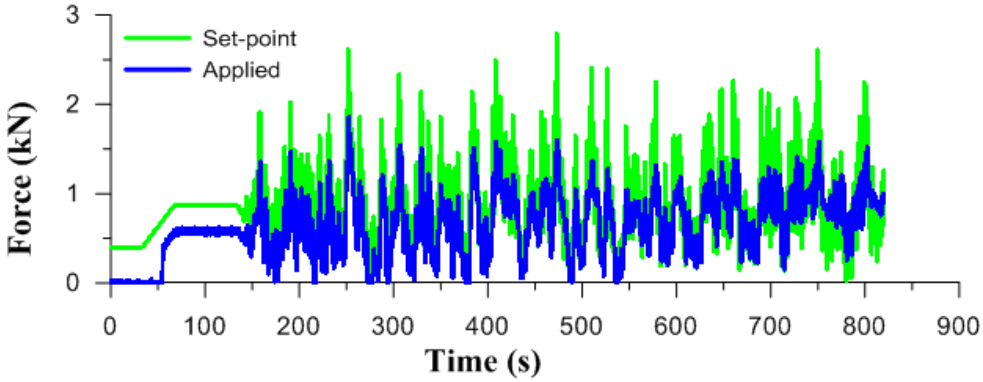

Figure F.22: 20 m/s load time history for Specimen RD2

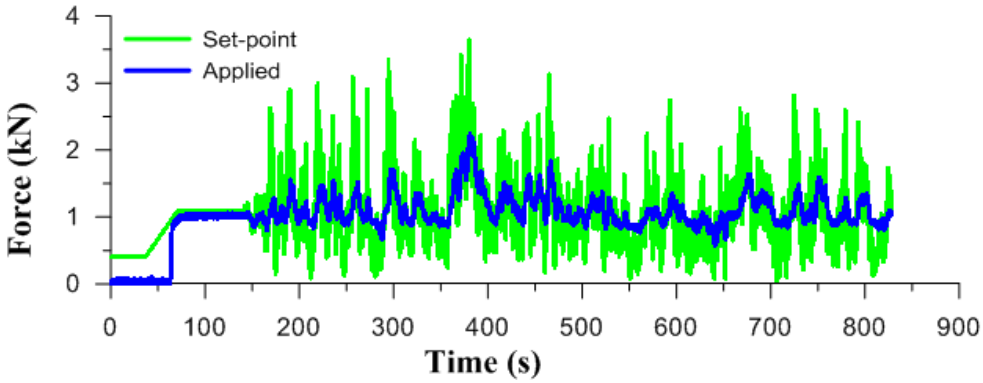

Figure F.23: 22 m/s load time history for Specimen RD2

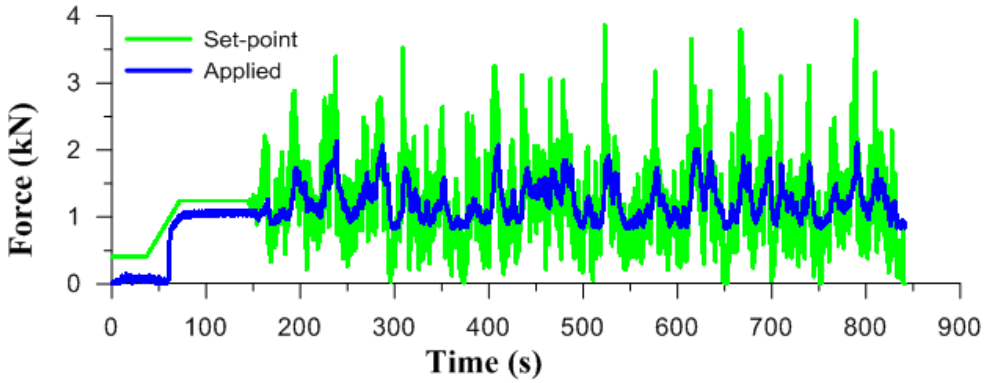

Figure F.24: 24 m/s load time history for Specimen RD2

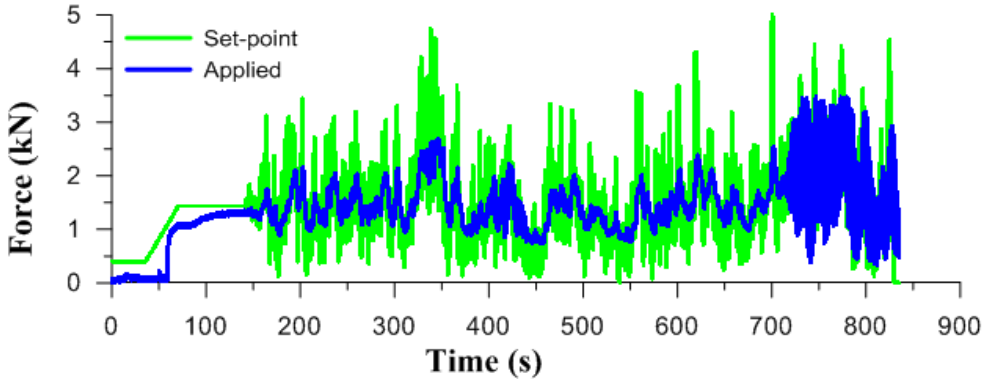

Figure F.25: 26 m/s load time history for Specimen RD2

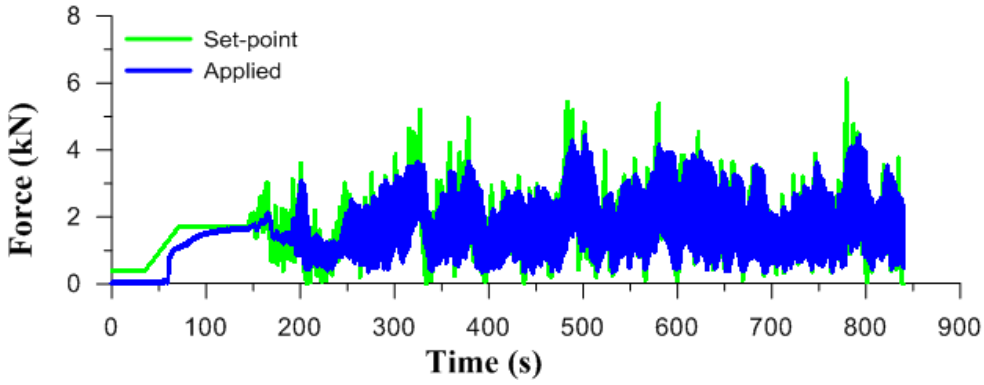

Figure F.26: 28 m/s load time history for Specimen RD2

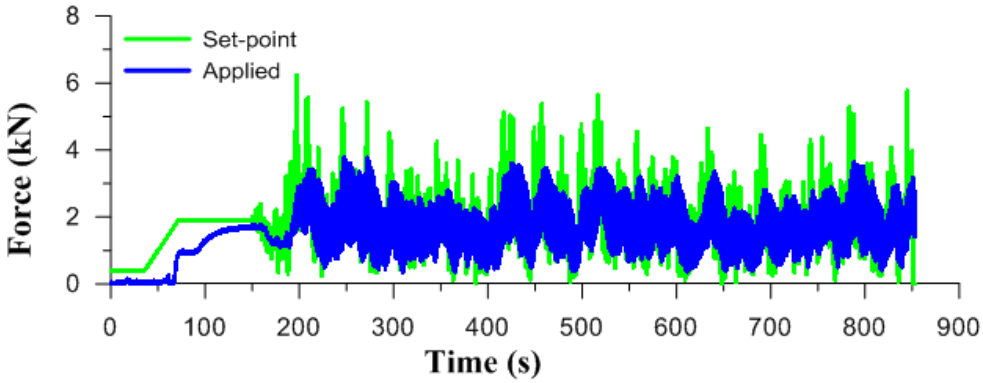

Figure F.27: 30 m/s load time history for Specimen RD2

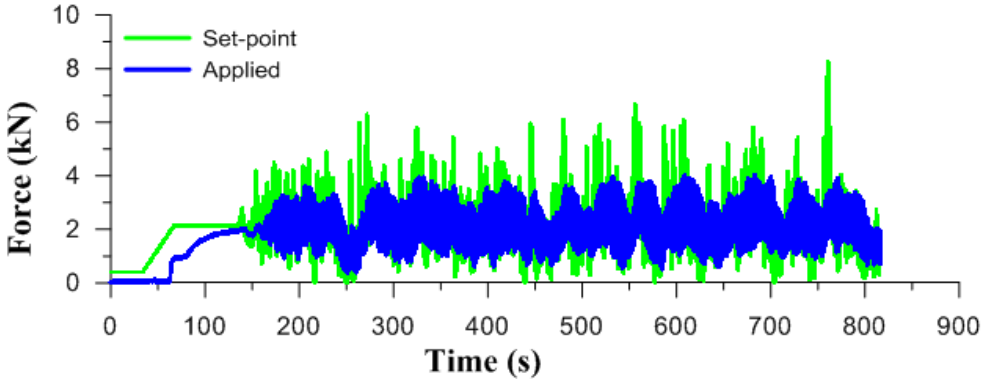

Figure F.28: 32 m/s load time history for Specimen RD2

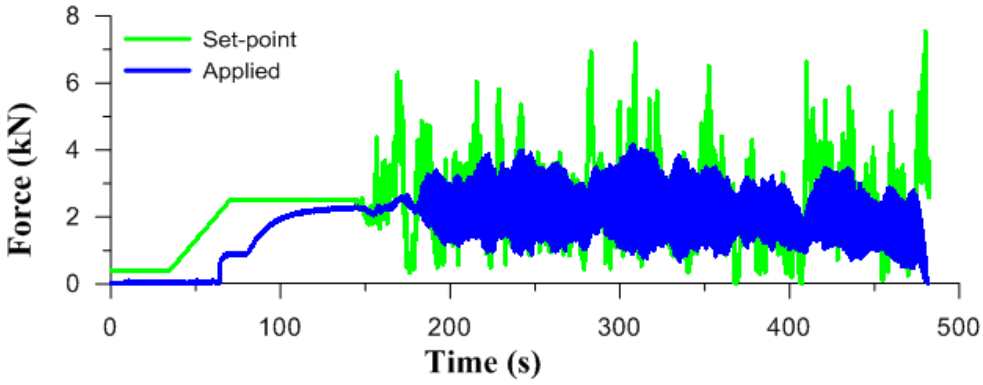

Figure F.29: 34 m/s load time history for Specimen RD2

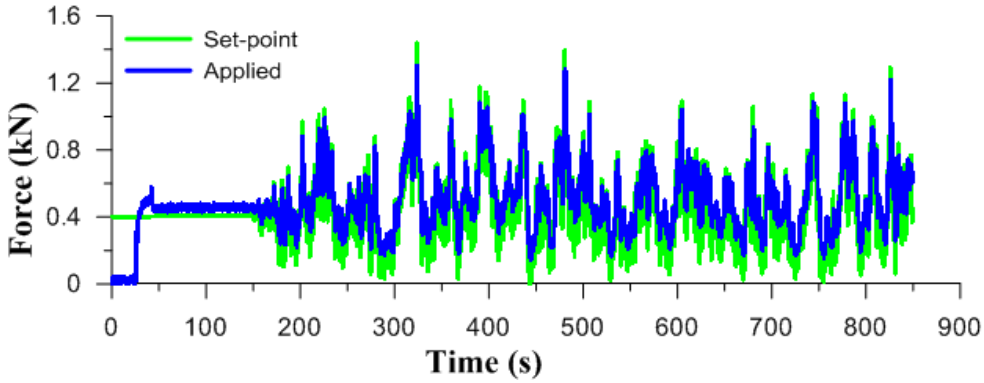

Figure F.30: 14 m/s load time history for Specimen RD3

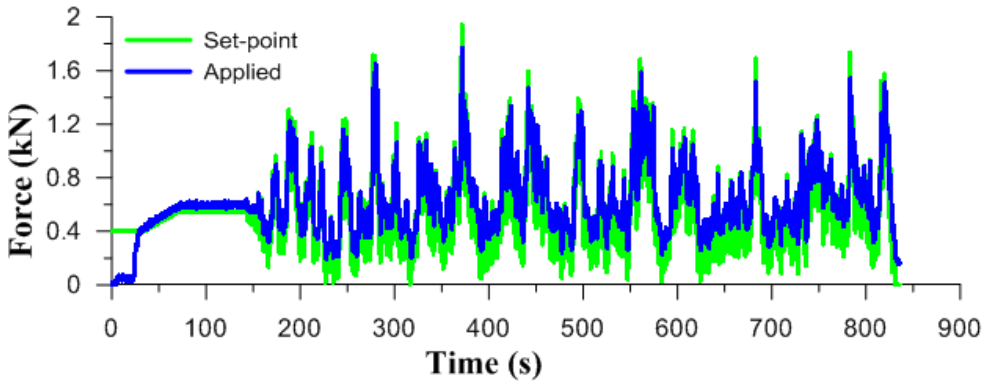

Figure F.31: 16 m/s load time history for Specimen RD3

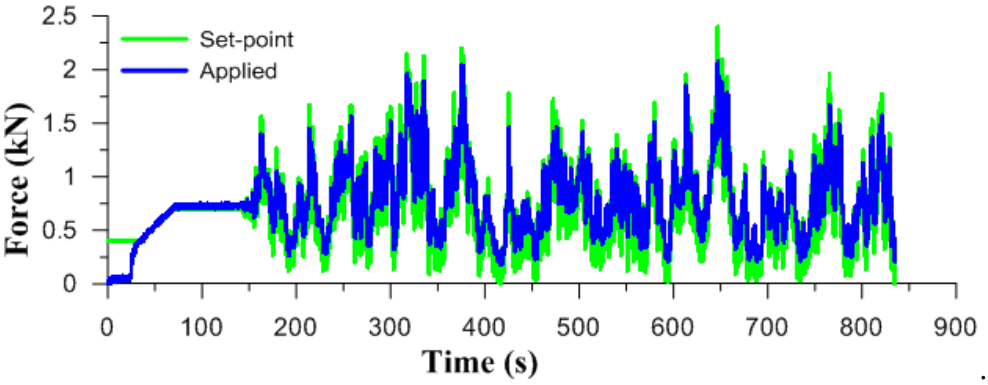

Figure F.32: 18 m/s load time history for Specimen RD3

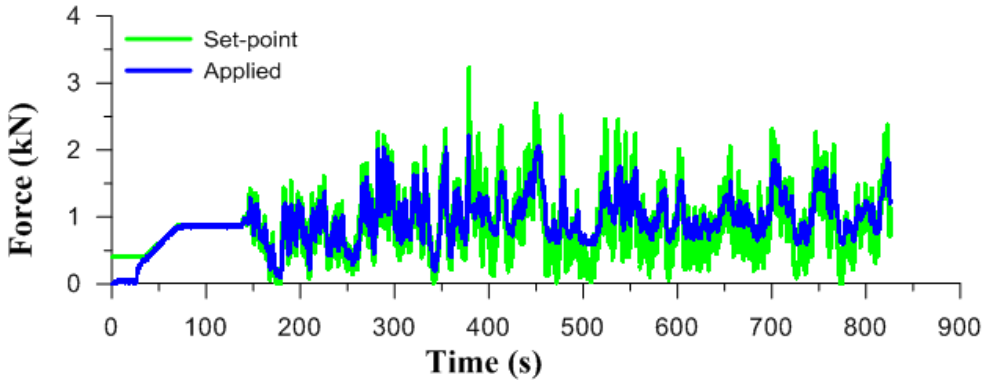

Figure F.33: 20 m/s load time history for Specimen RD3

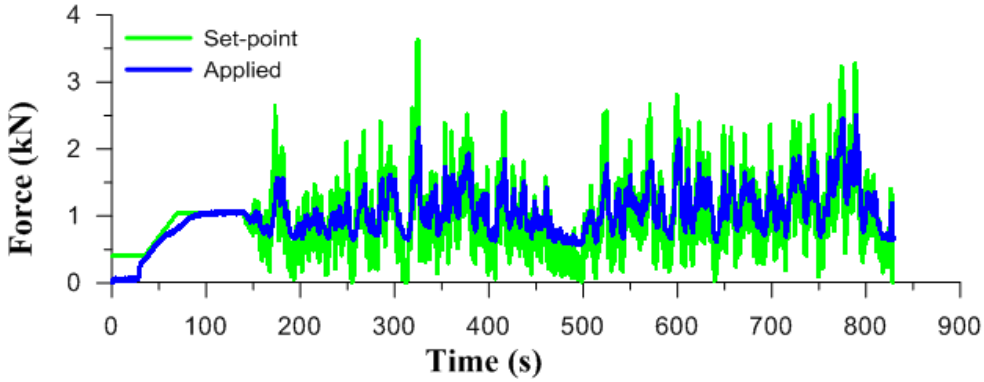

Figure F.34: 22 m/s load time history for Specimen RD3

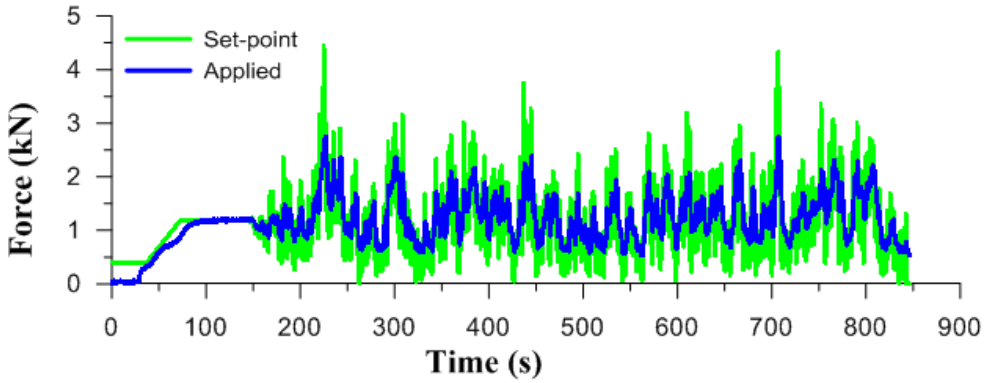

Figure F.35: 24 m/s load time history for Specimen RD3

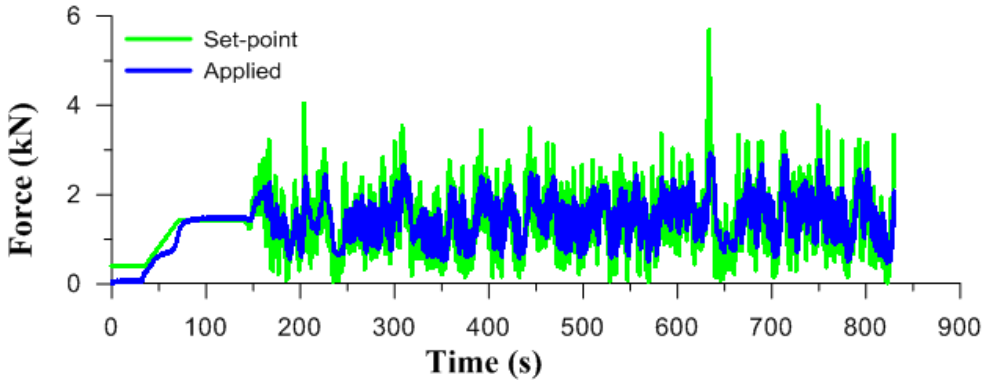

Figure F.36: 26 m/s load time history for Specimen RD3

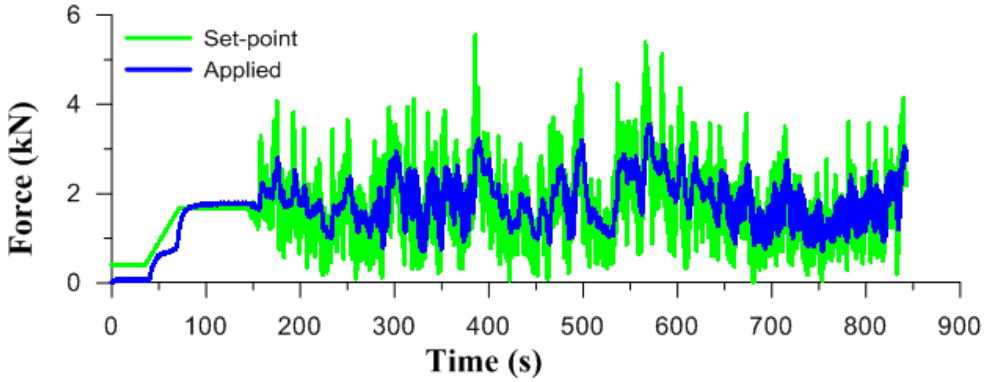

Figure F.37: 28 m/s load time history for Specimen RD3

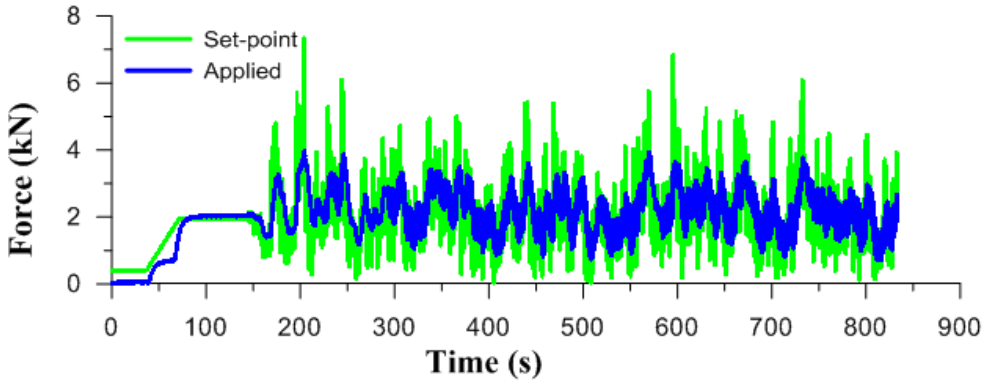

Figure F.38: 30 m/s load time history for Specimen RD3

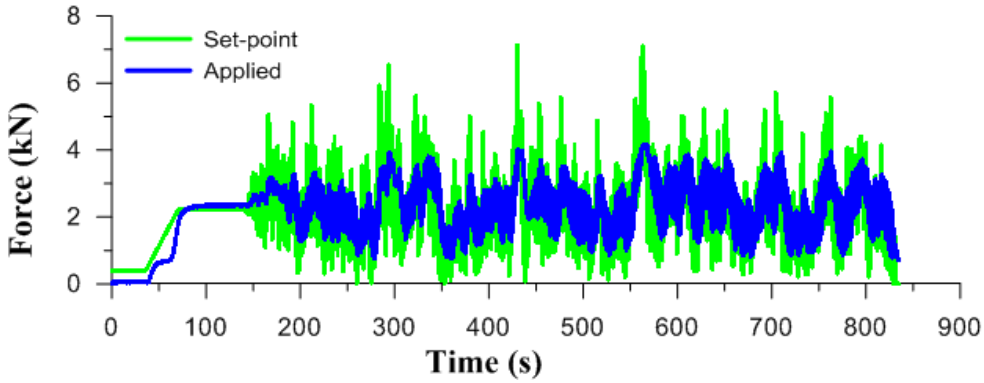

Figure F.39: 32 m/s load time history for Specimen RD3

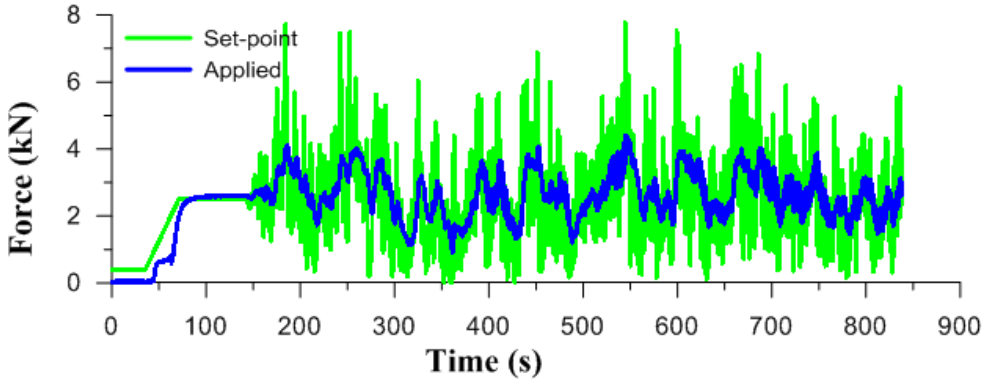

Figure F.40: 34 m/s load time history for Specimen RD3

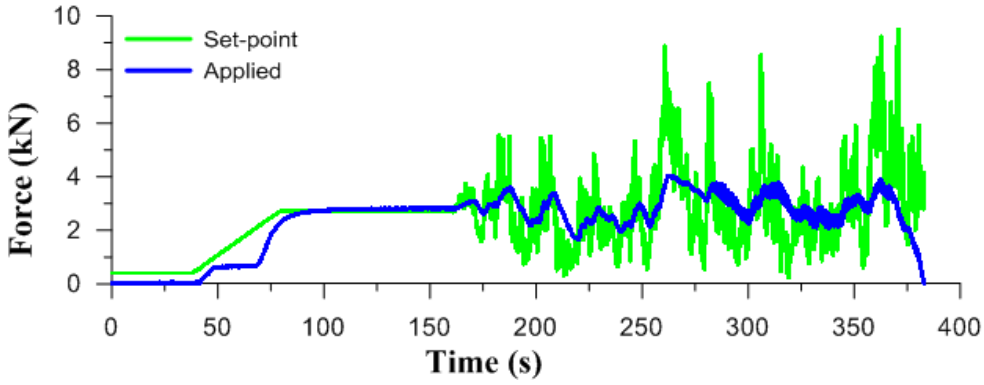

Figure F.41: 36 m/s load time history for Specimen RD3

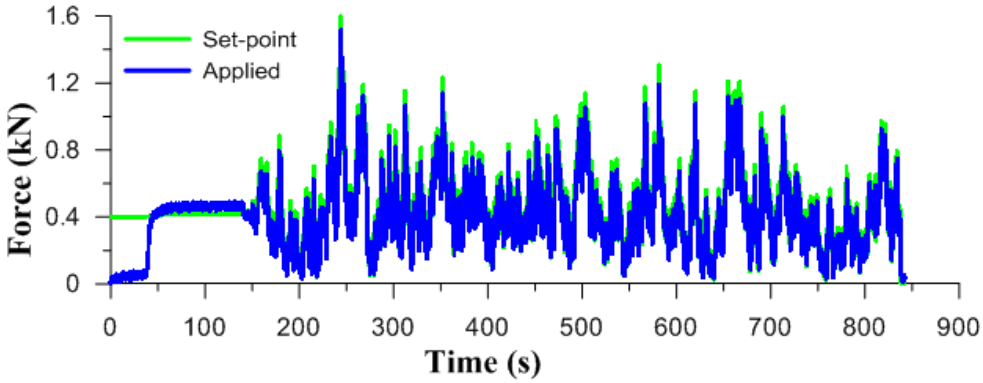

Figure F.42: 14 m/s load time history for Specimen RD4

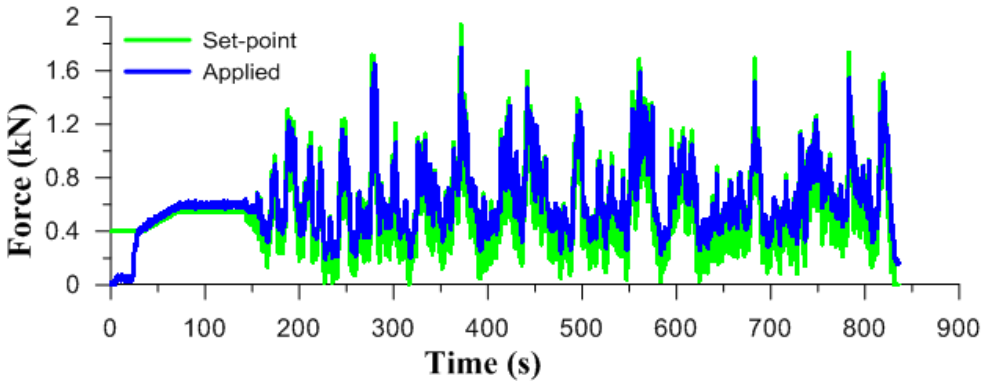

Figure F.43: 16 m/s load time history for Specimen RD4

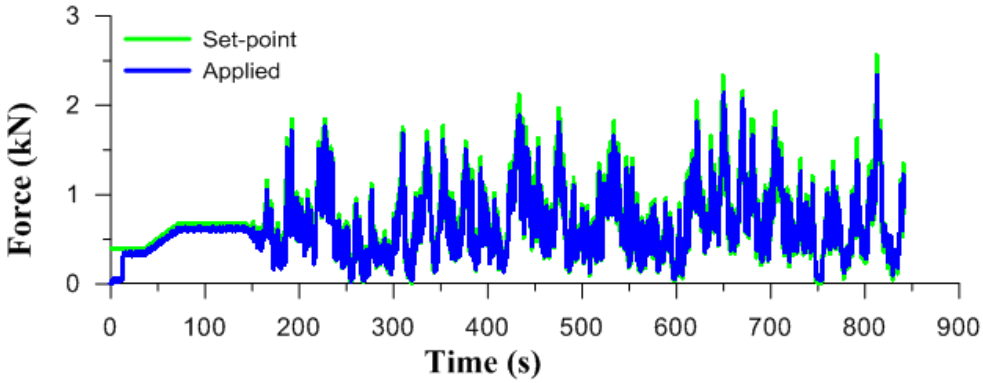

Figure F.44: 18 m/s load time history for Specimen RD4

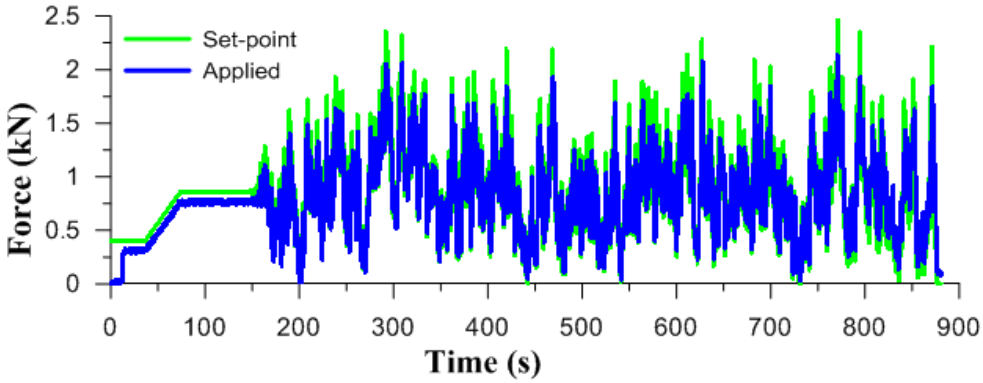

Figure F.45: 20 m/s load time history for Specimen RD4

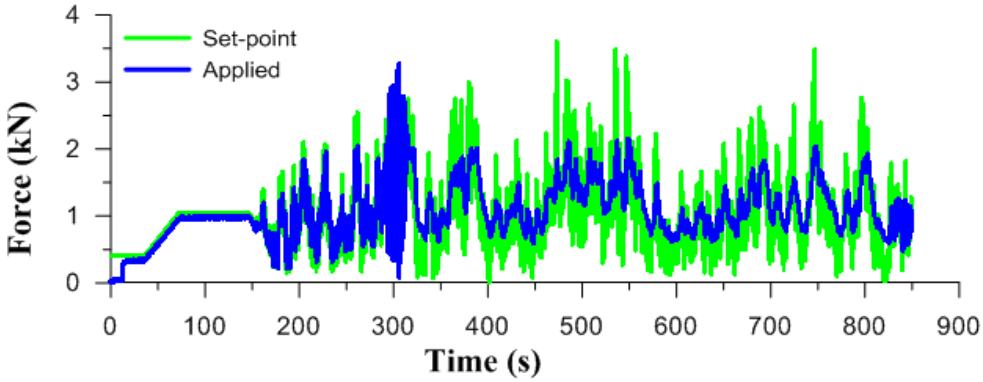

Figure F.46: 22 m/s load time history for Specimen RD4

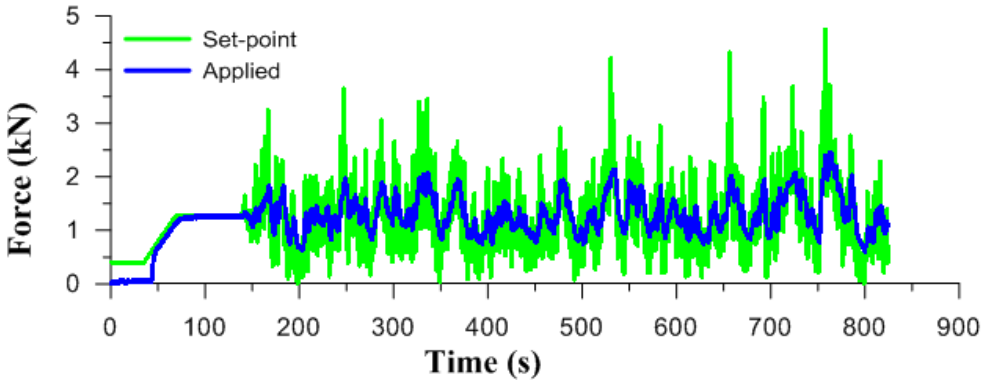

Figure F.47: 24 m/s load time history for Specimen RD4

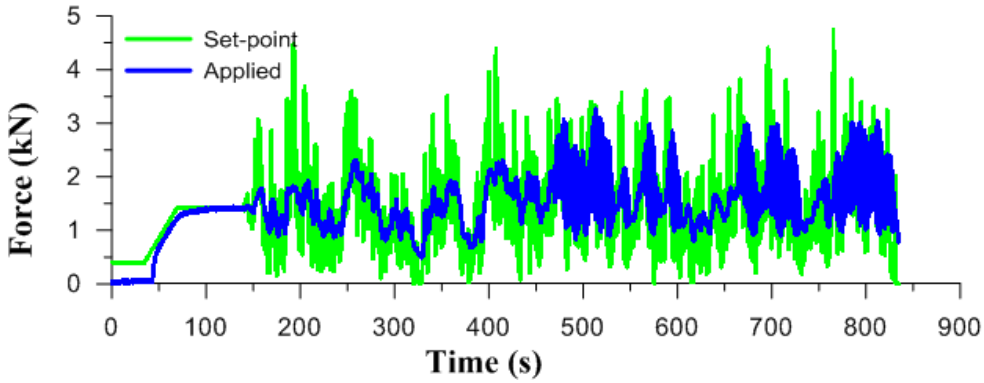

Figure F.48: 26 m/s load time history for Specimen RD4

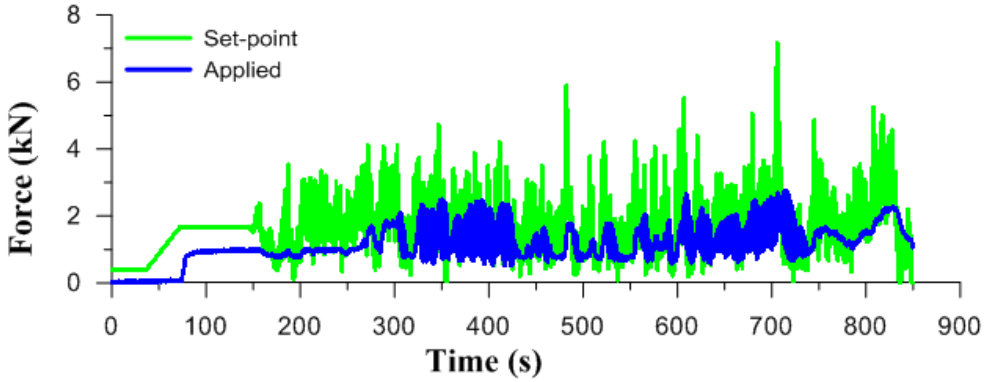

Figure F.49: 28 m/s load time history for Specimen RD4

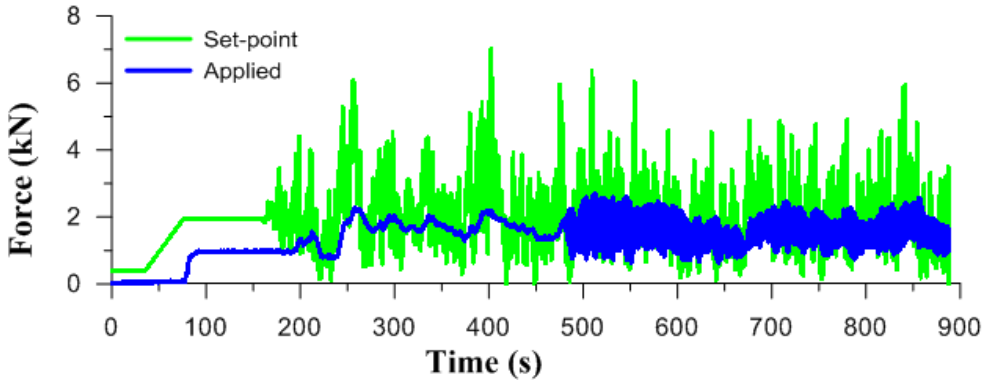

Figure F.50: 30 m/s load time history for Specimen RD4

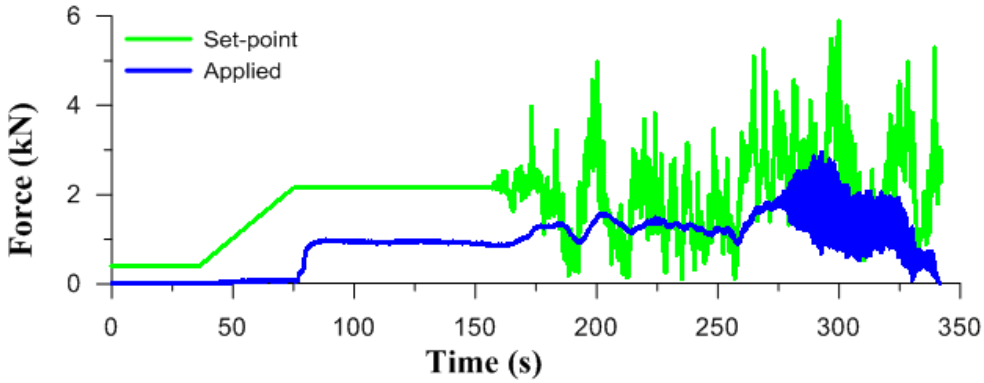

Figure F.51: 32 m/s load time history for Specimen RD4

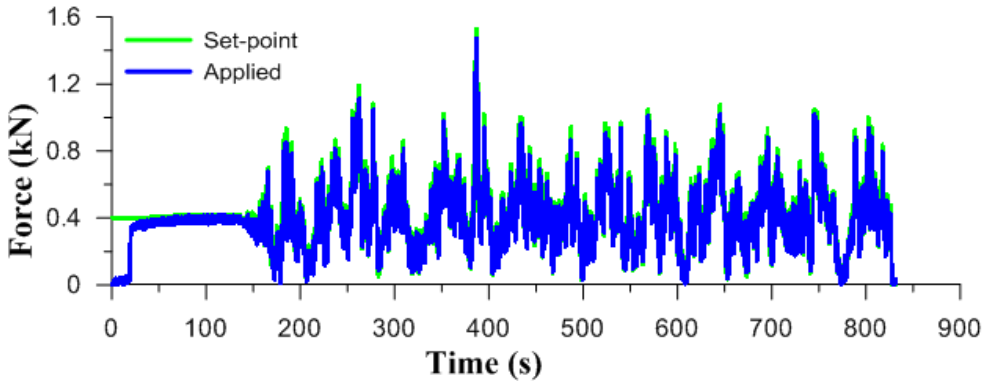

Figure F.52: 14 m/s load time history for Specimen RD5

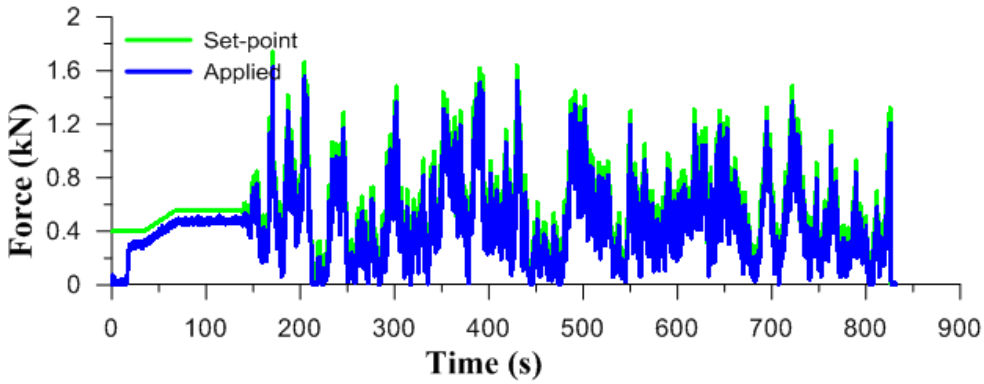

Figure F.53: 16 m/s load time history for Specimen RD5

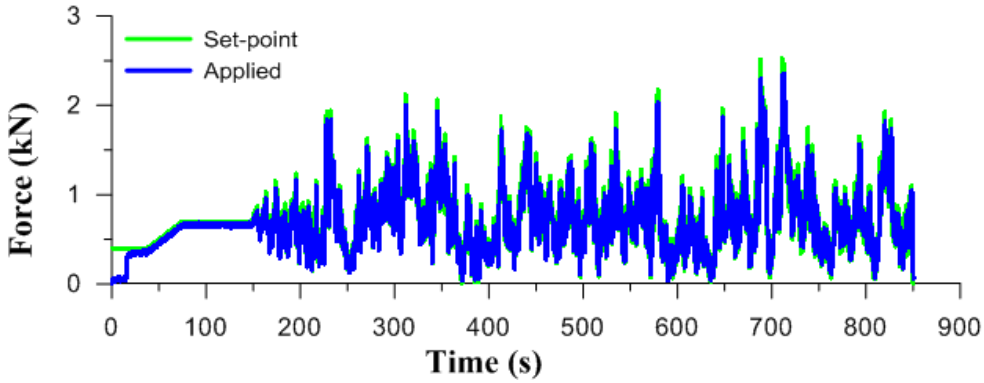

Figure F.54: 18 m/s load time history for Specimen RD5

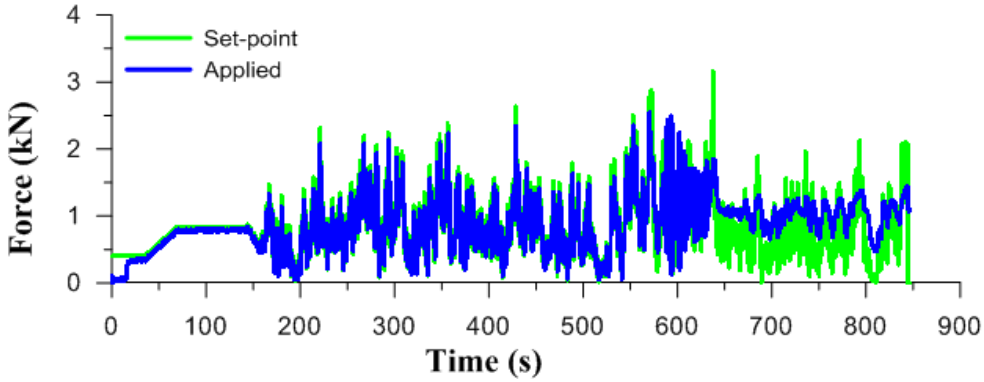

Figure F.55: 20 m/s load time history for Specimen RD5

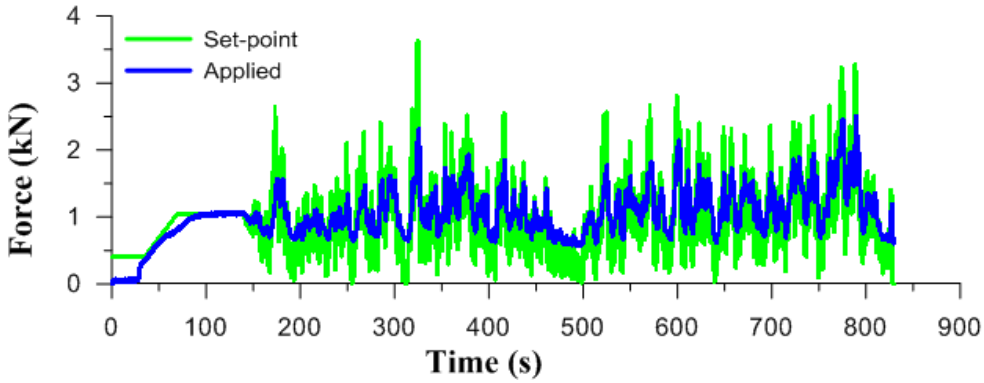

Figure F.56: 22 m/s load time history for Specimen RD5

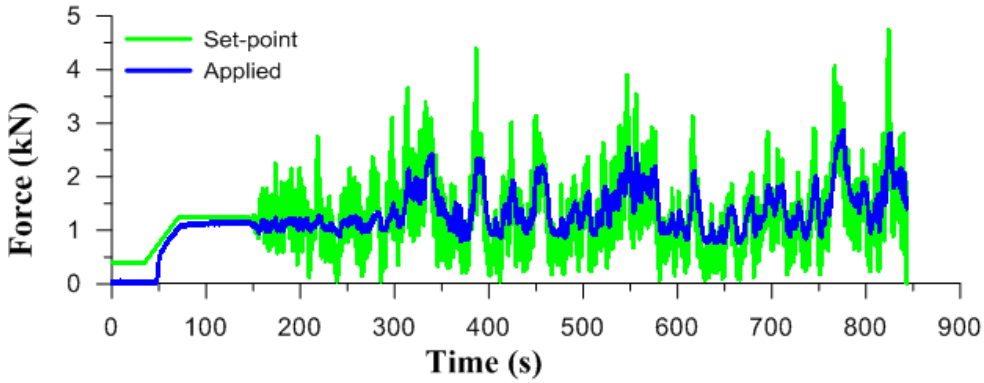

Figure F.57: 24 m/s load time history for Specimen RD5

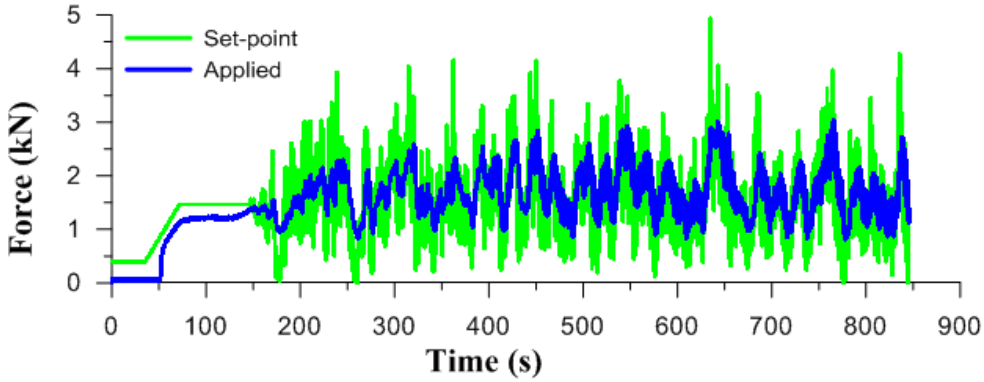

Figure F.58: 26 m/s load time history for Specimen RD5

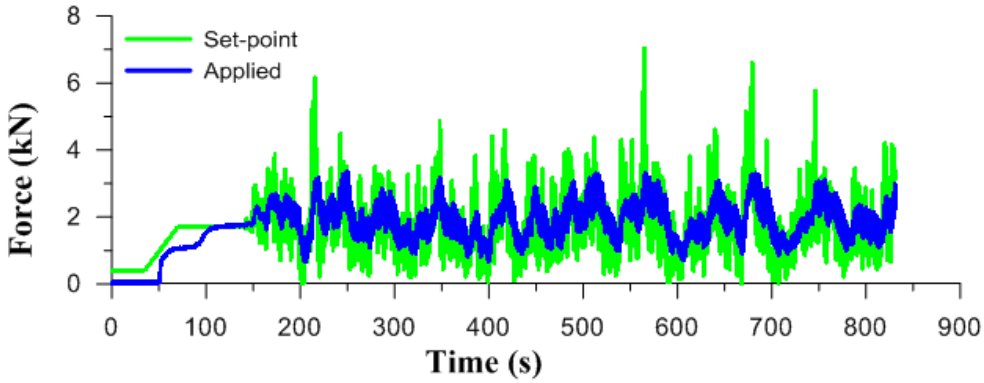

Figure F.59: 28 m/s load time history for Specimen RD5

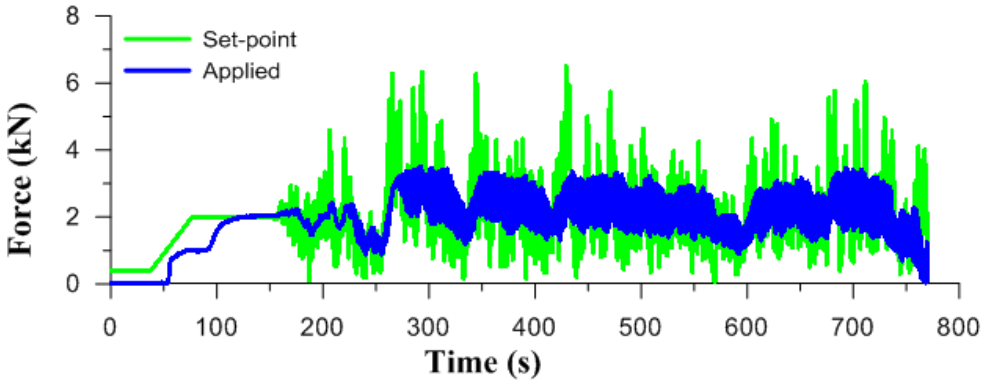

Figure F.60: 30 m/s load time history for Specimen RD5

Appendix G: Displacement Time Histories

This appendix presents the displacement behaviour of the masonry wall specimens that were dynamically loaded. Displacement plots of the horizontal and vertical center lines are presented. The displacement plots for the dynamically loaded walls are plotted against time. Trials that occurred after the LVDTs were removed from the walls are not presented.

Figure G.1 to Figure G.8 present the Horizontal center-line time history plots loaded ideally-pinned walls.
Figure G.9 to Figure G.36 present the Horizontal center-line time history plots loaded realistically-pinned walls.
Figure G.37 to Figure G.44 present the Vertical center-line time history plots loaded ideally-pinned walls.
Figure G.45 to Figure G.72 present the Vertical center-line time history plots loaded realistically-pinned walls.

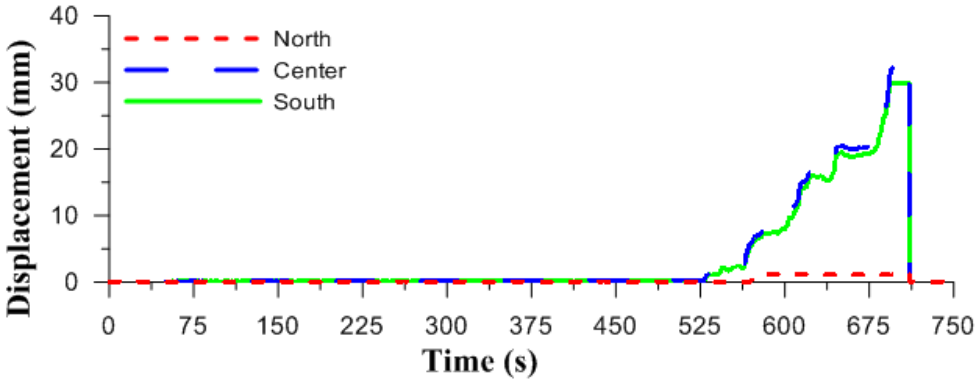

Figure G.1: 14 m/s horizontal center-line displacement time history for Specimen ID1

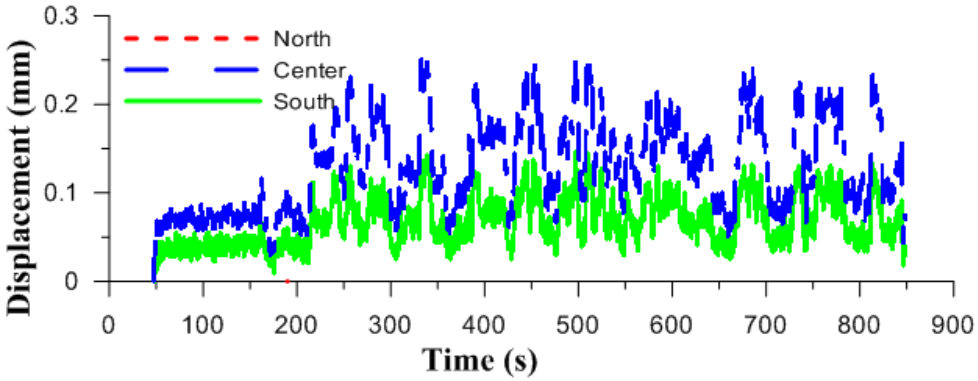

Figure G.2: 14 m/s horizontal center-line displacement time history for Specimen ID2

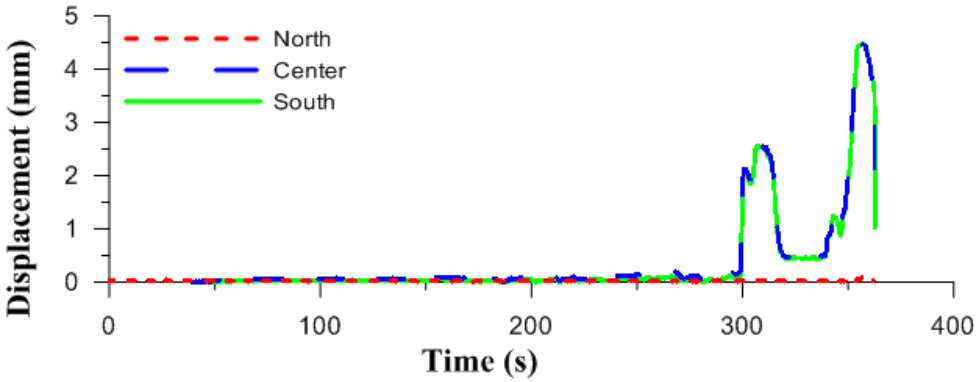

Figure G.3: 16 m/s horizontal center-line displacement time history for Specimen ID2

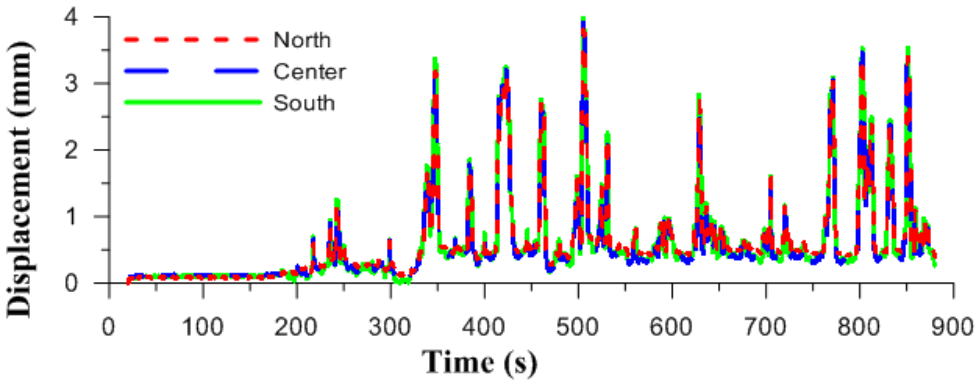

Figure G.4: 14 m/s horizontal center-line displacement time history for Specimen ID3

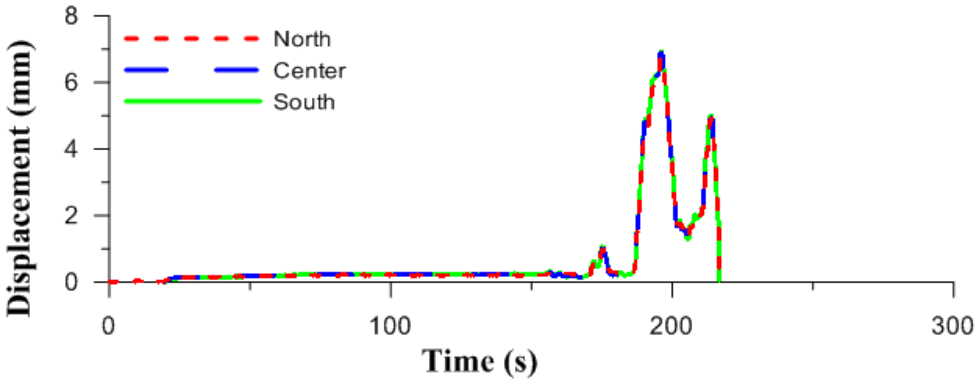

Figure G.5: 16 m/s horizontal center-line displacement time history for Specimen ID3

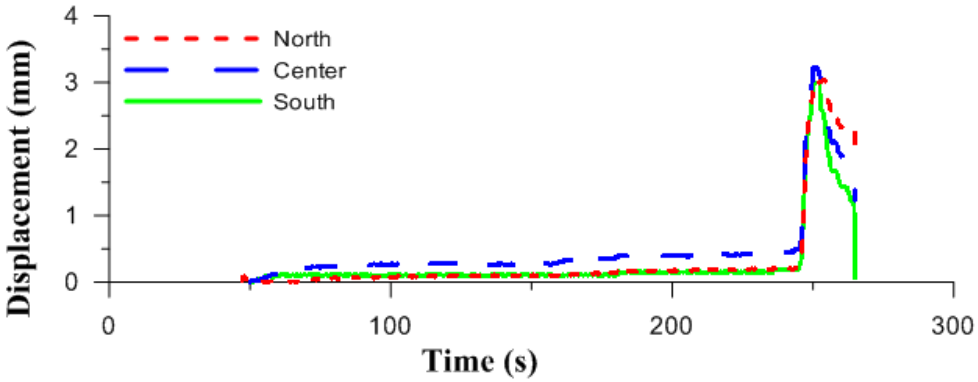

Figure G.6: 14 m/s horizontal center-line displacement time history for Specimen ID4

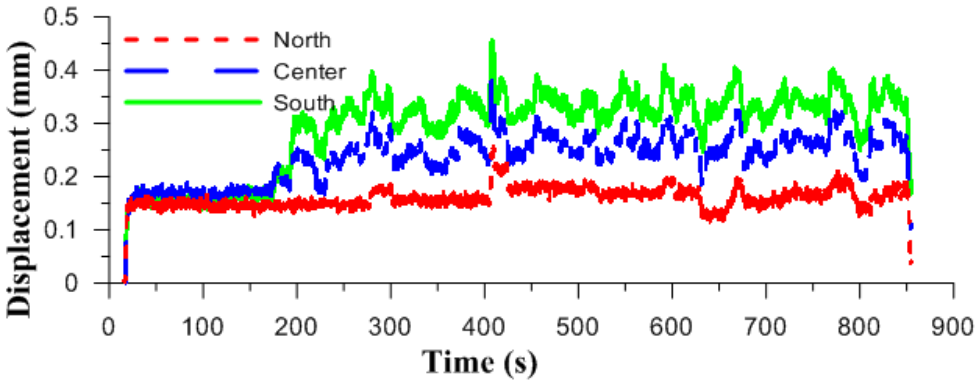

Figure G.7: 14 m/s horizontal center-line displacement time history for Specimen ID5

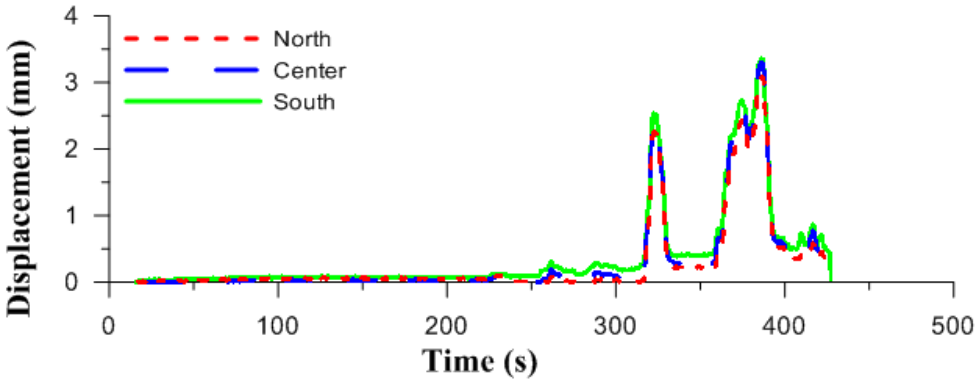

Figure G.8: 16 m/s horizontal center-line displacement time history for Specimen ID5

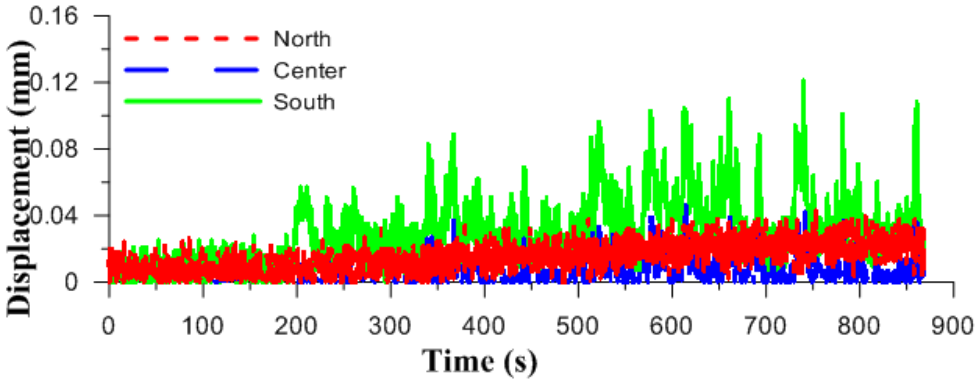

Figure G.9: 14 m/s horizontal center-line displacement time history for Specimen RD1

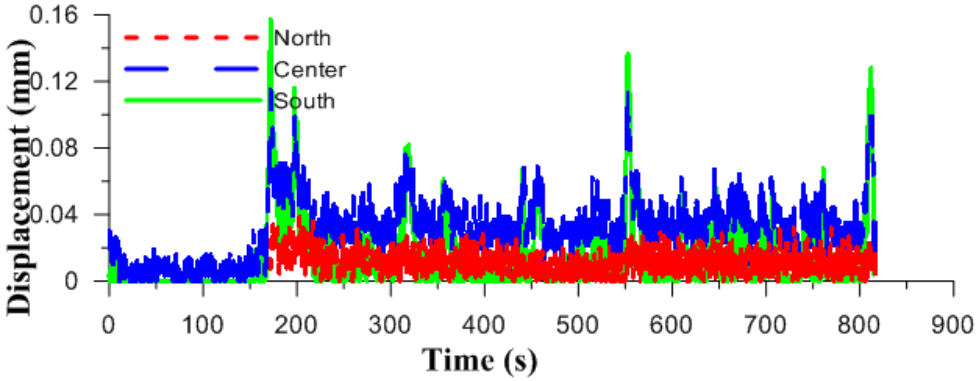

Figure G.10: 16 m/s horizontal center-line displacement time history for Specimen RD1

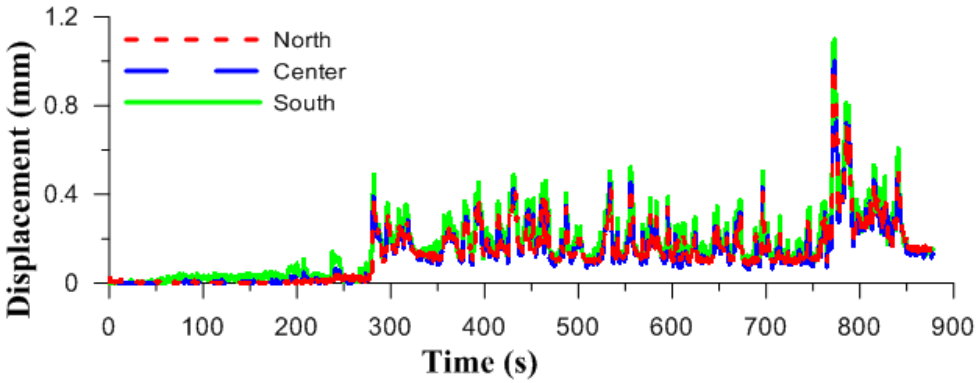

Figure G.11: 18 m/s horizontal center-line displacement time history for Specimen RD1

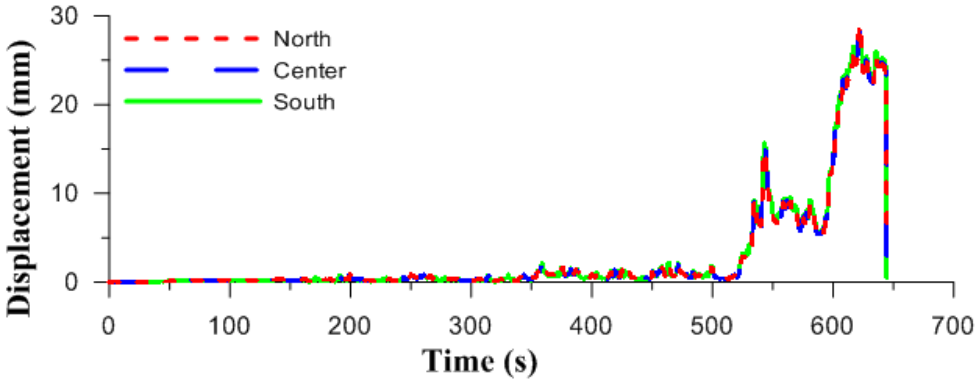

Figure G.12: 20 m/s horizontal center-line displacement time history for Specimen RD1

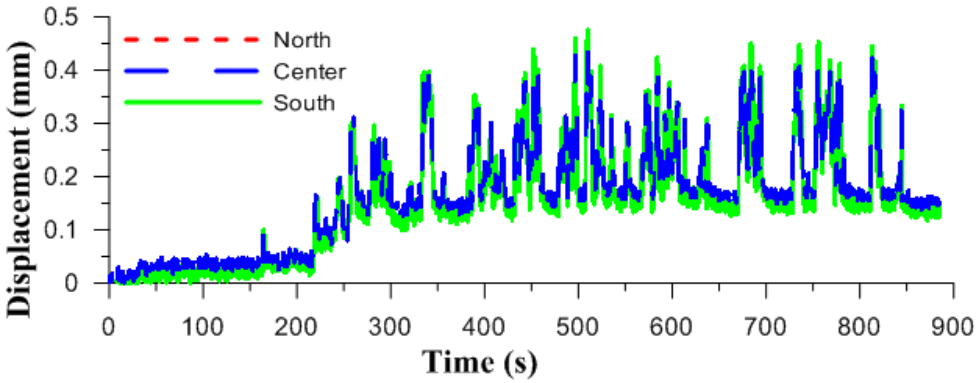

Figure G.13: 14 m/s horizontal center-line displacement time history for Specimen RD2

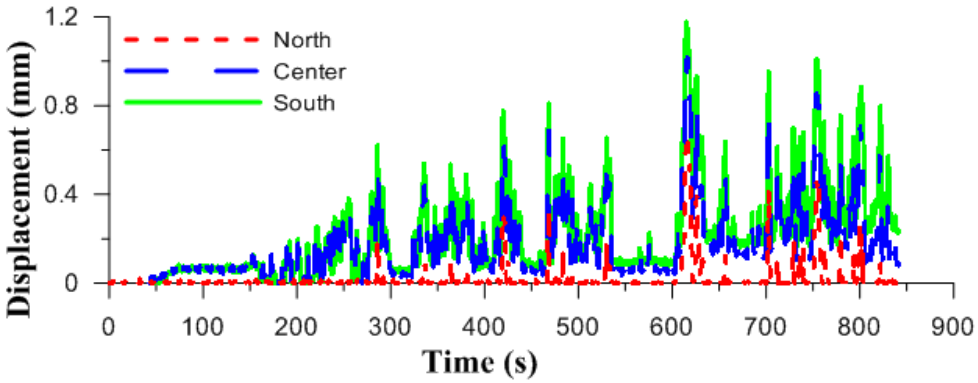

Figure G.14: 16 m/s horizontal center-line displacement time history for Specimen RD2

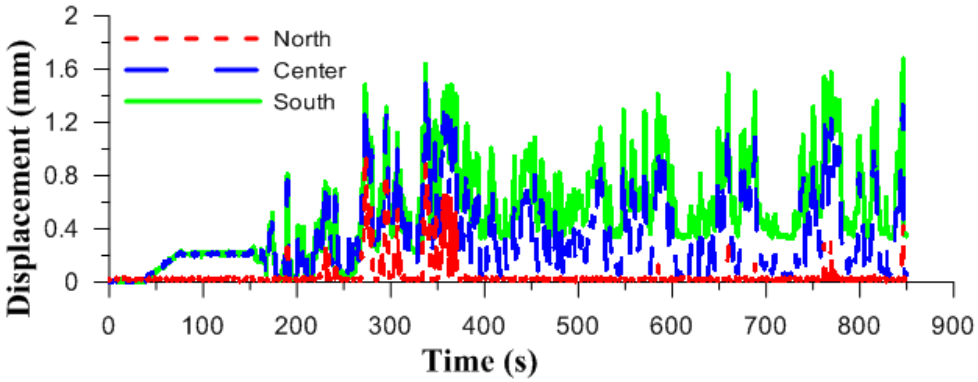

Figure G.15: 18 m/s horizontal center-line displacement time history for Specimen RD2

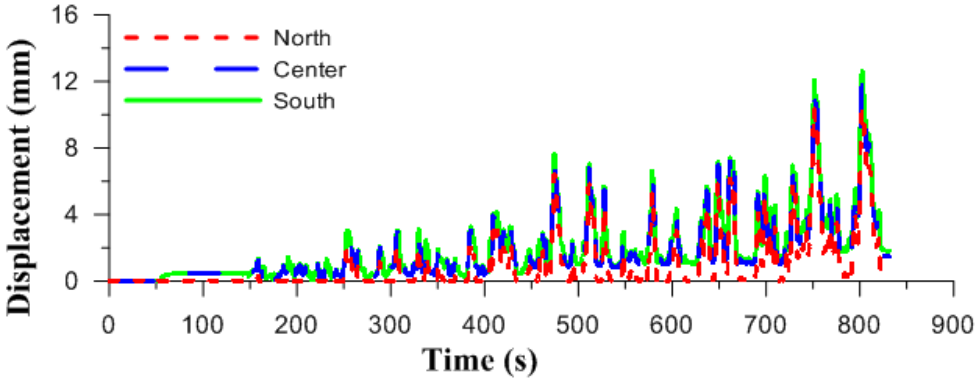

Figure G.16: 20 m/s horizontal center-line displacement time history for Specimen RD2

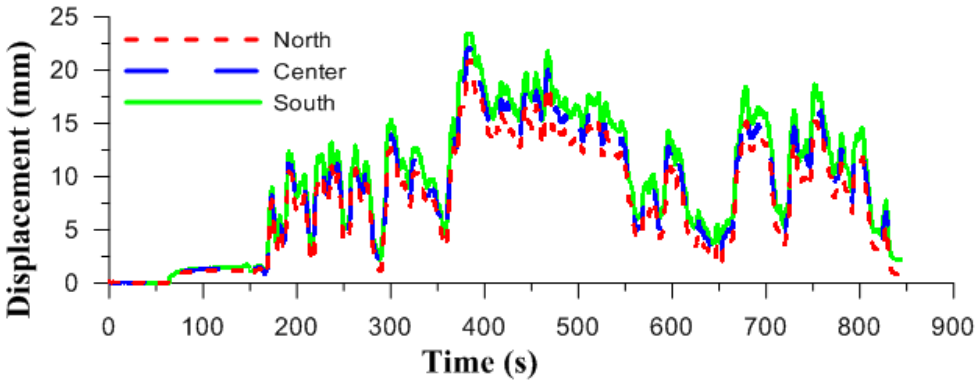

Figure G.17: 22 m/s horizontal center-line displacement time history for Specimen RD2

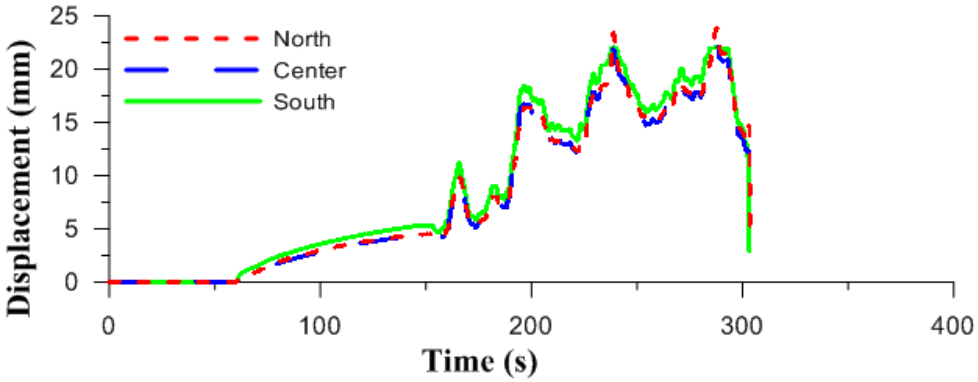

Figure G.18: 24 m/s horizontal center-line displacement time history for Specimen RD2

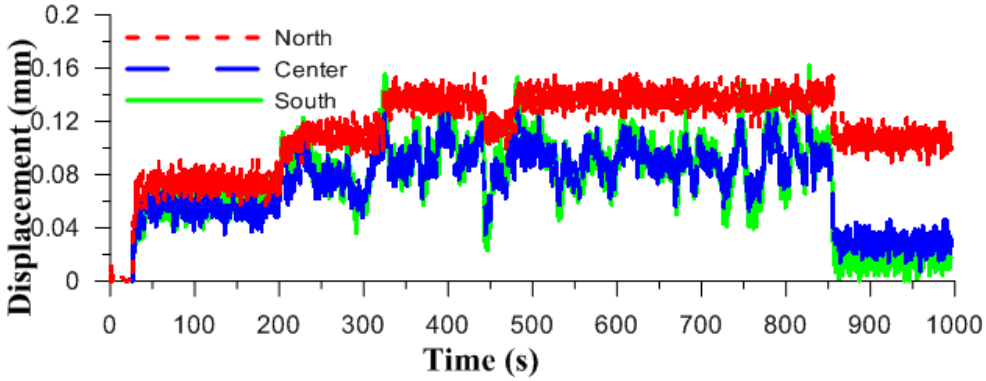

Figure G.19: 14 m/s horizontal center-line displacement time history for Specimen RD3

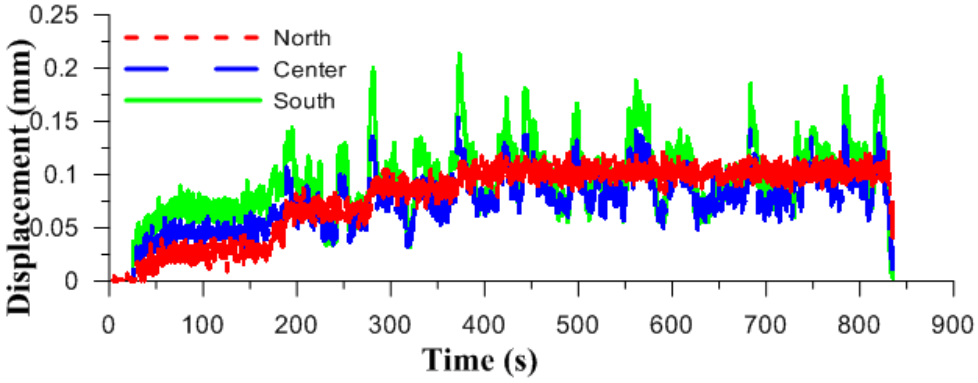

Figure G.20: 16 m/s horizontal center-line displacement time history for Specimen RD3

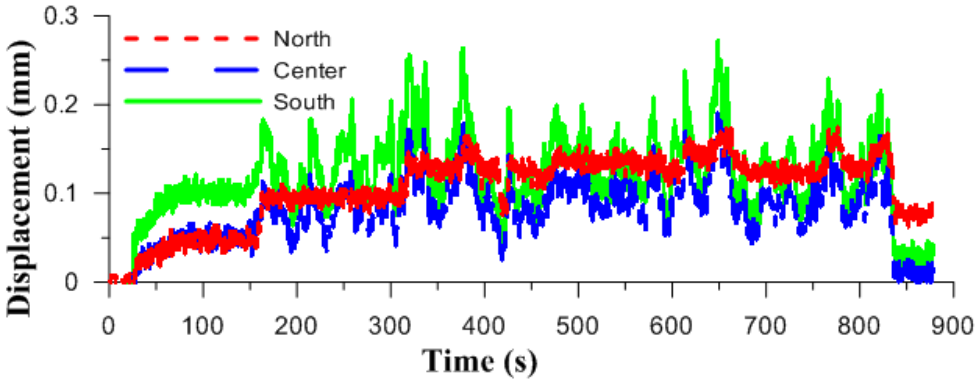

Figure G.21: 18 m/s horizontal center-line displacement time history for Specimen RD3

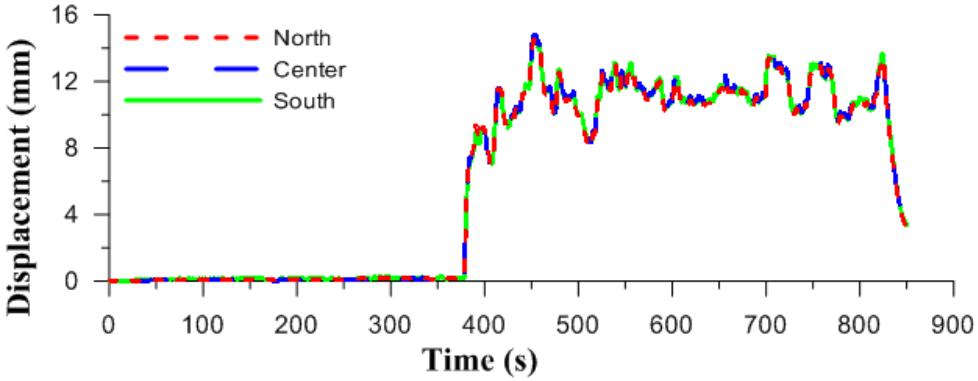

Figure G.22: 20 m/s horizontal center-line displacement time history for Specimen RD3

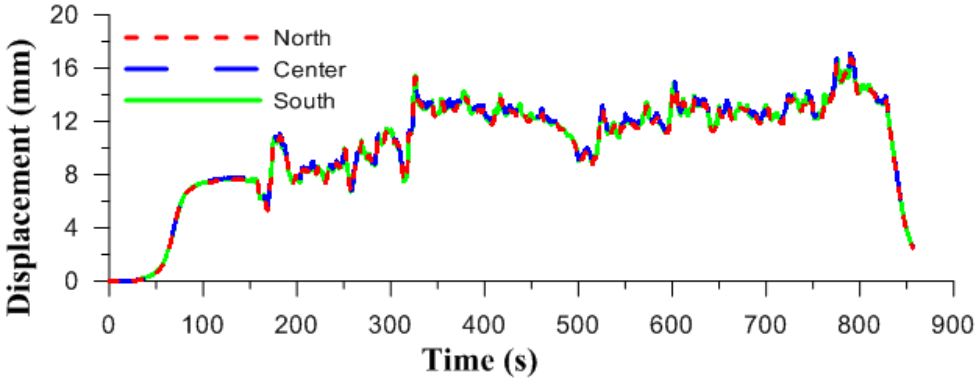

Figure G.23: 22 m/s horizontal center-line displacement time history for Specimen RD3

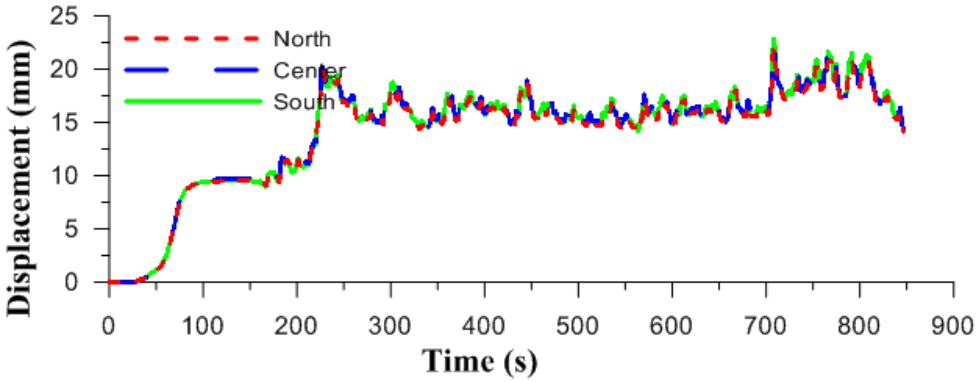

Figure G.24: 24 m/s horizontal center-line displacement time history for Specimen RD3

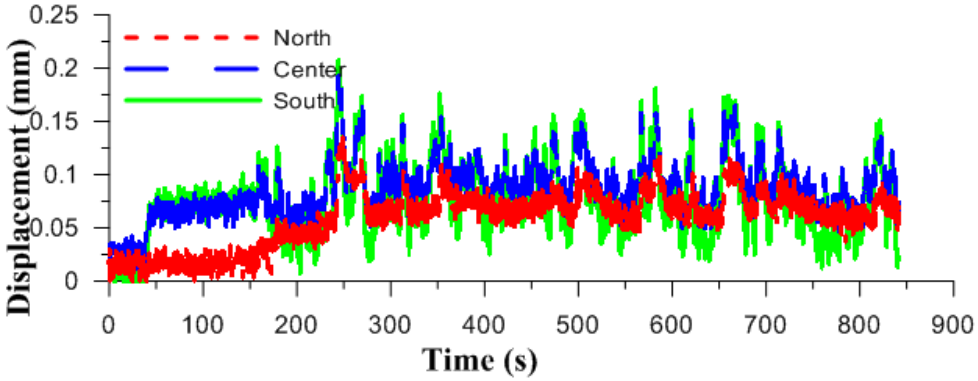

Figure G.25: 14 m/s horizontal center-line displacement time history for Specimen RD4

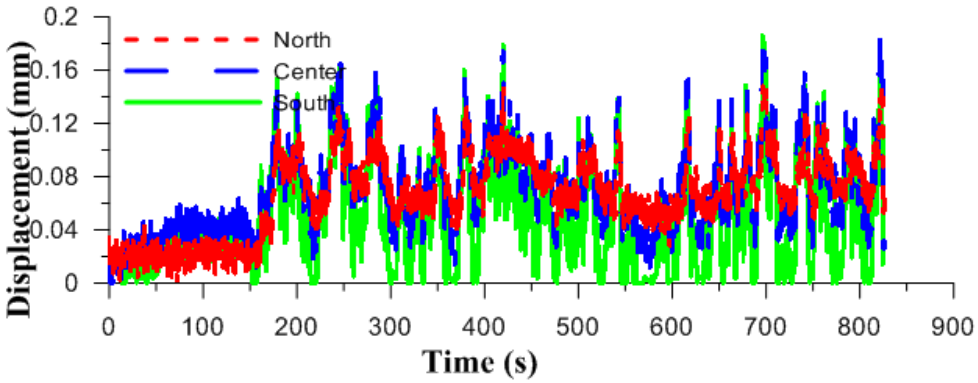

Figure G.26: 16 m/s horizontal center-line displacement time history for Specimen RD4

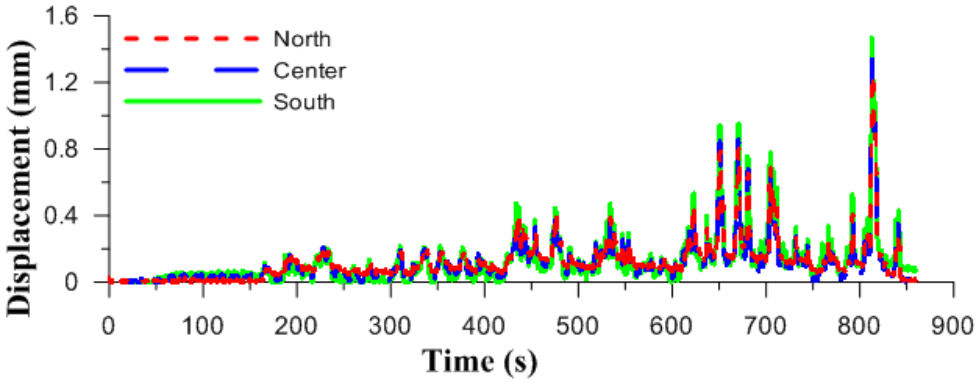

Figure G.27: 18 m/s horizontal center-line displacement time history for Specimen RD4

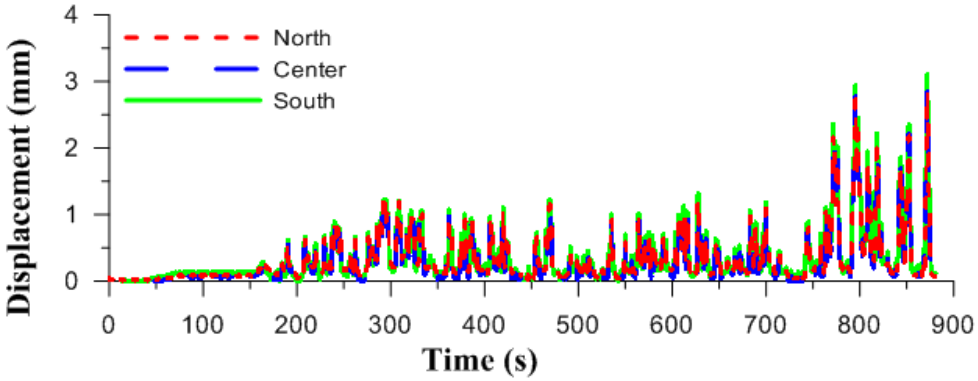

Figure G.28: 20 m/s horizontal center-line displacement time history for Specimen RD4

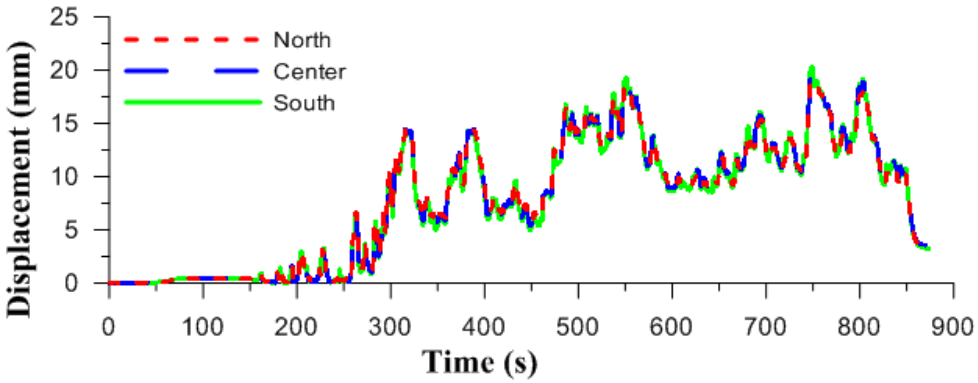

Figure G.29: 22 m/s horizontal center-line displacement time history for Specimen RD4

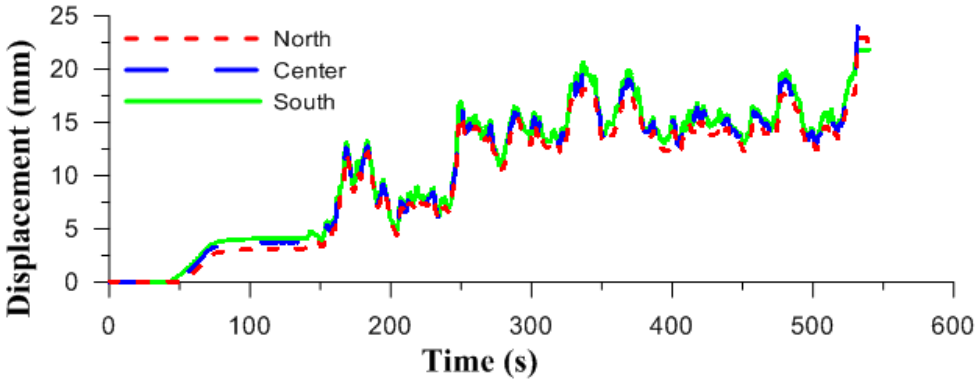

Figure G.30: 24 m/s horizontal center-line displacement time history for Specimen RD4

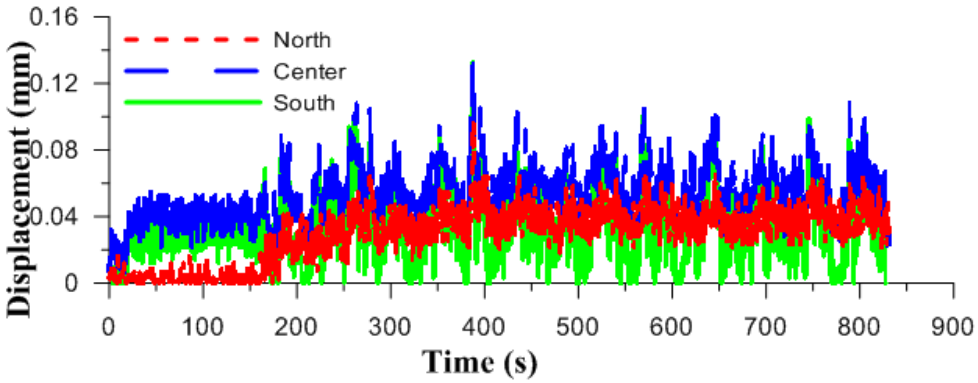

Figure G.31: 14 m/s horizontal center-line displacement time history for Specimen RD5

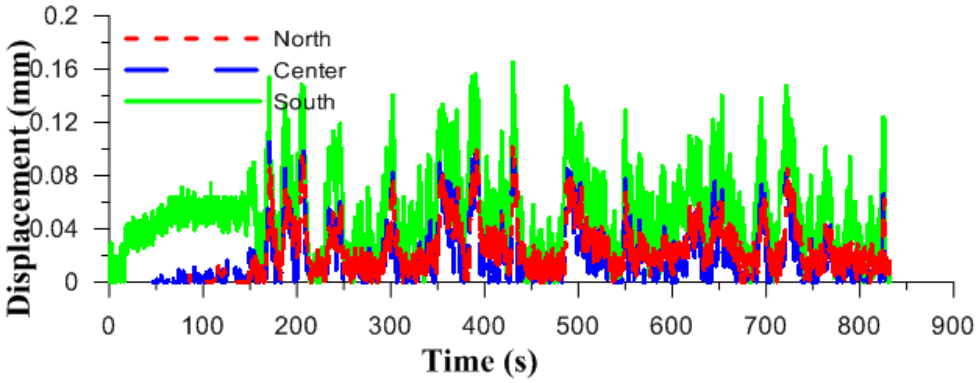

Figure G.32: 16 m/s horizontal center-line displacement time history for Specimen RD5

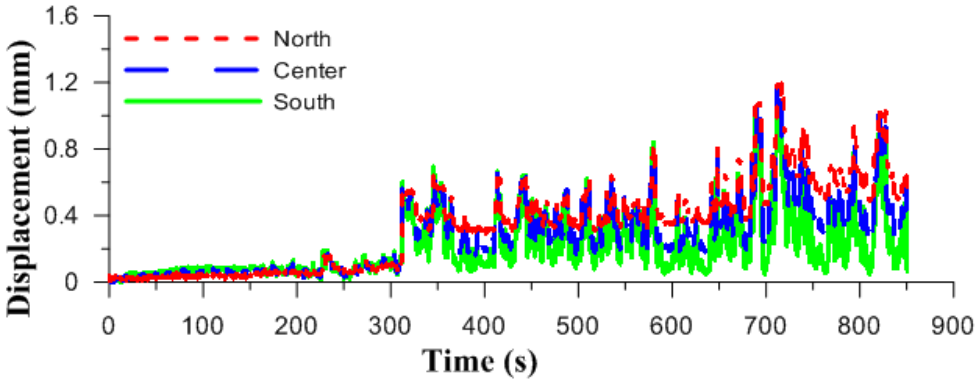

Figure G.33: 18 m/s horizontal center-line displacement time history for Specimen RD5

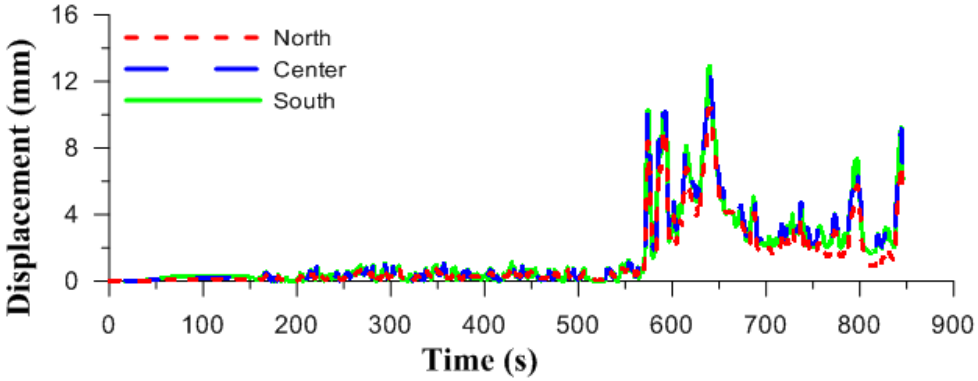

Figure G.34: 20 m/s horizontal center-line displacement time history for Specimen RD5

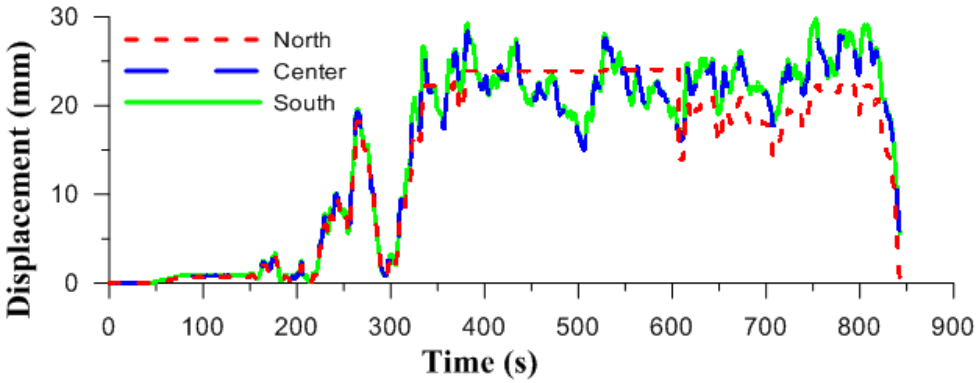

Figure G.35: 22 m/s horizontal center-line displacement time history for Specimen RD5

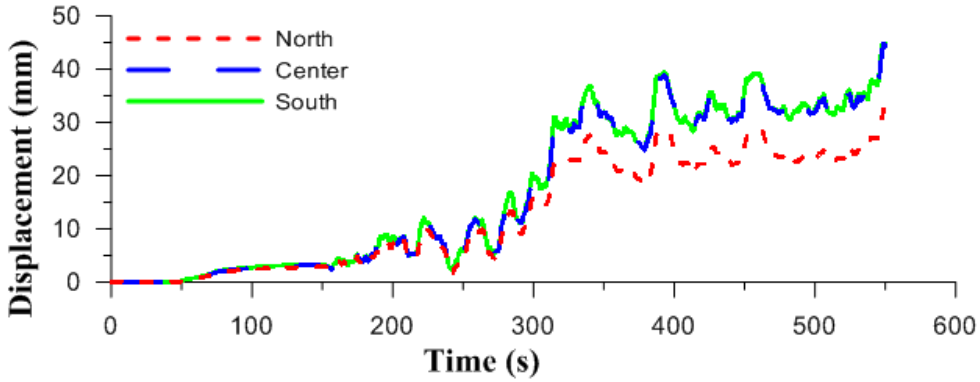

Figure G.36: 24 m/s horizontal center-line displacement time history for Specimen RD5

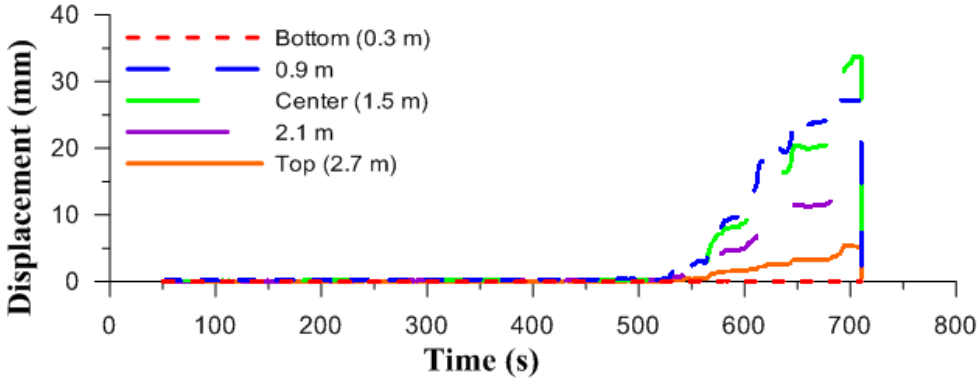

Figure G.37: 26 m/s vertical center-line displacement time history for Specimen ID1

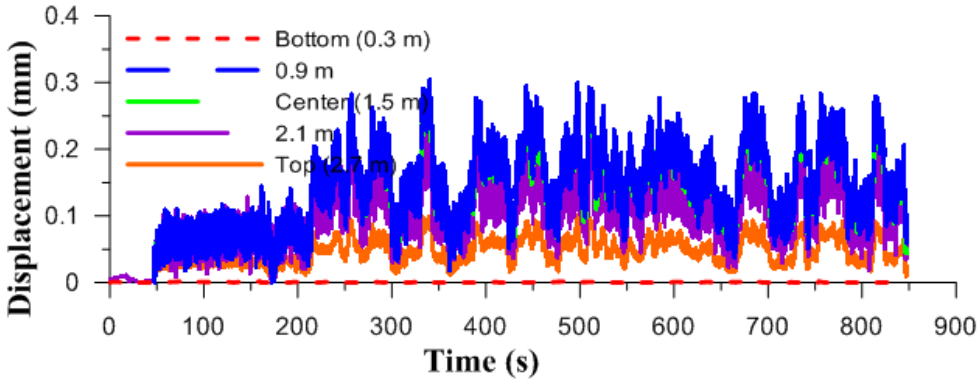

Figure G.38: 14 m/s vertical center-line displacement time history for Specimen ID2

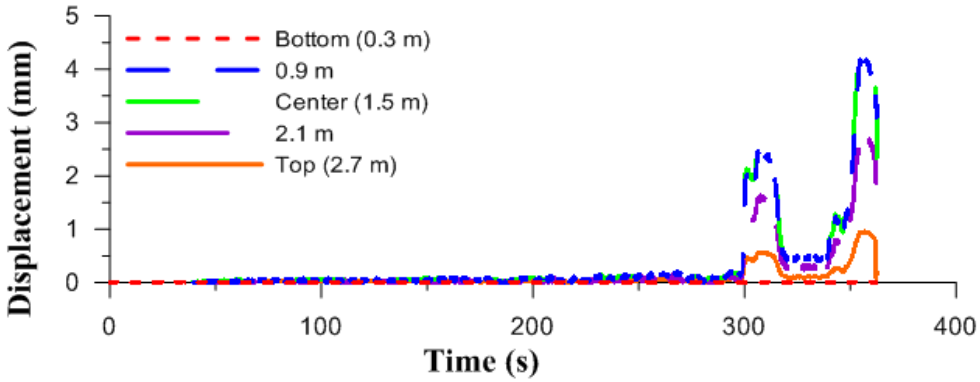

Figure G.39: 16 m/s vertical center-line displacement time history for Specimen ID2

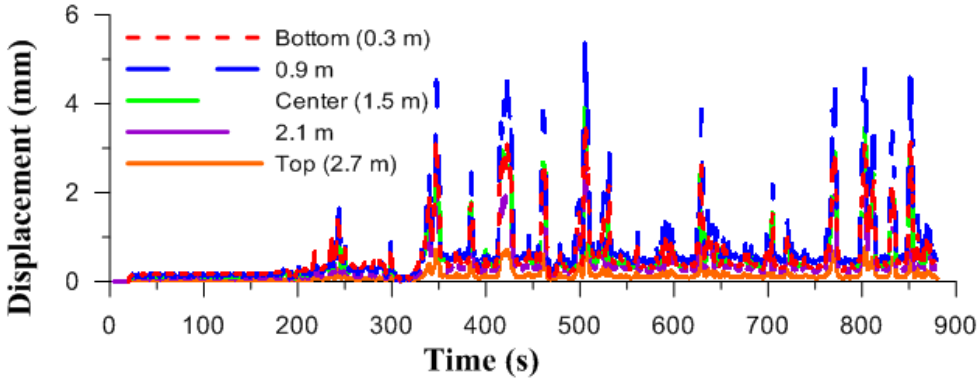

Figure G.40: 14 m/s vertical center-line displacement time history for Specimen ID3

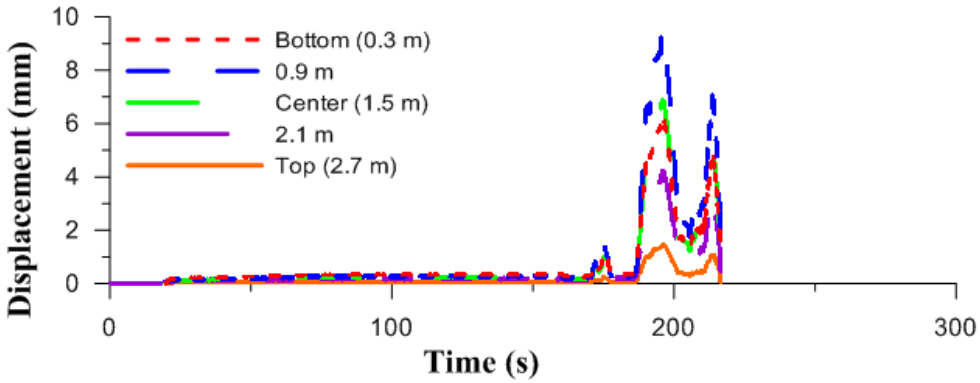

Figure G.41: 16 m/s vertical center-line displacement time history for Specimen ID3

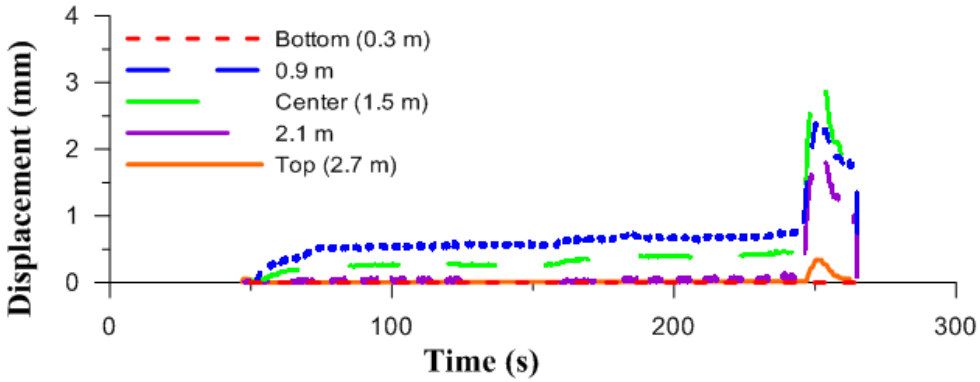

Figure G.42: 14 m/s vertical center-line displacement time history for Specimen ID4

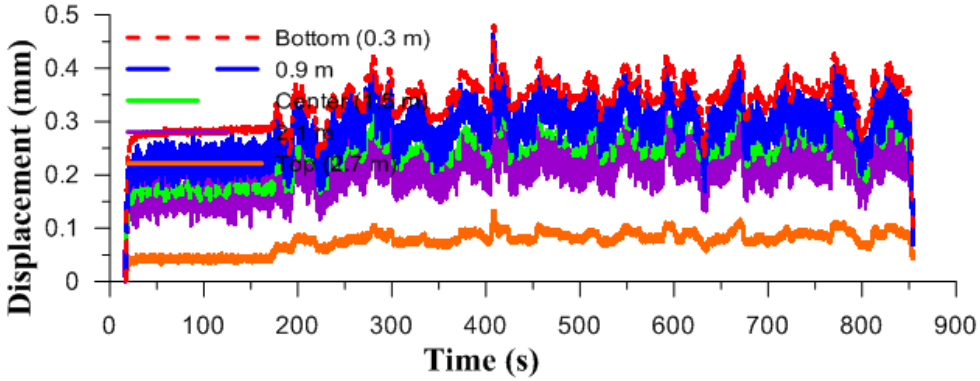

Figure G.43: 14 m/s vertical center-line displacement time history for Specimen ID5

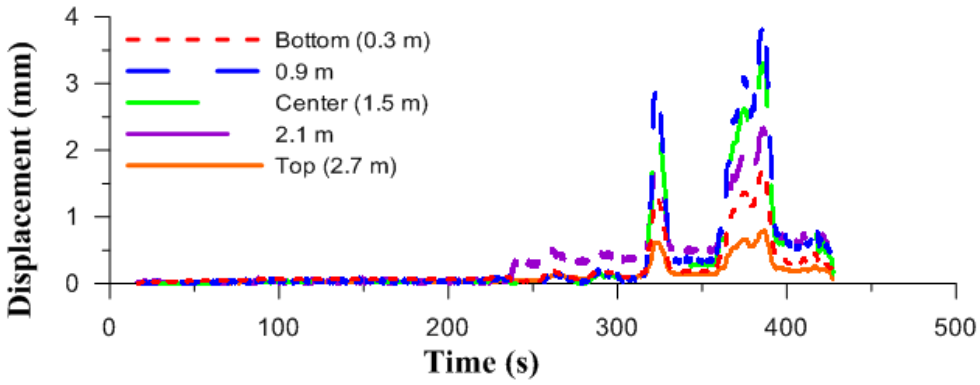

Figure G.44: 16 m/s vertical center-line displacement time history for Specimen ID5

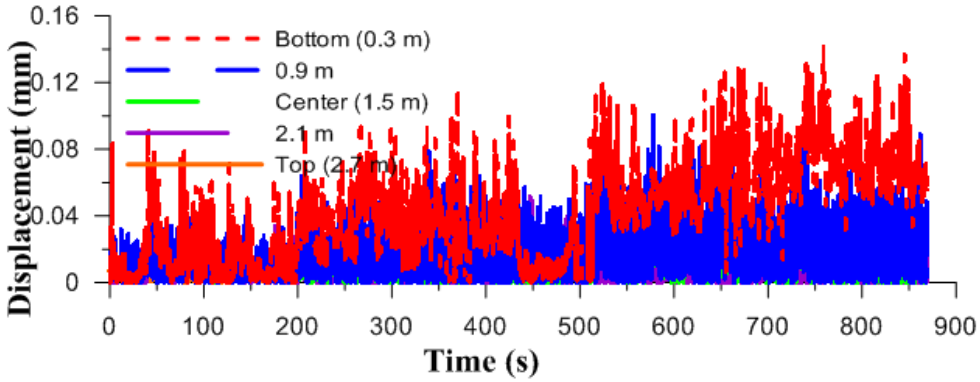

Figure G.45: 14 m/s vertical center-line displacement time history for Specimen RD1

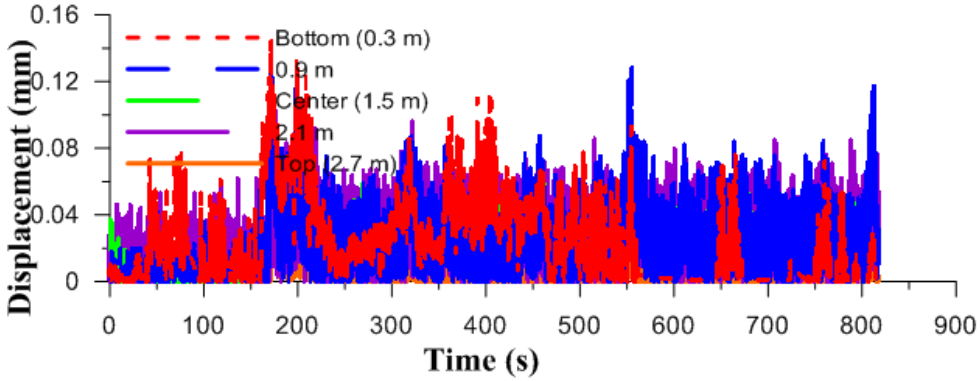

Figure G.46: 16 m/s vertical center-line displacement time history for Specimen RD1

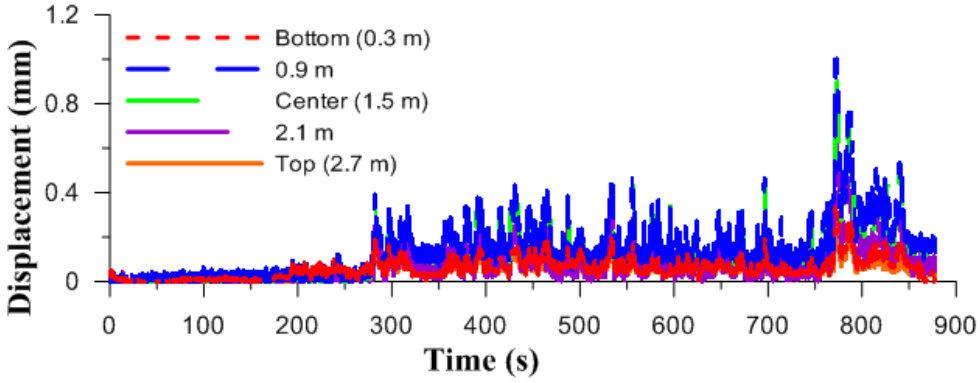

Figure G.47: 18 m/s vertical center-line displacement time history for Specimen RD1

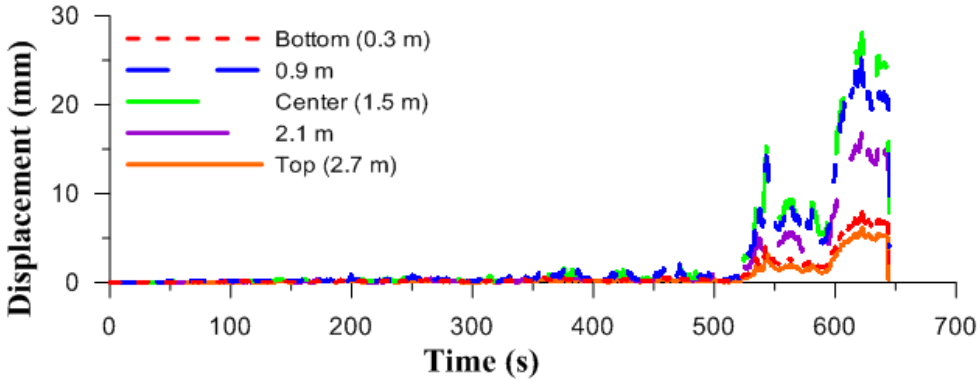

Figure G.48: 20 m/s vertical center-line displacement time history for Specimen RD1

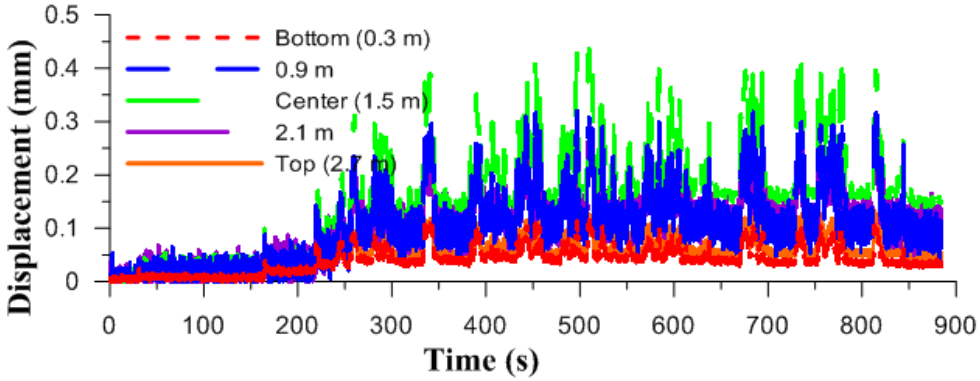

Figure G.49: 14 m/s vertical center-line displacement time history for Specimen RD2

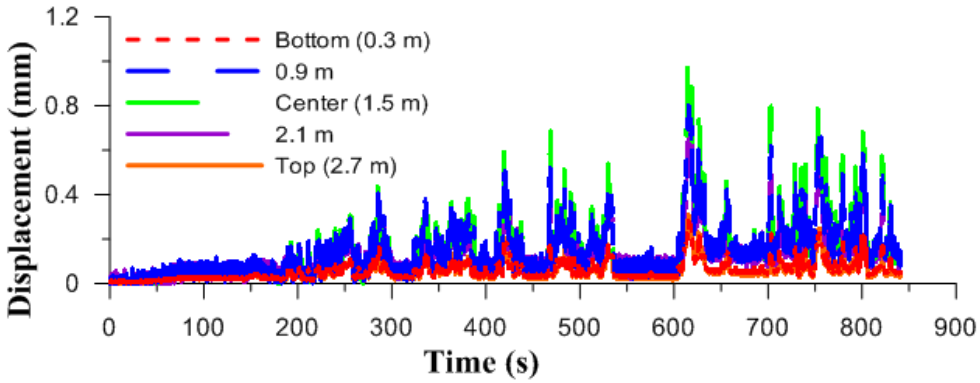

Figure G.50: 16 m/s vertical center-line displacement time history for Specimen RD2

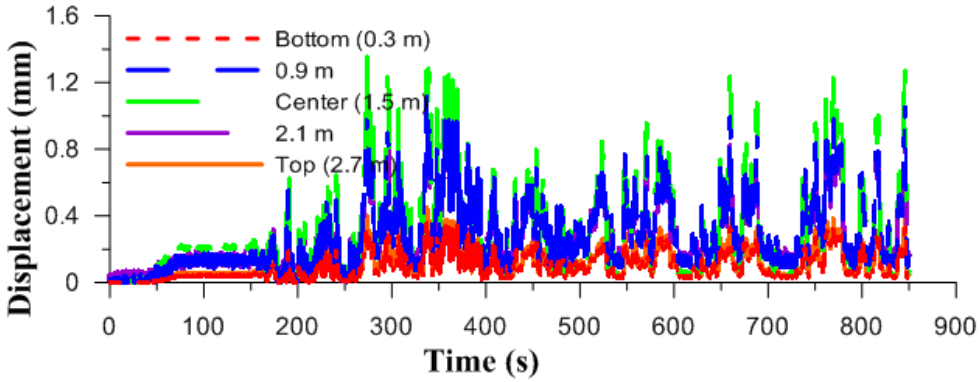

Figure G.51: 18 m/s vertical center-line displacement time history for Specimen RD2

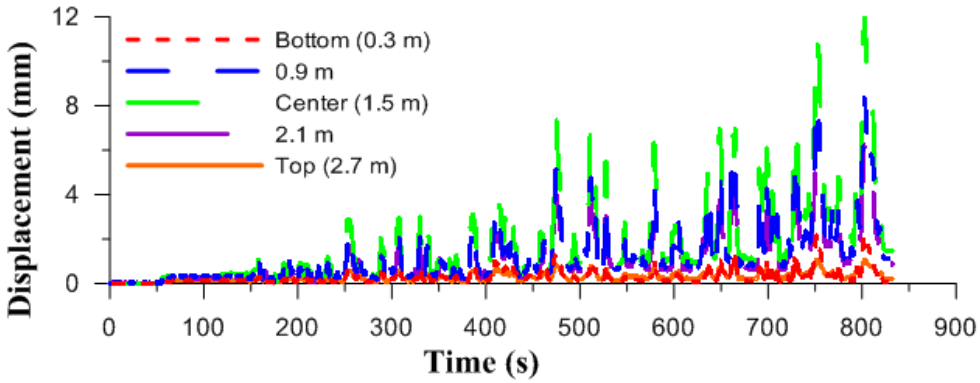

Figure G.52: 20 m/s vertical center-line displacement time history for Specimen RD2

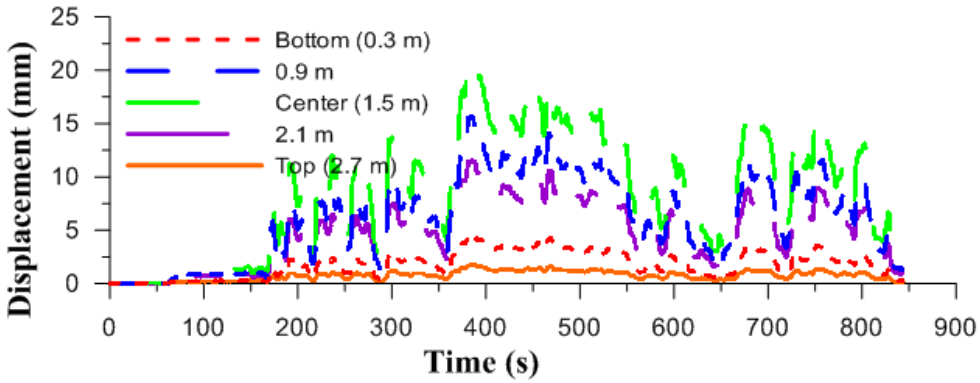

Figure G.53: 22 m/s vertical center-line displacement time history for Specimen RD2

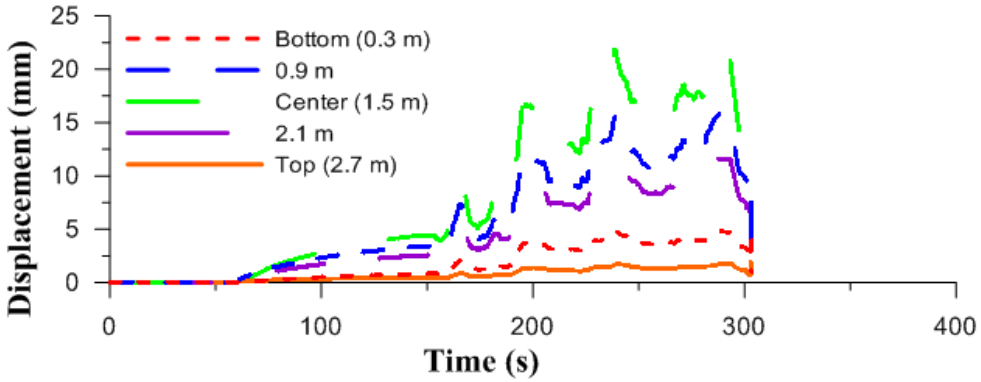

Figure G.54: 24 m/s vertical center-line displacement time history for Specimen RD2

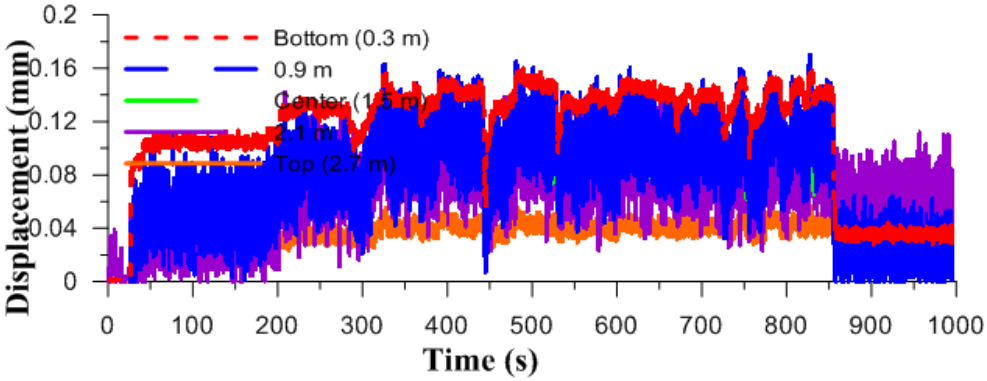

Figure G.55: 14 m/s vertical center-line displacement time history for Specimen RD3

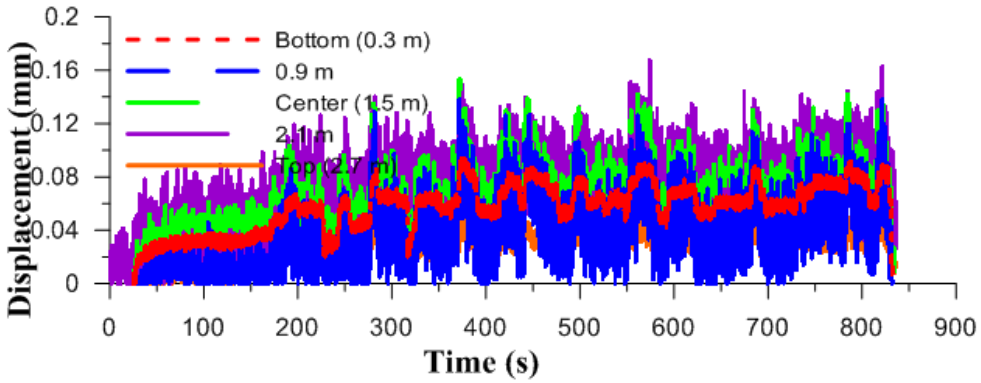

Figure G.56: 16 m/s vertical center-line displacement time history for Specimen RD3

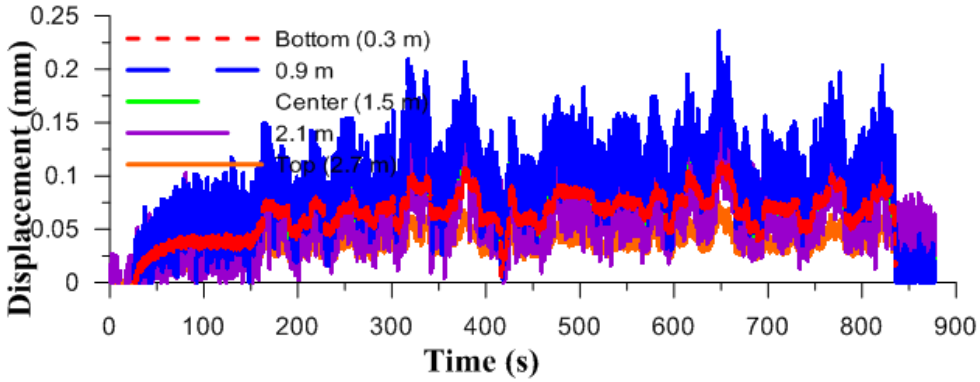

Figure G.57: 18 m/s vertical center-line displacement time history for Specimen RD3

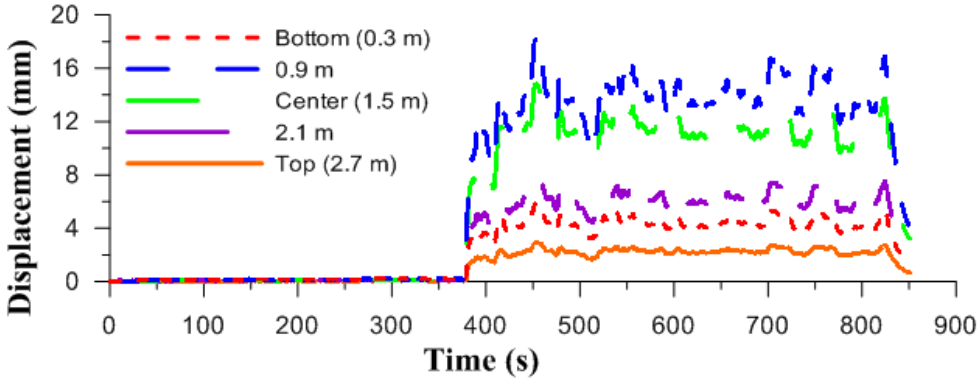

Figure G.58: 20 m/s vertical center-line displacement time history for Specimen RD3

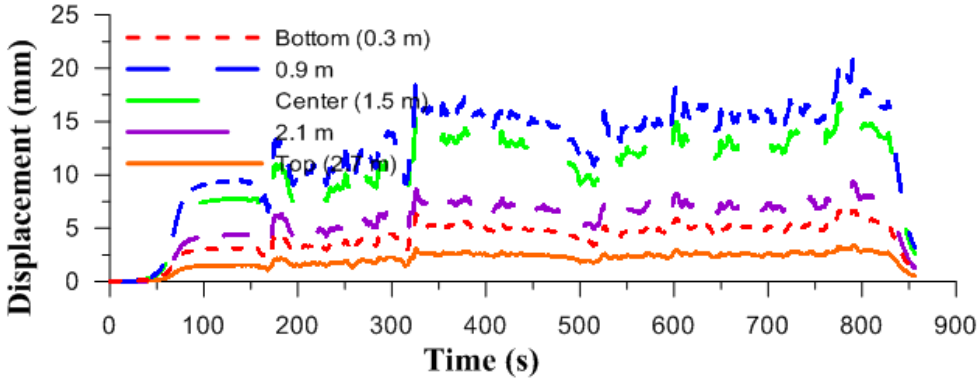

Figure G.59: 22 m/s vertical center-line displacement time history for Specimen RD3

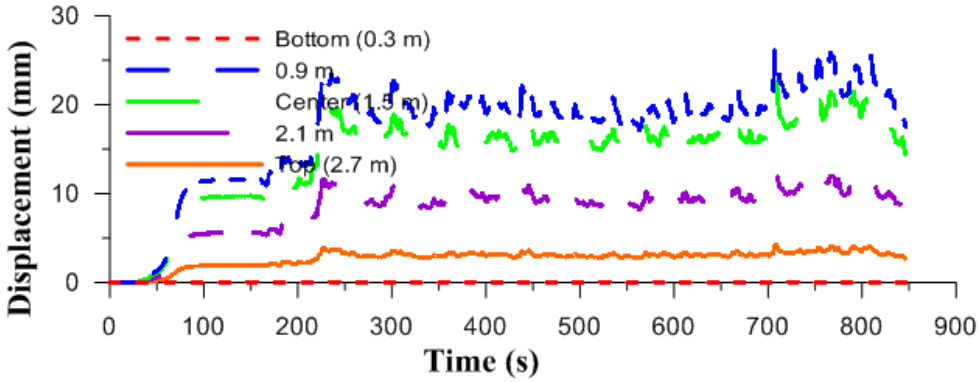

Figure G.60: 24 m/s vertical center-line displacement time history for Specimen RD3

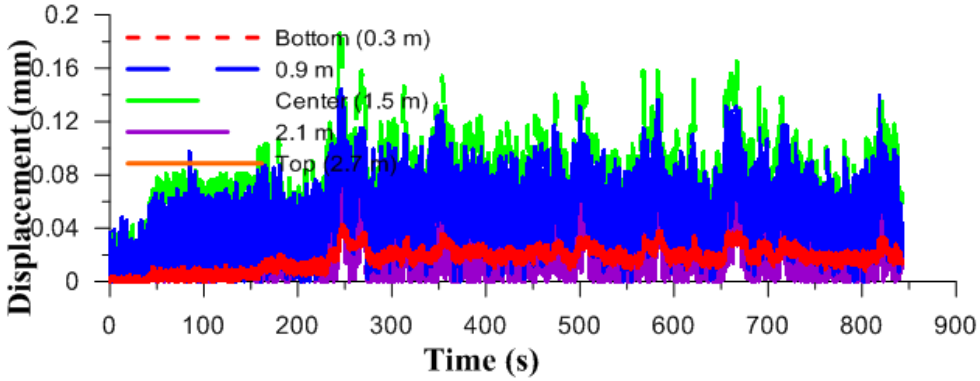

Figure G.61: 14 m/s vertical center-line displacement time history for Specimen RD4

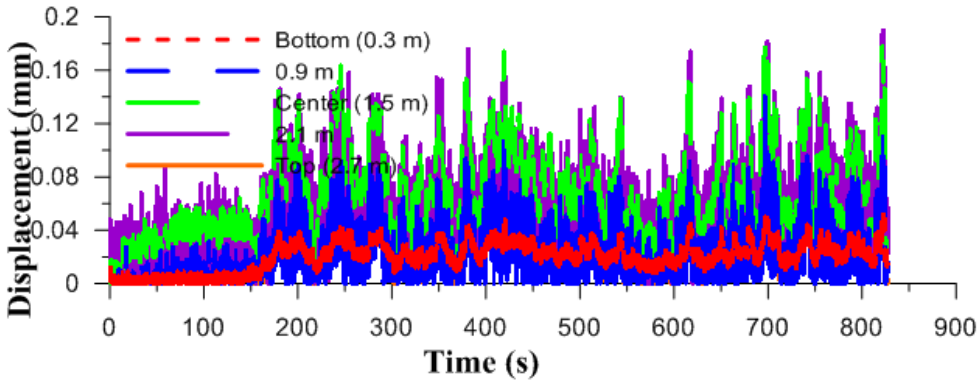

Figure G.62: 16 m/s vertical center-line displacement time history for Specimen RD4

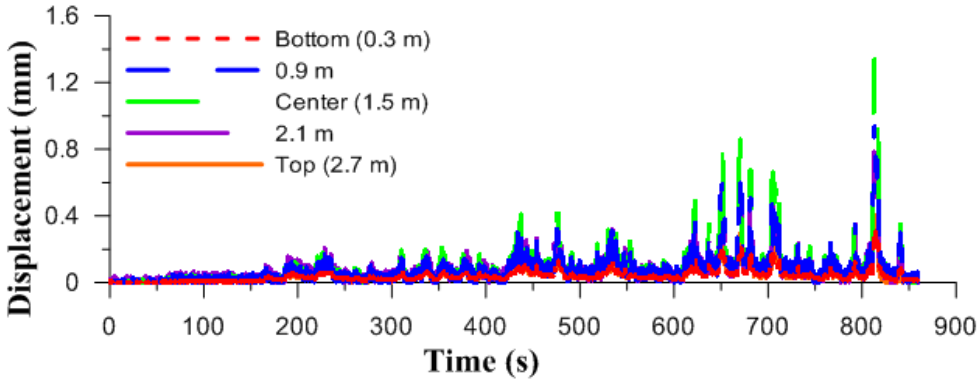

Figure G.63: 18 m/s vertical center-line displacement time history for Specimen RD4

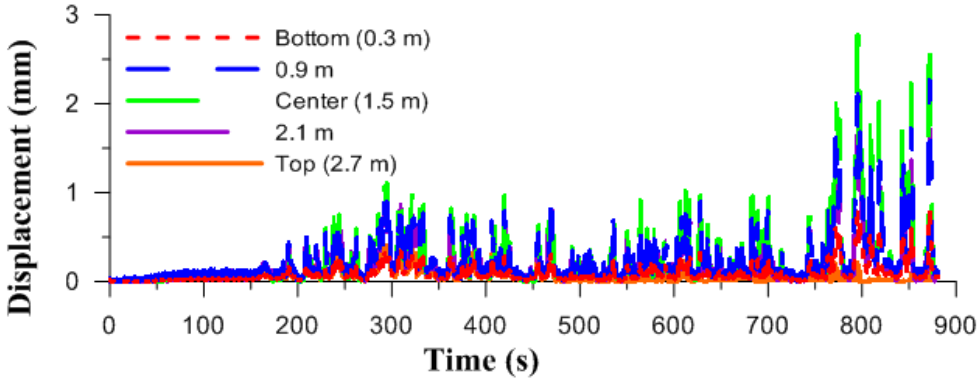

Figure G.64: 20 m/s vertical center-line displacement time history for Specimen RD4

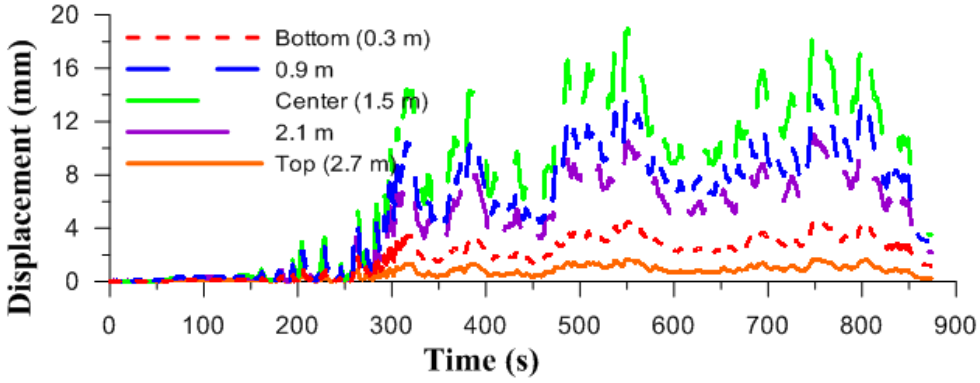

Figure G.65: 22 m/s vertical center-line displacement time history for Specimen RD4

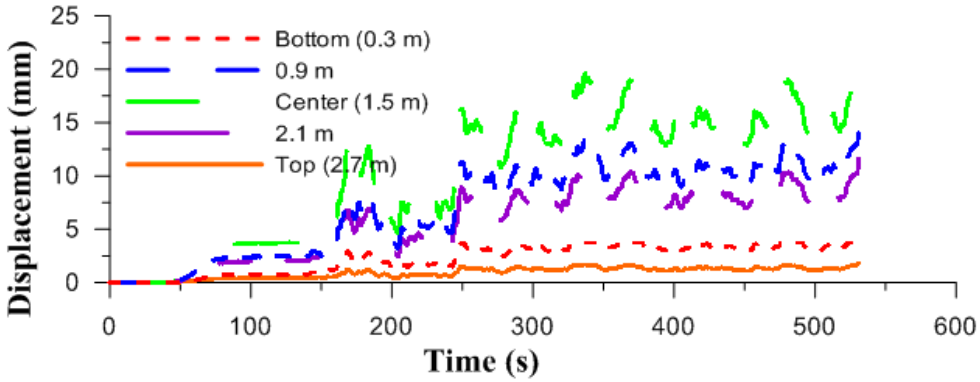

Figure G.66: 24 m/s vertical center-line displacement time history for Specimen RD4

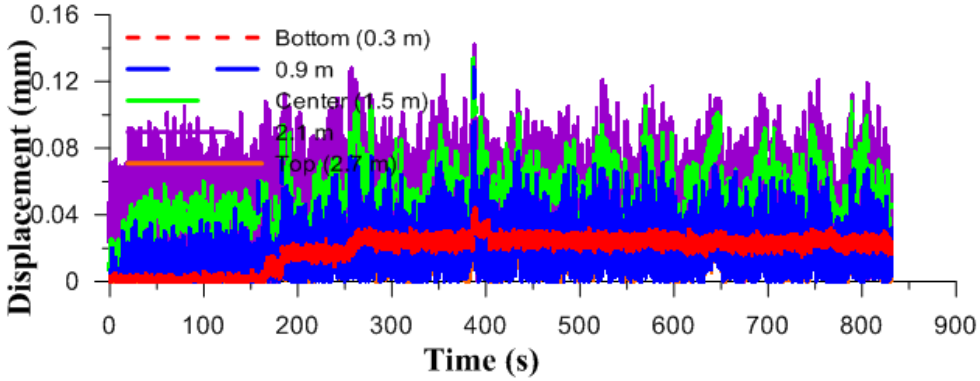

Figure G.67: 14 m/s vertical center-line displacement time history for Specimen RD5

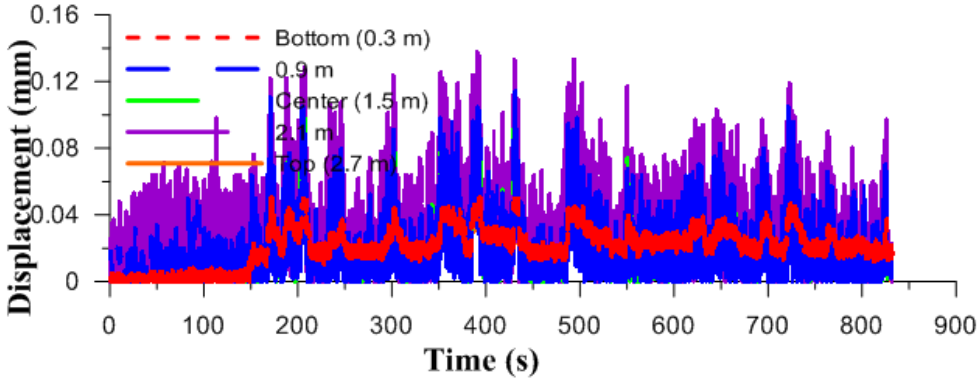

Figure G.68: 16 m/s vertical center-line displacement time history for Specimen RD5

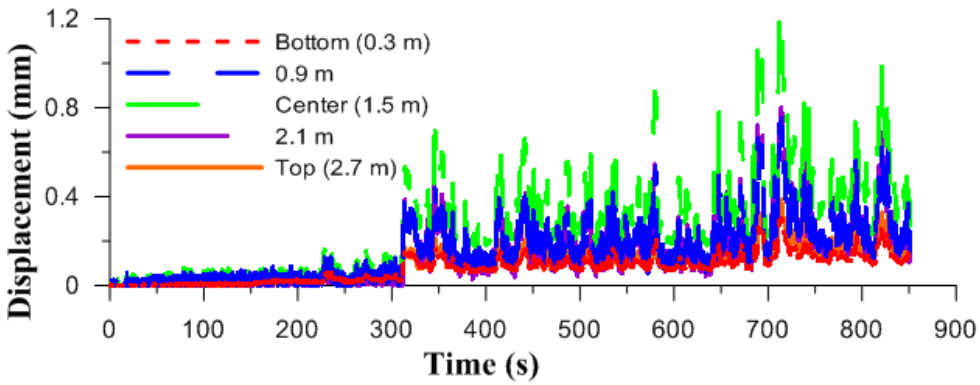

Figure G.69: 18 m/s vertical center-line displacement time history for Specimen RD5

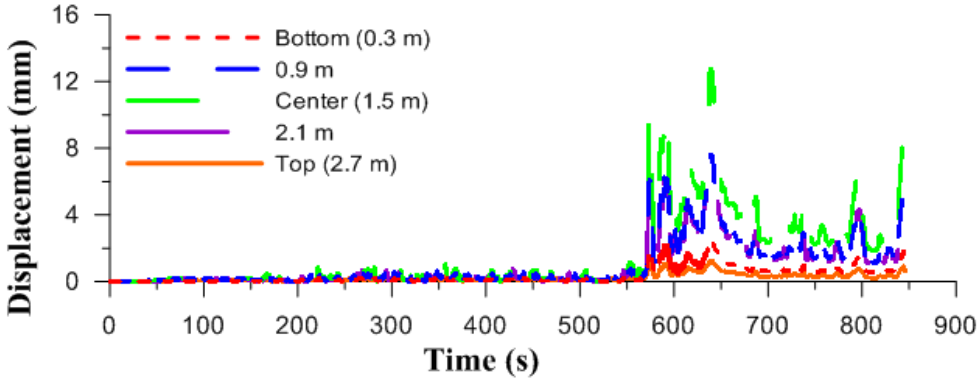

Figure G.70: 20 m/s vertical center-line displacement time history for Specimen RD5

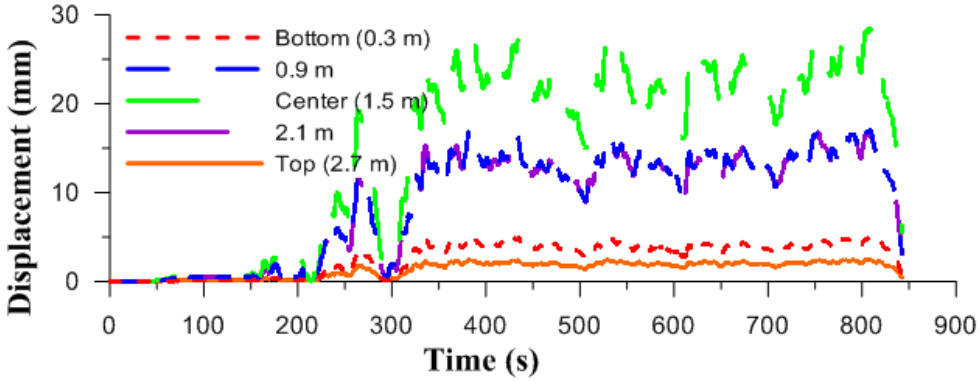

Figure G.71: 22 m/s vertical center-line displacement time history for Specimen RD5

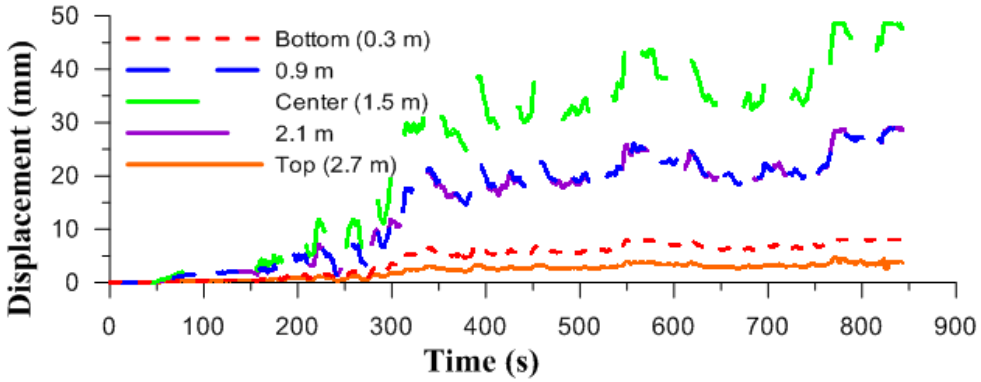

Figure G.72: 24 m/s vertical center-line displacement time history for Specimen RD5

Appendix H: Mathcad Model

This appendix presents the single degree of freedom, dynamic model that was created for this study in MathCad 15©.

Read Wind Time History Data

Define Physical System Properties

$y_h := 1600mm$ — Location of Mid-Height crack

$L := 3000mm$ — Total height of wall

$y := 0mm, 1mm .. L$ — Height increments of wall

$crit := 1\%$ — Critical dampening

Define Mode Shape

$$\Psi(y) := \begin{cases} x \leftarrow \frac{y}{y_h} & \text{if } y \le y_h \\ x \leftarrow 1 - \frac{y - y_h}{L - y_h} & \text{otherwise} \end{cases}$$

Shape Function of Cracked Wall

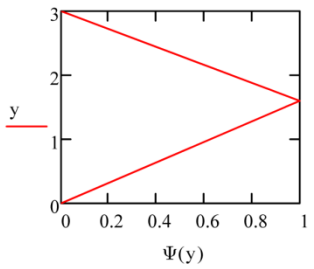

Define System Mass

$mass := 2.0\frac{kN}{m}$ — Unit mass of the wall, Measured from Specimen ID4

$M_{sys} := \int_0^L \frac{mass}{g} \cdot \Psi(x) \cdot \Psi(x)\, dx = 203.94kg$ — System Mass

Interpolate Additional Data points in the Wind Time History to reduce time step increments using Sinc function

$\Delta\tau := 0.057s$ — Initial time steps of time history

$b := 10$ — Number of data points to add

$\Delta t := \frac{\Delta\tau}{b} = 0.0057\,s$ — New time steps of time history

$n := 15$ — Terms included in interpolated series

Interpolate new time history using the *sinc* function

$$
\begin{aligned}
u := \;& \text{for } k \in n+1 \,..\, \text{rows}(TH) - (n+1) \\
& \quad \text{for } i \in 1 \,..\, b \\
& \quad\quad z_{[(k)\cdot b]+i} \leftarrow 0 \\
& \quad\quad \text{for } j \in -n \,..\, n+1 \\
& \quad\quad\quad a \leftarrow \frac{1}{2} \quad \text{if } (j = -n) \vee (j = n+1) \\
& \quad\quad\quad a \leftarrow 1 \quad \text{otherwise} \\
& \quad\quad\quad z_{[(k)\cdot b]+i} \leftarrow z_{[(k)\cdot b]+i} + a \cdot \left[TH_{(k+j)}\right] \cdot \frac{\sin\left[\pi \cdot \left(\frac{i\cdot\Delta t}{\Delta\tau} - j\right)\right]}{\pi \cdot \left(\frac{i\cdot\Delta t}{\Delta\tau} - j\right)} \\
& \quad \text{for } i \in 1 \,..\, (n+1)\cdot b \\
& \quad\quad z_i \leftarrow 400N \\
& z
\end{aligned}
$$

Time increment array for graphing

$$
\begin{aligned}
t := \;& \text{for } i \in 1 \,..\, \text{rows}(u) \\
& \quad tt_i \leftarrow (i-1)\cdot\Delta t \\
& tt
\end{aligned}
$$

Generate the System Forcing Function

Determine Force at time step in sec. Rather than array location

$$
\begin{aligned}
F(t) := \;& i \leftarrow \frac{t}{\Delta t} \\
& F \leftarrow u_i
\end{aligned}
$$

System Forcing Function

$$F_{sys}(t) := \frac{F(t)}{2}\cdot\Psi(1100mm) + \frac{F(t)}{2}\cdot\Psi(1900mm)$$

System Stiffness

Determine Static Stiffness

Initial Stiffness determined from the cracking of RS3

$$K_{in} := \frac{3.095kN}{0.277mm} = 1.117 \times 10^7 \cdot \frac{N}{m}$$

Modification factor for Static Stiffness

$$ucf := 1.3 \qquad K_{inn} := \frac{K_{in}}{ucf} = 8.595 \times 10^6 \, \frac{kg}{s^2}$$

Generate Non-Linear Stiffness, using Cubic Spline Curve

Initial Non-linear stiffness, Cracking at the base of the wall to mid-height cracking

$$VALS1 := \begin{pmatrix} 0 \\ 0.8 \\ 1.16 \\ 2.9 \\ 10 \\ 19 \\ 30 \\ 42 \end{pmatrix} \cdot mm \qquad VALS2 := \begin{pmatrix} 0 \\ 0.45 \\ 0.6 \\ 1.01 \\ 1.71 \\ 2.41 \\ 3.2 \\ 3.9 \end{pmatrix} 4.7kN$$

The points used to generate the Cubic Spline Curve

X-ordinate values are modified (4.7) to increase the model stiffness, from the inital measured static stiffness.

$$x := 0, 0.001mm .. VALS1_{rows(VALS1)}$$

The displacement range that is used to generate cubic spline curve

$$z := cspline(VALS1, VALS2)$$

Function that generates the coefficients for the cubic spline curve

$$ew(x) := interp(z, VALS1, VALS2, x)$$

The mathematical equation for the cubic spline curve

$$dCS_{47}(x) := \frac{d}{dx} ew(x)$$

The derivative of the cubic spline curve to determine the stiffness - used in the model

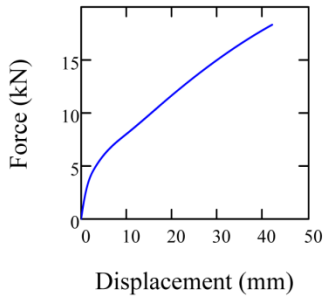

Cubic Spline Curve

Non-linear stiffness, Mid-height cracking to second increment of damage

$$VALS1 := \begin{pmatrix} 0 \\ 0.8 \\ 1.16 \\ 2.9 \\ 10 \\ 20 \\ 30 \\ 42 \end{pmatrix} \cdot mm \qquad VALS2 := \begin{pmatrix} 0 \\ 0.45 \\ 0.6 \\ 1.0 \\ 1.73 \\ 2.5 \\ 3.2 \\ 3.9 \end{pmatrix} \cdot 1.4kN$$

$$z := cspline(VALS1, VALS2) \qquad ew(x) := interp(z, VALS1, VALS2, x) \cdot 1.0$$

$$dCS_{14}(x) := \frac{d}{dx} ew(x)$$

Non-linear stiffness, second increment of damage to collapse of wall

$$VALS1 := \begin{pmatrix} 0 \\ 0.8 \\ 1.16 \\ 2.9 \\ 10 \\ 20 \\ 30 \\ 42 \end{pmatrix} \cdot mm \qquad VALS2 := \begin{pmatrix} 0 \\ 0.45 \\ 0.6 \\ 1.0 \\ 1.73 \\ 2.5 \\ 3.2 \\ 3.9 \end{pmatrix} \cdot 0.9kN$$

$z := cspline(VALS1, VALS2)$

$ew(x) := interp(z, VALS1, VALS2, x) \cdot 1.0$

$dCS_{09}(x) := \frac{d}{dx} ew(x)$

System Stiffness

$$K_{sys}(c,x,z) := \begin{| j \leftarrow K_{in} \cdot \Psi(1500mm) \quad \text{if } c = 0 \\ j \leftarrow dCS_{47}(x) \cdot \Psi(1500mm) \quad \text{if } c = 1 \\ j \leftarrow dCS_{14}(x) \cdot \Psi(1500mm) \quad \text{if } c = 2 \\ j \leftarrow dCS_{47}(x)\,\Psi(1500mm) \cdot \left(1 - \frac{z}{2000}\right) \ldots \quad \text{if } c = 3 \\ \quad + dCS_{14}(x) \cdot \Psi(1500mm) \cdot \left(\frac{z}{2000}\right) \\ j \leftarrow dCS_{09}(x) \cdot \Psi(1500mm) \quad \text{if } c = 4 \\ j \leftarrow dCS_{14}(x)\,\Psi(1500mm) \cdot \left(1 - \frac{z}{2000}\right) \ldots \quad \text{if } c = 5 \\ \quad + dCS_{09}(x) \cdot \Psi(1500mm) \cdot \left(\frac{z}{2000}\right) \\ j \leftarrow K_{in} \cdot \Psi(1500mm) \cdot \left(1 - \frac{z}{2000}\right) \ldots \quad \text{if } c = 6 \\ \quad + dCS_{47}(x) \cdot \Psi(1500mm) \cdot \left(\frac{z}{2000}\right) |$$

c = 0; Initial Static Stiffness

c = 1; Initial Non-linear Stiffness, occurring with cracking at the base of the wall (4.7 modification)

c = 2; Non-linear Stiffness after mid-height cracking (1.4 modification)

c = 3; Linear Transition from Base cracking to mid-height cracking stiffness (4.7 to 1.4)

c = 4; Additional Incremental Damage (0.9 Modification)

c = 5; Transition from Mid-height cracking stiffness to additional damage stiffness (1.4 to 0.9)

c = 6; Transition from Static Stiffness to Non-linear stiffness (Kin to 4.7 Modification)

Numark's β Method Factors

$\beta := \frac{1}{4}$ $\qquad \gamma := 0.5$

Damage Indication

$cracked := 0$

0 = undamaged wall
1 = cracking at the base of wall
2 = mid-height cracking occured

Step-by-step Newmark's β Method Model

$\eta :=$ | $CRACKED \leftarrow cracked$

$Z \leftarrow 0$

$n' \leftarrow 0\,\frac{m}{s}$

$n'' \leftarrow 0\,\frac{m}{s^2}$ — Initialize variables

$n \leftarrow 0m$

$F \leftarrow F_{sys}(\Delta t)$ — Initial Force Applied at the start of test

$n \leftarrow \frac{F}{K_{sys}(CRACKED, n, Z)}$ — Initial Static Displacement

while $\delta F > 1N$

$\delta F \leftarrow F - K_{sys}(CRACKED, n, Z)\cdot n$

$\delta n \leftarrow \frac{\delta F}{K_{sys}(CRACKED, n, Z)}$ — Determine Displacement Due to Initial Force

$n \leftarrow n + \delta n$

$F \leftarrow K_{sys}(CRACKED, n, Z)\cdot n$

for $i \in 1 .. rows(u) - 1$

$t \leftarrow \Delta t\cdot i$

$k_c \leftarrow K_{sys}(CRACKED, n, Z)$

$c_{crit} \leftarrow 2\cdot\sqrt{M_{sys}\cdot k_c}$ — Determine Linear Displacement Newmark's β Method using incremental forces

$C_{sys} \leftarrow crit\cdot c_{crit}$

$K_{psu} \leftarrow k_c + \frac{1}{\beta\cdot\Delta t^2}\cdot M_{sys} + \frac{\gamma}{\beta\cdot\Delta t}\cdot C_{sys}$

$\Delta F_{psu} \leftarrow \left(F_{sys}(t + \Delta t) - F_{sys}(t)\right) + M_{sys}\cdot\left(\frac{1}{\beta\cdot\Delta t}\cdot n' + \frac{1}{2\cdot\beta}\cdot n''\right) \ldots + C_{sys}\cdot\left[\frac{\gamma}{\beta}\cdot n' + \left(\frac{\gamma}{2\beta} - 1\right)\cdot(\Delta t)\cdot n''\right]$

$\Delta n \leftarrow \Delta F_{psu}\cdot\frac{1}{K_{psu}}$

$\Delta n'' \leftarrow \frac{1}{\beta\cdot(\Delta t)^2}\cdot\Delta n - \frac{1}{\beta\cdot\Delta t}\cdot n' - \frac{1}{2\cdot\beta}\cdot n''$

$\Delta n' \leftarrow \frac{\gamma}{\beta\cdot\Delta t}\cdot\Delta n - \frac{\gamma}{\beta}\cdot n' - \left(\frac{\gamma}{2\cdot\beta} - 1\right)\cdot(\Delta t)\cdot n''$

$n \leftarrow \Delta n + n$

$n' \leftarrow \Delta n' + n'$

$n'' \leftarrow \Delta n'' + n''$

$\delta F \leftarrow F_{sys}(t + \Delta t) - M_{sys}\cdot n'' - C_{sys}\cdot n' - K_{sys}(CRACKED, n, Z)\cdot n$

while $\delta F > 1N$ — Iterative loop to determine non-linear displacement of wall at current time step

$k_c \leftarrow K_{sys}(CRACKED, n, Z)$

$c_{crit} \leftarrow 2\cdot\sqrt{M_{sys}\cdot k_c}$

$K_{psu} \leftarrow k_c + \frac{1}{\beta\cdot\Delta t^2}\cdot M_{sys} + \frac{\gamma}{\beta\cdot\Delta t}\cdot C_{sys}$

$$\delta n \leftarrow \frac{\delta F}{K_{psu}}$$

$$\delta n' \leftarrow \frac{\gamma}{\beta \cdot \Delta t} \cdot \delta n$$

$$\delta n'' \leftarrow \frac{1}{\beta \cdot (\Delta t)^2} \cdot \delta n$$

$n \leftarrow n + \delta n$

$n' \leftarrow n' + \delta n'$

$n'' \leftarrow n'' + \delta n''$

$\delta F \leftarrow F_{sys}(t + \Delta t) - M_{sys} \cdot n'' - C_{sys} \cdot n' - K_{sys}(CRACKED, n, Z) \cdot n$ Incremental Force used in next time step

$\eta_i \leftarrow n$

if CRACKED = 0 Displacement Triggers for changes in Stiffness.

  if $n \geq 0.18mm$ Cracking at the base of the wall is triggered at 0.18 mm of calculated model displacement

    $Z \leftarrow 0$

    $CRACKED \leftarrow 6$

  $CRACKED \leftarrow 0$ otherwise

if CRACKED = 1

  if $(n) \geq 1.5mm$ Mid-height cracking is triggered at 1.5 mm of calculated model displacement

    $Z \leftarrow 0$

    $CRACKED \leftarrow 3$

  $CRACKED \leftarrow 1$ otherwise

if CRACKED = 2 The additional damage incronment (determined from RD5-22) is triggered at 14.7 mm of displacement.

  if $(n) \geq 14.7mm$

    $CRACKED \leftarrow 5$

    $Z \leftarrow 0$

  $CRACKED \leftarrow 2$ otherwise

if CRACKED = 6 Counters for the Linear Transitions between stiffnesses. Equil Aproximetly 10 sec.

  $Z \leftarrow Z + 1$

  $CRACKED \leftarrow 1$ if $Z > 2000$

if CRACKED = 3

  $Z \leftarrow Z + 1$

  $CRACKED \leftarrow 2$ if $Z > 2000$

if CRACKED = 5

  $Z \leftarrow Z + 1$

  $CRACKED \leftarrow 4$ if $Z > 2000$

break if $n > 40mm$ End Program if Displacement is over 40 mm (Near end of cubic spline curve) The wall has collapsed

η

Appendix I: Displacement Time Histories from Model Study

This appendix presents the results from the single degree of freedom, dynamic model that was created for this study in MathCad 15©.

Figure I.1 to Figure I.24 present the displacement time histories of the model calibrated to Wall RD4,

Figure I.1 to Figure I.5 present the displacement subjected to the first wind series.

Figure I.6 to Figure I.10 present the displacement subjected to the second wind series.

Figure I.11 to Figure I.14 present the displacement subjected to the third wind series.

Figure I.15 to Figure I.19 present the displacement subjected to the fourth wind series.

Figure I.20 to Figure I.24 present the displacement subjected to the fifth wind series.

Figure I.25 to Figure I.47 present the displacement time histories of the model calibrated to Wall RD5,

Figure I.25 to Figure I.29 present the displacement subjected to the first wind series.

Figure I.30 to Figure I.34 present the displacement subjected to the second wind series.

Figure I.35 to Figure I.38 present the displacement subjected to the third wind series.

Figure I.39 to Figure I.43 present the displacement subjected to the fourth wind series.

Figure I.44 to Figure I.47 present the displacement subjected to the fifth wind series.

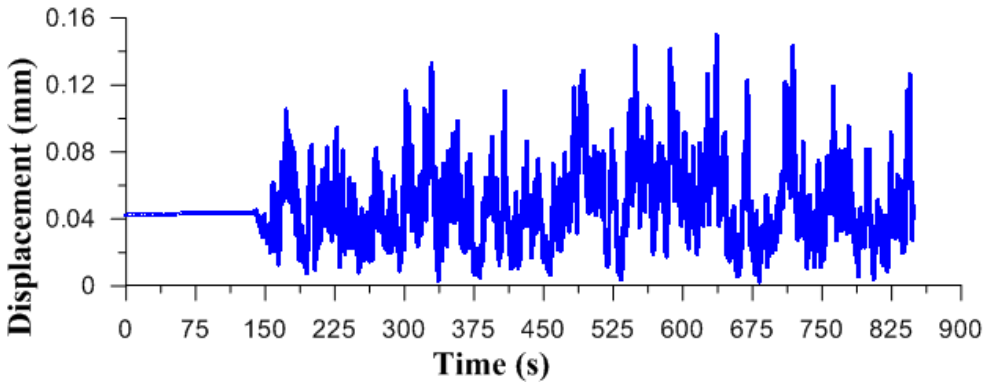

Figure I.1: Model calibrated to RD4, 14 m/s displacement time history for wind series 1

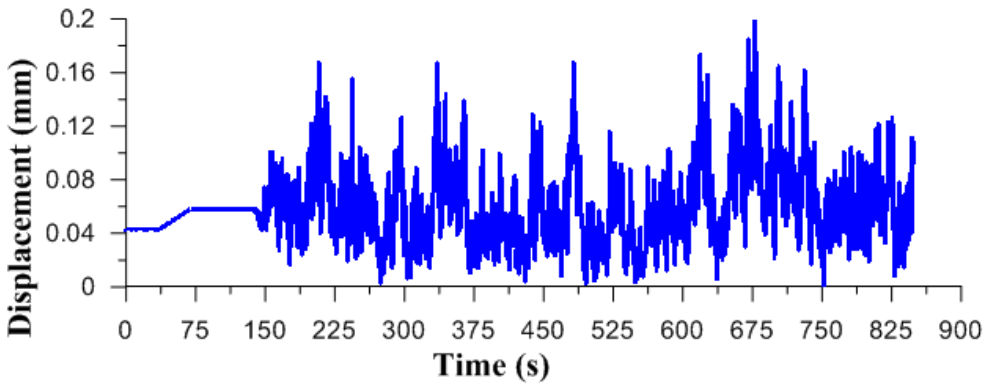

Figure I.2: Model calibrated to RD4, 16 m/s displacement time history for wind series 1

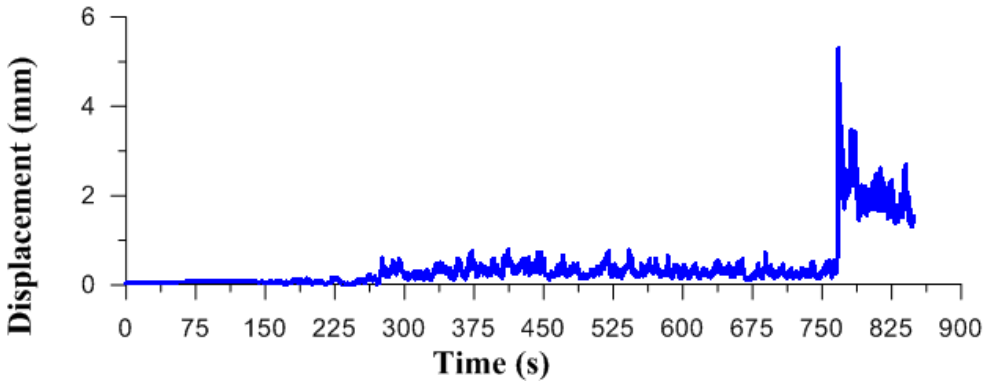

Figure I.3: Model calibrated to RD4, 18 m/s displacement time history for wind series 1

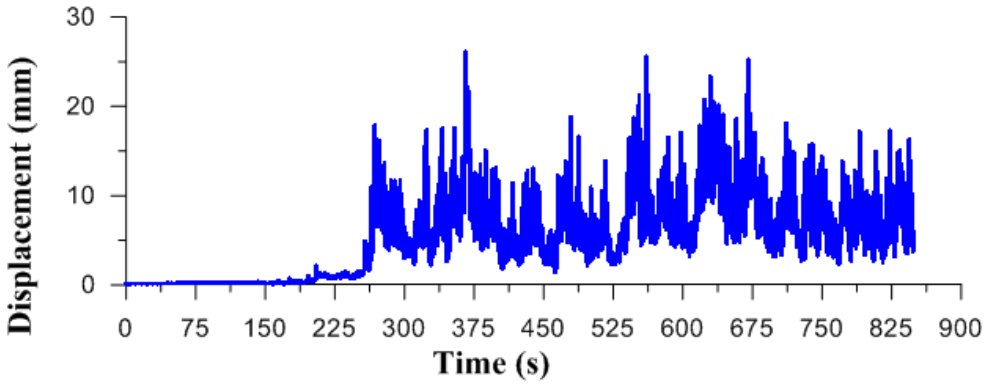

Figure I.4: Model calibrated to RD4, 20 m/s displacement time history for wind series 1

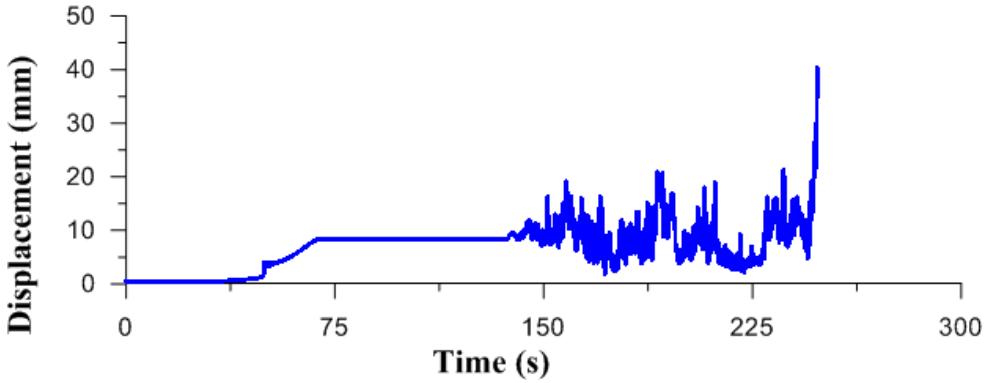

Figure I.5: Model calibrated to RD4, 22 m/s displacement time history for wind series 1

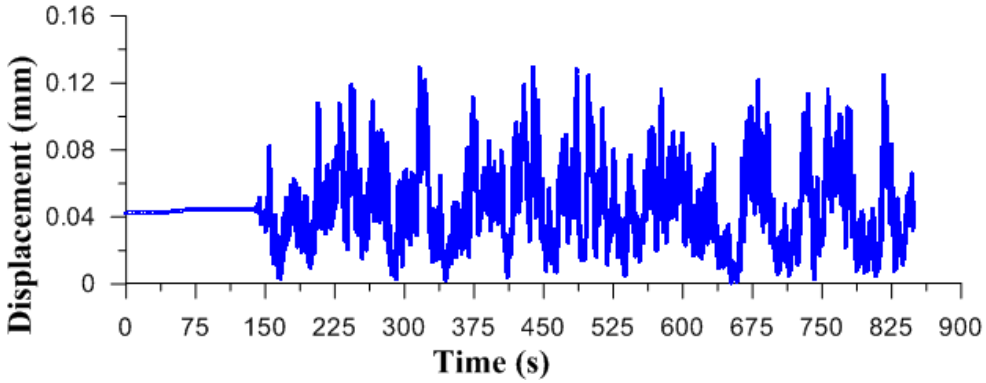

Figure I.6: Model calibrated to RD4, 14 m/s displacement time history for wind series 2

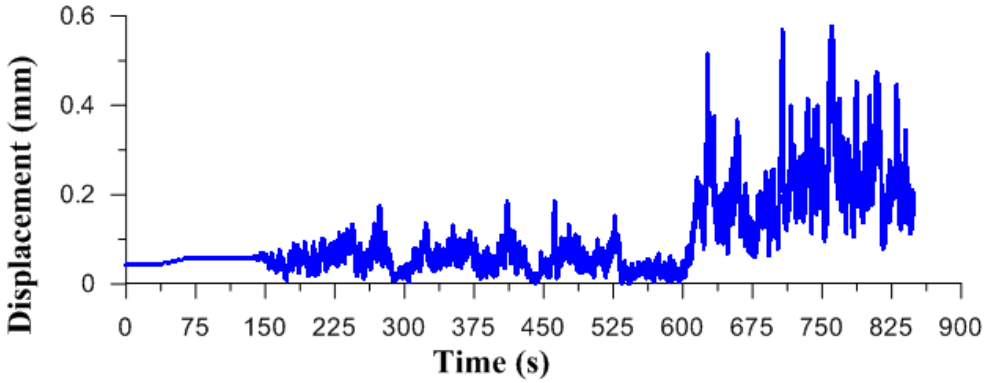

Figure I.7: Model calibrated to RD4, 16 m/s displacement time history for wind series 2

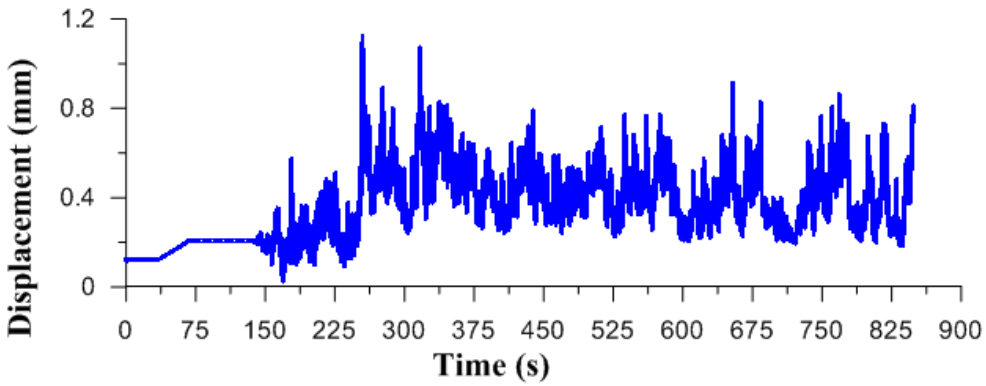

Figure I.8: Model calibrated to RD4, 18 m/s displacement time history for wind series 2

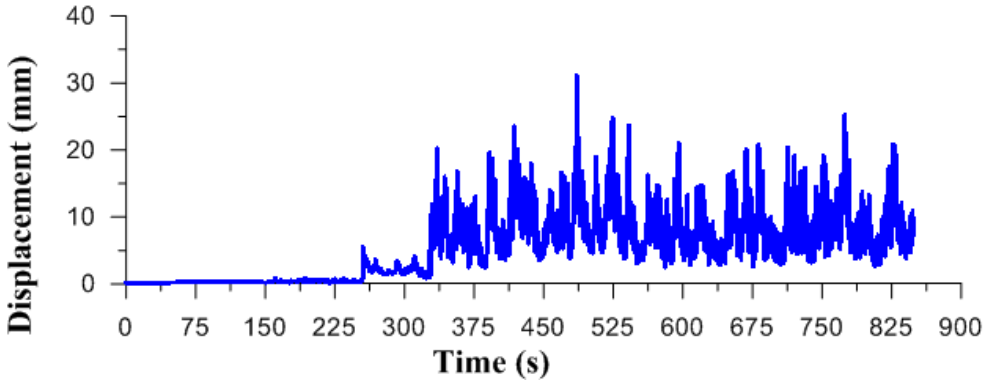

Figure I.9: Model calibrated to RD4, 20 m/s displacement time history for wind series 2

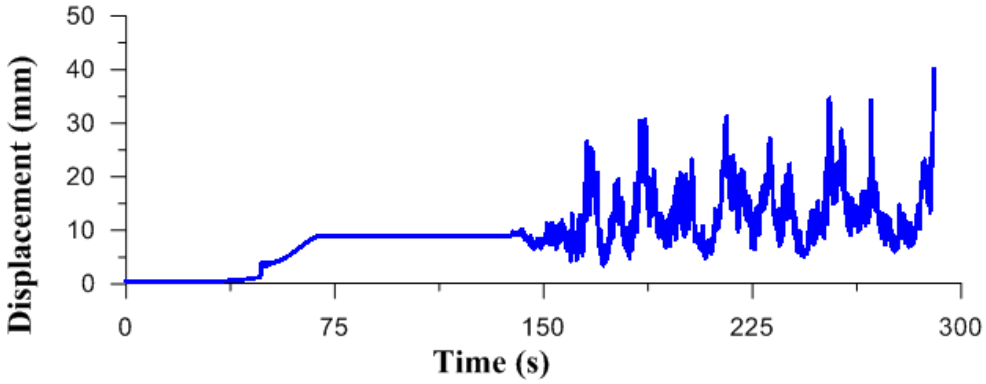

Figure I.10: Model calibrated to RD4, 22 m/s displacement time history for wind series 2

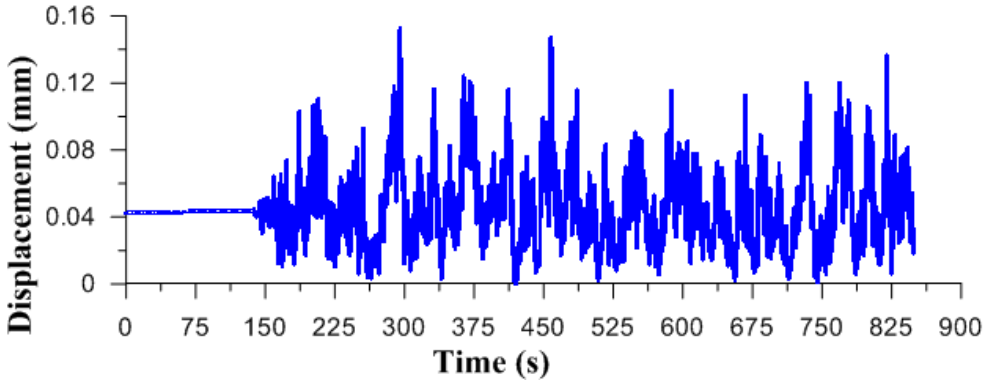

Figure I.11: Model calibrated to RD4, 14 m/s displacement time history for wind series 3

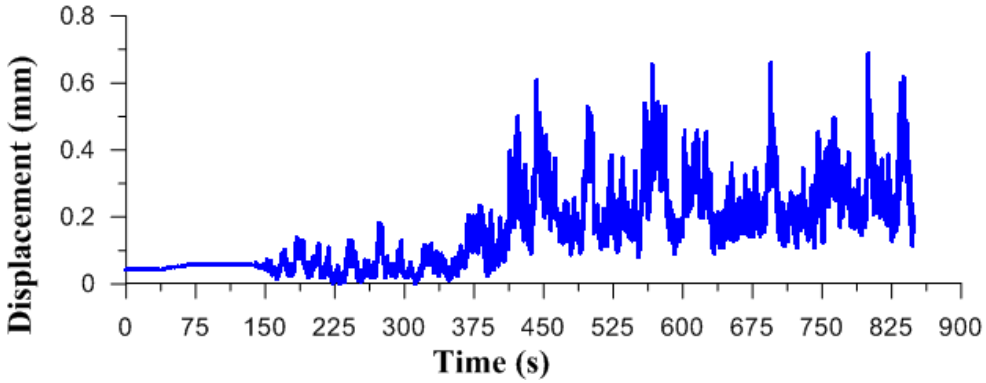

Figure I.12: Model calibrated to RD4, 16 m/s displacement time history for wind series 3

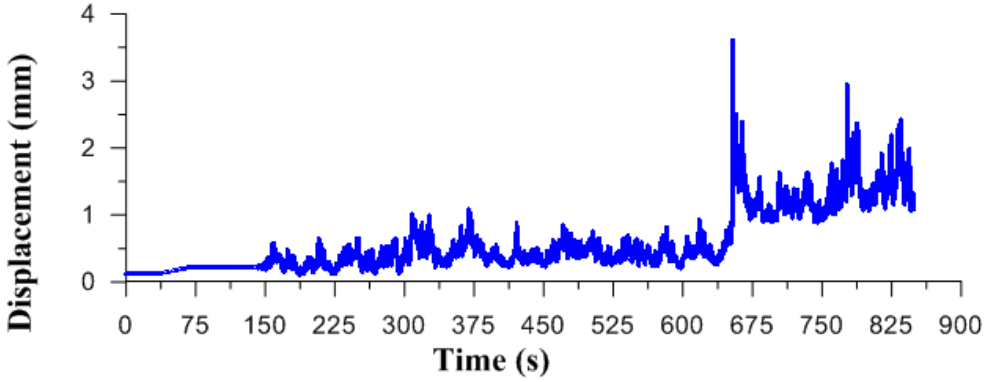

Figure I.13: Model calibrated to RD4, 18 m/s displacement time history for wind series 3

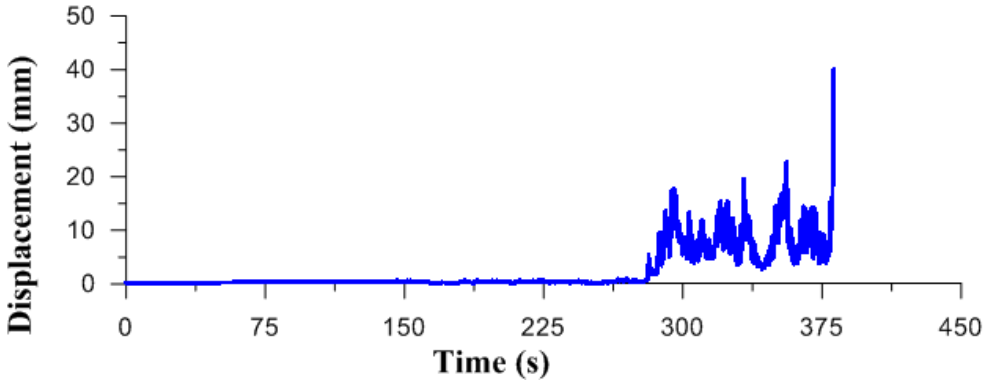

Figure I.14: Model calibrated to RD4, 20 m/s displacement time history for wind series 3

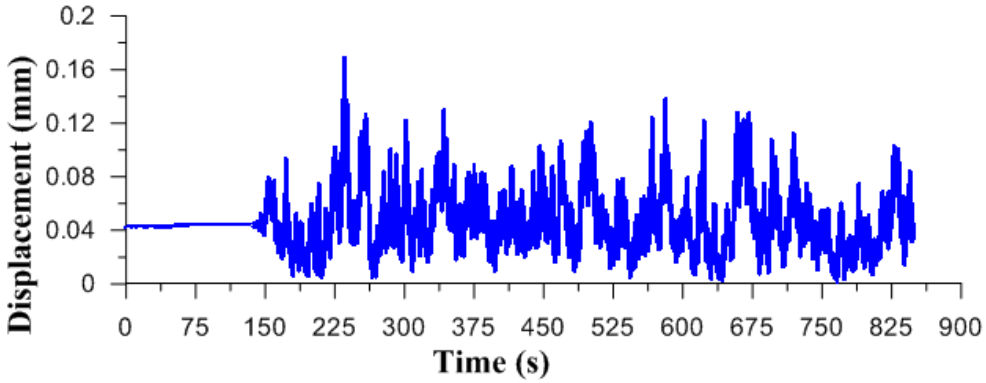

Figure I.15: Model calibrated to RD4, 14 m/s displacement time history for wind series 4

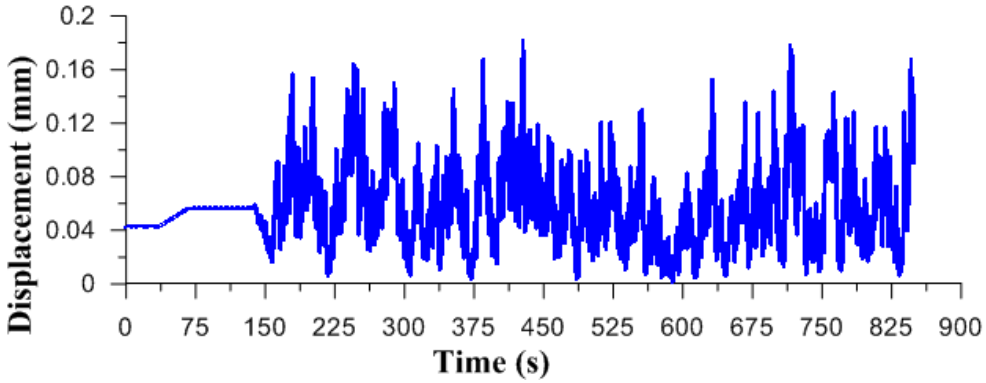

Figure I.16: Model calibrated to RD4, 16 m/s displacement time history for wind series 4

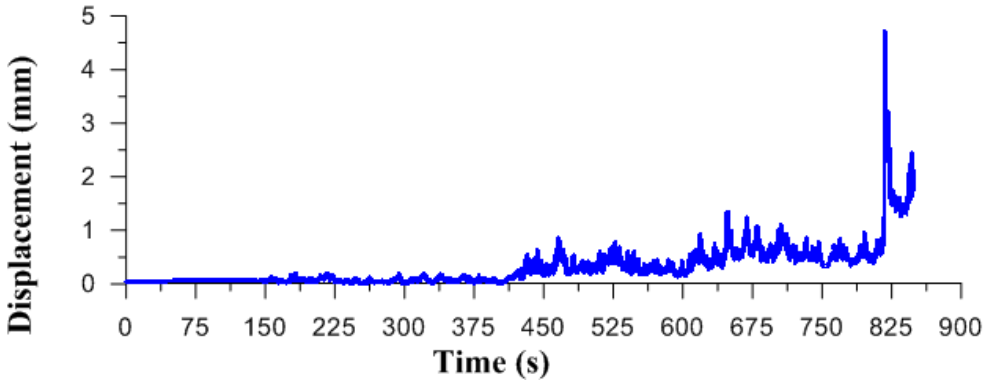

Figure I.17: Model calibrated to RD4, 18 m/s displacement time history for wind series 4

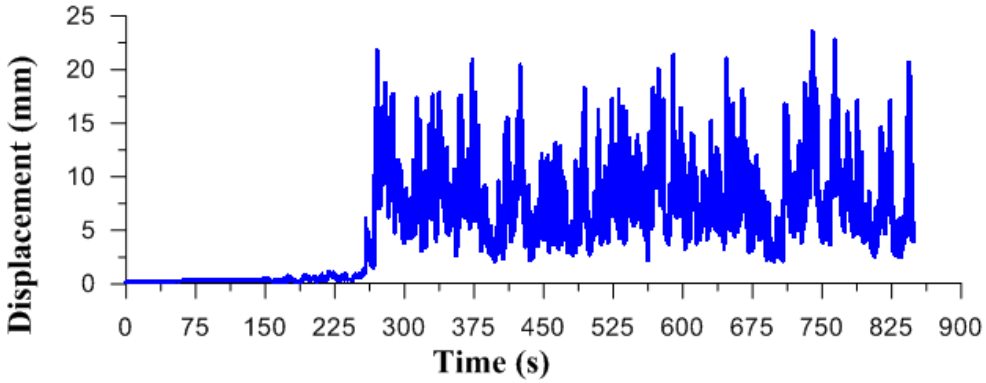

Figure I.18: Model calibrated to RD4, 20 m/s displacement time history for wind series 4

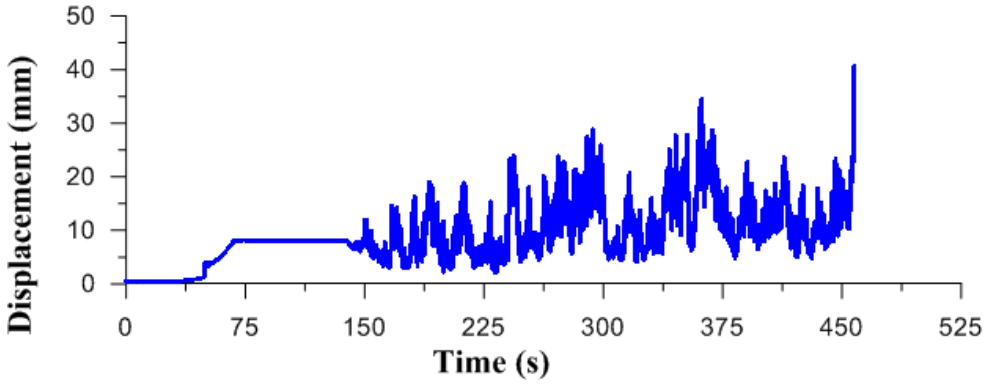

Figure I.19: Model calibrated to RD4, 22 m/s displacement time history for wind series 4

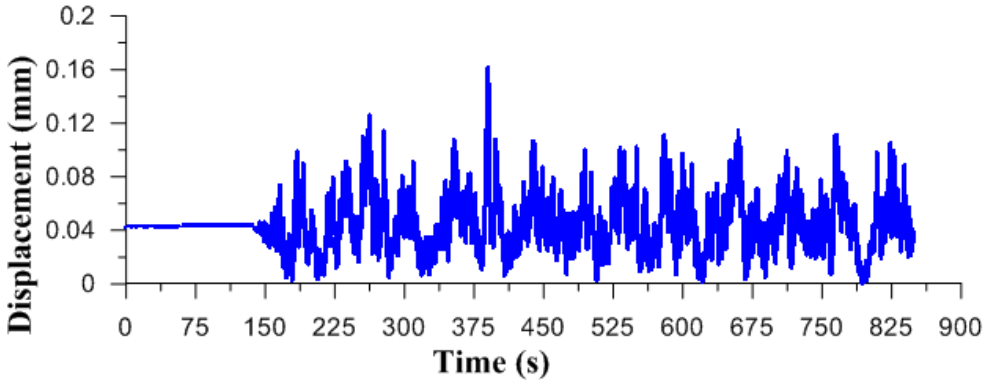

Figure I.20: Model calibrated to RD4, 14 m/s displacement time history for wind series 5

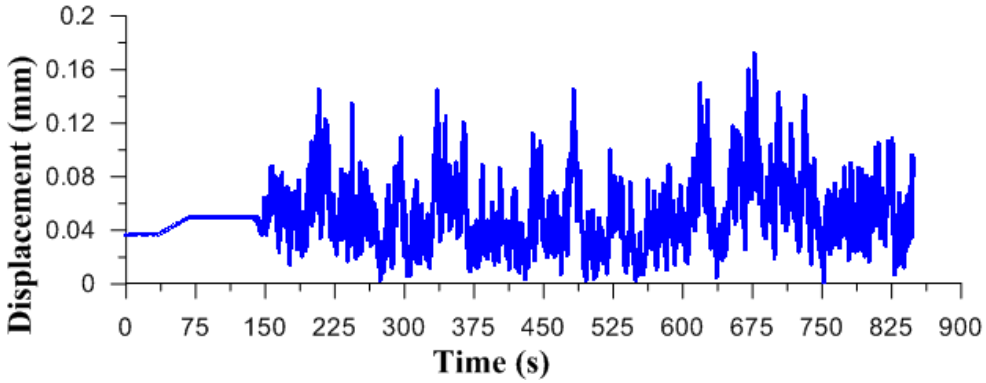

Figure I.21: Model calibrated to RD4, 16 m/s displacement time history for wind series 5

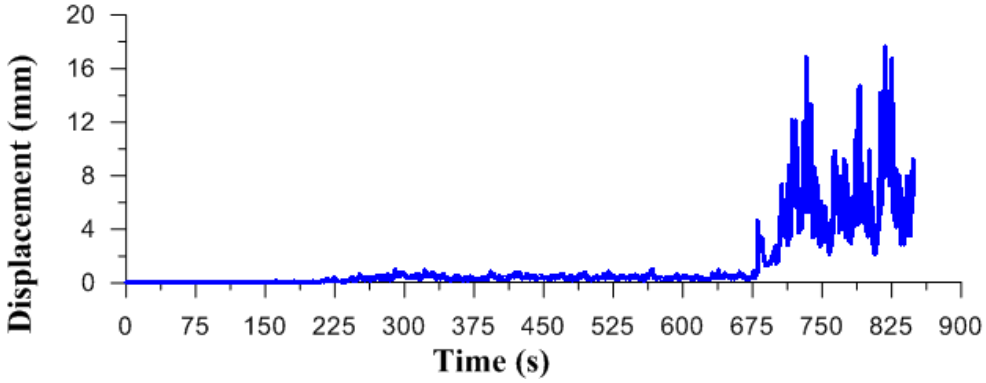

Figure I.22: Model calibrated to RD4, 18 m/s displacement time history for wind series 5

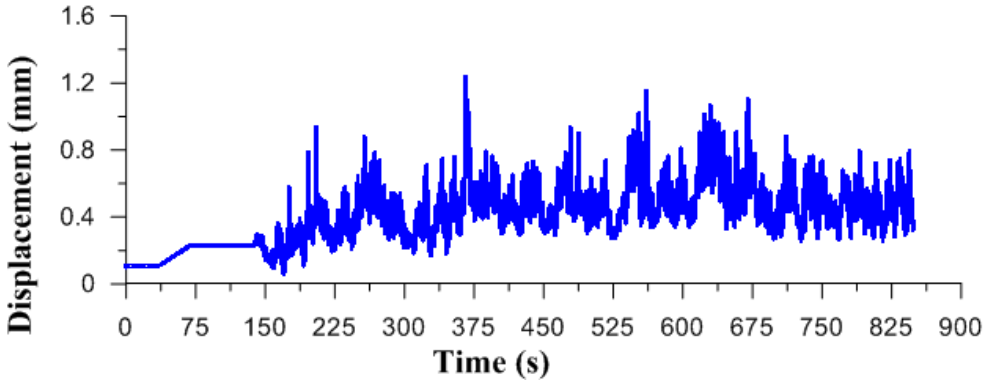

Figure I.23: Model calibrated to RD4, 20 m/s displacement time history for wind series 5

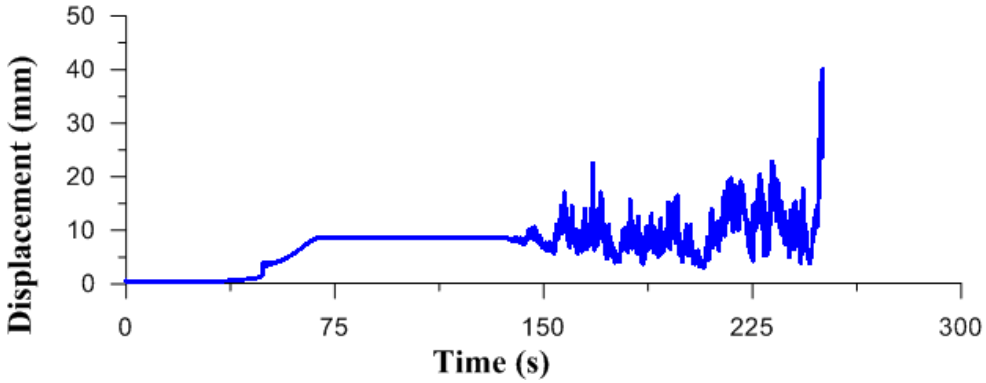

Figure I.24: Model calibrated to RD4, 22 m/s displacement time history for wind series 5

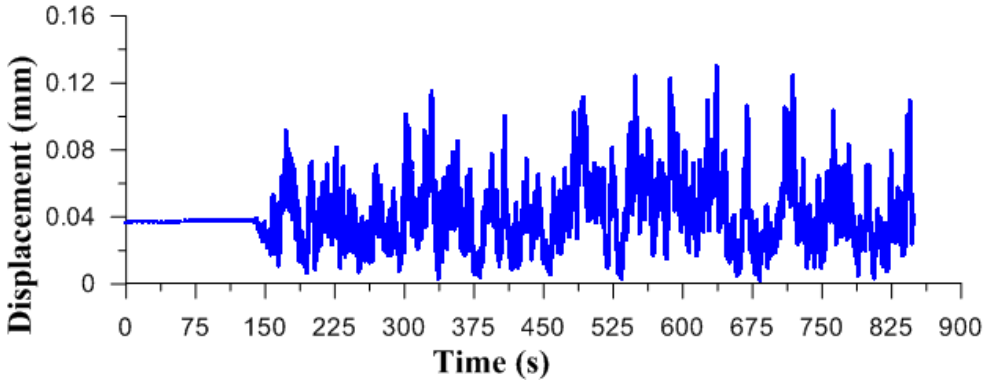

Figure I.25: Model calibrated to RD5, 14 m/s displacement time history for wind series 1

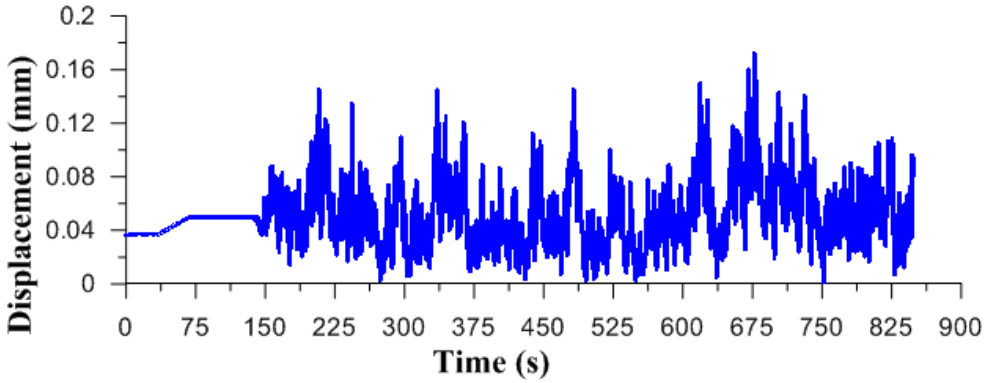

Figure I.26: Model calibrated to RD5, 16 m/s displacement time history for wind series 1

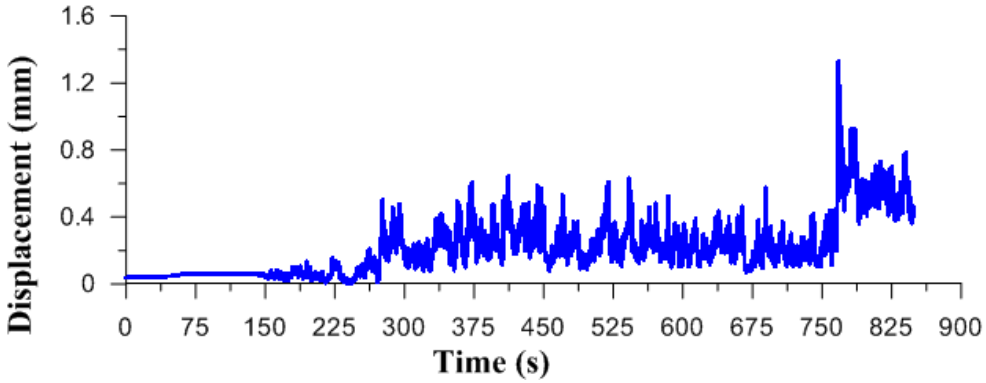

Figure I.27: Model calibrated to RD5, 18 m/s displacement time history for wind series 1

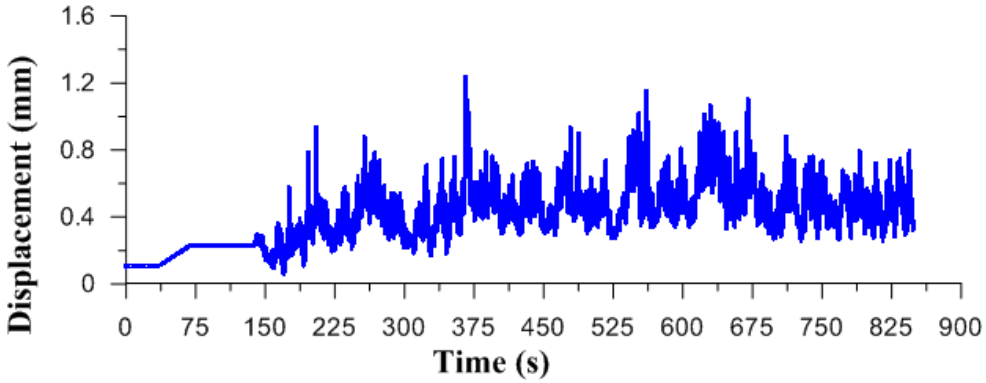

Figure I.28: Model calibrated to RD5, 20 m/s displacement time history for wind series 1

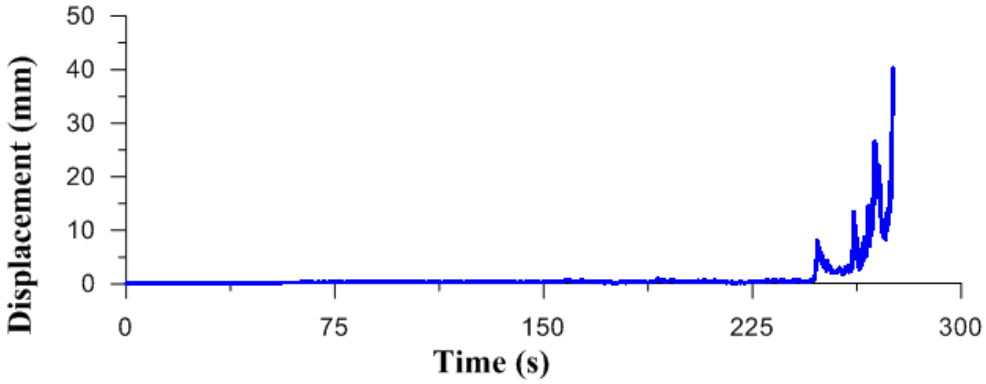

Figure I.29: Model calibrated to RD5, 22 m/s displacement time history for wind series 1

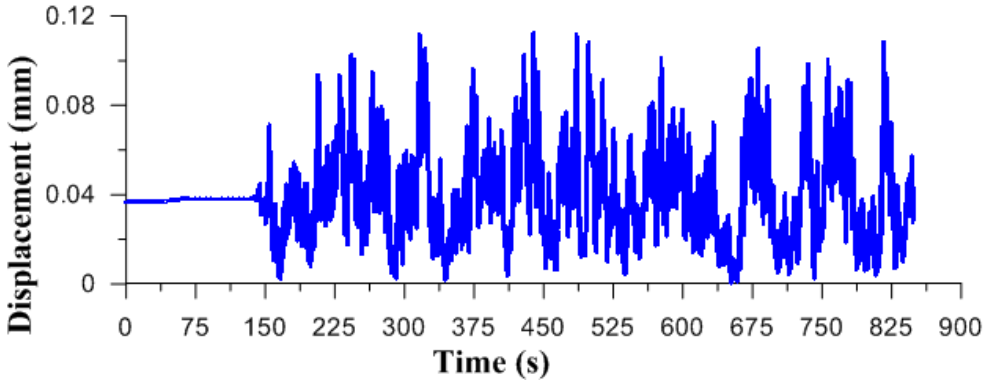

Figure I.30: Model calibrated to RD5, 14 m/s displacement time history for wind series 2

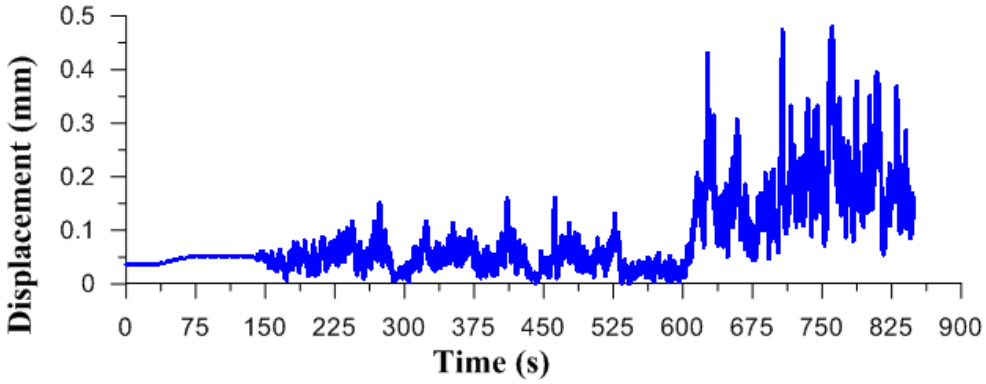

Figure I.31: Model calibrated to RD5, 16 m/s displacement time history for wind series 2

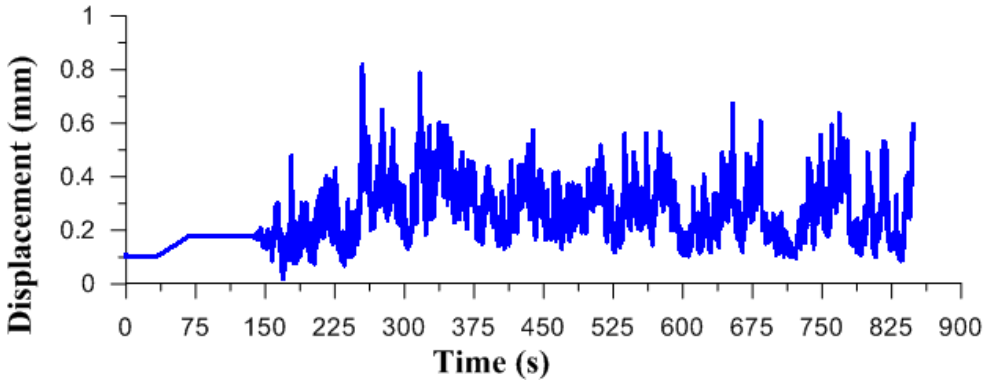

Figure I.32: Model calibrated to RD5, 18 m/s displacement time history for wind series 2

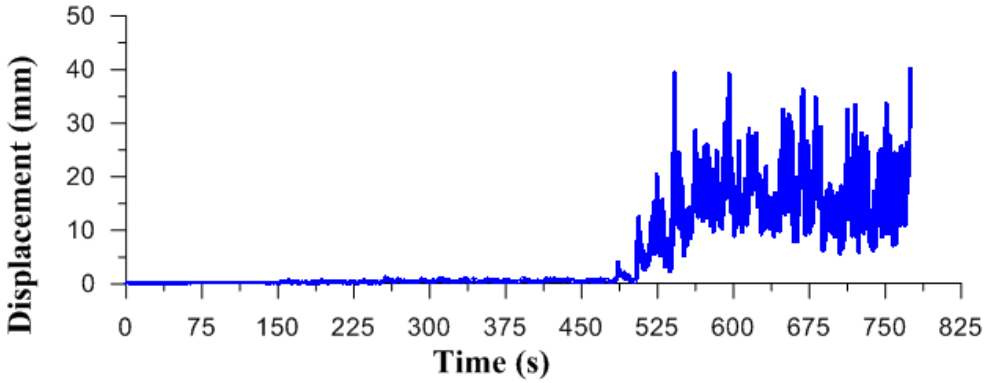

Figure I.33: Model calibrated to RD5, 20 m/s displacement time history for wind series 2

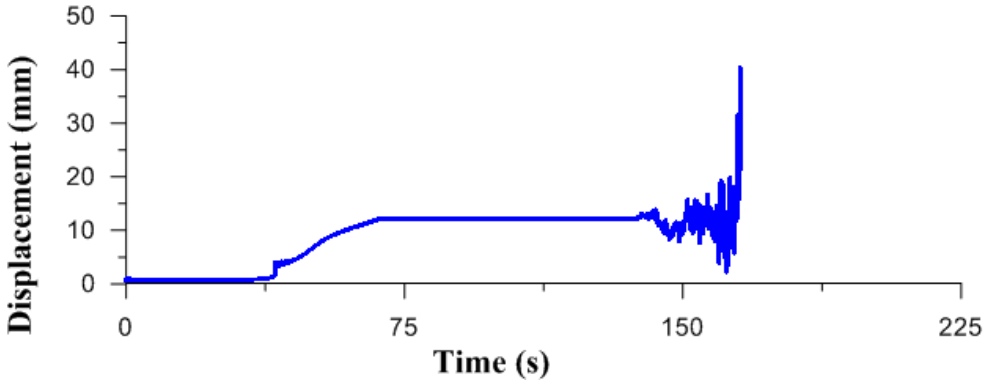

Figure I.34: Model calibrated to RD5, 22 m/s displacement time history for wind series 2

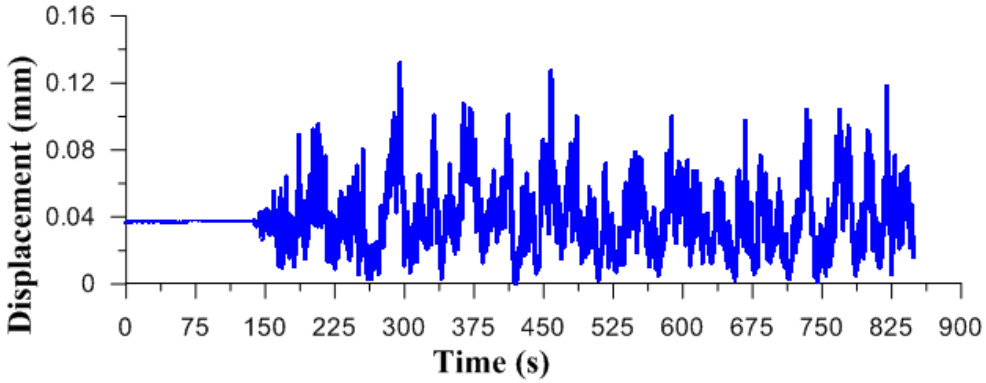

Figure I.35: Model calibrated to RD5, 14 m/s displacement time history for wind series 3

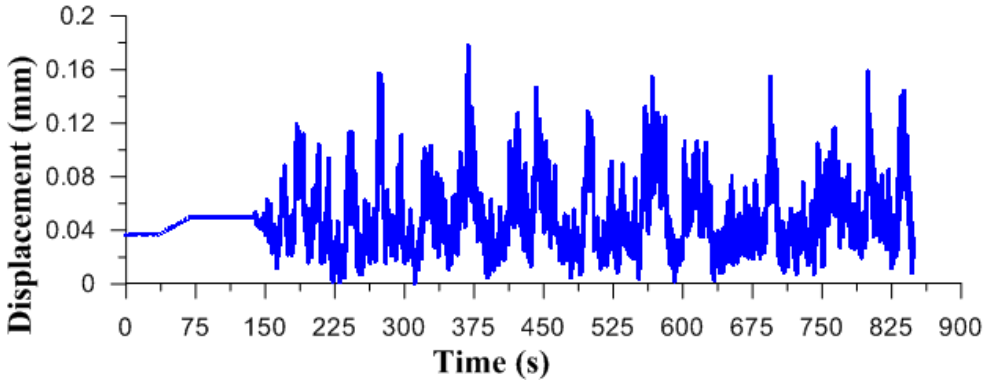

Figure I.36: Model calibrated to RD5, 16 m/s displacement time history for wind series 3

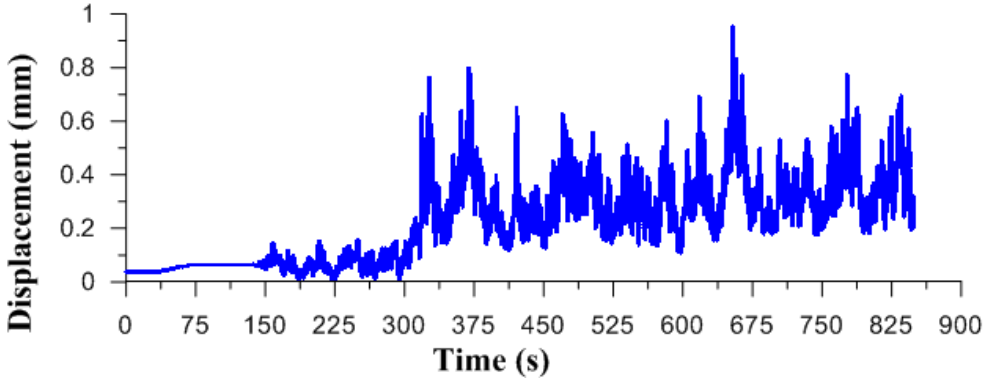

Figure I.37: Model calibrated to RD5, 18 m/s displacement time history for wind series 3

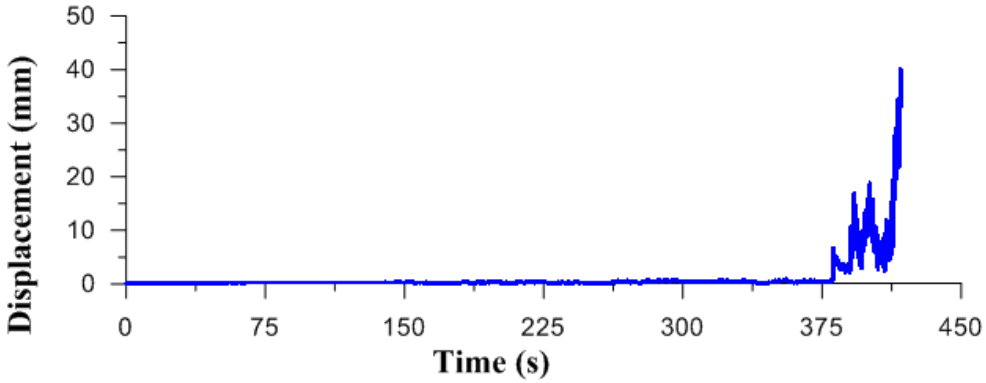

Figure I.38: Model calibrated to RD5, 20 m/s displacement time history for wind series 3

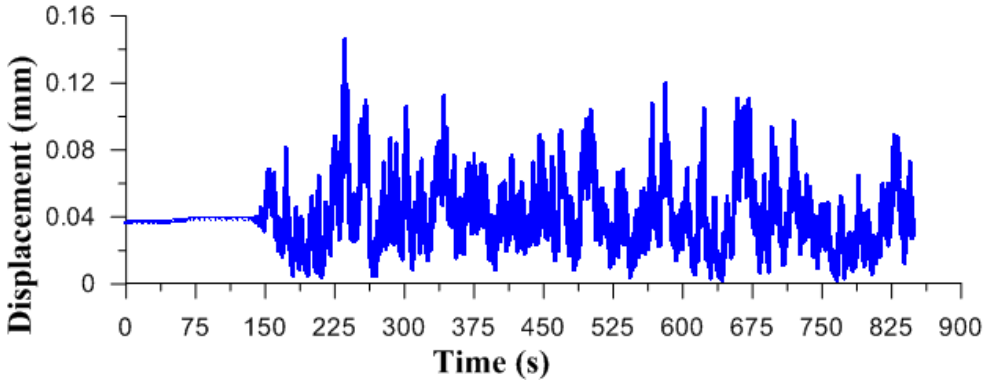

Figure I.39: Model calibrated to RD5, 14 m/s displacement time history for wind series 4

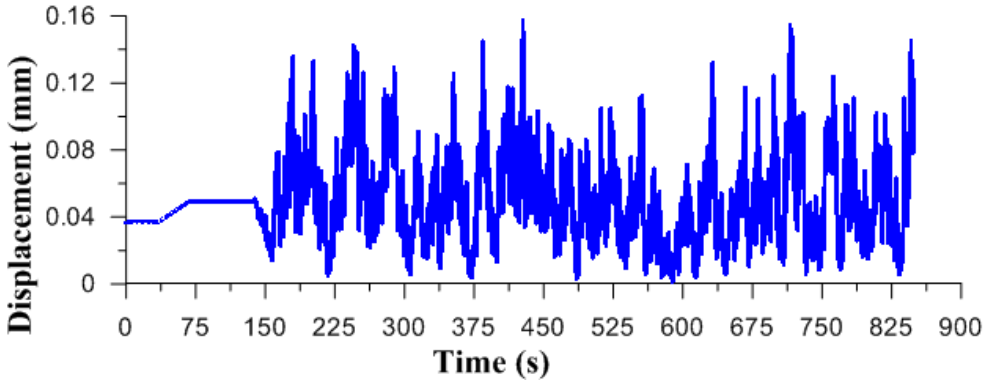

Figure I.40: Model calibrated to RD5, 16 m/s displacement time history for wind series 4

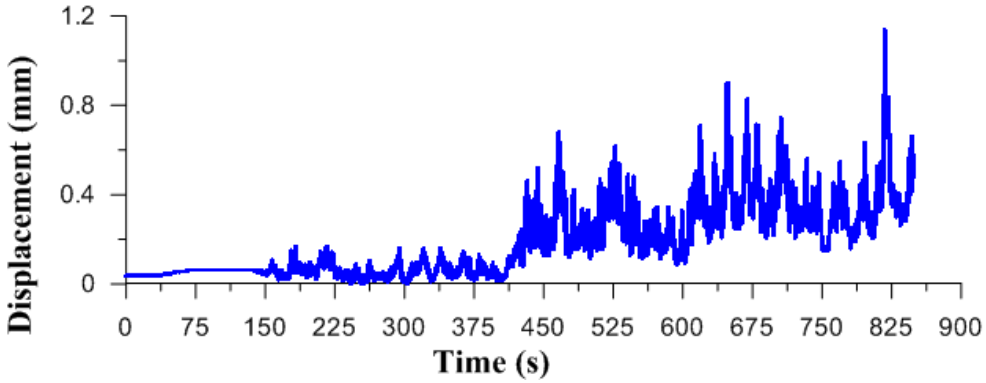

Figure I.41: Model calibrated to RD5, 18 m/s displacement time history for wind series 4

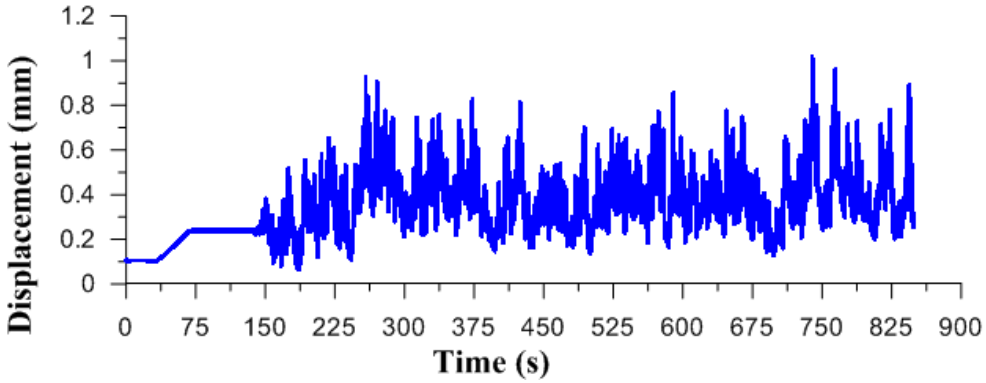

Figure I.42: Model calibrated to RD5, 20 m/s displacement time history for wind series 4

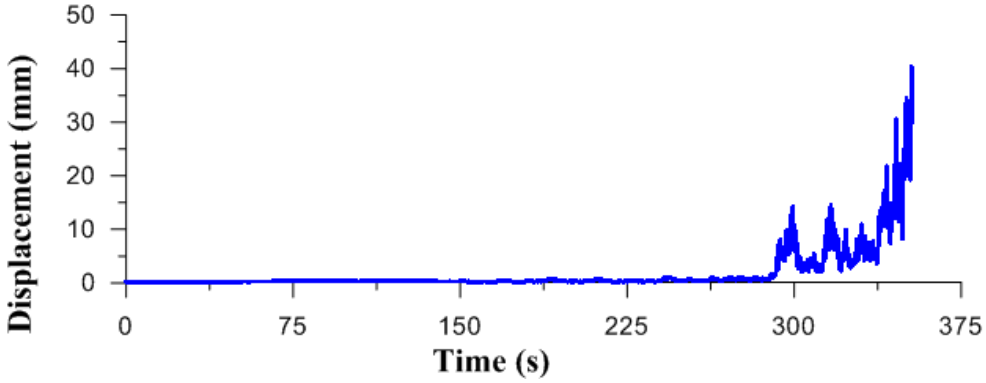

Figure I.43: Model calibrated to RD5, 22 m/s displacement time history for wind series 4

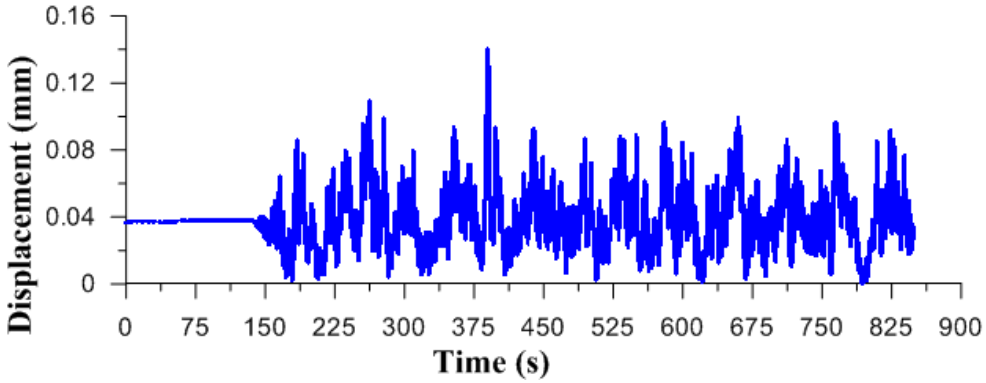

Figure I.44: Model calibrated to RD5, 14 m/s displacement time history for wind series 5

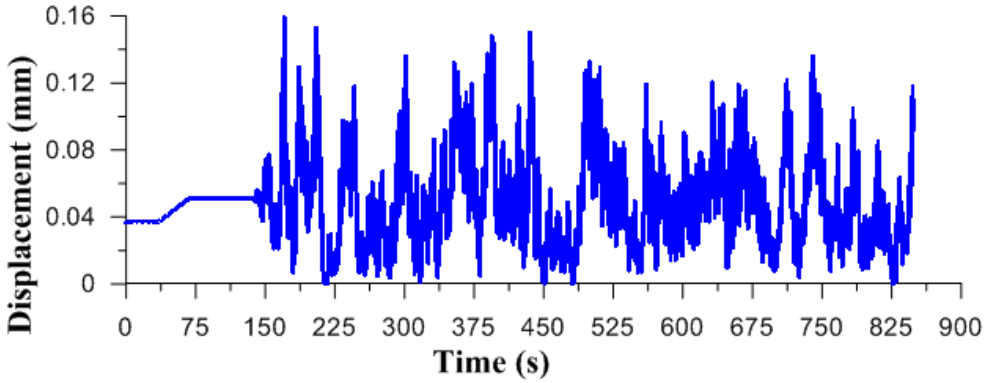

Figure I.45: Model calibrated to RD5, 16 m/s displacement time history for wind series 5

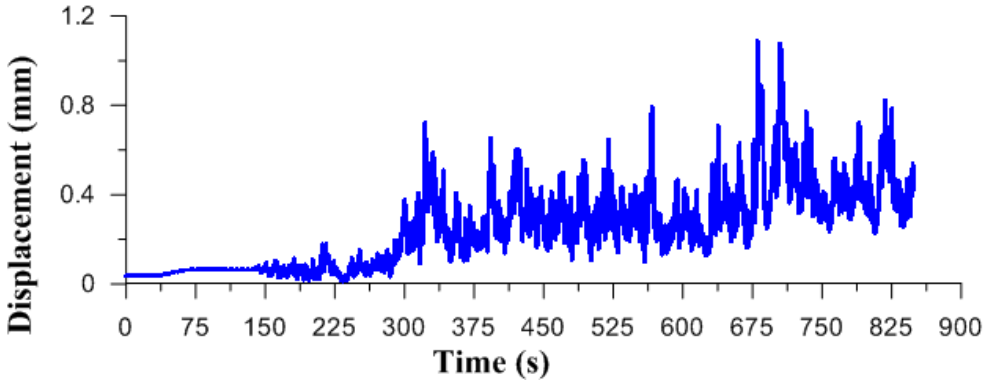

Figure I.46: Model calibrated to RD5, 18 m/s displacement time history for wind series 5

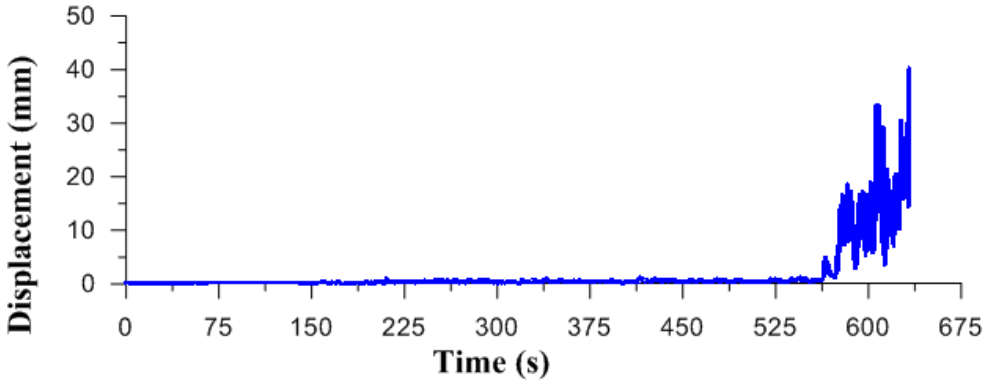

Figure I.47: Model calibrated to RD5, 20 m/s displacement time history for wind series 5